

***Continuous Dynamic Simulation of Nonlinear
Aerodynamics/Nonlinear Structure Interaction (NANSI) for
Morphing Vehicles***

STTR PHASE II FINAL REPORT

Contract No. FA9550-08-C-0004

Contractor: ZONA Technology, Inc.
9489 E. Ironwood Square Drive
Scottsdale, AZ 85258
Tel (480) 945-9988 / Fax (480) 945-6588
PI: Ping-Chih Chen, pc@zonatech.com

Subcontractor: Arizona State University
Office of Research and Sponsored Projects Administration
Tempe, AZ 85287-3503
Tel (480) 965-3086 / Fax (480) 965-5479

Issued by: USAF/AFRL, AFOSR
Timothy Harr
875 North Randolph Street, Room 3112
Arlington, VA 22203-1977
Tel: 703-696-5906
Email: timothy.harr@afosr.af.mil

Program Manager: Dr. Fariba Fahroo
Air Force Office of Scientific Research
875 North Randolph Street, Suite 325, Room 3112
Arlington, VA 22203-1977
Tel (703) 696-8429
Email: fariba.fahroo@afosr.af.mil

Contract No. FA9550-08-C-0004
STTR Topic No.: AF05-T027
Report No.: 0001F
Item No. 0001F
Report Date: March 31, 2010
Period of Performance: 10/01/07 – 3/31/10
Contract Start Date: October 1, 2007
Contract End Date: March 31, 2010

20120918127

DISTRIBUTION STATEMENT A:
DISTRIBUTION APPROVED FOR PUBLIC RELEASE; DISTRIBUTION UNLIMITED



***Continuous Dynamic Simulation of Nonlinear
Aerodynamics/Nonlinear Structure Interaction (NANSI) for
Morphing Vehicles***

Contract No. FA9550-08-C-0004

Progress Report Period (10/01/07 ~ 3/31/10)

TABLE OF CONTENTS

Summary	1
1.0 Nonlinear Structural ROM and Morphing Dynamics for Folding Wing	3
1.1 Folding Wing Structural Model and its Morphing	3
1.2 Folding Wing Substructure Modeling/Component Mode Synthesis	4
1.3 Validation of Angular Velocity and Angular Acceleration Terms	21
2.0 Nonlinear Aeroelasticity of Continuous Morphing Folding Wing by Full-Order Approach	23
2.1 Validation of the Linear Substructure Model: Two-Piece vs. One- Piece Wings	24
2.2 Quasi-Steady Flutter Boundary: Folding Wing	27
2.3 Continuous Morphing Simulation: Folding Wing	28
2.4 Validation of the Non-Linear Substructure Model: Two-Piece vs. One Piece Wings	32
2.5 Comparison of the Aeroelastic Responses between the Two-Pieces Linear and Non-Linear Models	33
3.0 Aerodynamic ROM/Aeroelastic ROM-ROM Methodology for Folding Wing	36
3.1 Aerodynamic ROM Methodology	38
3.2 LCO Solutions for the Folding Wing using ROM-ROM	39
4.0 3D Gridless Boundary Condition Cartesian (GBCC) Development	45
4.1 The GBCC Flow Solver	45

4.2	The Improved GBCC Stencil.....	46
4.3	New GBCC2D Solutions	47
4.4	GBCC3D Grid Cutting Procedure	49
4.5	GBCC3D Solver Development: Verification and Validation.....	55
4.6	Unsteady Computation.....	59
5.0	MAV Modal Testing, Structural FEM and Aeroelastic Investigation	62
5.1	Digitization, Modal and Material Testing.....	64
5.2	MAV Finite Element Modeling	69
5.3	MAV Aeroelastic Investigation	78
6.0	ZONA's Euler Unsteady Aerodynamic Solver (ZEUS).....	86
6.1	Body-Fitted Grid for Body Modeling	86
6.2	Surface Mesh with Triangular Cells	89
6.3	Preconditioning	92
6.4	Vorticity Confinement	93
7.0	Consideration of Uncertainty in the Morphing Wing	97
7.1	Nonparametric Stochastic Modeling.....	98
7.2	Applications to the Morphing Wing Aeroelasticity.....	101
8.0	References	108
9.0	Personnel Supported.....	110
10.0	Publications	111
11.0	Interactions/Transitions	112
12.0	New Discoveries, Inventions, or Patent Disclosures	113
13.0	Honors/Awards.....	114
Attachment A – <i>Continuous Dynamic Simulation of Nonlinear Aerodynamic/Nonlinear Structure Interaction (NANSI) for Morphing Vehicles</i> Presentation Slides.....		A-1
Attachment B – <i>Nonlinear Aeroelastic Methodology for a Membrane-on- Ballute Model with Hypersonic Bow Shock</i> Presentation Slides		B-1
Attachment C – <i>Reduced Order Modeling for Geometrically Nonlinear Structural Dynamic Problems</i> Presentation Slides		C-1

Attachment D – <i>Aeroelastic ROM-ROM Methodology</i> Presentation Slides....	D-1
Attachment E – <i>Morphing Wing Aeroelasticity by Continuous Dynamic Simulation using Nonlinear Aerodynamic/Nonlinear Structure Interaction (NANSI) Methodology</i> Presentation Slides.....	E-1
Attachment F – <i>Equations of Motion</i>	F-1
Attachment G – <i>Nonlinear Reduced Order Modeling of Flat Cantilevered Structures</i>	G-1
Attachment H – <i>Nonlinear Reduced Order Modeling of Flat Cantilevered Structures</i> P.h.D. Thesis.....	H-1

SUMMARY

In this report, we present the ZONA team's effort for this Phase II project. The ZONA team is made up of ZONA Technology, Inc. (ZONA), Arizona State University (Research Institute), and Professor Feng Liu (Consultant). The objective for this project was to develop a nonlinear aerodynamic and nonlinear structural interaction (NANSI) methodology as an expedient aeroelastic tool to handle continuous dynamic motion of morphing vehicles/wings from incompressible/subsonic to transonic flight regimes. The proposed vehicle for method demonstration was the Lockheed Folding wing (the Folding wing). Results showing the Flutter/LCO of the Folding wing in continuous pitching and the Finite Element Model (FEM) development/aeroelastic stability analysis of a morphing MAV, or the Gull wing/MAV, are presented.

Chapter 1 describes the development of the nonlinear structural reduced order modeling (ROM) and morphing dynamics in terms of sub-structural formulation for the Folding wing. Chapter 2 presents the results of direct, and full-order aeroelastic solutions in terms of flutter/LCO for the Folding wing in quasi-steady and continuous dynamic morph motions. Chapter 3 presents the establishment of the aerodynamic ROM methodology based on a system identification strategy, with which an aeroelastic ROM-ROM methodology has been successfully developed. In terms of flutter/LCO solutions of the Folding wing, a selected example shows that ROM-ROM dramatically reduces the computing time by 2-orders of magnitude as opposed to that required by the direct method. Chapter 4 presents the gridless boundary condition Cartesian (GBCC) developmental procedure. The GBCC solver procedure was properly verified and its computed result for a Golland wing validated. Chapter 5 presents a complete aeroelastic investigation procedure of a Gull wing/MAV designed and fabricated by University of Florida. Basic procedures for the Gull wing/MAV including modal testing, development of a Structural FEM and aeroelastic investigations are presented in detail. Chapter 6 presents the development of several new capabilities in ZONA's Euler Unsteady Aerodynamic Solver (ZEUS. ZEUS has been integrated into RETINAS to increase the fidelity, accuracy and computational savings. Chapter 7 presents a nonparametric stochastic modeling technique for the consideration of uncertainty in the morphing wing.

Key Accomplishments

The ZONA team has accomplished the following:

- (i) A Nonlinear/Linear ROM procedure including morphing dynamics for one and two piece wing components
- (ii) A full-order (direct) CFD/Structure close coupling procedure for the morph Folding wing in quasi-steady motions as well as in continuous dynamic motions up to a morph dihedral angle of 60°.

- (iii) An Aerodynamic ROM and Aeroelastic ROM-ROM procedures for the folding wing. This topic has been presented in the AFRL organized Aeroelastic Workshop in Sedona October 2008, and at the AVT-168 Symposium on Morphing Vehicles, Lisbon, Portugal April 2009.
- (iv) A GBCC procedure for 2D/3D grid cutting procedure was developed. With the GBCC solver developed, transonic aerodynamic solutions were obtained for the Folding wing and Golland wing.
- (v) The dynamic test of the Gull wing (MAV) was carried out in the ASU structural Lab. FEM has been developed for this MAV. Accordingly, flutter/divergence results were obtained and analyzed for this MAV at various dihedral angles.

Chapter 1.

NONLINEAR STRUCTURAL ROM AND MORPHING DYNAMICS FOR THE FOLDING WING

Summary

The work carried out focused on the validation of the proposed dynamic substructuring (or component mode synthesis) approach of the folding wing into inboard and outboard components, especially in the context of a geometrically nonlinear response. Improvements in the nonlinear reduced order modeling scheme, most notably the inclusion of inplane displacements in the model, were found to be necessary and were performed through a novel strategy for the determination of the ROM stiffness coefficients. With this modified approach, a very good prediction of the nonlinear response of the entire folding wing was achieved for tip deflections up to 1/4 of the span. The consideration of structural uncertainty in the model has been completed. The MORPH code providing the dynamic assembly of the nonlinear inboard and outboard wing models has been validated.

1.1 Folding Wing Structural Model and its Morphing

The folding wing considered in Phase I (see Figure 1.1) was again selected for the Phase II effort. In Phase I, it was argued that the hinges could properly operate only if the hinge lines remained straight which would not be guaranteed in general due to the structural deformations unless the sides of the hinges were rendered perfectly rigid. The model in Phase I was thus modified and the lines of the nodes of the finite element model (FEM) corresponding to the hinge lines were rigidified using a series of rigid bars elements (RBAR elements in Nastran). The remaining finite element model was kept as in Phase I and consists of 99 nodes and 80 CQUAD4 elements for the inboard wing and 189 nodes and 160 CQUAD4 elements for the outboard wing. The thickness is constant throughout, i.e. 1.15 in, and aluminium was selected for the wings material.

Note in Figure 1.1(b) Γ denotes the morphing angle and that the outboard wing would remain horizontal through the morphing in the absence of structural deformations. Thus, the inboard wing rotates with an absolute angular velocity, $\dot{\Gamma}\underline{X}$, while the outboard wing rotates with respect to the inboard wing with a relative angular velocity of $\dot{\Gamma}\underline{X}'$ where \underline{X}' is the unit vector in the direction of the hinge line including those from the structural deformations of the inboard wing.

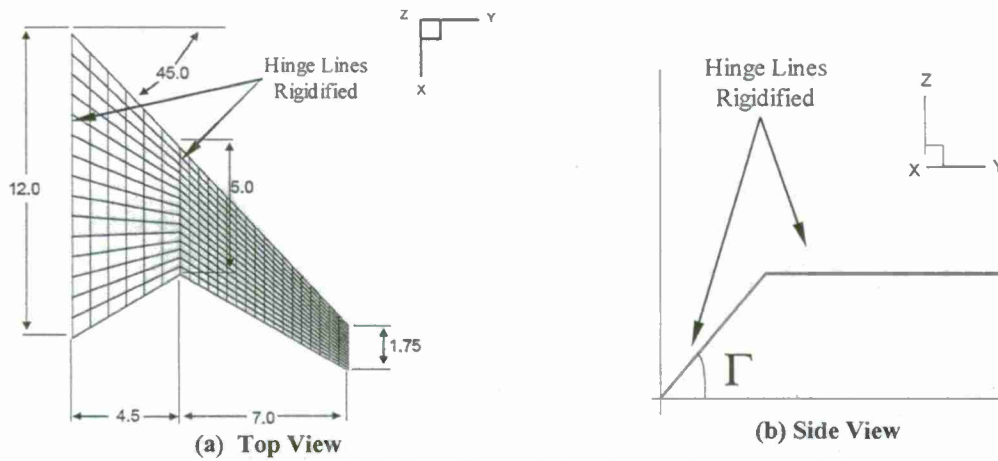


Figure 1.1. Folding Wing Model. Dimensions are in feet.

1.2 Folding Wing Substructure Modeling/Component Mode Synthesis

During morphing, the angle between the inboard and outboard wings will vary and thus even a rigid body dynamic analysis of the system requires a separate consideration for the two components. The characterization of the structural deformations in the entire folding wing must proceed with separate descriptions of the elastic displacements in the inboard and outboard wings, and then the reassembly of the entire wing. Procedures to perform these tasks are usually referred to as dynamic substructuring or component mode synthesis and have been investigated in detail in the case of linear structures. Before discussing the available options, note that the total displacement fields of the inboard and outboard wings can be expressed as:

$$\underline{u}^{(i)}(x, y, z, t) = \underline{u}_R^{(i)}(x, y, z, t) + \underline{u}_E^{(i)}(x, y, z, t) \quad (1.1)$$

and

$$\underline{u}^{(o)}(x, y, z, t) = \underline{u}_R^{(o)}(x, y, z, t) + \underline{u}_E^{(o)}(x, y, z, t) \quad (1.2)$$

where the superscripts (i) and (o) refer to the inboard and outboard wings, while subscripts R and E relate to rigid and elastic bodies, respectively.

The rigid body displacement of the outboard wing, $\underline{u}_R^{(o)}(x, y, z, t)$, will be deduced from the motions of the rigid hinge line, $\underline{u}_H(x, y, z, t)$. Then, in the decomposition of Eq.(1.2), the elastic motions, $\underline{u}_E^{(o)}(x, y, z, t)$, will vanish at all times on the hinge line. Accordingly, it is appropriate to express $\underline{u}_E^{(o)}(x, y, z, t)$ in terms of the cantilevered modes of the outboard wing with the hinge line clamped.

As for the outboard wing, the rigid body displacement of the inboard wing, $\underline{u}_R^{(i)}(x, y, z, t)$, are associated with the rotation around the rigid root of the wing. Thus the elastic displacements $\underline{u}_E^{(i)}(x, y, z, t)$ must vanish there at all times. With this observation, one can formulate the three following dynamic substructuring (or component mode synthesis) strategies for the expansion of $\underline{u}_E^{(i)}(x, y, z, t)$:

- (i) express $\underline{u}_E^{(i)}(x, y, z, t)$ in terms of the *free* interface modes (i.e. cantilevered modes of the inboard, clamped at the root, free at the hinge line) and of attachment modes at the hinge line following the procedures of McNeal, Rubin, or Craig and Chang (see [1.1] for review)
- (ii) express $\underline{u}_E^{(i)}(x, y, z, t)$ in terms of the *fixed* interface modes (i.e. modes of the inboard, clamped at both the root and the hinge line) and of constraint modes at the hinge line following a Craig-Bampton format
- (iii) express $\underline{u}_E^{(i)}(x, y, z, t)$ in terms of the *loaded* interface modes following Benfield and Hruda's procedure.

The first two procedures involve generalized coordinates associated with the modes of the structure (either free or fixed interface modes) but also with "modes" corresponding to the boundary, and forces at the boundary (the attachment modes of approach (i)) or its displacements (the constraint modes of approach (ii)). In the linear case, the inclusion of a handful of extra degrees-of-freedom is not a significant penalty. In nonlinear problems, however, the computational cost and complexity increase significantly with the increasing number of generalized coordinates and thus an approach that is thrifty in generalized coordinates is desired. In contrary to strategies (i) and (ii), the approach of Benfield and Hruda, option (iii) above, satisfies this requirement and thus will be adopted.

The loaded interface modes of the Benfield and Hruda approach correspond to the clamped inboard wing exhibiting additional mass and stiffness matrices on the degrees-of-freedom at the hinge which together form the *loading* of the interface. These mass and stiffness matrices result from the motions of the *outboard* wing induced by the allowed displacements of the interface, i.e. the hinge. For this specific problem, only the allowed displacements of the interface induce the rigid body motions of the outboard wing. Accordingly, there is no stiffness generated and thus no stiffness loading of the inboard wing. Further, the mass loading is associated with the rigid motions of the outboard and thus can be accounted for directly by considering the inboard with the outboard attached as a heavy (i.e. not massless) but rigid component.

Thus, the loaded interface modes of the inboard wing are those corresponding to the flexible inboard to which the outboard wing rigid at $\Gamma=0$ is appended, both components having their respective mass distributions. According to approach (iii), the elastic deformations of the inboard will thus be expressed directly as a linear combination of these loaded interface modes. This component mode synthesis approach is the one suggested and preliminarily validated in Phase I.

1.2.1 Equations of Motion of the Inboard, Outboard, and Complete Morphing Wing

The equations of motion for the flexible inboard and outboard wings has been described in Phase I, see Attachment E for detailed derivation. Since both substructures exhibit similar properties, in particular a rigid interface around which they are rotating (the root for the inboard and the hinge line for the outboard), it is sufficient to consider one of the structures. In this regard, note that it is also necessary to evaluate the forces induced by the outboard on the inboard (see the Phase I report for discussion). Assembling these three sets of equations (equations of motion for the inboard, & outboard, and the expressions for the interface forces) leads to a system of nonlinear equations for the generalized coordinates of the inboard and outboard, stacked in the vector $\underline{q}(t)$ and of components $q_i(t)$.

These equations have the general form

$$\begin{aligned} & M_{ij}^{(1)} \ddot{q}_j + M_{ijl}^{(2)} q_j \ddot{q}_l + C_{ij}^{(1)} \dot{q}_j + \bar{C}_{ij}^{(1)} \omega \dot{q}_j + C_{ijl}^{(2)} \dot{q}_j \dot{q}_l + \bar{C}_{ijl}^{(2)} \omega q_j \dot{q}_l + C_{ijlp}^{(3)} \omega q_j q_l \dot{q}_p \\ & + \bar{C}_{ijlp}^{(3)} q_j \dot{q}_l \dot{q}_p + K_{ij}^{(1)} q_j + \bar{K}_{ij}^{(1)} \omega^2 q_j + \hat{K}_{ij}^{(1)} \dot{\omega} q_j + \hat{K}_{ijl}^{(2)} \omega^2 q_j q_l + \bar{K}_{ijl}^{(2)} \dot{\omega} q_j q_l \\ & + \bar{K}_{ijlp}^{(3)} \omega^2 q_j q_l q_p + K_{ijl}^{(2)} q_j q_l + K_{ijlp}^{(3)} q_j q_l q_p = F_{aero} + F_1 \omega^2 + F_2 \dot{\omega} \end{aligned} \quad (1.3)$$

in which $\omega = \dot{\Gamma}$ and $C_{ij}^{(1)} \dot{q}_j$ is an additional damping term. Note that the nonlinear terms $M_{ijl}^{(2)} q_j \ddot{q}_l$, $C_{ijl}^{(2)} \dot{q}_j \dot{q}_l$, $\bar{C}_{ijl}^{(2)} \omega q_j \dot{q}_l$, $C_{ijlp}^{(3)} \omega q_j q_l \dot{q}_p$, $\bar{C}_{ijlp}^{(3)} q_j \dot{q}_l \dot{q}_p$, $\hat{K}_{ijl}^{(2)} \omega^2 q_j q_l$, $\bar{K}_{ijl}^{(2)} \dot{\omega} q_j q_l$, and $\bar{K}_{ijlp}^{(3)} \omega^2 q_j q_l q_p$ arise from the cross effects of the inboard deformations dependent angular velocity of the hinge (and thus of the outboard wing) and the position and deformations of points on the outboard wing. These terms are quite unusual and only would arise in multibody dynamic systems in which nonlinear terms of the deformations are kept. The investigators are not aware of any available commercial or academic code that could be use to validate/verify the current code (MORPH) implementing the set of equations in Eq.(1.3). Thus, the current validation/verification effort will extend only to the other terms and the details of this effort are described in the ensuing sections. Note finally that the point of the validation/verification is not only to demonstrate the correctness of the formulation and the coding, but also to confirm the adequacy of the dynamic substructuring (or CMS) approach based on Benfield and Hruda's strategy, especially since the modes are determined at $\Gamma=0$, but the motion extends to a broad set of the morphing angles, Γ .

1.2.2 Linear Natural Frequencies and Mode Shapes

The first validation/verification effort focused on the comparison of the natural frequencies and mode shapes of the folding wing, at constant, both zero and nonzero values of Γ , as obtained by the MORPH code and by the Nastran analysis of the corresponding one-piece structure. These computations validate/verify the terms $M_{ij}^{(1)} \ddot{q}_j$ and $K_{ij}^{(1)} q_j$. Shown in Figures 1.2 and 1.3 are the prediction errors of the MORPH estimates of the natural frequencies (Figure 1.2) and mode shapes (Figure 1.3) vs. their counterparts from Nastran. Note that these errors are all less than

1% for the first six modes thereby demonstrating the adequacy of Benfield and Hruda's approach, even at large angles of Γ .

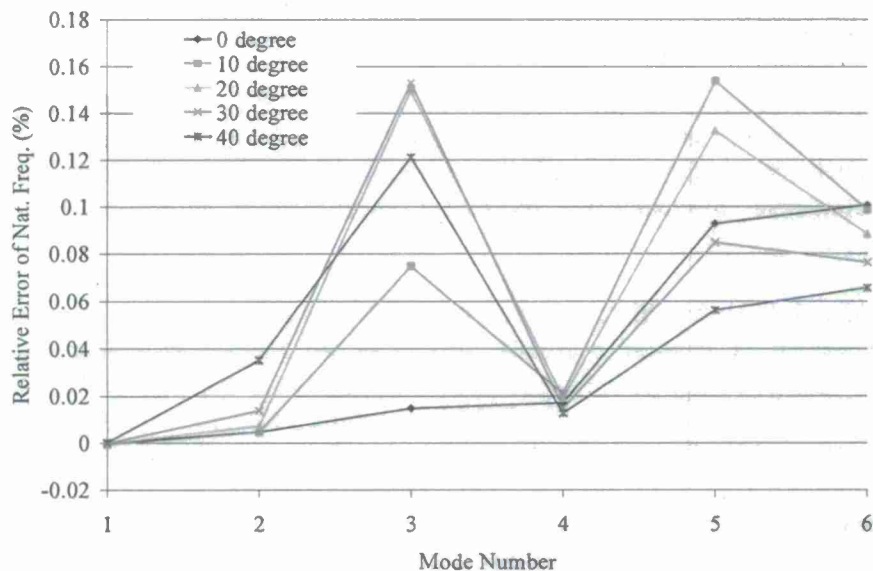


Figure 1.2. Relative Errors of Natural Frequencies Obtained from the Substructuring Approach vs. Full Nastran.

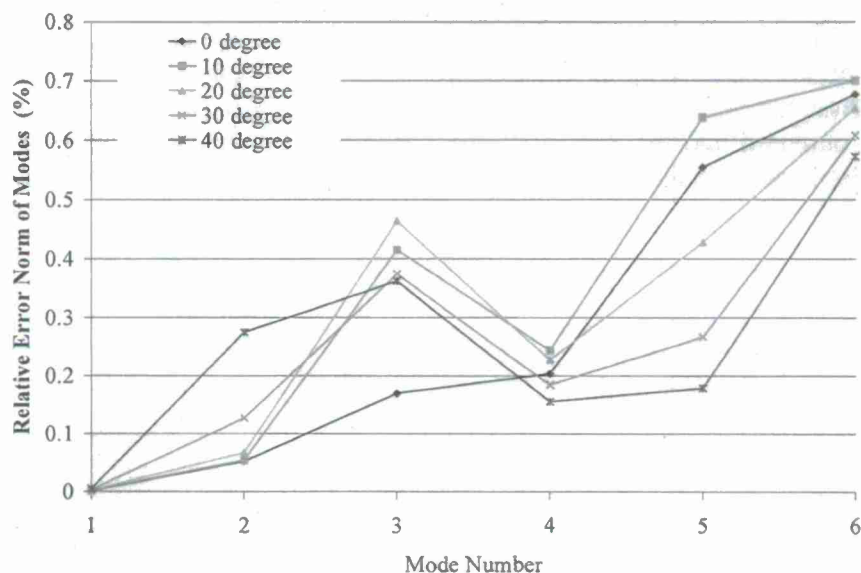


Figure 1.3. Relative Errors of Mode Shapes from Substructuring Approach vs. Full Nastran.

1.2.3 Preliminary Nonlinear ROM Development and Validation: Condensed Models

It was emphasized in the Phase I report that the development of a nonlinear reduced order model (ROM) for cantilevered structures is more challenging than for structures fixed at all or most boundaries. The difficulty is numerical and is associated with the nearly linear behavior of the

transverse response vs. the applied load level, even for very large deformations. This near linearity implies a very small positive effective cubic nonlinearity which still must be captured accurately. It was demonstrated in Phase I that the ELSTEP/FAT methodology used in prior ASU/ZONA work, i.e. the STEP algorithm of [1.2], may lead to negative estimates of the effective cubic nonlinearity and thus numerical instabilities occur.

This difficulty was resolved in Phase I by modifying the ROM procedure to only focus on the transverse displacements *with inplane displacements taking place but not observed*, i.e. the inplane displacements were condensed, thus yielding a so-called "condensed" reduced order model. This condensed approach was successfully demonstrated in Phase I on a model of the entire folding wing at $\Gamma=0^\circ$.

Based on these good results, this condensed approach was selected at the beginning of Phase II for the development of separate nonlinear ROMs of the inboard and outboard wings in the context of the MORPH code for the prediction of the nonlinear response of the complete folding wing. As discussed in Section 1.2, the basis utilized for the outboard wing ROM involved its first cantilevered modes while the loaded modes were selected for the inboard wing ROM basis.

These nonlinear ROMs were first validated by comparing the transverse displacements predicted by the ROMs and the corresponding full Nastran finite element models at the middle of the tip of the wing part (inboard or outboard) due to a series of equal static forces applied at each node of the tip of that wing. The comparison of these displacements is presented in Figures 1.4 and 1.5 for the outboard and inboard wings alone. Since the displacement at the tip of the entire wing will not only depend on the displacements of the inboard and outboard wings at their respective tips, but also on the rotations at the tip of the inboard wing. The ROM vs. Nastran comparison is extended to these inboard rotations, see Figures 1.6 and 1.7. Clearly, both the 4-mode nonlinear ROM of the outboard and the 9-mode ROM of the inboard lead to an excellent match to the Nastran results with the most significant difference being on the small magnitude rotation, R2, see Figure 1.7.

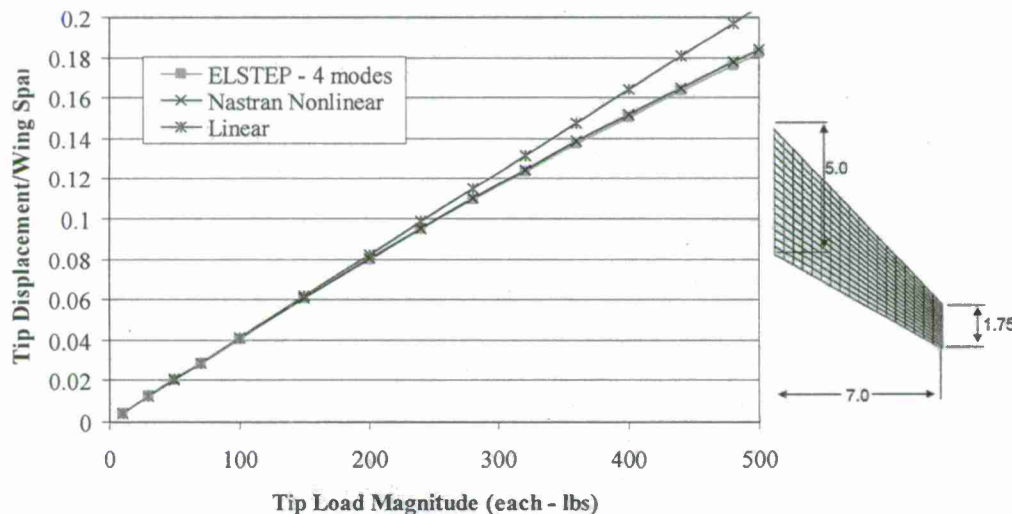


Figure 1.4. Comparison of Tip Displacements Obtained by NASTRAN and by the ELSTEP ROM of the Outboard Wing Alone (normalized by the wing span of the entire wing).

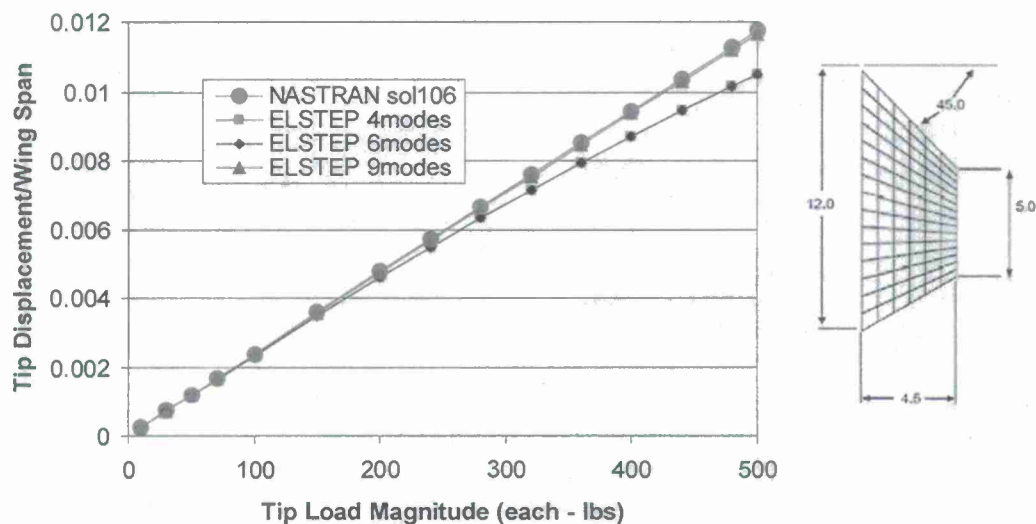


Figure 1.5. Comparison of Tip Displacements Obtained by NASTRAN and by the ELSTEP ROM of the Inboard Wing Alone (normalized by the wing span of the entire wing).

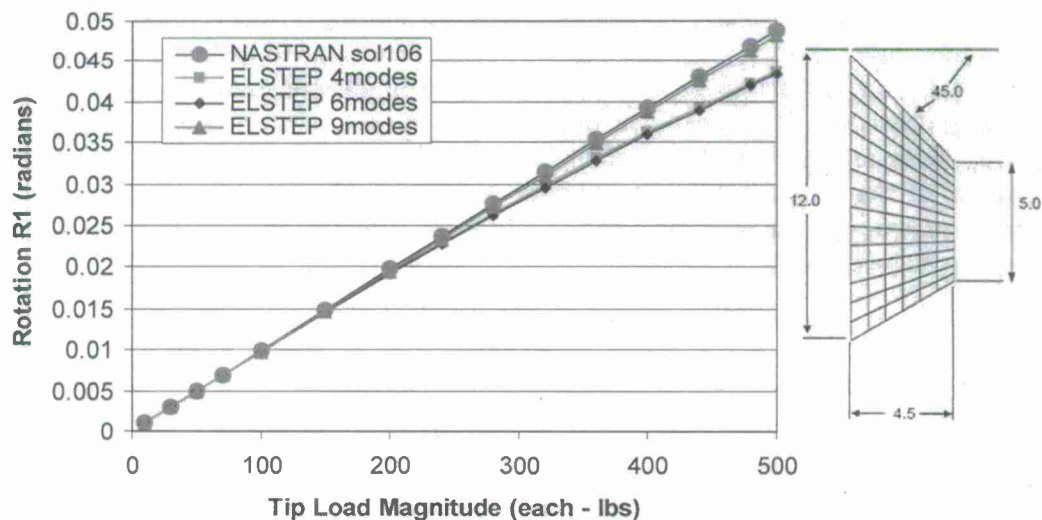


Figure 1.6. Comparison of Tip Rotations (R1) Obtained by NASTRAN and by the ELSTEP ROM of the Inboard Wing Alone.

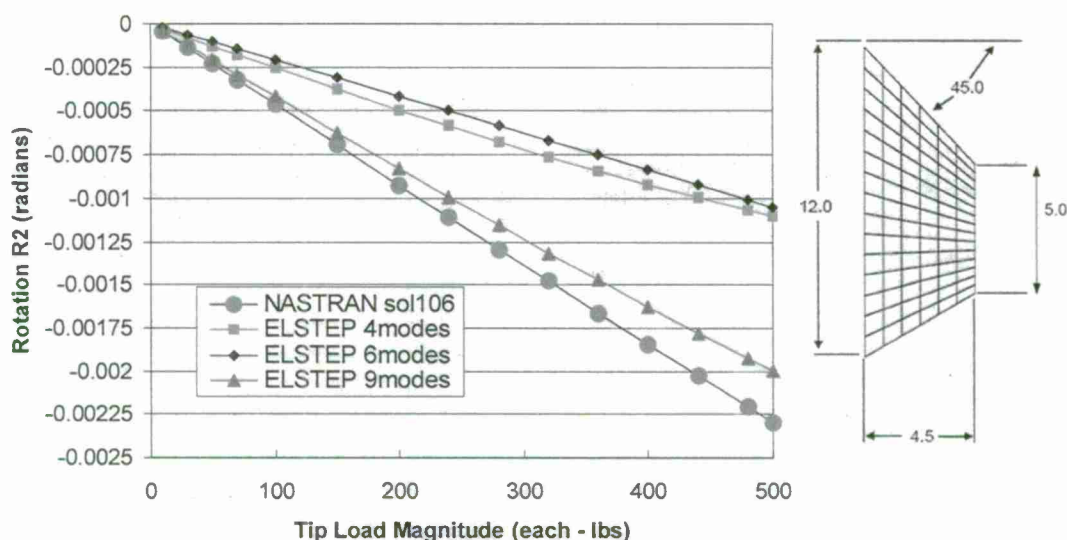


Figure 1.7. Comparison of Tip Rotations (R2) Obtained by NASTRAN and by the ELSTEP ROM of the Inboard Wing Alone.

The next validation effort of the inboard and outboard ROMs focused on the prediction of the response of the entire wing through the MORPH code, first for $\Gamma=0^\circ$ and then for nonzero values at this morphing angle. The results obtained for $\Gamma=0^\circ$ and 10° are shown in Figures 1.8 and 1.9 for a loading consisting of concentrated forces located at each of the 9 nodes of the entire wing. Comparing these results, with those of Phase I and Figures 1.4 and 1.5, it is found that the combination of the two components, inboard and outboard wings, has led to a significant decrease in accuracy in the prediction of the transverse displacements by ROM as compared to the component alone results.

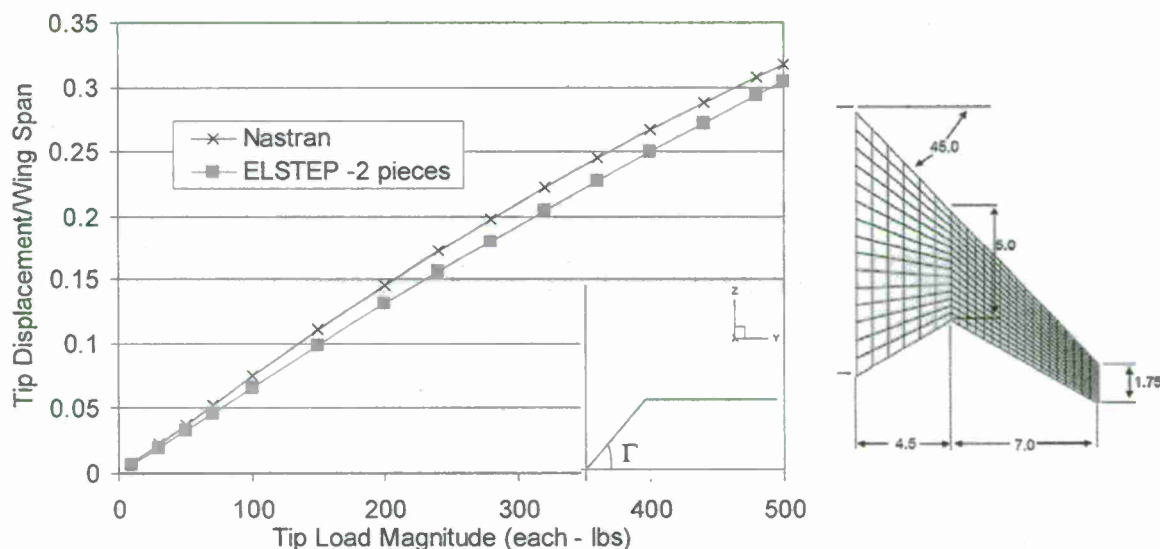


Figure 1.8. Comparison of Tip Displacements Obtained by NASTRAN and by the ELSTEP ROM and Multibody Morphing Formulation. Full wing - $\Gamma=0^\circ$ Configuration.

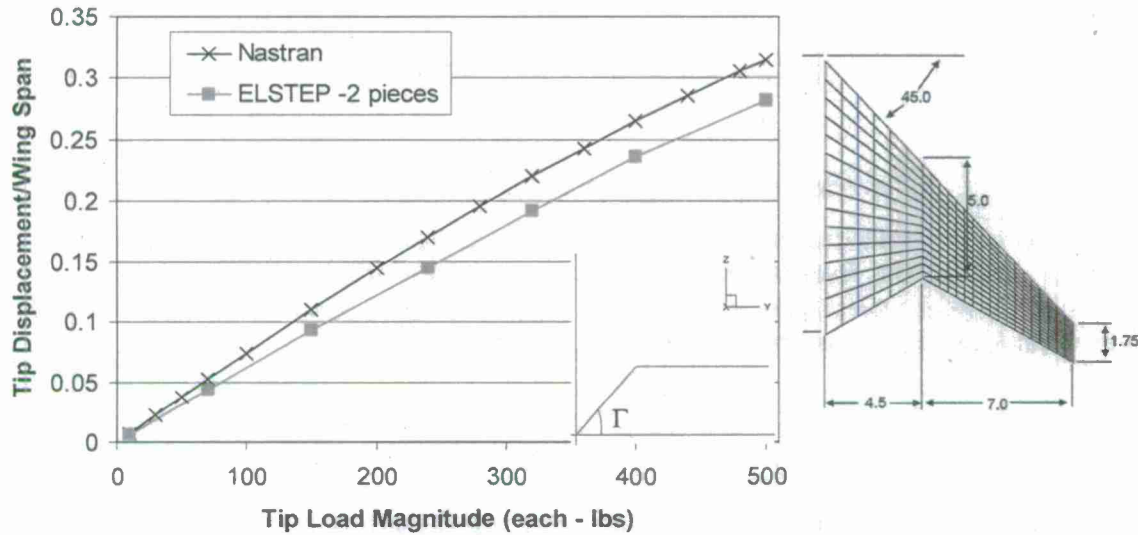


Figure 1.9. Comparison of Tip Displacements Obtained by NASTRAN and by the ELSTEP ROM and Multibody Morphing Formulation. Full wing - $\Gamma = 10^\circ$ Configuration.

A detailed investigation of the results has demonstrated that the decrease in accuracy noted in Figures 1.8 and 1.9 originate from the lack of consideration of the inplane force transmitted from outboard to inboard. Indeed, since the condensed ROMs only involve transverse displacements, inplane forces cannot be considered in the model nor can the inplane forces be transmitted from the outboard to the inboard be evaluated from the outboard ROM. These observations led to the conclusion that the condensed model was not sufficient for the purpose of determining accurately the response of the entire folding wing. Thus a revised approach, including both transverse and inplane displacements was required. Such a new approach is discussed in the next section.

1.2.4 Final Nonlinear ROM Development and Validation: "Decondensed" Models

The previous results have demonstrated the need to introduce an inplane modeling to the nonlinear reduced order models of the inboard wing. However, following the discussions of Phase I, this process cannot be achieved in the usual manner (see [1.2]) because of the numerical accuracy issues discussed earlier. Accordingly, a revised procedure had to be designed. Since the condensed model performed so well; it was questioned whether one could simply "insert into it" an inplane displacement modeling, e.g. through the dual modes of [1.3]. This process is referred to here as the "decondensation" process since the inplane displacements initially condensed are reverted to observed variables.

• "Decondensation" Process - Formulation

In formulating the decondensation process, it must first be recognized that Nastran's nonlinear finite element modeling is based on the von Karman strain assumptions. Under this hypothesis, it has been shown that the general form of a corresponding nonlinear ROM would be:

$$M_{ij}^{(t)} \ddot{q}_j^{(t)} + K_{ij}^{(1t)} q_j^{(t)} + K_{ijl}^{(2t)} q_j^{(t)} q_l^{(t)} + K_{ijlp}^{(3t)} q_j^{(t)} q_l^{(t)} q_p^{(t)} = F_i^{(t)} \quad (1.4)$$

and

$$M_{ij}^{(i)} \ddot{q}_j^{(i)} + K_{ij}^{(1i)} q_j^{(i)} + K_{ijl}^{(2i)} q_j^{(i)} q_l^{(i)} = F_i^{(i)} \quad (1.5)$$

where $q_j^{(i)}$ and $q_j^{(t)}$ denote the generalized coordinates associated with the inplane (superscript (i)) and transverse (superscript (t)) motions. Assuming that there are no forces in the inplane direction and that the frequencies of the excitation bandwidth are small with respect to the inplane mode frequencies (quasi-static inplane response), Eq. (1.5) can be directly solved for the inplane displacements in terms of their transverse counterparts as:

$$q_j^{(i)} = -[K^{(1i)}]_{js}^{-1} K_{srl}^{(2i)} q_r^{(t)} q_l^{(t)} \quad (1.6)$$

Introducing Eq. (1.6) into Eq. (1.4) leads to the transverse only set of equations:

$$M_{ij} \ddot{q}_j^{(t)} + K_{ij}^{(1t)} q_j^{(t)} + \hat{K}_{ijlp}^{(3t)} q_j^{(t)} q_l^{(t)} q_p^{(t)} = F_i^{(t)} \quad (1.7)$$

where

$$\hat{K}_{ijlp}^{(3t)} = K_{ijlp}^{(3t)} - K_{ijr}^{(2t)} [K^{(1t)}]_{rs}^{-1} K_{slp}^{(2i)} \quad (1.8)$$

In fact, Eq.(1.7) represents the condensed model introduced in Phase I and $\hat{K}_{ijlp}^{(3t)}$ is the corresponding tensor of the cubic stiffness terms which is positively definite both in theory and in the condensed ROM, albeit with "small" eigenvalues (as demonstrated by the near linear behavior of the response vs. load level). The difficulties encountered in Phase I with the standard formulation, e.g. based on the algorithm of [1.2], are highlighted in Eq.(1.8). Specifically, the tensor $K_{ijlp}^{(3t)}$ which corresponds to transverse motions with blocked (zero) inplane motions has large positive eigenvalues and so $K_{ijr}^{(2t)} [K^{(1t)}]_{rs}^{-1} K_{slp}^{(2i)}$. However, the difference in Eq.(1.8) is much smaller than any of the terms and thus *may not remain* positive definitely because of numerical accuracy. Specifically, both tensors $K_{ijlp}^{(3t)}$ and $K_{ijr}^{(2t)} [K^{(1t)}]_{rs}^{-1} K_{slp}^{(2i)}$ are typically obtained with about 4 significant digits in the algorithm of [1.2] but this is not sufficient to get a good approximation of their differences.

The decondensation problem is used to create a full model in the form of Eqs.(1.4) and (1.5) from the condensed one of Eqs.(1.7) and (1.8). Clearly, there is not enough information to do so and thus a two step approach was formulated.

- (a) A condensed model is first developed providing the tensor $\hat{K}_{ijlp}^{(3t)}$.
- (b) A full, inplane and transverse, model is then developed using the approach of [1.2], giving estimates of the various tensors of Eqs.(1.7) and (1.8) and in particular $K_{ij}^{(1t)}$, $K_{ijr}^{(2t)}$, and $K_{slp}^{(2i)}$ but the tensor $K_{ijlp}^{(3t)}$ obtained by this approach *is not used further*. Rather, the cubic stiffness tensor $K_{ijlp}^{(3t)}$ of Eq.(1.7) is obtained from Eq.(1.8) as

$$K_{ijlp}^{(3t)} = \hat{K}_{ijlp}^{(3t)} + K_{ijr}^{(2t)} \left[K^{(1t)} \right]_{rs}^{-1} K_{slp}^{(2i)} . \quad (1.9)$$

Note that selecting the cubic stiffness tensor $K_{ijlp}^{(3t)}$ according to Eq.(1.9) assures that the system will remain stable as the condensation of the decondensed model recovers the original condensed model which is stable.

- Assessment on a Beam Model

The decondensation procedure of the previous subsection was first validated on a cantilevered beam model, see Table 1.1 for its properties. The ROM was built from the first 4 transverse modes and the corresponding 4 duals (generation 2, see [1.3]). Shown in Figures 1.10-1.11 are the predictions of the transverse and inplane deflections of the beam tip when subjected to a uniform pressure, as predicted by the decondensation method and by full Nastran computations. An excellent agreement is obtained over a broad range of tip deflections demonstrating the well foundedness of the decondensation algorithm.

Table 1.1. Properties of the Cantilevered Beam (from [1.4])

Beam Length	19.985 inch
Cross-section Width	0.4999 inch
Cross-section Thickness	0.1251 inch
Mass per unit length	$1.971 \cdot 10^{-4} \text{ lb-s}^2/\text{inch}^2$
Young's Modulus	$10.576 \cdot 10^6 \text{ lb/inch}^2$
Shear Modulus	$4.0383 \cdot 10^6 \text{ lb/inch}^2$

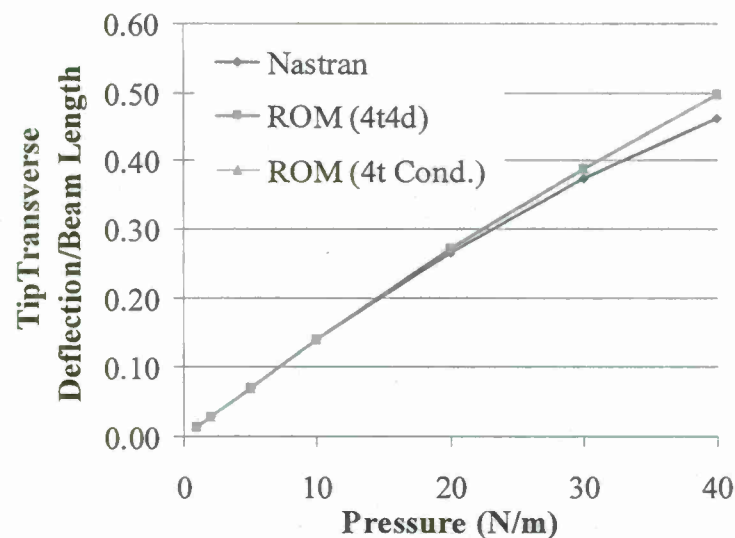


Figure 1.10. Tip Transverse Deflection vs. Load, Beam Model. Full Nastran, 4-Mode Condensed ("4t Cond."), and 4 Transverse - 4 Dual Modes Decondensed ("4t4d") Reduced Order Models ("ROM").

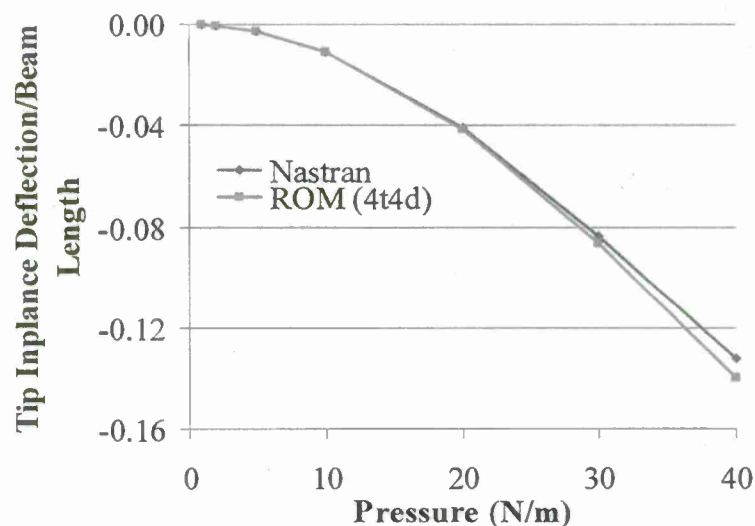


Figure 1.11. Tip Inplane Deflection vs. Load, Beam Model. Full Nastran and 4 Transverse - 4 Dual Modes Decondensed Reduced Order Model ("ROM(4t4d)").

Since the morphing of the folding wing involves both transverse and an inplane loading, it was also desired to assess the appropriateness of the decondensed model in the additional presence of an inplane force at the tip. The corresponding results and their Nastran counterparts are shown in Figures 1.12 and 1.13 and again the agreement is excellent, which strongly supports the validity of the decondensed model for the, folding wing application.

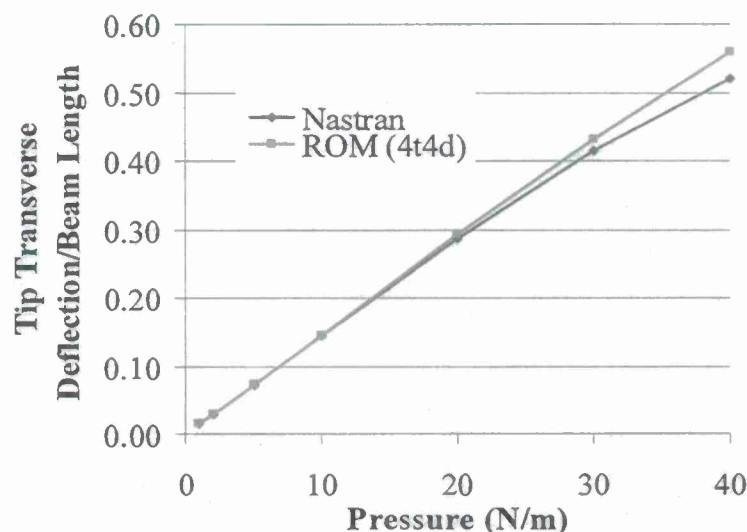


Figure 1.12. Tip Transverse Deflection vs. Load, Beam Model. Full Nastran and 4 Transverse - 4 Dual Modes Decondensed Reduced Order Model ("ROM(4t4d)"), 10% Inplane Compressive Tip Load.

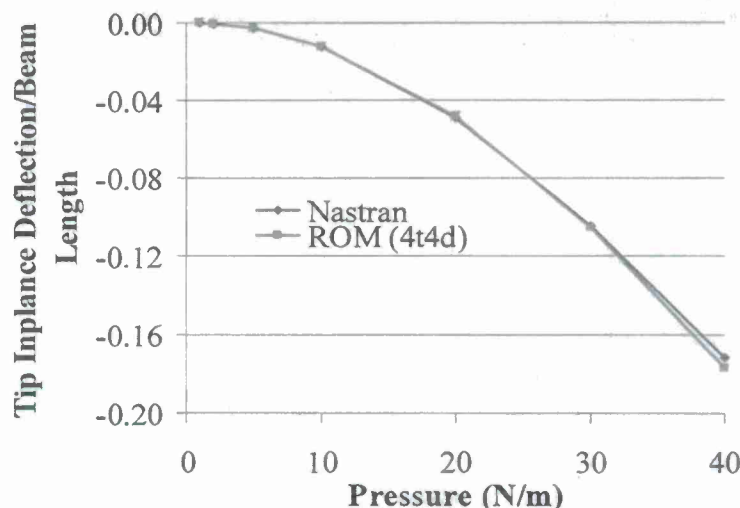


Figure 1.13. Tip Inplane Deflection vs. Load, Beam Model. Full Nastran and 4 Transverse - 4 Dual Modes Decondensed Reduced Order Model ("ROM(4t4d)"), 10% Inplane Compressive Tip Load.

- Assessment of the Inboard and Outboard Wings

The next validation effort of the decondensed model focuses on the separate models of the inboard and outboard wings of the folding wing. To approximately simulate the morphing conditions, the full (inboard + outboard) wing model at $\Gamma = 0^\circ$ was first subjected to a transverse loading (equal forces on each of the nodes of the full wing tip) and the reactions at the hinge line determined by Nastran. These forces were then applied to the inboard wing and the corresponding deflections were estimated from both Nastran and the inboard ROM model consisting of its first 9 transverse modes and the corresponding 9 duals (generation 2, see [1.3]). Shown in Figures 1.14-1.16 are the transverse displacements and rotations obtained at the tip of the inboard wing by both Nastran and the decondensed model ("ROM (9t9d)"). Note the

excellent agreement of these results even in the presence of the inplane force transmitted by the outboard.

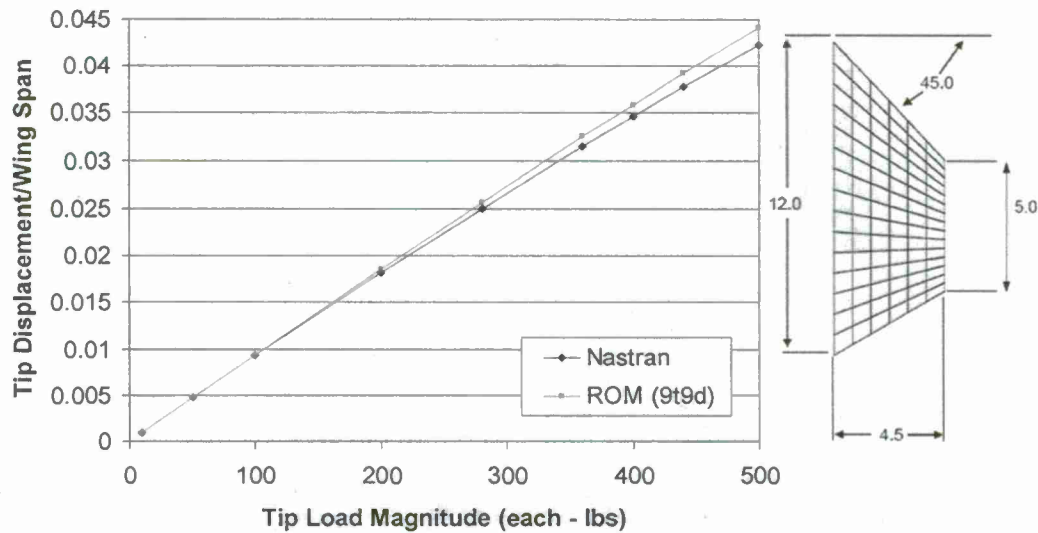


Figure 1.14. Comparison of Inboard Transverse Tip Displacement Obtained by NASTRAN and by the Decondensed ROM (normalized by the wing span of the entire wing).

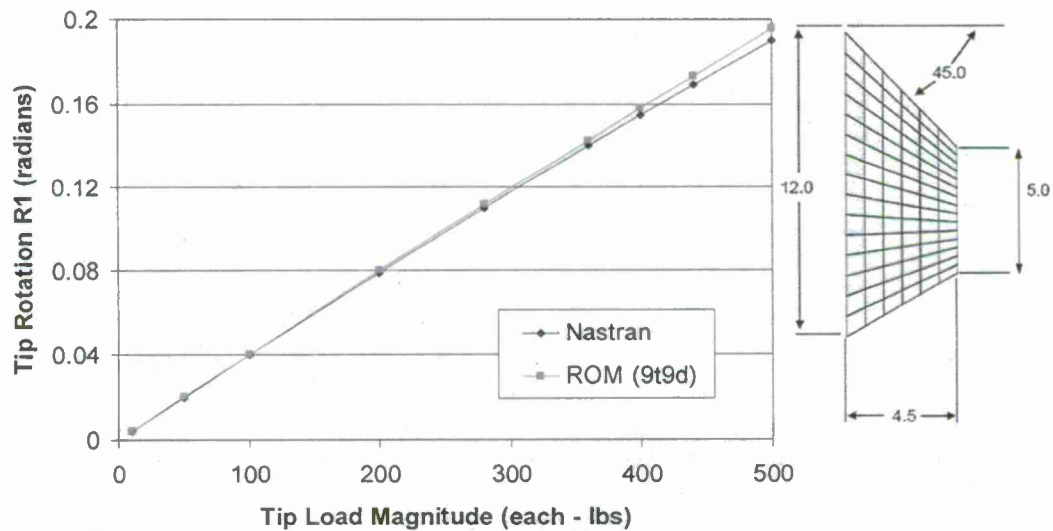


Figure 1.15. Comparison of Tip Rotations (R1) Obtained by NASTRAN and by the Decondensed ROM of Inboard Wing Alone.

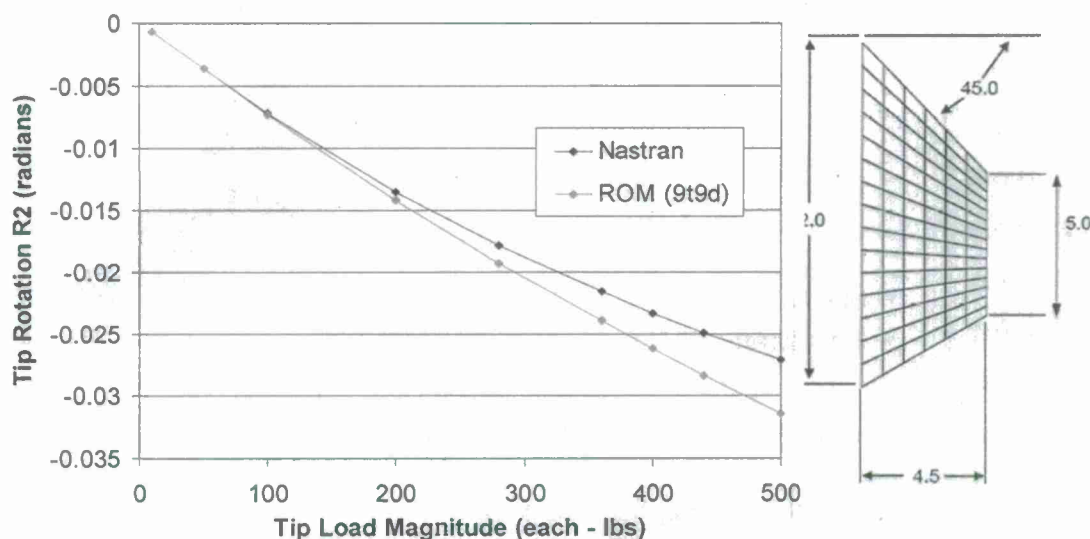


Figure 1.16. Comparison of Tip Rotation (R2) Obtained by NASTRAN and by the Decondensed ROM of Inboard Wing Alone.

The validation of the decondensed model of the outboard was achieved by comparing the tip displacements of that wing under the given loading, both in the transverse and inplane directions, as predicted by Nastran and ROM (first 4 transverse modes and corresponding duals). These results are presented in Figures 1.17-1.19. The excellent matching of these results demonstrates again the well foundedness of the decondensation approach.

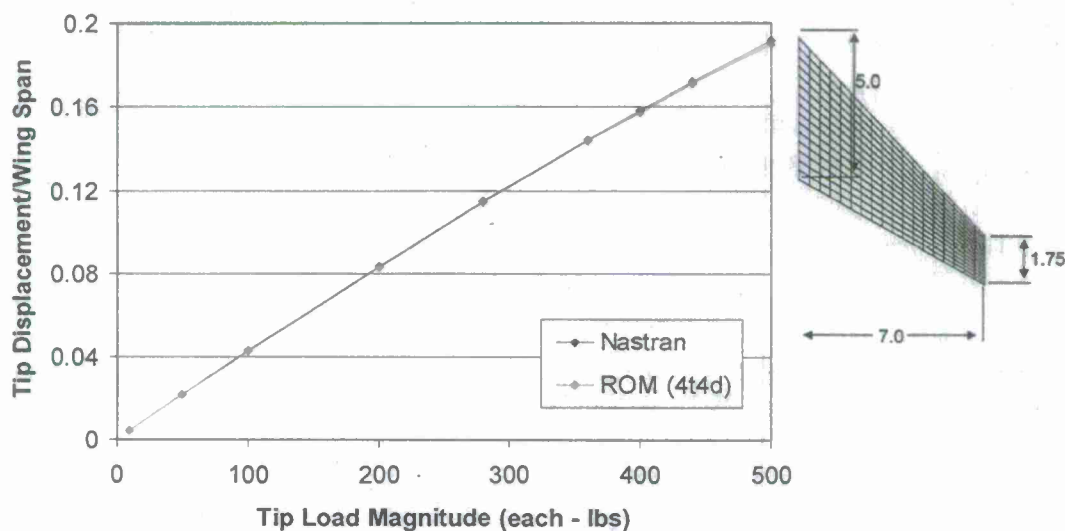


Figure 1.17. Comparison of Outboard Transverse Tip Displacement Obtained by NASTRAN and by the Decondensed ROM (normalized by the wing span of the entire wing).

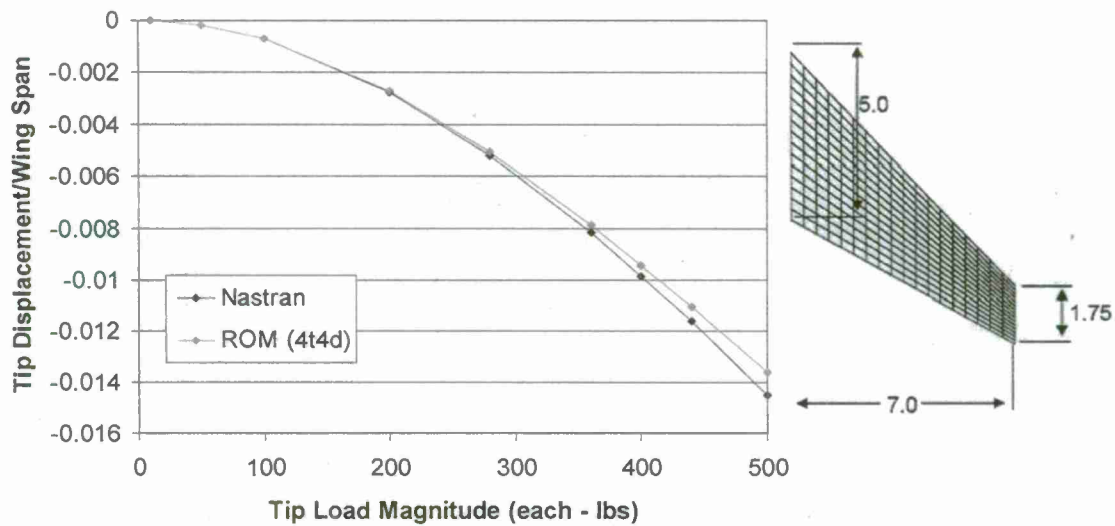


Figure 1.18. Comparison of Outboard Tip Displacement along X Obtained by NASTRAN and by the Decondensed ROM (normalized by the wing span of the entire wing).

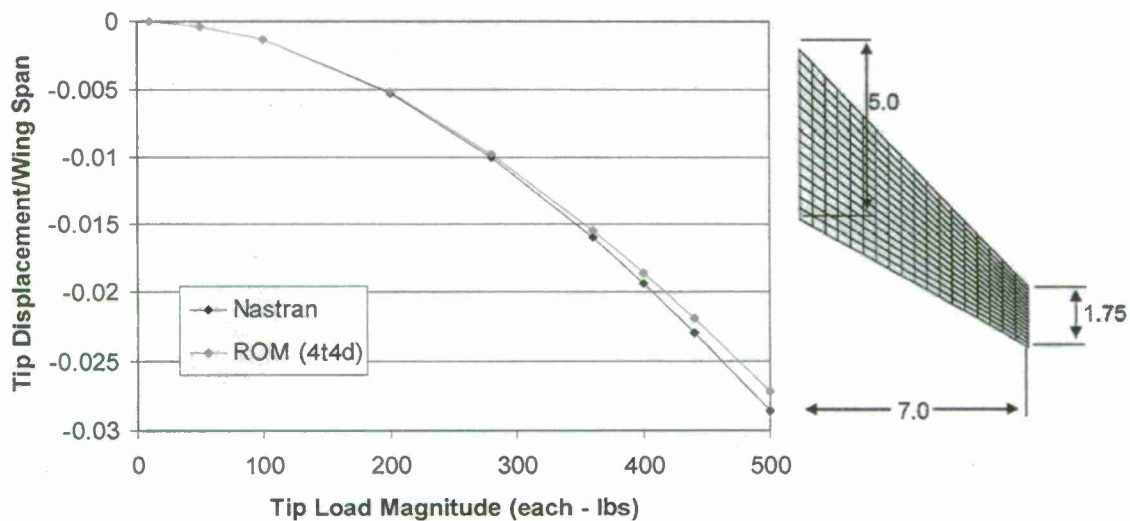


Figure 1.19. Comparison of Outboard Tip Displacement along Y Obtained by NASTRAN and by the Decondensed ROM (normalized by the wing span of the entire wing).

- Assessment on the Folding Wing through the Multibody Formulation

The final assessment of the decondensation formulation was performed by assembling the inboard and outboard wings following the multibody approach of section 1.3, i.e. with the code MORPH. Shown in Figures 1.20-1.24 are the prediction of the transverse displacement (Z) at the tip of the combined wing (node 288) and the displacements in the Y and Z directions in the middle of the hinge (node 95), all for different values of Γ . In these comparisons, the wing (complete, inboard and outboard) was assumed to be subjected to concentrated forces of equal magnitudes at every node and acting in the Z direction (i.e. perpendicular to the wing at $\Gamma=0$ degree). Very good agreement is shown between Nastran and the ROMs/MORPH package,

which demonstrates the applicability of the proposed dynamic substructuring formulation and implementation.

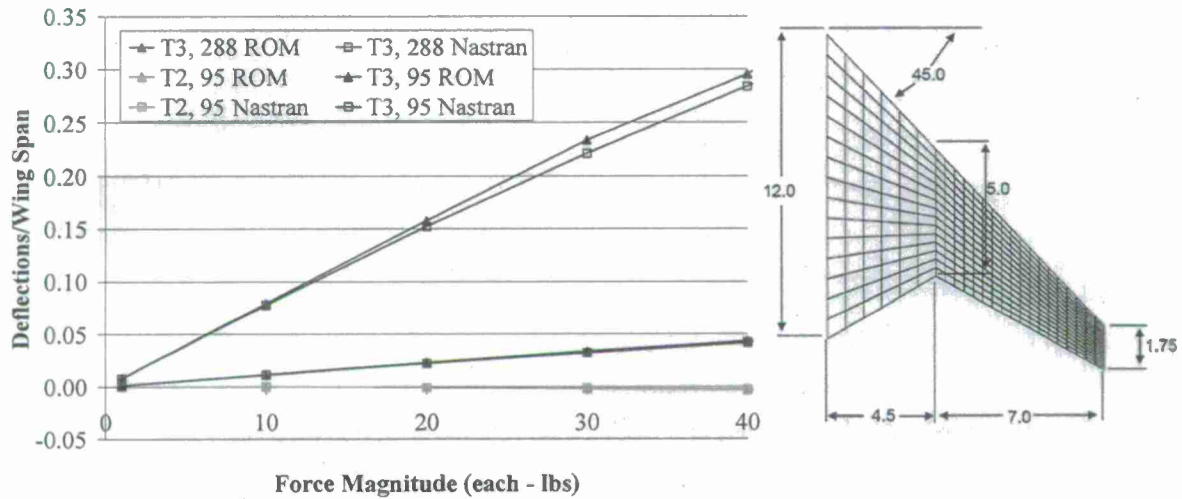


Figure 1.20. Comparisons of Z Displacements at the Wing Tip (node 288) and Y and Z Displacements at the Middle of the Hinge (node 95), $\Gamma=0^\circ$.

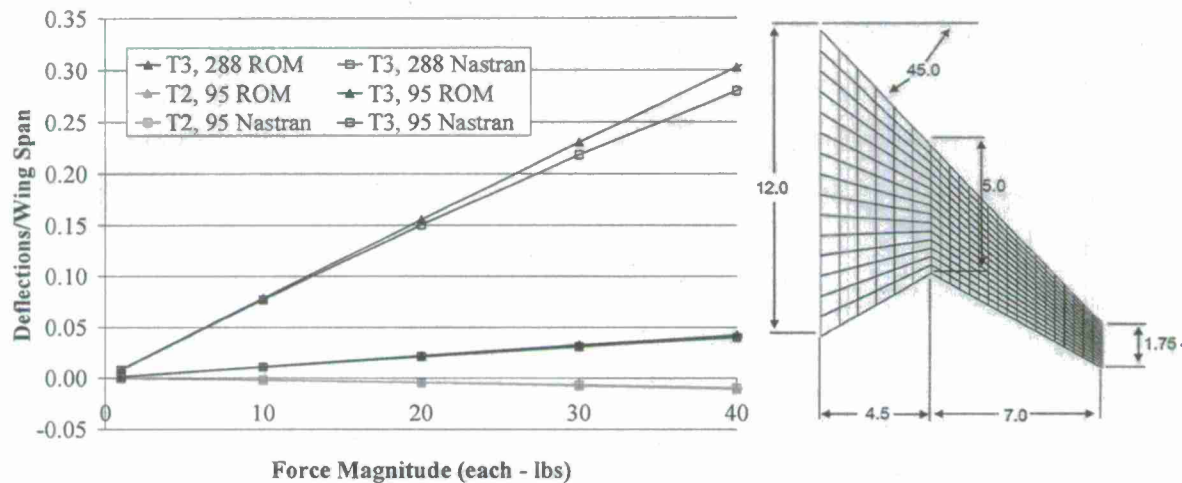


Figure 1.21. Comparisons of Z Displacements at the Wing Tip (node 288) and Y and Z Displacements at the Middle of the Hinge (node 95), $\Gamma=10^\circ$.

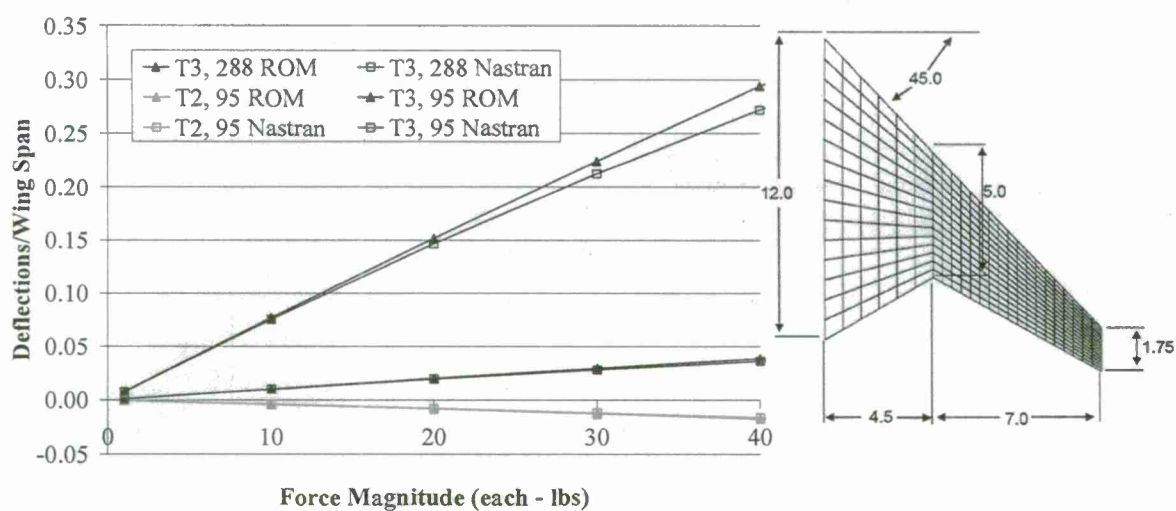


Figure 1.22. Comparisons of Z Displacements at the Wing Tip (node 288) and Y and Z Displacements at the Middle of the Hinge (node 95), $\Gamma=20^\circ$.

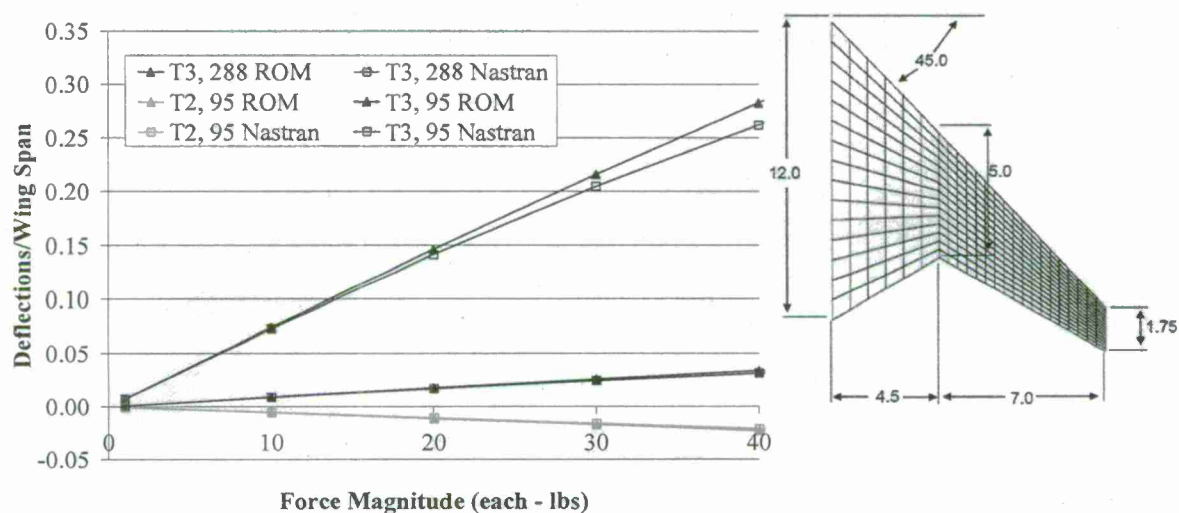


Figure 1.23. Comparisons of Z displacements at the wing tip (node 288) and Y and Z displacements at the middle of the hinge (node 95), $\Gamma=30^\circ$.

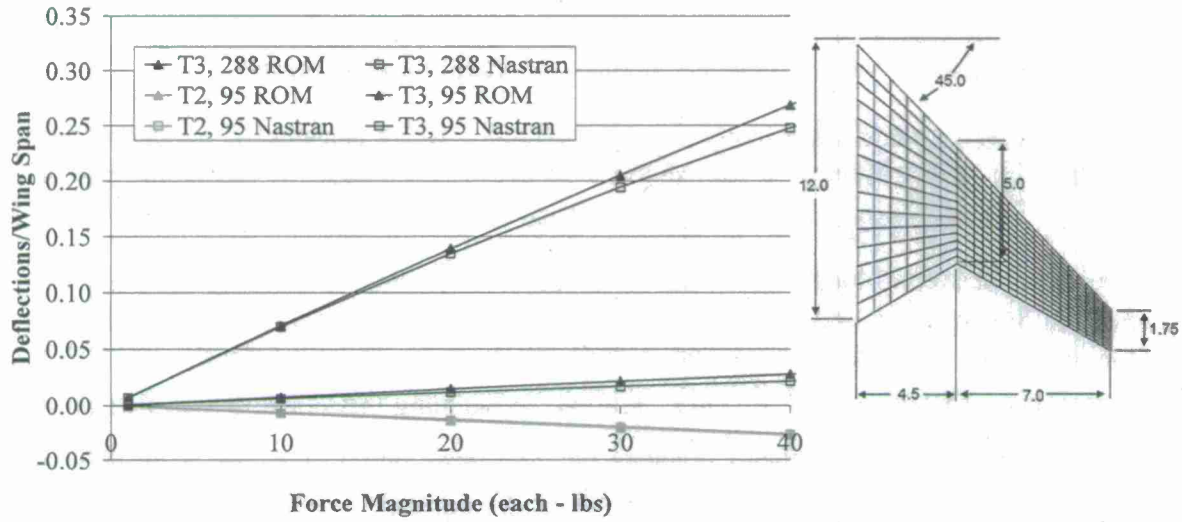


Figure 1.24. Comparisons of Z displacements at the wing tip (node 288) and Y and Z displacements at the middle of the hinge (node 95), $\Gamma=40^\circ$.

1.3 Validation of Angular Velocity and Angular Acceleration Terms

The next validation focused on the linear stiffness terms involving the angular velocity and angular acceleration, i.e. $\bar{K}_{ij}^{(1)} \omega^2 q_j$ and $\hat{K}_{ij}^{(1)} \dot{\omega} q_j$, and their excitation counterparts $F_1 \omega^2$ and $F_2 \dot{\omega}$, in Eq. (1.3). The latter two terms correspond to the “inertial loading” of the folding wing induced by the imposed rotation while the former two terms are variations of stiffness induced by the stress distribution associated with this inertial loading. The terms $F_1 \omega^2$ and $F_2 \dot{\omega}$ do not involve the deformations and thus can be determined from pure rigid body considerations. That is, the components of these forces on node i of the grid are

$$(F_1 \omega^2)_i = m_i \underline{\omega} \times (\underline{\omega} \times \underline{r}_i) \quad (1.10)$$

and

$$(F_2 \dot{\omega})_i = m_i \dot{\underline{\omega}} \times \underline{r}_i \quad (1.11)$$

where m_i is the lumped mass at node i and \underline{r}_i is its position from any point on the wing root.

The validation of the implementation of the terms $F_1 \omega^2$ and $F_2 \dot{\omega}$ was achieved as follows. First, the two sets of forces given by Eqs.(1.10) and (1.11) were evaluated by a separate program for the particular values of ω , $\dot{\omega}$ and angle, Γ . Then, these force distributions were applied, one at a time, to the folding wing for different morphing angles Γ and the corresponding static linear responses were determined using Nastran. Finally, those same responses were determined from the code MORPH by ignoring the dynamic and nonlinear terms and considering the two cases (a) ω specified and $\dot{\omega}=0$ and (b) $\omega=0$ and $\dot{\omega}$ specified, and a comparison of these Nastran and

MORPH responses was performed. Shown in Figure 1.25 are the relative norms of the difference between the two sets of responses for different angles, Γ . Clearly, the matching is excellent; which demonstrates the correct implementation of the inertial loading terms.

As discussed above, these terms imply a stress distribution which changes the overall stiffness of the wing. This effect appears in the MORPH formulation through the linear stiffness terms $\bar{K}_{ij}^{(1)} \omega^2 q_j$ and $\hat{K}_{ij}^{(1)} \dot{\omega} q_j$. The validation of these two terms is as follows. Once the linear responses to the inertial loads $F_1 \omega^2$ and $F_2 \dot{\omega}$ were determined, an ensuing computation was carried out in Nastran to obtain the natural frequencies and modes of the stressed folding wing. Those results were then to be compared to their counterparts obtained from the MORPH code with the terms $\bar{K}_{ij}^{(1)} \omega^2 q_j$ and $\hat{K}_{ij}^{(1)} \dot{\omega} q_j$ present. In pursuing this effort, it was first observed that the change in natural frequency obtained for even large values of ω and $\dot{\omega}$ is quite small, i.e. of the order of 0.5% or less for $\omega = 2 \text{ rad/sec}$ or $\dot{\omega} = 2 \text{ rad/sec}^2$. Accordingly, this effect was of the same level as the differences between MORPH and Nastran in the absence of rotation and thus could not be reliably detected this way. Increasing the angular velocities and/or rotations would of course lead to larger frequency changes but then the Nastran solution would also exhibit stiffening due to the large deformations which would then be compared with MORPH with the nonlinear stiffness terms linearized around the static equilibrium configuration. The same issue of detectability then resurfaces. After a series of attempts, it was concluded that this specific validation/verification could not be successfully conducted with the current version of Nastran.

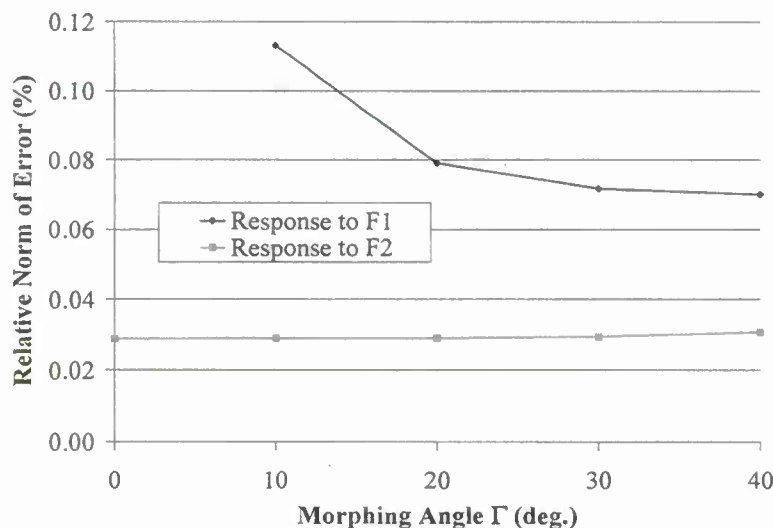


Figure 1.25. Relative Norm of the Error in Prediction of the Displacement Due to the Forces $F_1 \omega^2$ and $F_2 \dot{\omega}$ Computed by MORPH vs. Nastran.

Chapter 2.

NONLINEAR AEROELASTICITY OF CONTINUOUS MORPHING FOLDING WING BY FULL-ORDER APPROACH

Summary

With the accomplishment of developing a NL/Linear Structural ROM procedure for substructure models (one-piece/two-piece) of a folding wing, a full-order (direct) CFD/Structure simulation has been achieved by closely coupling an unsteady EULER solver called CartEULER with the NL/Linear Structural ROM procedure. The two-piece wing model including morphing dynamics thus can be used for either quasi-steady (morphing time only) or continuous morphing simulations. First, quasi-steady results are presented showing the validation of the two-piece wing model which was done by comparing the aeroelastic responses from both one-piece and two-piece linear models at fixed morphing angles (Figures 2.1-2.6). Next, continuous morphing results are obtained using the two-piece model ROM coupled with CartEULER which is capable of generating time-accurate unsteady aerodynamic forces for the folding wing in continuous morphing motions (see Figures 2.9, 2.11, 2.12). With the nonlinear substructure model developed, full-order (direct) CFD/Structure simulations were performed for the folding wing with fixed morphing angles (quasi-steady)(Figure 2.13). Finally, the comparison of the aeroelastic responses between the two-piece nonlinear and two-piece linear models is presented to investigate the nonlinear structural effects on the LCO behavior of the folding wing.(Figures 2.14 and 2.15).

The folding wing considered in the current effort has inboard and outboard wing components which are connected by a rigid hinge line so that the outboard wing can rotate with respect to the inboard hinge line. In our proposed morphing motion, the morphing angle of the inboard wing is changing with time while the outboard wing rotates accordingly around the hinge line in order to remain horizontal. The one-piece model has 6 modes whose modal shapes are defined in the global frame and thus are different for different morphing angles. The one-piece model is only for fixed morphing angle simulations. The two-piece model has 13 modes for both inboard and outboard components, and the outboard wing has an additional 6 modes related to the rigid-body motion. The modes from both components are combined to build up a model with 32 modes whose modal shapes are defined in the local wing plane so that one set of modal shapes serve for all morphing angles. The ROM solver for the two-piece model requires input of the morphing angle as well as the morphing angular velocity and acceleration of the inboard wing component to account for continuous morphing motion.

2.1 Validation of the Linear Substructure Model: Two-Piece vs. One-Piece Wings

The linear structure is obtained by removing all the nonlinear terms from equation 1.3. ASU has assured that the modal shapes and frequencies of the linear substructure two-piece model at different morphing angles matched well with those of linear Nastran's one-piece model. A full-order (direct) CFD/Linear Structure simulation was performed for both models to further verify the equivalence of the two models at fixed morphing angles. The comparison of aeroelastic responses in terms of wing tip displacement are shown in Figures 2.1-2.6. For all 6 cases with morphing angles of $\Gamma = 0^\circ, 10^\circ, 20^\circ, 30^\circ, 40^\circ, 60^\circ$ and 4 different altitudes ($H = 0 \text{ Kft}, 10 \text{ Kft}, 20 \text{ Kft}, 30 \text{ Kft}$), the time histories of the wing tip's displacement of a (locked) two-piece model match well with those of one-piece model. All solutions were obtained for Mach number = 0.95 and angle of attack = 0° . The initial kick is to apply a small velocity for all the structure grid points. All results showed proper LCO and convergent solutions which were found to confirm the correct physics.

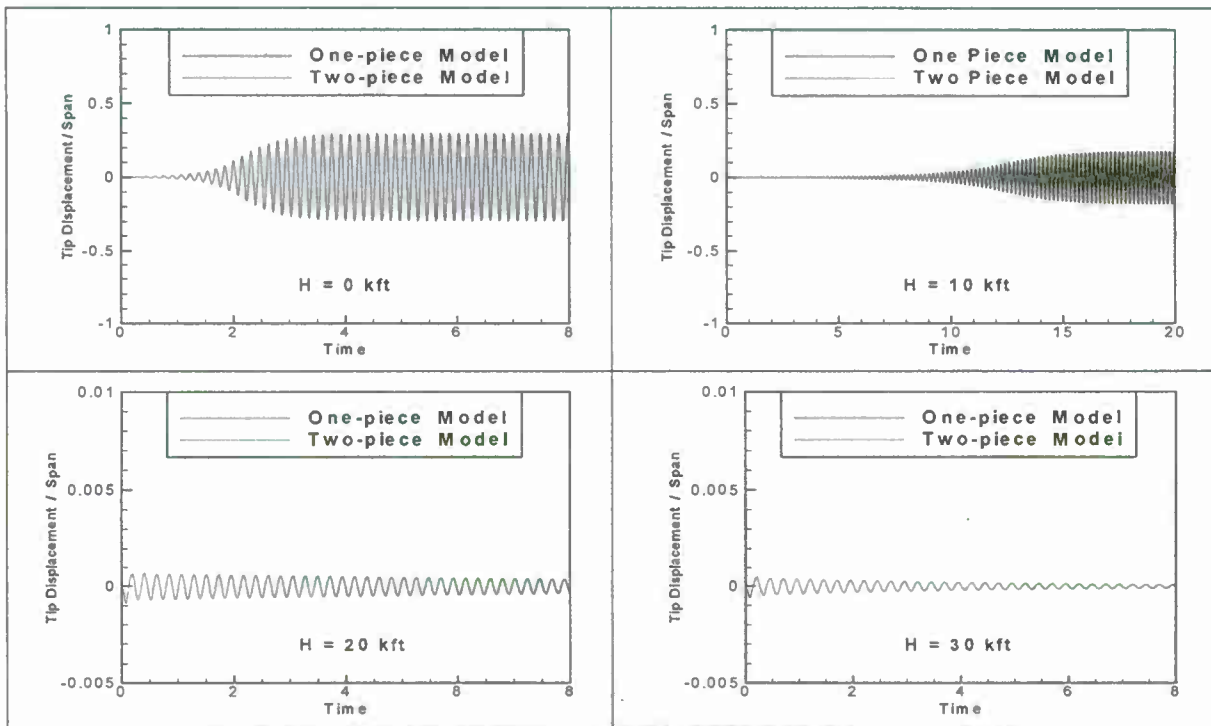


Figure 2.1. Validation of the Linear Two-Piece Model at Dihedral Angle 0° .

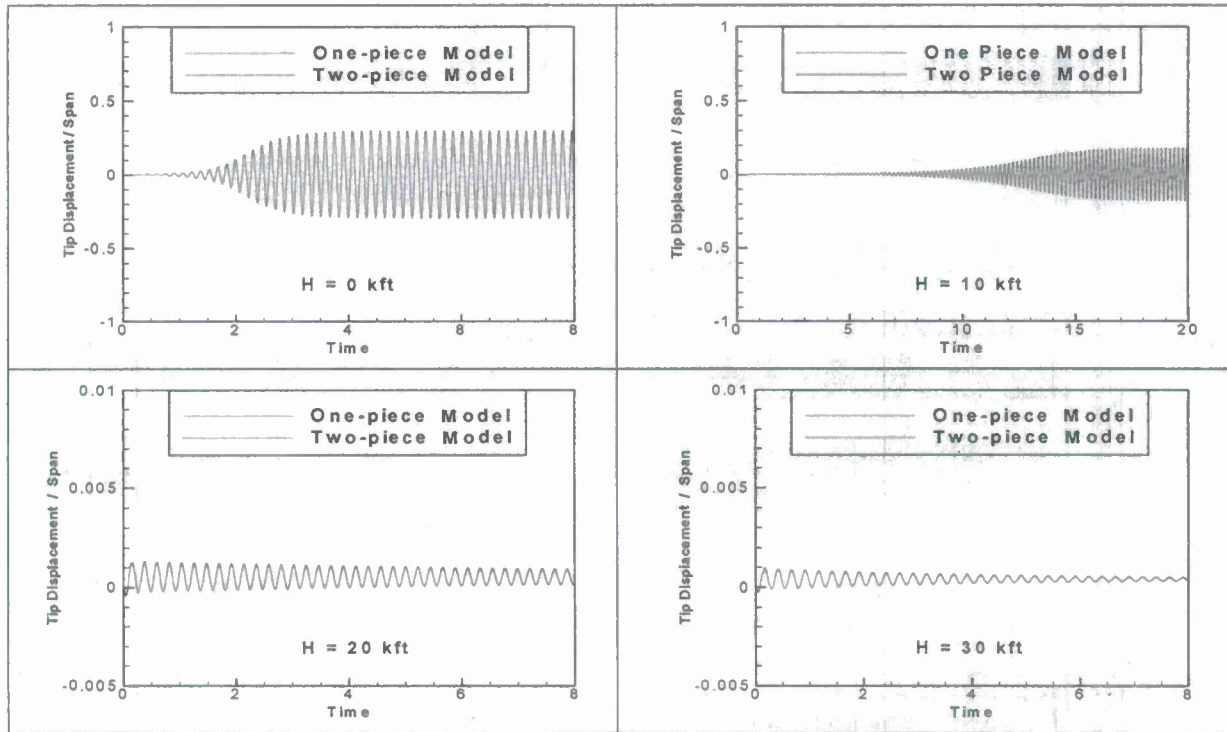
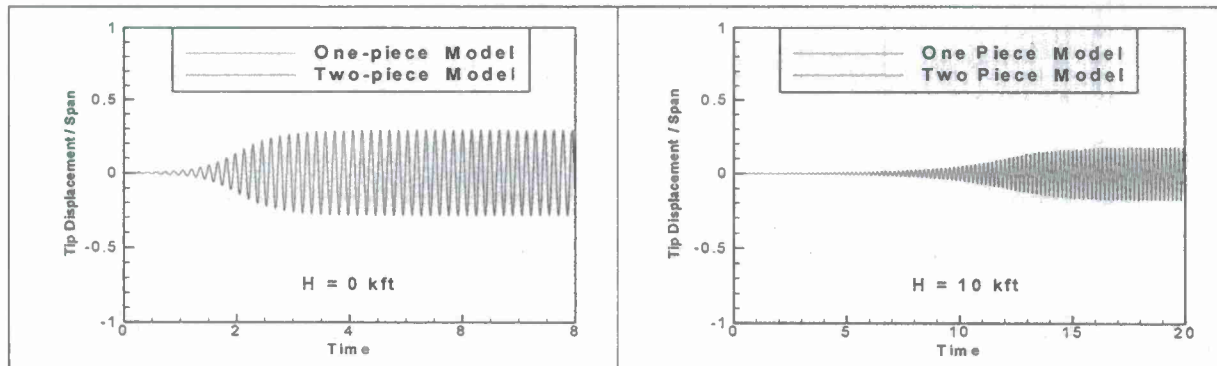
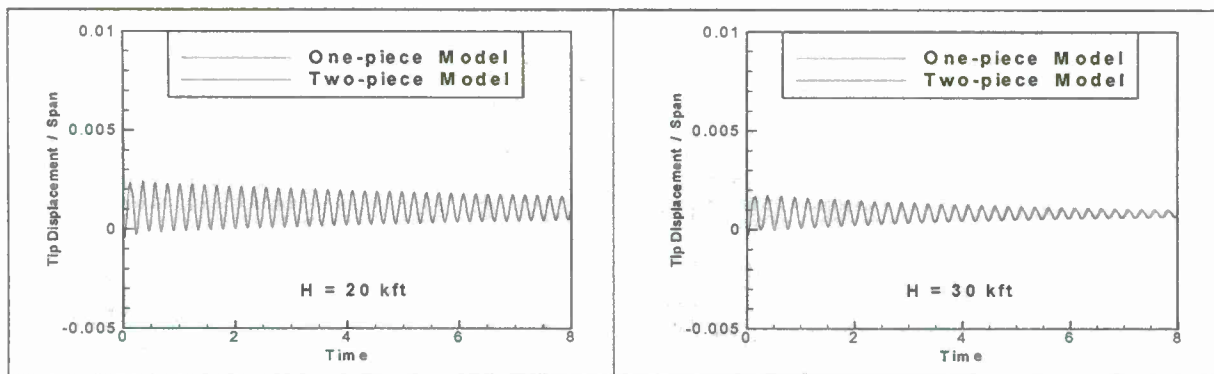
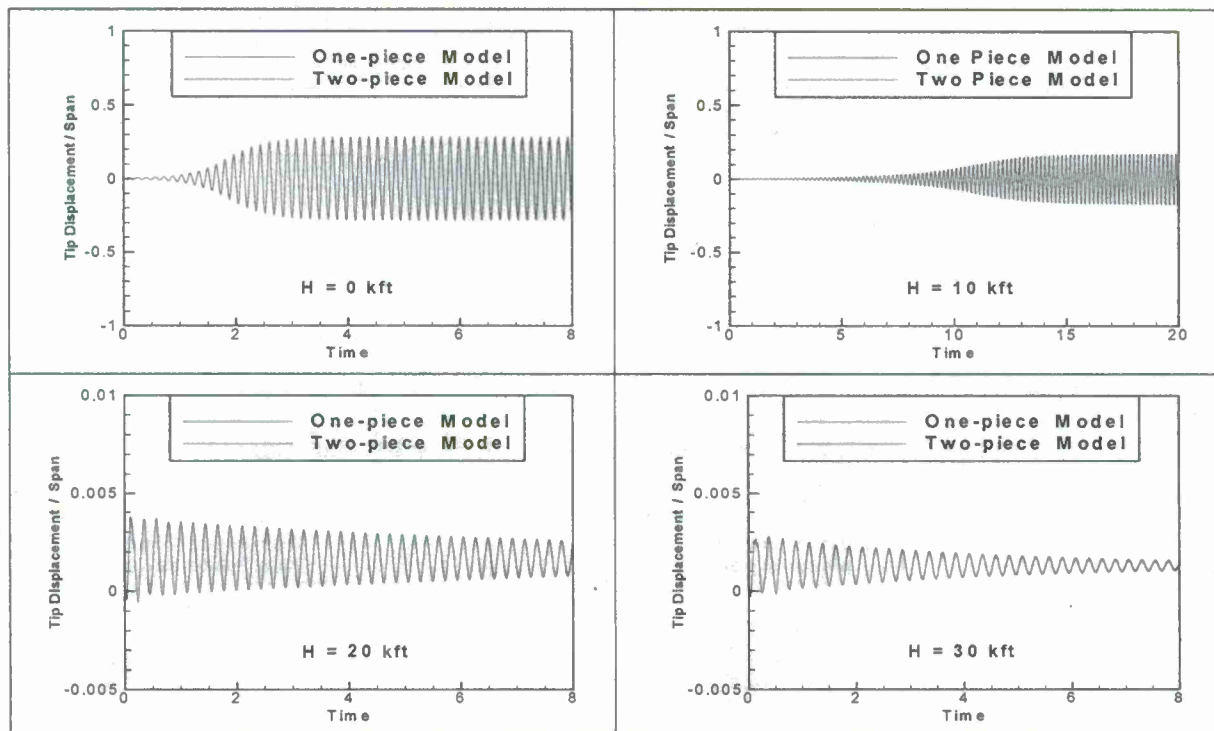
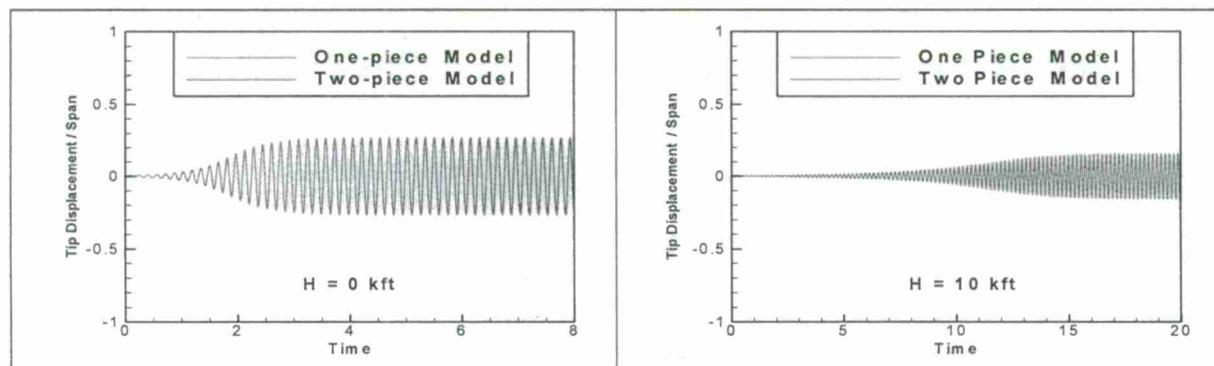


Figure 2.2. Validation of the Linear Two-Piece Model at Dihedral Angle 10° .



Figure 2.3. Validation of the Linear Two-Piece Model at Dihedral Angle 20° .Figure 2.4. Validation of the Linear Two-Piece Model at Dihedral Angle 30° .

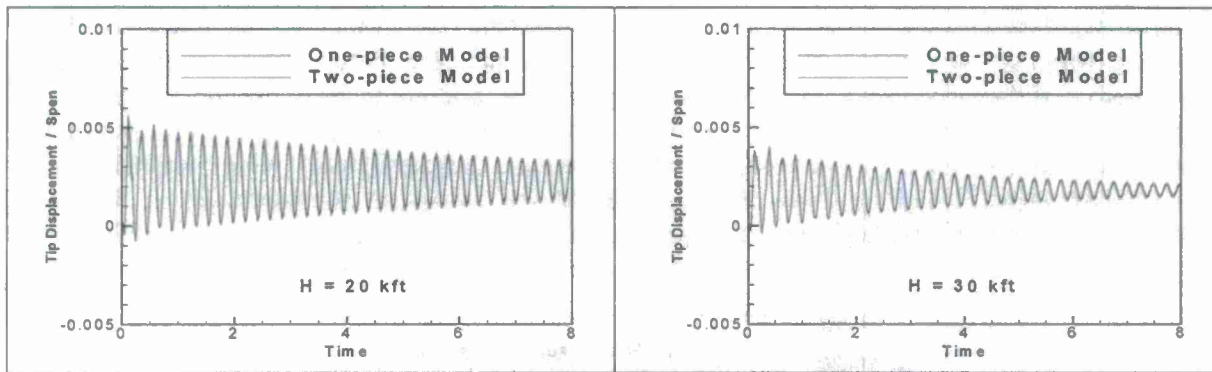


Figure 2.5. Validation of the Linear Two-Piece Model at Dihedral angle 40°.

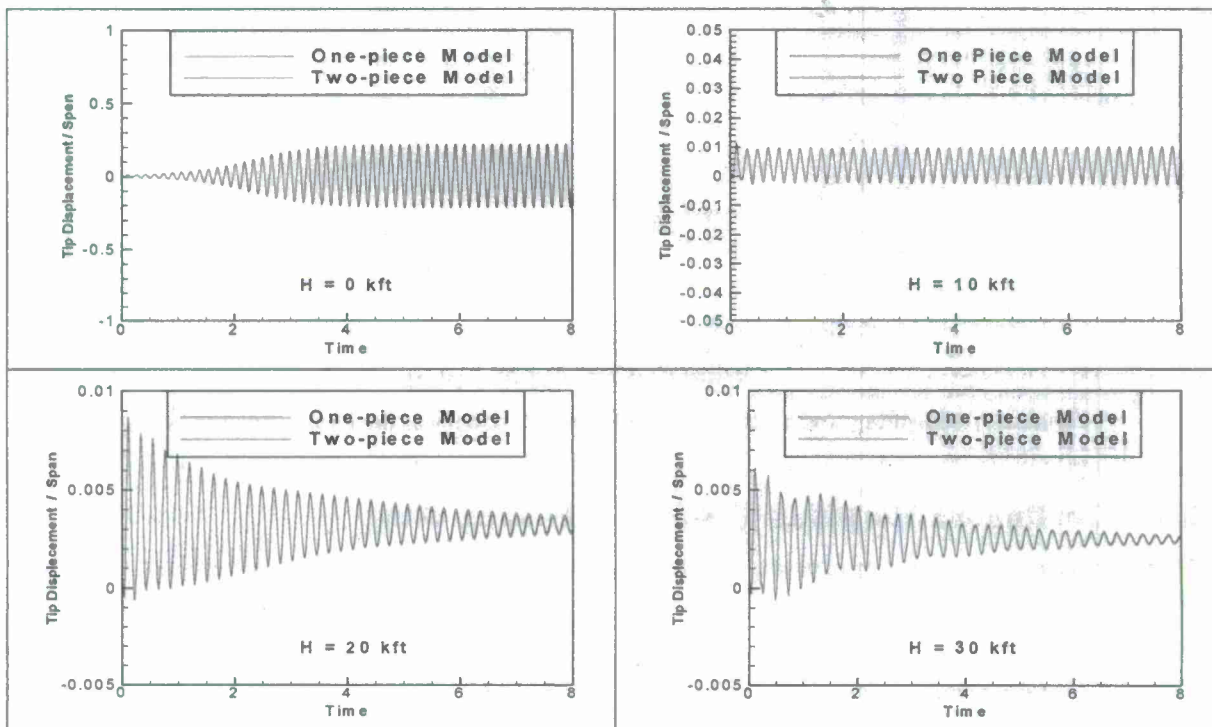


Figure 2.6. Validation of the Linear Two-Piece Model at Dihedral Angle 60°.

2.2 Quasi-Steady Flutter Boundary: Folding Wing

There exists two time scales in the physical wing morphing problem. While the wing is morphing at one speed, the wing undergoes a different time scale as measured by its aeroelastic "vibration frequency". When the morphing time scale is much larger (or larger) than the aeroelastic time, then as an approximation the aeroelastic analysis can be performed at a fixed morphing position. This is known as the quasi-steady for morphing. When these two time scales are comparable, transient aeroelastic behavior is of interest. We call the latter "continuous dynamic morphing".

Employing Nastran/Linear and ZAERO, Lee and Weisshaar [2.1] found that the flutter trend of a folding wing of two-piece substructures is one in which the flutter dynamic pressure first increases and then decreases with an increasing morphing angle from 0° to 90°. Their flutter solutions were obtained in a frequency-domain using ZAERO and the wing morphs in a quasi-steady manner (Figure 2.7). The present study also adopts the quasi-steady wing-morph approach by applying CartEULER and NL Structural ROM (of two-piece substructures) in the time-domain to a different folding wing. The present findings also indicate a slight increase in flutter dynamic pressure with an increasing morphing angle (Figure 2.7).

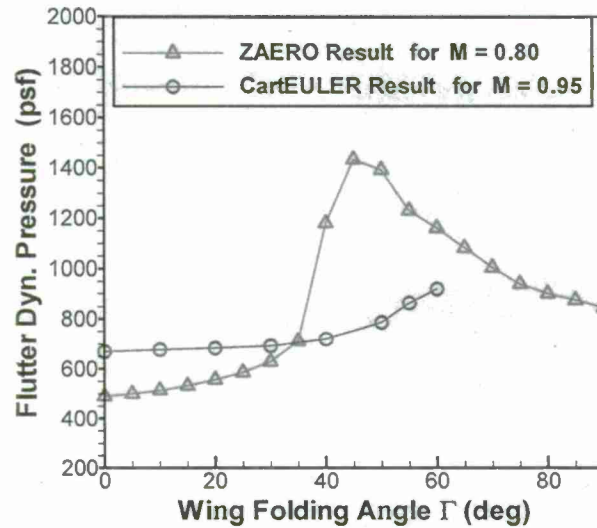


Figure 2.7. Morphing Angle Effects on the Flutter Boundary of the Linear Folding Wing.

2.3 Continuous Morphing Simulation: Folding Wing

Therefore for continuous morphing simulations, we define two types of morphing schedules (Eqs. (2.1) and (2.2)) as follows:

$$\text{Constant Speed:} \quad \Gamma(t) = \Gamma_0 + \frac{(\Gamma_1 - \Gamma_0)}{t_1 - t_0}(t - t_0) \quad (2.1)$$

$$\text{Exponential:} \quad \Gamma(t) = \Gamma_1 - (\Gamma_1 - \Gamma_0) \frac{1 - e^{-\lambda(t-t_1)}}{1 - e^{-\lambda(t_0-t_1)}} \quad (2.2)$$

Note that the duration of morphing is from $t = t_0$ to $t = t_1$ when the morphing angles are Γ_0 and Γ_1 , respectively.

Shown in Figure 2.8 is time variations of the morphing angle, Γ , for three different morphing schedules. Figure 2.9 presents the comparison of the aeroelastic responses from the above-mentioned three different morphing schedules. The flight conditions are $M=0.95$, $AOA=0^\circ$ and $H=10Kft$. The same initial kick as in Section (2.1) was employed.

To better understand the differences of the time histories due to different morphing schedules, the continuous morphing responses are shown together with the fixed morphing angle responses for $\Gamma=0^\circ$ and $\Gamma=60^\circ$ at the same flight conditions of Figure 2.10. For a fixed $\Gamma=0^\circ$, it will develop into LCO, while it is small amplitude close to neutral response for $\Gamma=60^\circ$. As the morphing schedule with $\lambda = -0.4$ delays the effective increase of the morphing angle until the late stage of the morphing period, the response of this kind of morphing schedule is mostly similar to the one for fixed $\Gamma=0^\circ$ before $t = 15s$. On the other hand, the morphing schedule with $\lambda = 0.6$ increases the morphing angle very quickly at the earlier stage of the morphing period, and thus the response is a small amplitude oscillation similar to the one for a fixed $\Gamma=60^\circ$. It comes without surprise that the response for the constant speed morphing case is somewhat in-between the other two.

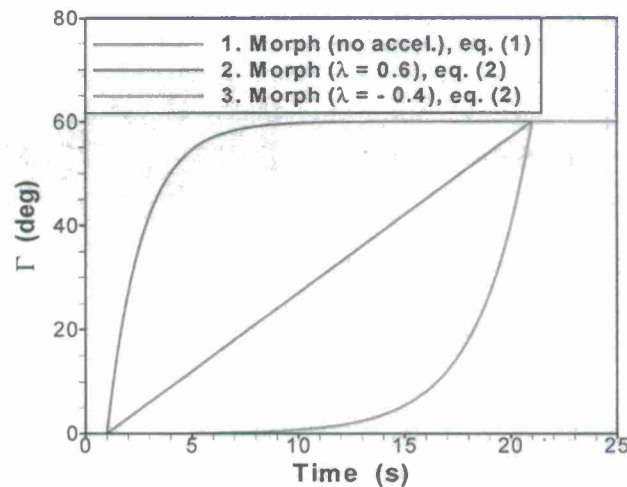
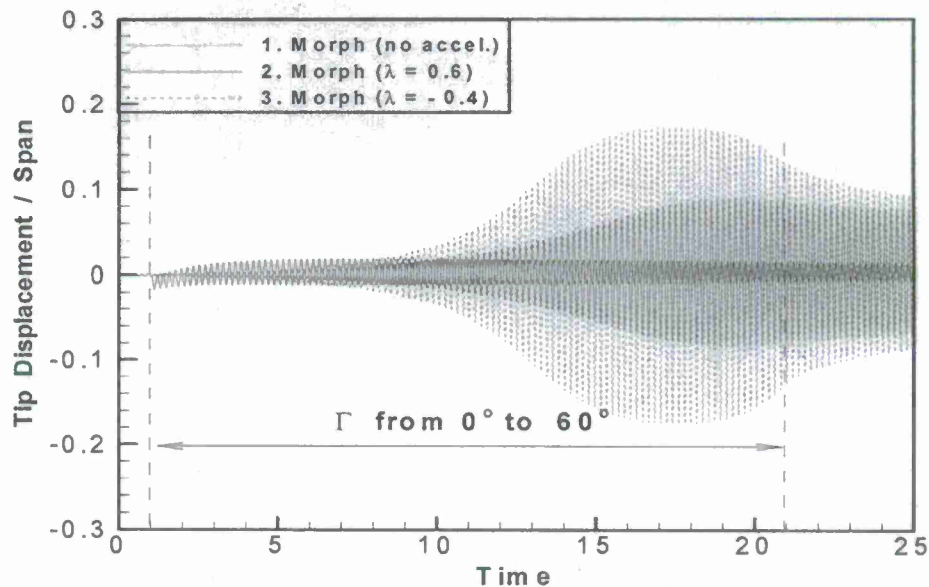


Figure 2.8. Three Different Morphing Schedules.



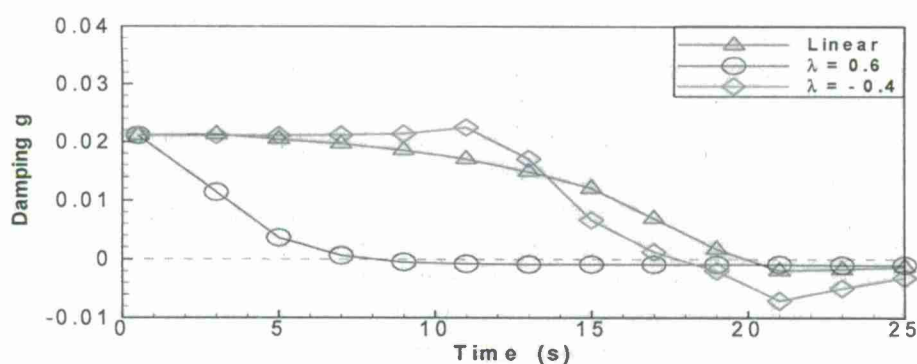
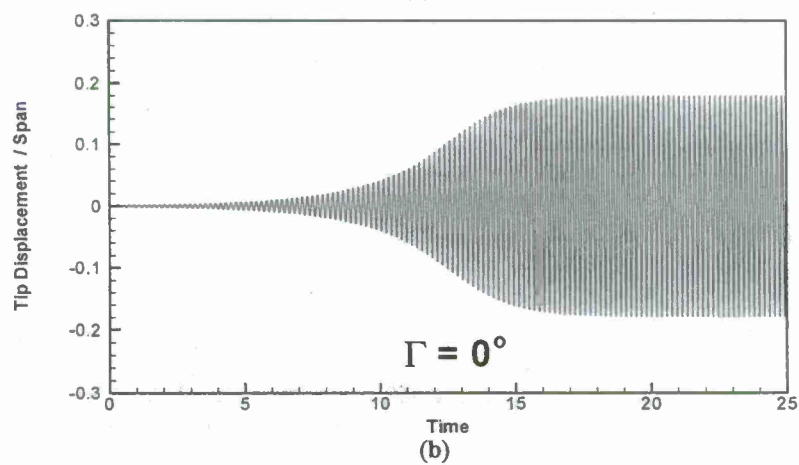
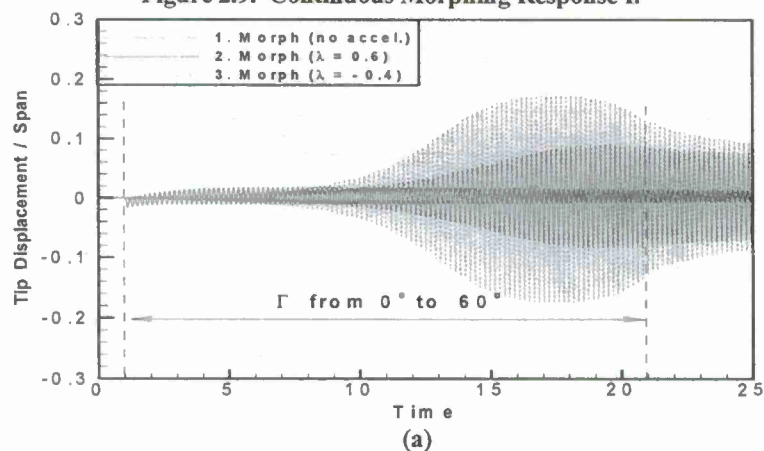


Figure 2.9. Continuous Morphing Response I.



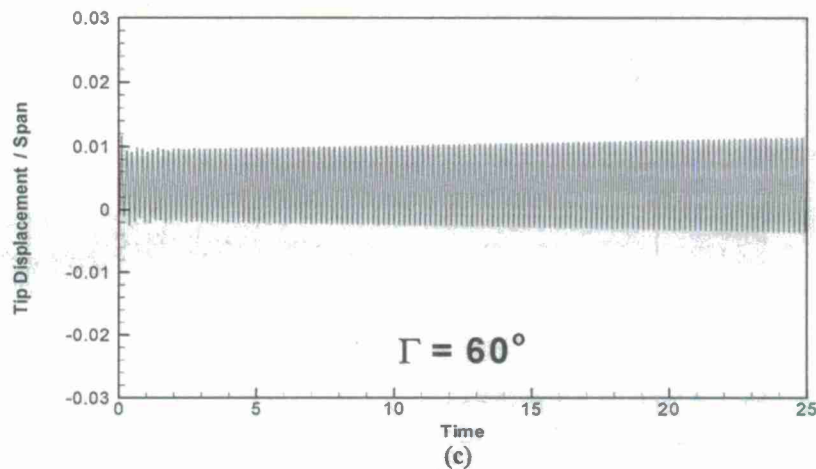


Figure 2.10. Comparison of Aeroelastic Responses.

From the results presented in Section (2.1), the flutter boundary of the folding wing can be roughly measured to be at an altitude $H=18\text{Kft}$ for the morphing angle of 0° , and $H=10\text{Kft}$ for the morphing angle of 60° . The direct simulation of a continuous morphing case is performed at $H=14\text{Kft}$ which is in-between the flutter boundaries of morphing angles 0° and 60° . The folding wing is scheduled to morph from 0° and 60° during the time period of $12\text{s} \sim 16\text{s}$. The wing tip displacement and damping time histories are shown in Figure 2.11. The aeroelastic response demonstrates a first diverging and then converging phenomenon. If the morphing schedule is reversed, i.e. morphing from 60° and 0° , the aeroelastic response shows the reverse in trend. Shown in Figure 2.12 a divergent oscillating persists up to 40s , presumably it will approach LCO of the $\Gamma=0^\circ$ case asymmetrically in time. For these two cases, a much larger velocity is applied on all structure grid points as the initial kick.

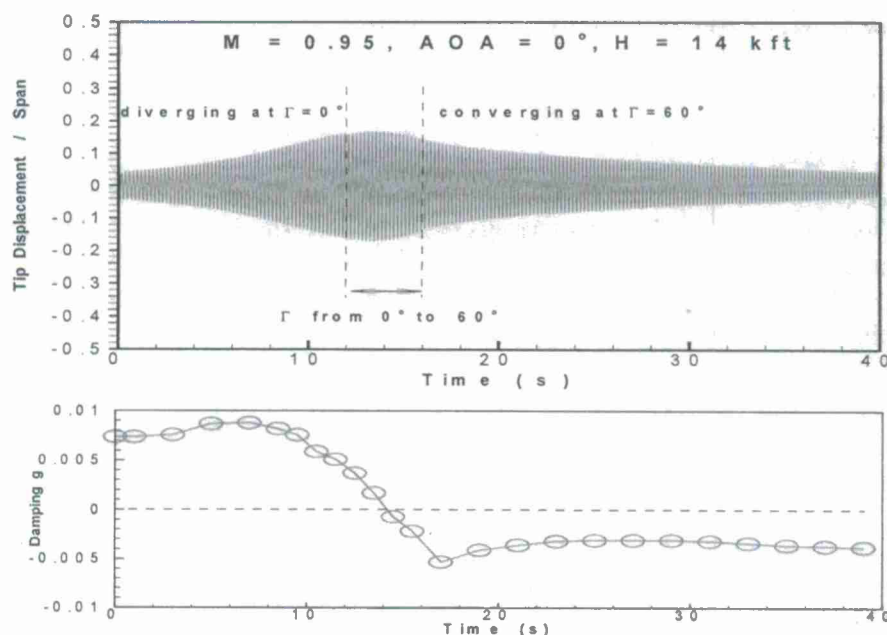


Figure 2.11. Continuous Morphing Response II.

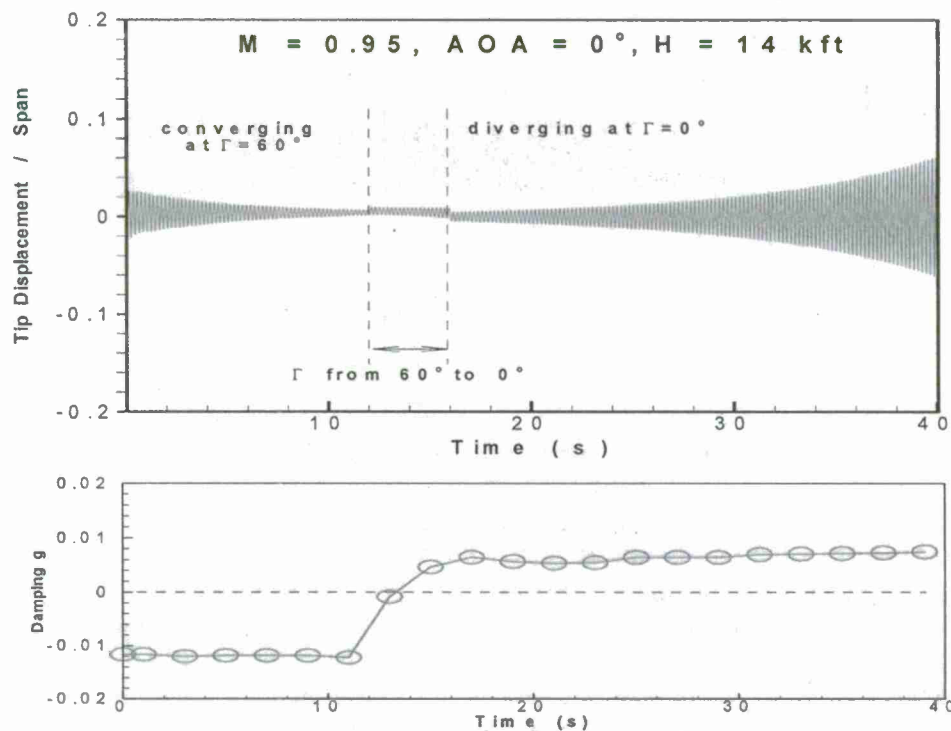


Figure 2.12. Continuous Morphing Response III.

2.4 Validation of the Non-Linear Substructure Model: Two-Piece vs. One-Piece Wings

After the linear structure model is validated, the nonlinear structure model is then constructed by including all the nonlinear terms in equation 1.3. This nonlinear structure model of the folding wing is validated by comparing the aeroelastic response between the nonlinear two-piece model and the nonlinear one-piece model. The foldig angle is fixed at $\Gamma = 0^\circ$. The wing tip's displacements at $M=0.95$, $AOA=0.0$ and $H=2\text{Kft}$, 10Kft , 20Kft and 30Kft computed by the two-piece and one-piece nonlinear models are presented in Figure 2.13. The initial kick is to apply a small velocity for all the structure grid points. Excellent agreement between these two sets of results can be seen. Both results also show that the foldig wing is unstable at $H=2.0\text{Kft}$ and becomes stable at altitude above 10Kft ; indicating that the flutter boundary of the folding wing at $M=0.95$ is between $H=2\text{kft}$ and 10kft .

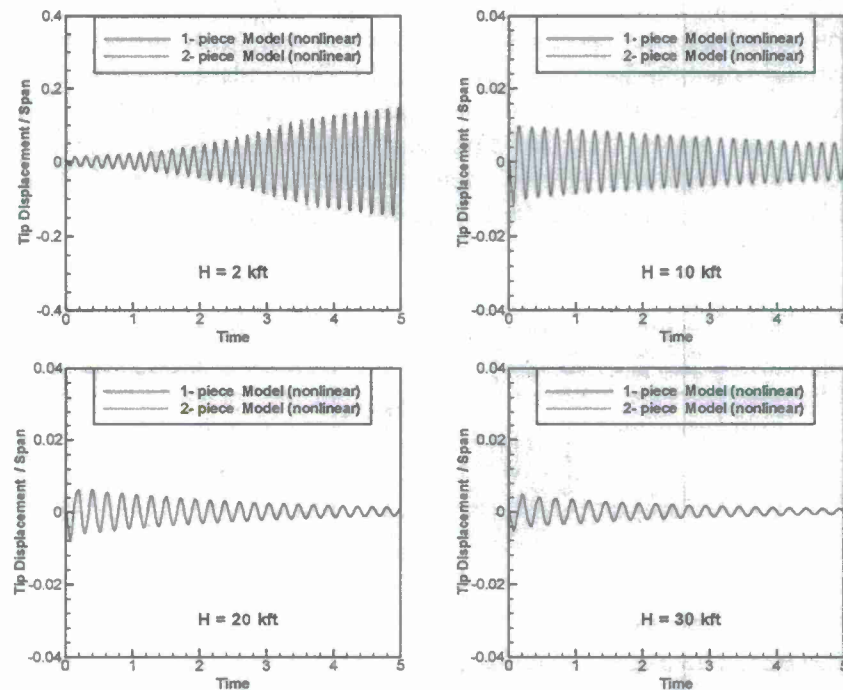


Figure 2.13. Validation of the Non-linear Two-Piece Model at Dihedral Angle 0° .

2.5 Comparison of the Aeroelastic Responses between the Two-piece Linear and Non-linear Models

The comparison of the wing tip's displacements computed using the two-piece linear and two-piece nonlinear structure models at $M=0.95$ and $H=2.0$ kft, 10. kft, 20.0kft and 30.0kft are presented in Figure 2.14 for the folding angle at 0 degrees and in Figure 2.15 for the folding angle at 20.0 degrees. The purpose of this comparison is to investigate the nonlinear structural effects on the aeroelastic response of the folding wing. Both two-piece linear and nonlinear models show that the folding wing is aeroelastically unstable at $H=2.0$ Kft and become stable when the altitude is above 10.0kft. In the stable region; i.e altitude is above 10.0kft, the wing tip displacements of the linear and nonlinear models are practically the same. This is expected since in the stable region the aeroelastic response is a decay motion after the structure is subjected to an initial kick. Therefore, the displacement is small in the entire time history. Because of the small displacement, structural nonlinear effects are negligible and the linear and nonlinear models become equivalent. However, at $H=2.0$ kft where the folding wing is unstable, a divergent response occurs initially and then the response becomes a limit cycle oscillation (LCO) whose oscillating amplitude is in the order of 20% of the wing span. Both the linear and nonlinear models show such a LCO. Apparently, the LCO computed by the linear structure model is only due to the nonlinear aerodynamics provided by the CartEuler whereas the LCO computed by the nonlinear structure model is due to both nonlinear structural and the nonlinear aerodynamic effects. This comparison between the LCO responses of the linear and nonlinear models allows us to investigate the contribution of the nonlinear structural and nonlinear aerodynamic effects in the LCO response of the folding wing. Both Figures 2.14 and 2.15 show that at $H=2.0$ kft the difference of the wing tip's displacements in the initial divergent motion

period between the linear and nonlinear models is very small. This is because in the initial divergent motion period the oscillating amplitude is small and the nonlinear structural effects are negligible. However, when the motion approaching LCO and the amplitude becoming large, the oscillating amplitude of the nonlinear model is significantly smaller than that of the linear model. This comparison clear shows that the nonlinear structural effects due to large structural deformation provide the stiffening effects to the aeroelastic system of the folding wing, thereby, resulting a smaller LCO amplitude than that of the linear structure model.

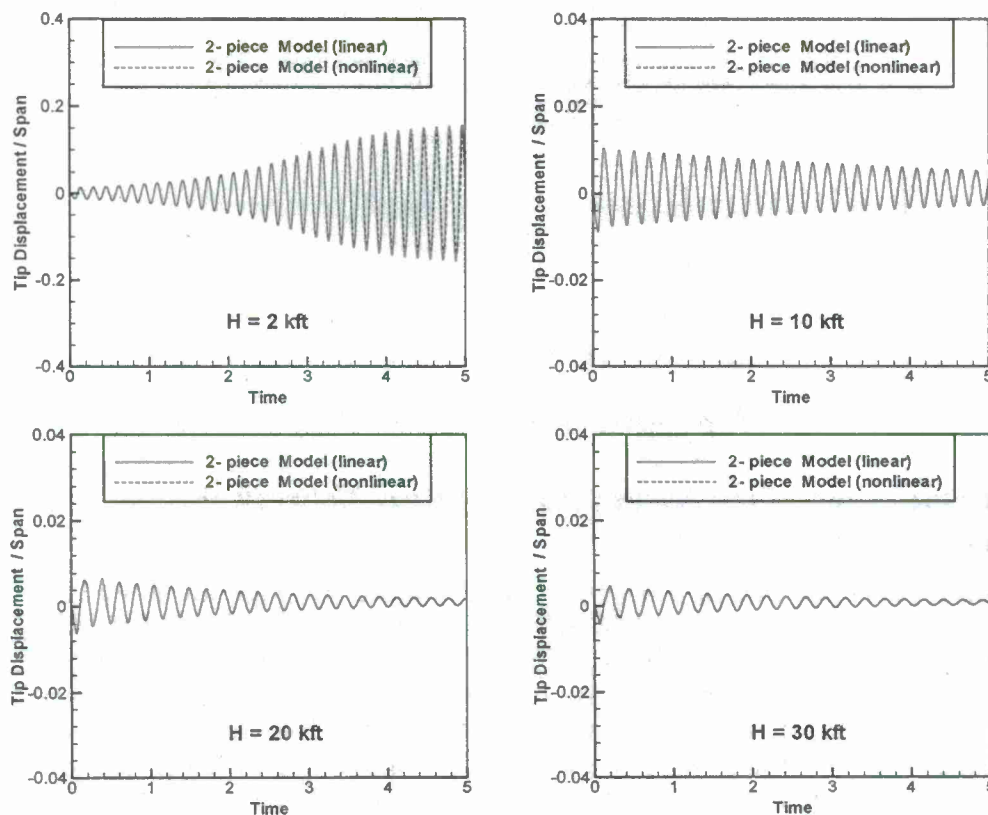


Figure 2.14. Comparison of the aeroelastic responses computed using the two-piece linear and nonlinear models at $\Gamma = 0^\circ$.

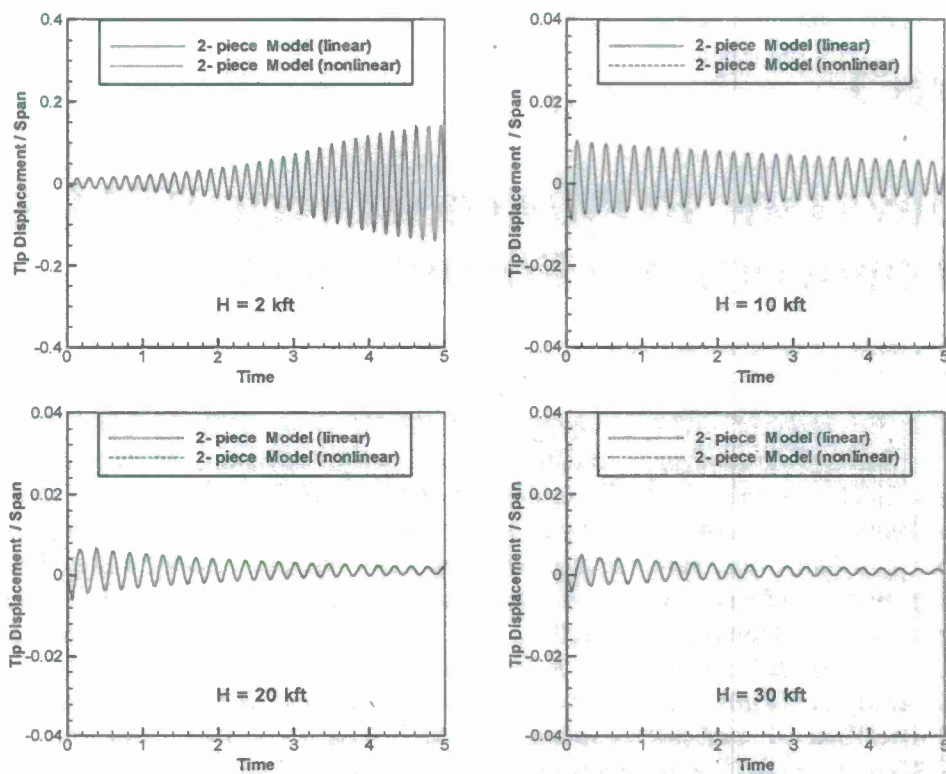


Figure 2.15. Comparison of the aeroelastic responses computed using the two-piece linear and nonlinear models at $\Gamma = 20^\circ$.

Chapter 3.

AERODYNAMIC ROM/AEROELASTIC ROM-ROM METHODOLOGY FOR FOLDING WING

Summary

ROM stands for reduced order modeling. ROM-ROM is used for solving the aeroelastic instability by solving the nonlinear structural ROM and Aerodynamic ROM jointly (Eq. (3.4)). Aerodynamic ROM was initiated by Silva, Dowell, Beran, and others. Figure 3.1 shows a survey on the development of Aerodynamic ROM. ZONA adopted a different approach which uses the CFD solver as a black box, hence a non-intrusive ROM method. ZONA's aerodynamic ROM methodology in fact adopts a system ID approach, which is a non-intrusive procedure. To implement the system identification method, it must be handled in time domain. It has been shown that a successful aerodynamic ROM is the key to achieving an accurate and rapid aeroelastic analysis. With a successive nonlinear structural ROM developed, ZONA then conceived (in Phase I) and fully implemented (in Phase II) a fully nonlinear Aero ROM-Structural ROM (or ROM-ROM) approach as a rapid nonlinear aeroelastic analysis procedure. In Section 3.2 we see that ROM-ROM dramatically reduces the computing time by 2-orders of magnitude for aeroelastic analysis applied to the Lockheed folding wing. Section 3.1 presents the establishment of the aerodynamic ROM methodology which yields ROM results in excellent agreement with that of the full-order (Section 2.0) for a folding wing at a fixed morph angle. The aerodynamic ROM methodology has been extended to include a morphing structure in which a multiple-component (or substructure) structural modeling approach is utilized. The aeroelastic ROM-ROM methodology has been extended accordingly. The ROM-ROM results have been validated with the full-order results in order to assume ROM-ROM's applicability to the quasi-steady as well as the continuous morphing of the folding wing with nonlinear substructure modeling.

Aero-ROM Type	System Outputs	Excitation Signal	Excitation Pattern	Frequency/Time Domain	Linear/Nonlinear
POD-ROM-HB (Dowell, Others)	Cp & Prime Variables	Sinusoidal	One by One	Frequency	Linear
Volterra (Silva, Others)	GAF	Impulse	One by One	Both	Both
		Step	One by One/Staggered	Both	Both
ERA (Kim, Others)	GAF	Impulse	One by One/Staggered	Time	Linear
POD (Beran, Others)	Cp & Prime Variables	Impulse	One by One	Time	Nonlinear
ARMA (Lai, Cowan, ZONA, Others)	GAF	3211 Multiple-Step	One by One	Time	Linear
		Gaussian-Filtered Noise	One by One	Time	Linear
		FIM	Staggered	Time	Linear
NNet (ZONA)	GAF	FIM	Staggered	Time	Nonlinear

Figure 3.1. Comparisons of Various Aerodynamic ROMs.

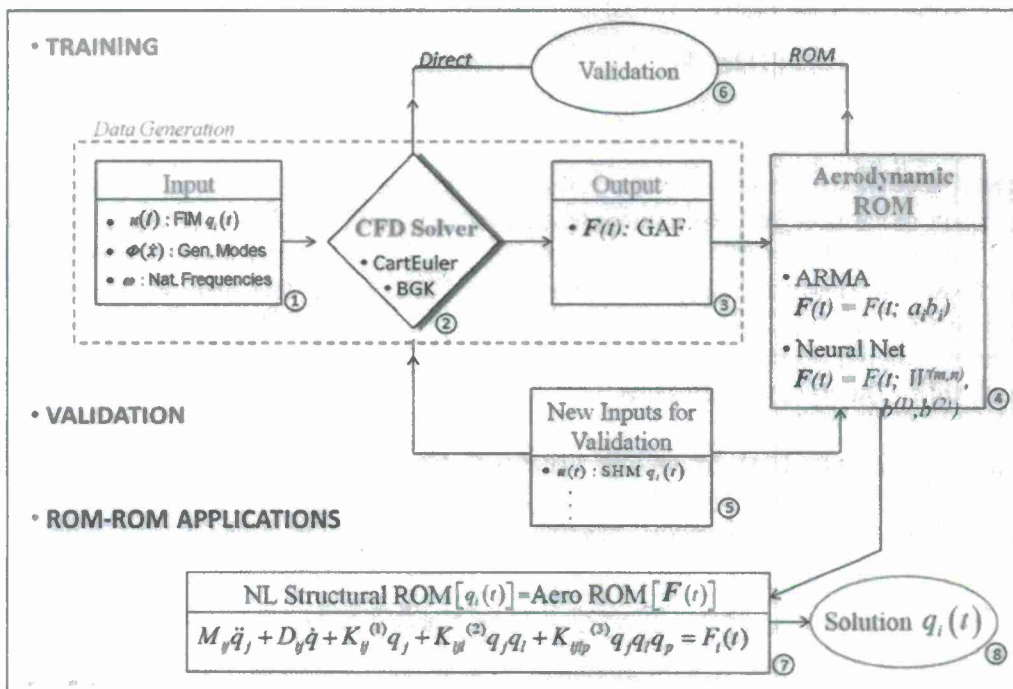


Figure 3.2. Aeroelastic ROM-ROM Roadmap.

As shown in the road map of Figure 3.2, ROM-ROM has three parts: Training, Validation and ROM-ROM Applications.

- *Training* was to build the AeroROM from (1) to (4) using the system ID approach. We selected a proper input such as a generalized coordinate in terms of an impulse function called filtered impulse model (FIM). Here we treat a given CFD solver as a black box. We get an output in terms of generalized aerodynamic forces (GAF). We then built up a response relation between the input and output. The linear relation is ARMA, nonlinear is NeuralNet.

- *Validation* was to assure that the aeroROM works. So we selected a new input, a simple harmonic signal. It goes through both ways and we validated the ROM result with the full order, or direct solution from CFD.
- *ROM-ROM Application* was built on the ROM-ROM equation where its RHS is the GAF of the neural net (or ARMA) and the LHS is the nonlinear Structural ROM provided by the method discussed in Chapter 1. Now we solve for the response in the general coordinate "q".

3.1 Aerodynamic ROM Methodology

We have developed a time-domain aerodynamic reduced order modeling (ROM) based on the CFD solver, CartEuler. The system identification technique was applied to find the simplified mathematical model (ROM) between the response of the aeroelastic system, i.e., the modal coordinates (or generalized coordinates), and the generalized aerodynamic forces (GAFs). The parameters defining the model structure are found through fitting a set of recorded (or measured) input/output data from the dynamic system; a process which usually is called training. Here, we implement the filtered impulse method (FIM) signals as the training excitation inputs.

A FIM signal is given by:

$$u(t) = \begin{cases} Ae^{a_0(\omega t - \omega t_0 - \pi)^2} \sin(\omega t - \omega t_0) & \text{when } t \geq t_0 \\ 0 & \text{when } t < t_0 \end{cases} \quad (3.1)$$

A staggered sequence (one after another) of FIM inputs of modal coordinates was employed for training. Each mode uses its own natural frequency as the ω in Eq.(3.1). The reason behind this choice is that it is believed that each mode would be excited around its own natural frequency. With the prescribed motion (staggered FIMs), the CFD solution by CartEuler is carried out and the time responses of the GAF are recorded so that the complete training data set in terms of the pair of inputs (modal coordinates) and outputs (GAFs) is obtained. Note that, the GAFs should be normalized by the dynamic pressure.

Two types of discrete time modeling structures are used to represent the ROM between generalized coordinates and normalized GAFs. The first one is the autoregressive moving average (ARMA) model. By denoting y as the output, and \mathbf{u} as the input vector, we have

$$y(t) = \sum_{i=1}^{n_a} a_i y(t-i) + \sum_{j=1}^{n_b} \mathbf{b}_j \mathbf{u}(t-j+1) \quad (3.2)$$

where n_a and n_b represent the order of the model.

The second is the feed-forward neural network (NNet). A two layer neural network is shown in Figure 3.1, which consists of an input layer and an output layer, to represent the forward dynamics of the plant. The input layer shown in Figure 3.1 includes vector \mathbf{U} which consists of the current and previous input signals, and, vector \mathbf{y}_p consisting of n_b the previous plant outputs, and S neurons. The size of vector \mathbf{U} would be the product of the number of components (or channels) of input signal and the delay order n_b .

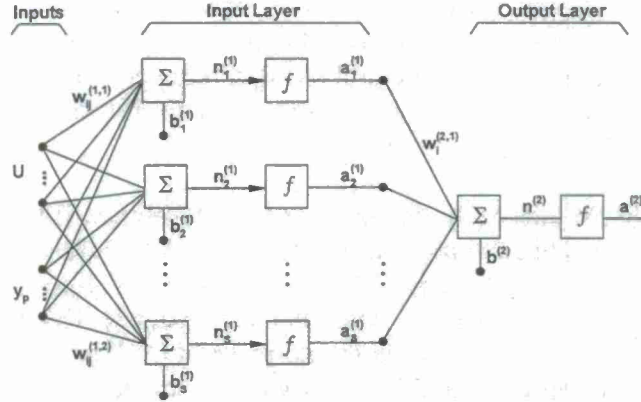


Figure 3.1. Two-layer Feed-Forward Neural Network.

The modeled plant output at time t by the neural network would be given in a concise notation as

$$y(t) = a^{(2)} = W^{(2,1)} \cdot \tanh \left(W^{(1,1)} \cdot U + W^{(1,2)} \cdot y_p + b^{(1)} \right) + b^{(2)} \quad (3.3)$$

When the neural network is given appropriate weights and biases, it provides the desired outputs. The process to get the proper set of weighted matrixes and the biases is called the training or learning of the network.

It can be seen that the ARMA model can be represented by one neuron model with linear transfer functions. We always start with the ARMA model to determine the proper delay order n_a and n_b .

Using the training data, an optimization procedure is implemented to search for the best parameters a_i , b_i in Equation (3.2) and $W^{(1,1)}$, $b^{(1)}$, $W^{(2,1)}$, and $b^{(2)}$ in Eq.(3.3) by minimizing the mean square of the error between the model output and targeted output (mse) or the generalized mean square error (msereg).

3.2 LCO Solutions for the Folding Wing using ROM-ROM

The purpose of the ROM-ROM procedure is to solve the time consuming issue of coupling the nonlinear structural dynamic equations with the generalized aerodynamic forces F_i directly computed by the CFD solver, e.g., CartEuler. With the aerodynamic ROM in lieu of the CFD solver, e.g., using the neural network model, the nonlinear aeroelastic equation is recast as

$$M_{ij} \ddot{q}_j + D_{ij} \dot{q}_j + K_{ij}^{(1)} q_j + K_{ijl}^{(2)} q_j q_l + K_{ijlp}^{(3)} q_j q_l q_p = \frac{1}{2} \rho V_\infty^2 \left(W_i^{(2,1)} \cdot \tanh \left(W_i^{(1,1)} \cdot U + W_i^{(1,2)} \cdot F_{lp} + b_i^{(1)} \right) + b_i^{(2)} \right) \quad (3.4)$$

Thus, Eq. (3.4) is a ROM-ROM approach ready to be time integrated. It can be seen that the time savings by using the ROM-ROM procedure could be dramatic.

Since the Phase I work, the folding wing structural model has been modified to accommodate the morphing dynamics modeling. The change mainly lies in the interface between the inboard and

outboard wing components. Rigid bars have been added in the interface. Therefore, new nonlinear ELSTEP ROM was developed for this new configuration. Figure 3.2 shows the comparison of the tip transverse displacement solutions by a different solver, from which we can see that the solution by the nonlinear structural ROM agrees very well with the nonlinear Nastran solution. Note that the loading factor of 1 corresponds to a series of unit concentrated forces on the nodes lying in the wing tip.

Following the ROM-ROM approach, the aerodynamic ROMs are firstly sought before solving Eq (3.4). The inputs (prescribed staggered motion of modal coordinates), and the normalized GAF solutions by CartEuler and the trained ROM are shown in Figure 3.3 for the folding wing at zero morphing angle (as a flat plate). After the aerodynamic ROMs are obtained through training, they were validated by comparing the normalized GAF predictions to the aerodynamic ROMs with the direct full-order CFD solutions where any modal coordinate are prescribed by a sinusoidal excitation. Figure 3.4 presents such a validation comparison at which the first modal coordinate is given a sinusoidal excitation while all others are kept at zero. We can clearly see that the aerodynamic ROMs have done an excellent job of prediction.

Two typical LCO solutions with the ROM-ROM approach are shown in Figures 3.5 and 3.6 along with the solutions obtained with CartEuler directly providing the aerodynamic forces. In both cases the attitude was 0 Kft and -10 Kft, LCO amplitudes predicted by the ROM-ROM approach agree very well with the direct CFD approach, but phase shifting occurs as the LCO develops.

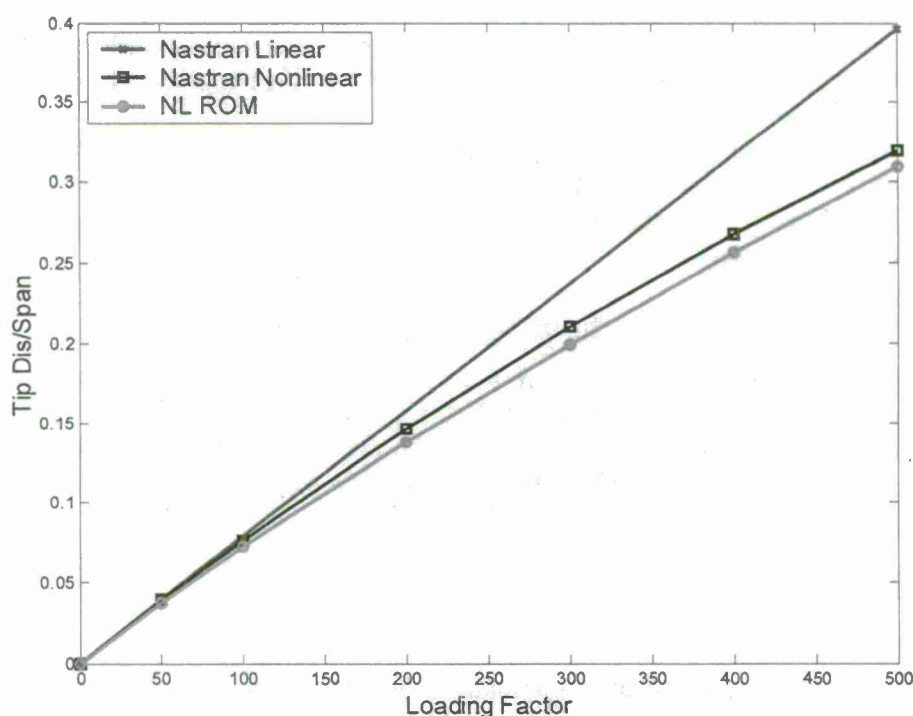


Figure 3.2. Validation of NL Structural ROM for the Folding Wing (zero Morphing angle).

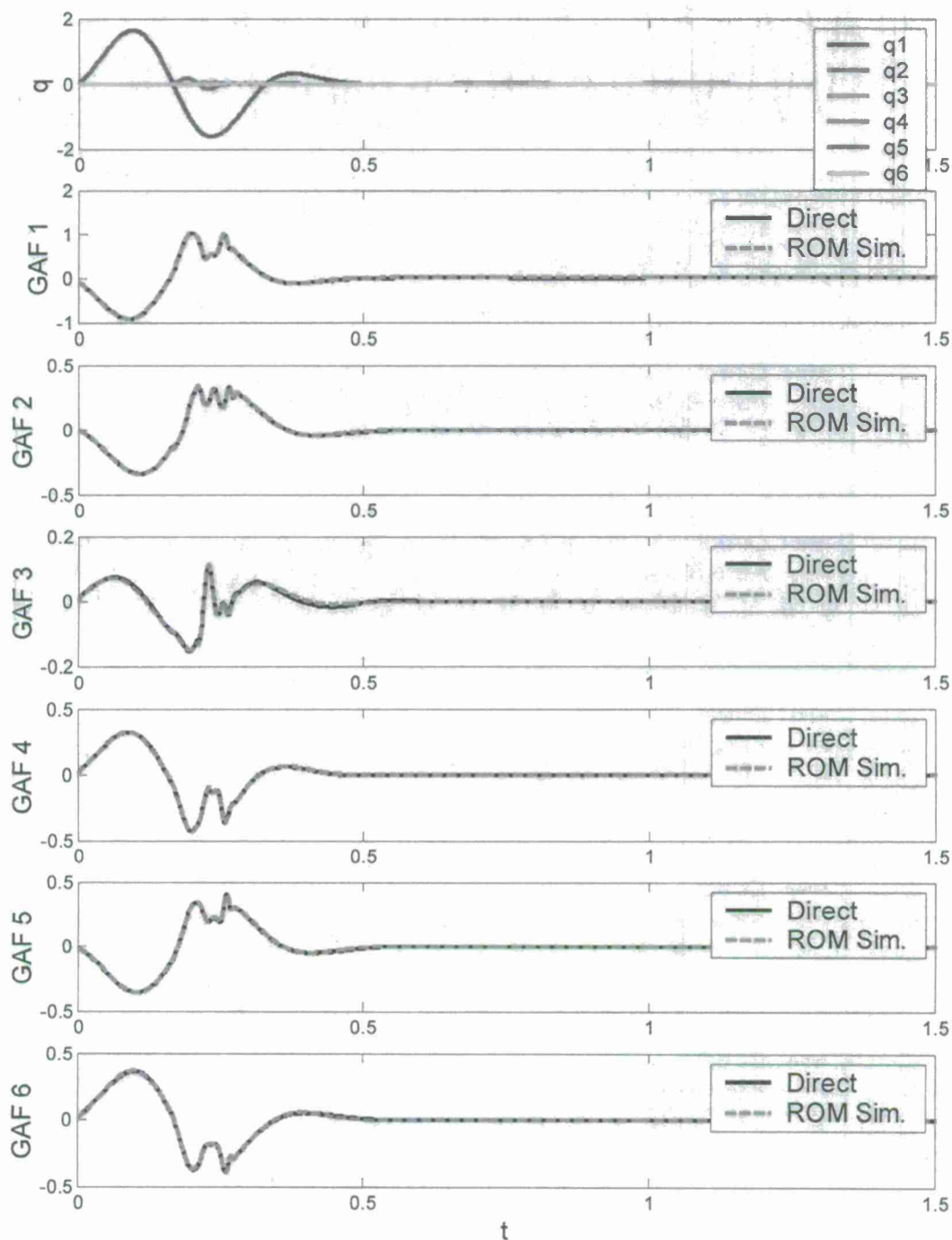


Figure 3.3. Aerodynamic ROM Training (Mach=0.95, AoA=0). System Inputs (staggered FIM excitations for the modal coordinates); System Outputs: Normalized GAFs.

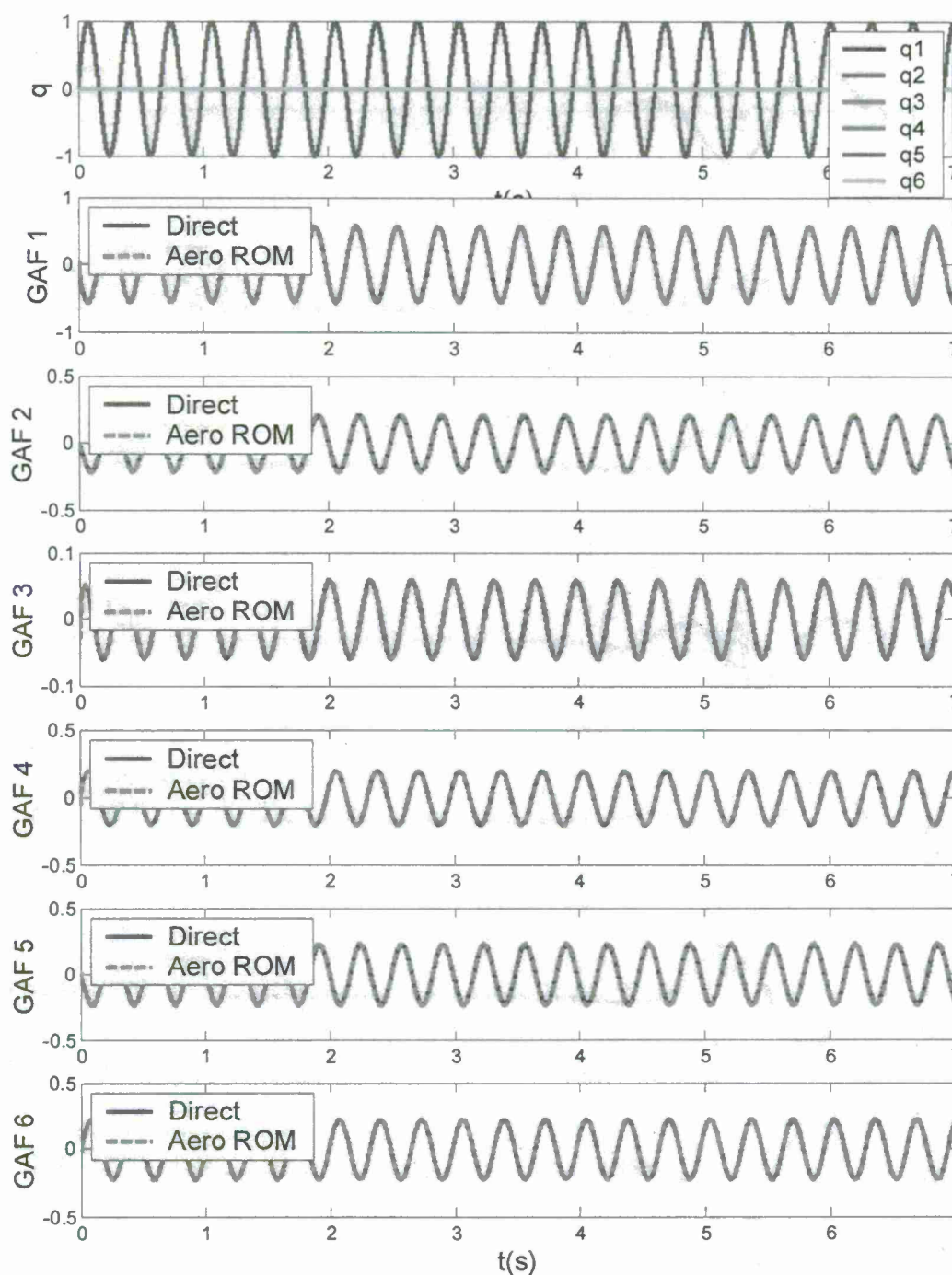


Figure 3.4. Validation of the Aerodynamic ROMs (Mach=0.95, AoA=0): Comparison Between the GAF Predictions by the Aerodynamic ROMs and the Direct Full-Order CFD Solutions (Mode 1 is given a sinusoidal excitation)

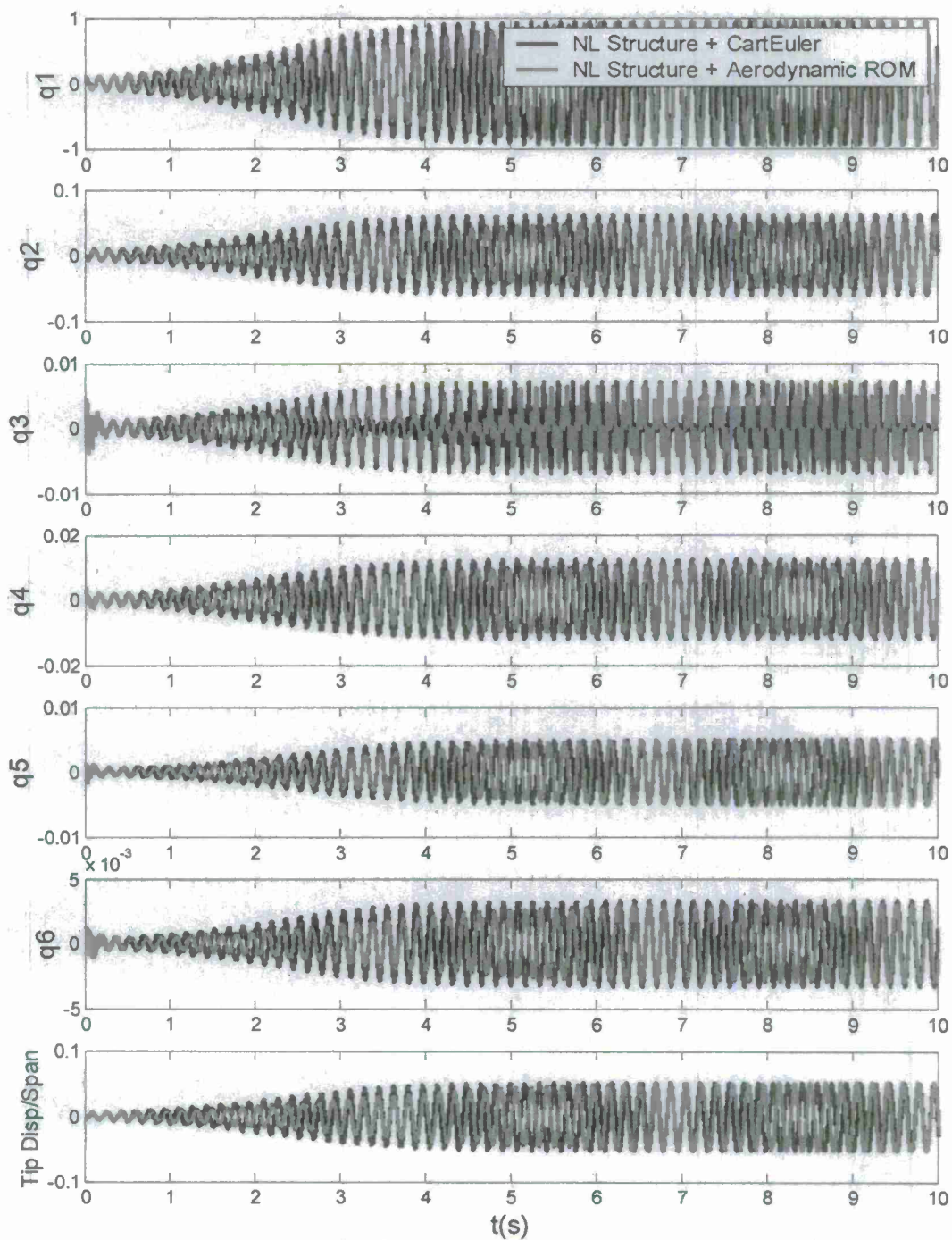


Figure 3.5. Nonlinear Aerodynamics/Nonlinear Structural Analyses for the Folding Wing (zero Morphing angle) at $M=0.95$, $H=0kft$; LCO: ROM-ROM (Red) vs Direct (Blue)

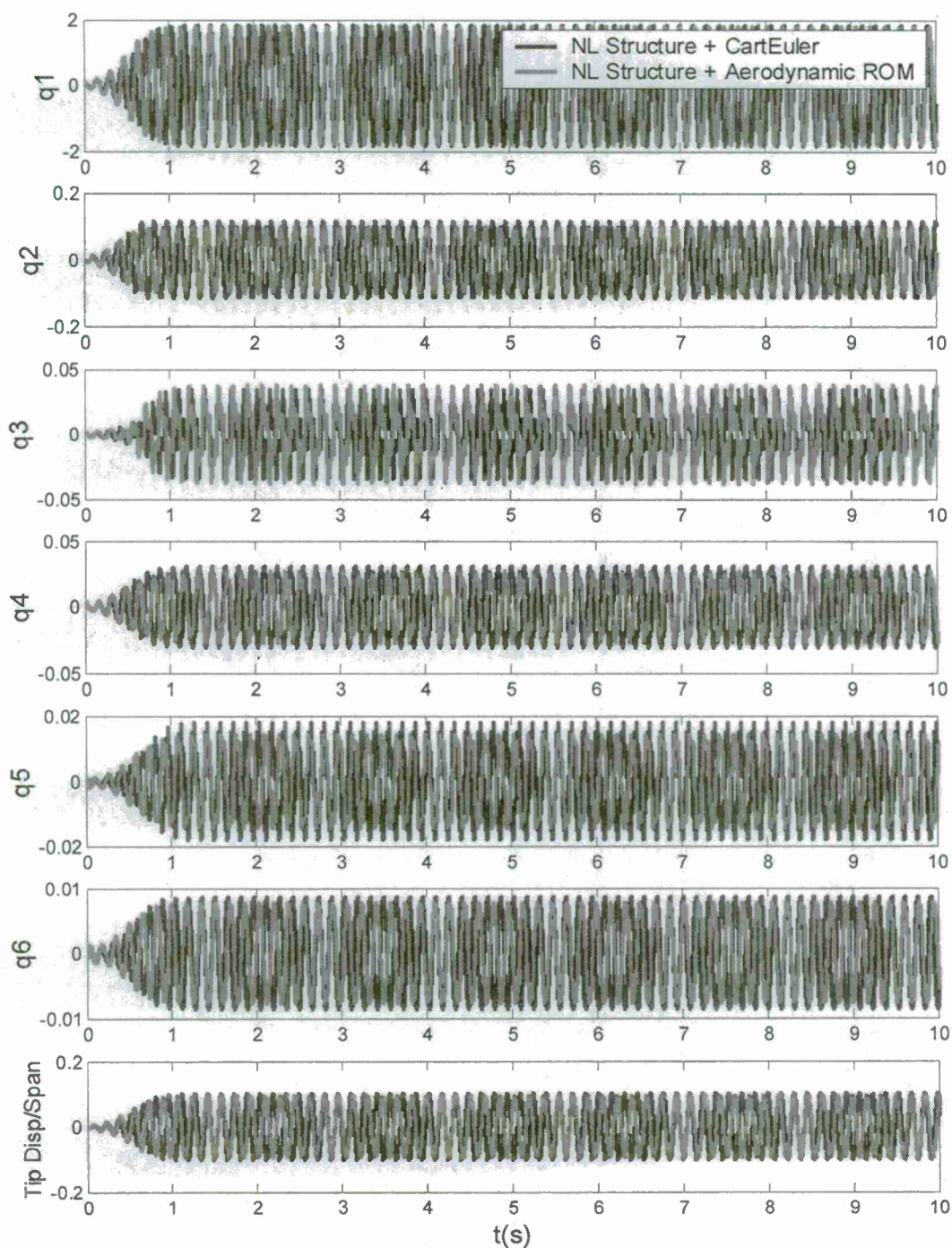


Figure 3.6. Nonlinear Aerodynamics/Nonlinear Structural Analyses for the Folding Wing (zero Morphing angle) at $M=0.95$, $H=10\text{kft}$; LCO: ROM-ROM (Red) vs Direct (Blue)

Chapter 4.

3D GRIDLESS BOUNDARY CONDITION CARTESIAN (GBCC) DEVELOPMENT

Summary

We have worked out a preliminary GBCC procedure for 2D/3D grid cutting. This cutting procedure has been tested for three wing planforms: the LANN wing, the Lockheed folding wing and the Goland wing. The GBCC solver development was followed by a rigorous verification and validation procedure. To validate the GBCC solver, it was required to verify that each grid system works properly following a three tier verification process. After the GBCC system was verified, we used it to compute for steady pressures on the Goland wing and to validate its results against that of ZEUS' body-fitted code (see Chapter 6 for more details on ZEUS). GBCC3D has been developed to handle time-domain aerodynamics in terms of wing oscillation and continuous wing pitching. With the improved GBCC3D it is now a viable method for expedient nonlinear aeroelastic applications to pitching wings. The GBCC3D has been validated by quasi-steady solutions and continuously pitching solutions with available solutions computed by ZONA's codes such as skewed CartEuler, CFL3D, and existing test data. The grid cutting procedure and ease of application have been improved to handle a wider class of wing planforms. We have also implemented the grid refinement to improve GBCC's solution accuracy and solution resolution. The improved GBCC scheme relaxes the far field grid density and built in the multigrid scheme in order to accelerate the computation.

4.1 The GBCC Flow Solver

A GBCC procedure has been worked out for grid cutting, the efforts continues in GBCC2D/3D computational procedure for the GBCC flow solver. The GBCC solver has two developmental stages, namely that of 2D and 3D. In the GBCC solver, the cell-centered finite volume used for the Cartesian grid and gridless method based on least square method is used for gridless points. The 2nd order and 4th order blending artificial dissipation is used to remove solution oscillations near the stagnation point and shock wave. Local time step, residual smoothing and enthalpy damping are used to accelerate the convergence. Multi-grid and local refinement is currently implemented into the solver. For demonstration, the developed GBCC code was applied to a 2D airfoil (NACA0012) and a 3D wing (Goland) in the transonic/supersonic Mach number range (see Figures 4.3, 4.4, 4.5, and Figures 4.15, 4.16, 4.17).

4.2 The Improved GBCC Stencil

During the course of our Phase II development, a new stencil for the GBCC was established to replace the one proposed. With this improved (also simplified) stencil, the surface boundary condition can be treated in a more convenient manner.

- Previously in Phase I, the grid points were divided into six different types, as shown in Figure 4.1(a). Before the computation, the six types of grid points have to be identified, and additional cloud nodes have to be added.

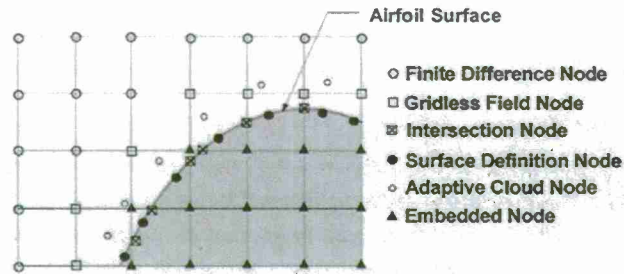


Figure 4.1(a). GBCC Gridless System from Phase I.

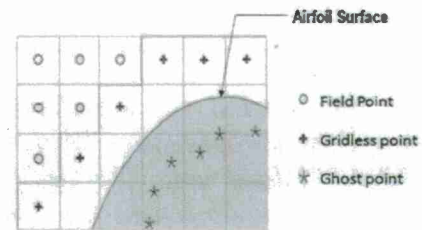


Figure 4.1(b). GBCC Gridless System from Phase I.

- In the Phase II proposal, the gridless stencil was reduced to three types, as shown in Figure 4.1(b). The ghost points are implemented to satisfy the boundary condition. The physical variables location was changed from cell vertex to cell center.

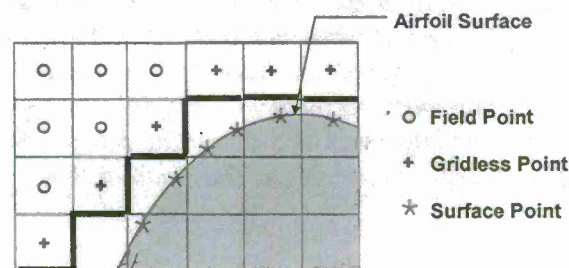


Figure 4.1(c). Current GBCC Gridless System.

- The improved stencil was to replace ghost points by the surface points, as shown in Figure 4.1(c), the boundary condition is directly applied to the wall surface point. Thus, with this set of stencil points specified on the exact wall surface, the pressure results can be readily obtained without solution interpolation which is required by the previous stencil methods.

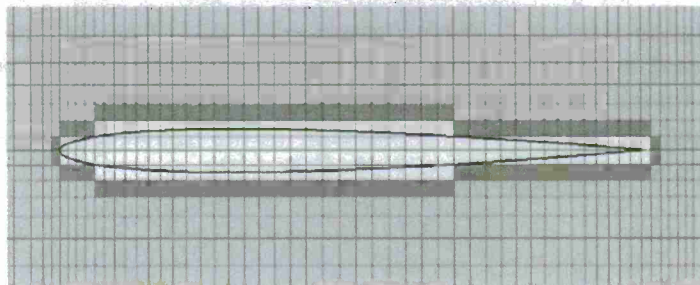


Figure 4.1(d). GBCC Gridless System for NACA 0006 airfoil.

4.3 New GBCC2D Solutions

- Symmetrical Airfoil in Subsonic, Transonic and Supersonic Flow

With the improved stencil (Figure 4.1(c)), we used the GBCC2D solver to compute for the flow field of a NACA 0012 airfoil at three Mach numbers, namely that of subsonic, transonic and supersonic, and at different angles of attack. Computed results are presented in Figures 4.2, 4.3 and 4.4. The surface pressure distributions of GBCC are plotted against that of the body-fitted grid showing comparable accuracy. The wiggles in the GBCC pressure distribution are believed to be caused by the grid cutting and the size of the Cartesian grid imposed. Further improvement to smooth out these wiggles is anticipated. The convergence speeds (transonic/subsonic) of the GBCC are also comparable to that of the body fitted solution according to previously published results.

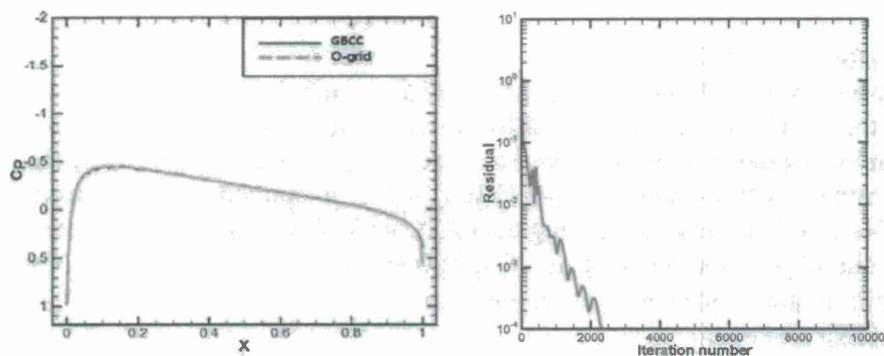


Figure 4.2. Pressure Distribution and Convergence History for NACA 0012 Airfoil at $M=0.4$, $\alpha=0^\circ$.

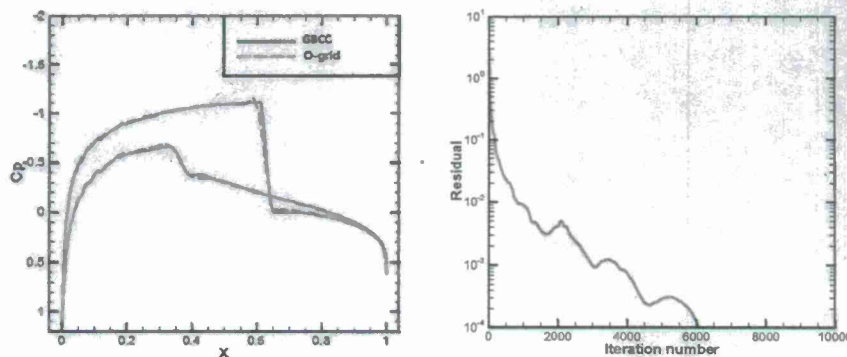


Figure 4.3. Pressure Distribution and Convergence History for NACA 0012 Airfoil at $M=0.8$, $\alpha=1.25^\circ$.

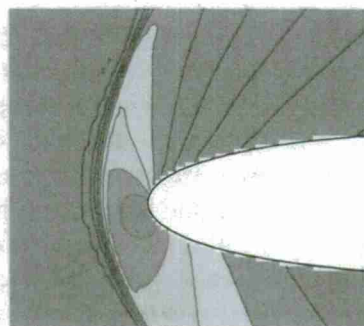
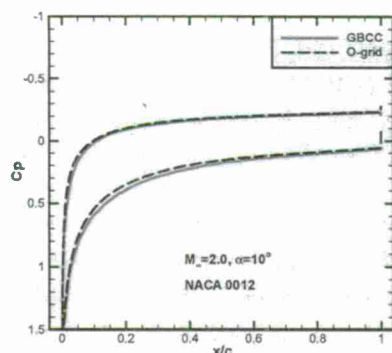


Figure 4.4. Pressure Distribution and Pressure Contour for NACA 0012 airfoil at $M=2.0$, $\alpha=10^\circ$.

• *Rotated Airfoil with GBCC Grid*

In order to work on a configuration with the relative motion of a folding wing in morph, the capability of the GBCC solver was tested for an airfoil in rotation for the 2D case. For GBCC, the background Cartesian is kept unmoved and the cut grid (with the gridless points) along with the airfoil is rotated with an angle δ . The GBCC solver is applied to this rotated airfoil GBCC system for a NACA 0012 at a rotated angle δ of 2° , while keeping the freestream flow unaltered (Figure 4.5). The GBCC surface pressure distributions are compared with that of the body-fitted grid whose freestream is placed at an angle of attack, α ($=\delta$), of 2° (Figure 4.6), following a conventional CFD practice.

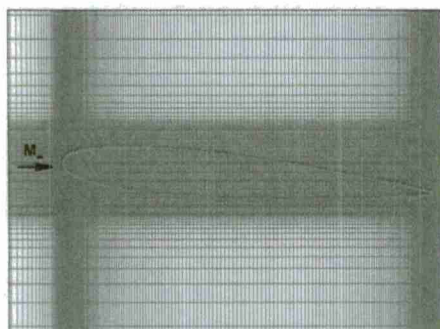


Figure 4.5. GBCC Grid.

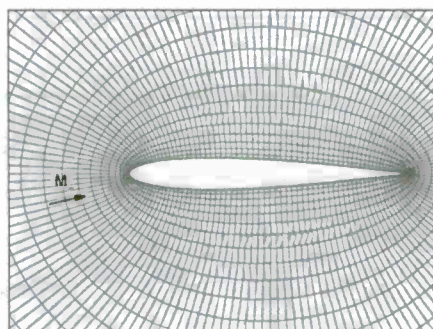


Figure 4.6. Body-Fitter O-Grid.

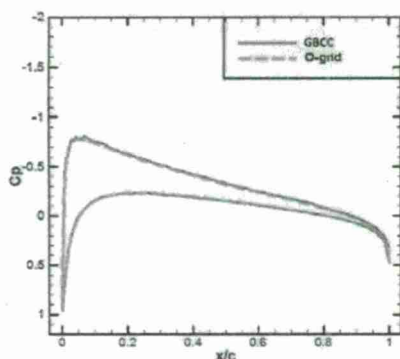


Figure 4.7. Pressure Distribution $M=0.4$, $\alpha=2^\circ$.

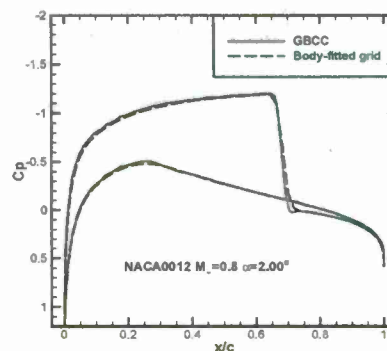


Figure 4.8. Pressure Distribution $M=0.8$, $\alpha=2^\circ$.

Figures 4.7 and 4.8 show the comparison for subsonic and transonic pressure distributions of a NACA0012 airfoil at rotation angle $\delta=2^\circ$ and at AoA $\alpha=2^\circ$. Good agreement between these two sets of results assures the capability of GBCC for future morphing applications.

4.4 GBCC3D Grid Cutting Procedure

- GBCC Terminology Revisited

The main task of GBCC was to develop an autonomous scheme that could define the boundary between the cut grid and the uncut grid (the black line boundary) and to figure out the solid body imbedded in the Cartesian grid system. Between the black line boundary and the solid surface are the whiteout cut cells that contains no computational points.

With reference to Figure 4.1(c), the three sets of points are defined as the *field point* (o) (the center point in a background Cartesian cell), the *gridless point* (+) (those in the uncut cells, or called the gridless cells, that are next to the whiteout cut cells), and the *surface points* (*). For a full airfoil in Figure 4.1(d), these points are respectively placed in the gray cells, the green cells and on the airfoil surface. Furthermore, a cloud of points, or a cloud, is defined (in 2D) by a 5 point system centered around, but also includes, a gridless point.

- GBCC3D Grid Cutting

Based on the 2D grid cutting tool and the procedure developed, we proceeded with the development of a 3D grid-cutting procedure. The 3D grid-cutting process was put forth with the following steps:

- Generate a background Cartesian grid and mark those Cartesian cells as regular cells,
- Define the wing surface through surface grid point interpolation
- Construct a rectangular *box* in the Cartesian system that contains the wing
- Through the interaction of the wing surface and the Cartesian grid lines, identify the Cartesian cells as cut cells
- Use *box* to identify the grids enclosed by the wing surface and mark them as solid cells
- Identify the gridless cells accordingly
- Collect clouds for all gridless cells and output the information for computation.

After the grid-cutting cell tool was established, the LANN wing was selected as the test case. The cutting-cell is shown in Figure 4.9. Figure 4.9(a) represents the cutting-cell for the LANN wing when the mean plan is parallel to the Cartesian grid. Figure 4.9(b) represents the case for a LANN wing in pitch; here the wing surface grid is rotated by 10° about a pitching axis.

The diagram of the cutting cell at the symmetric plan for the LANN wing is shown in Figure 4.10. There, the grid with purple lines represent the Cartesian cells that contain field points which shall be computed by a finite volume method. The cells bounded by red lines represent the cells that contain gridless points which shall be used for the gridless method computation. The cells bounded by blue lines represent those that contain cut cells. And the cells bounded by green lines, which is enclosed by the wing surface (in black dots), represent the cells inside the body. Both the cut cells and the body cells will be excluded from the computational domain.

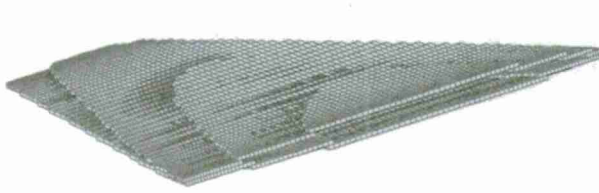


Figure 4.9(a). Cutting cell around LANN Wing ($\delta=0^\circ$).

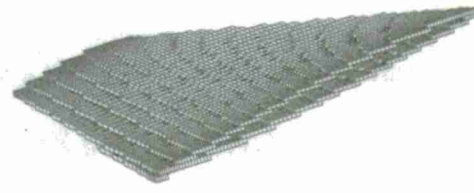


Figure 4.9(b). Cutting cell around LANN Wing ($\delta=10^\circ$).

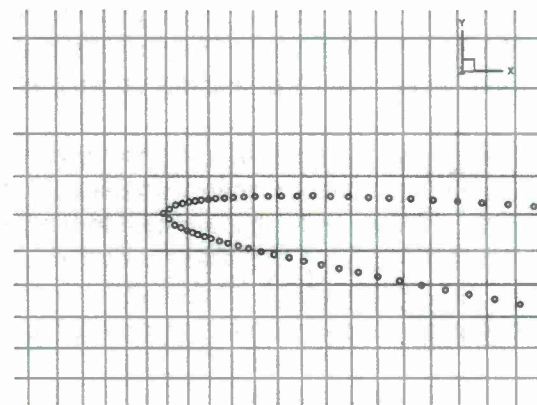
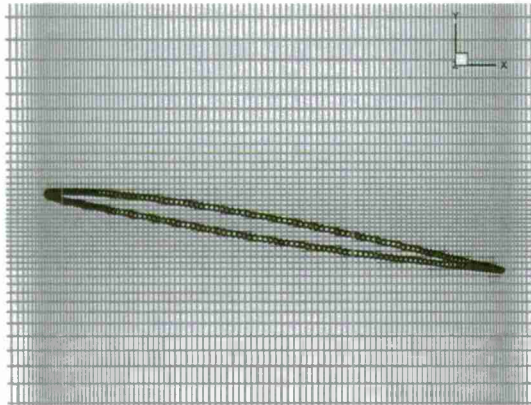
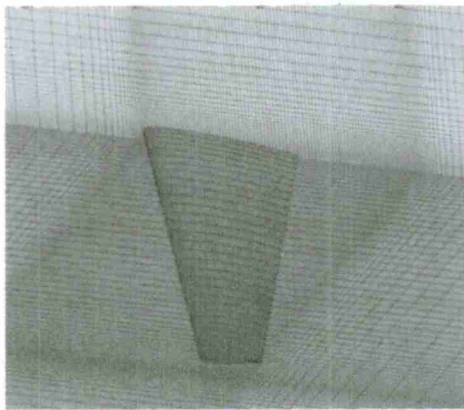
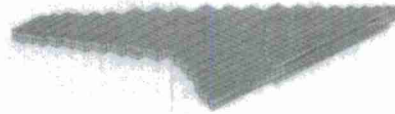
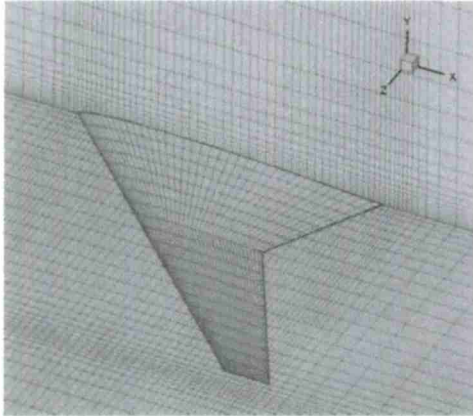


Figure 4.10. GBCC cell cutting for LANN Wing at symmetric plane ($\delta=10^\circ$).

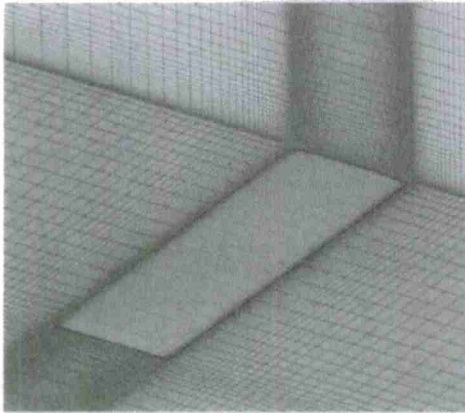
Three wing configurations were selected as candidate wings for GBCC computation cases. These are: i) the LANN wing; ii) the Lockheed folding wing; and iii) the Goland wing. Figure 4.11 shows the Cartesian grid system and grid cutting configuration of these wings.



(a) LANN Wing (AR=8) 12% Thickness Supercritical Airfoil.



b) Lockheed Folding Wing with NACA 0006 Airfoil (AR=4.4).



(c) Golland Wing (AR=6.67) 4% Thickness Parabolic Arc Section.

Figure 4.11. Three Candidate Wings for GBCC Grid.

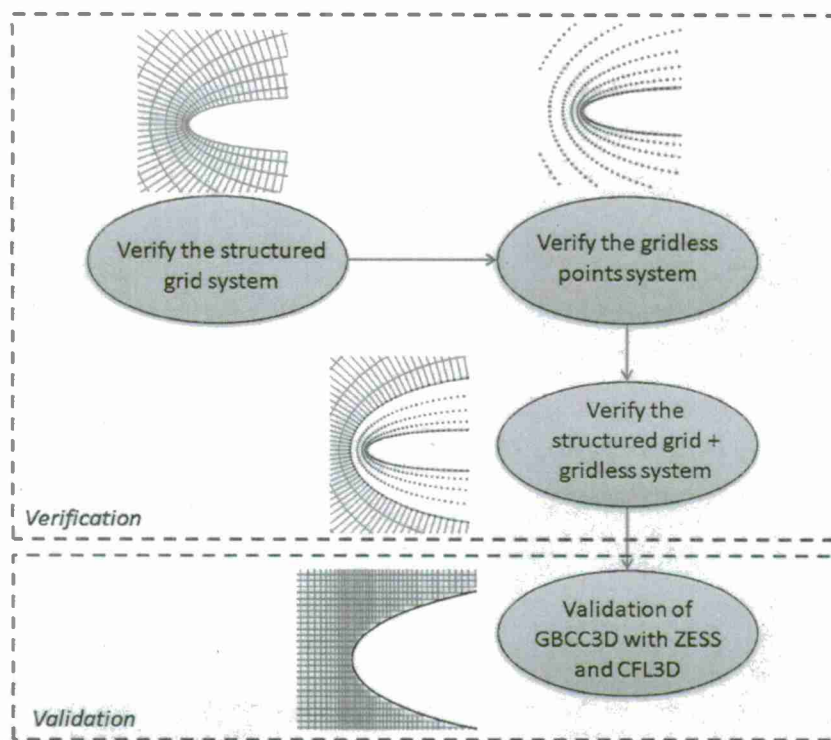
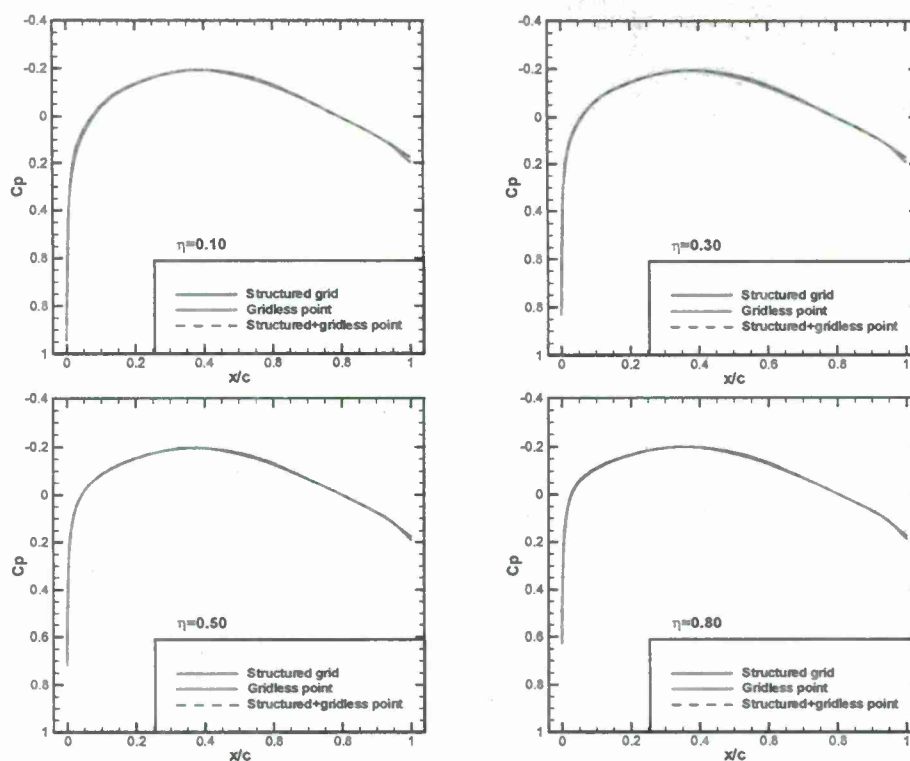


Figure 4.12. GBCC3D Development: Verification and Validation.

Figure 4.13(a). Pressure Distributions at Four Spanwise Locations of Lockheed's Folding Wing at $M=0.8$, $\alpha=0^\circ$.

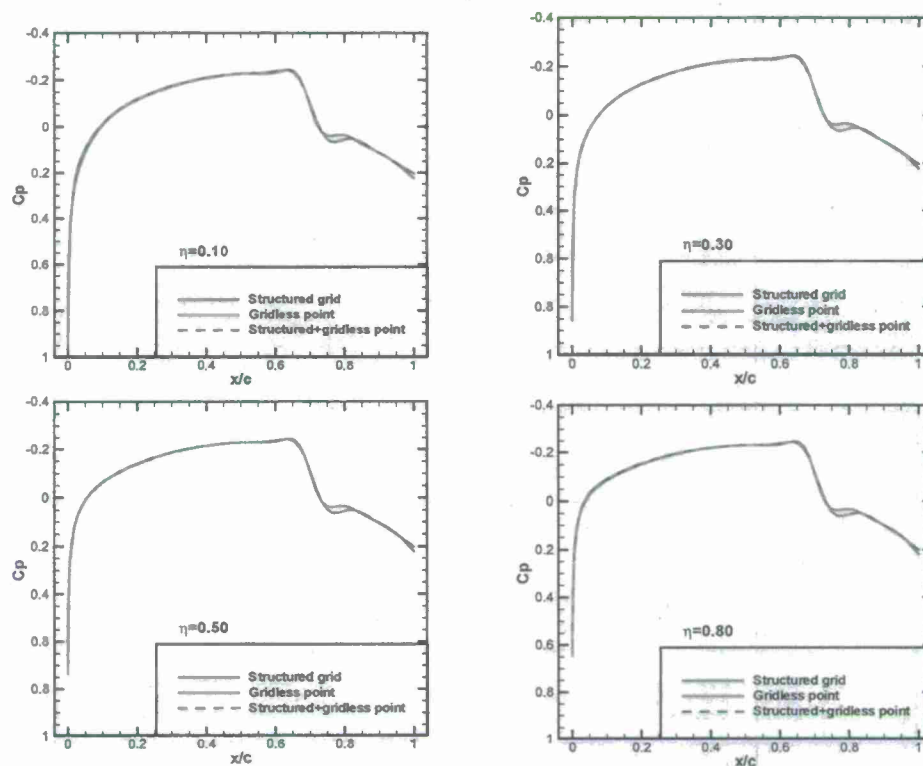


Figure 4.13(b). Pressure Distributions at Four Spanwise Locations of Lockheed Folding Wing at $M=0.95$, $\alpha=0^\circ$.

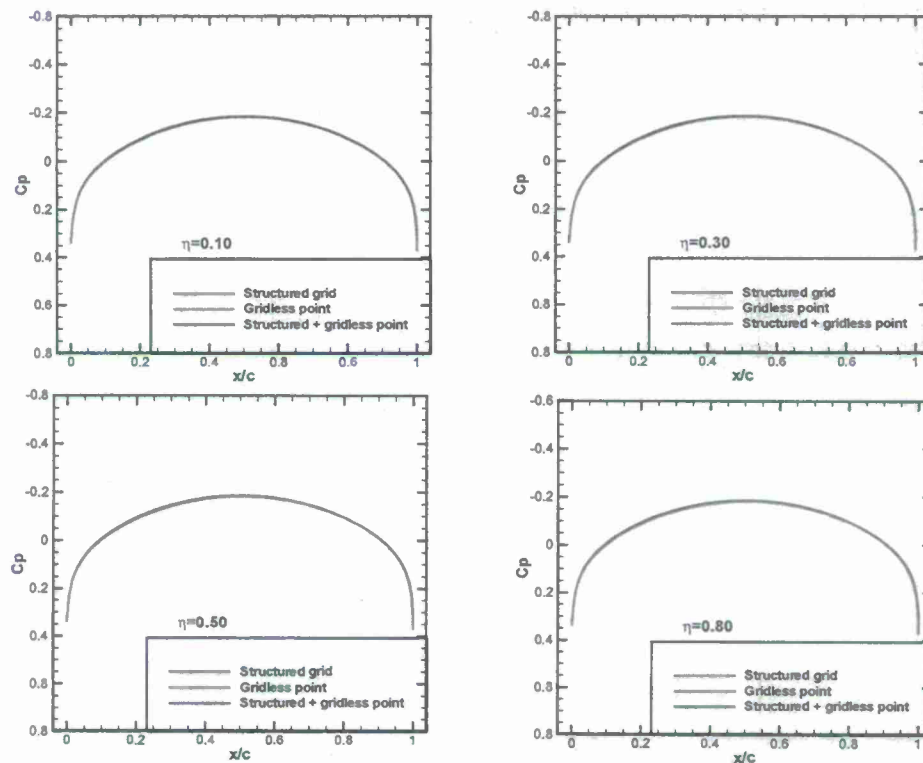


Figure 4.14(a). Pressure Distributions at Four Spanwise Locations of Goland Wing at $M=0.8$, $\alpha=0^\circ$

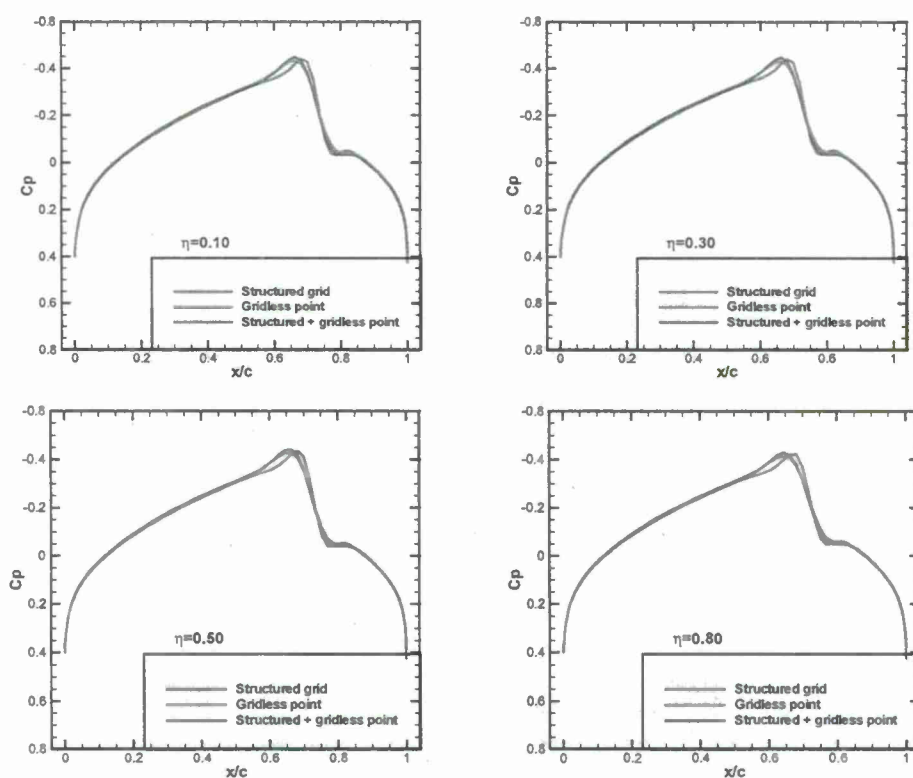


Figure 4.14(b). Pressure Distributions at Four Spanwise Locations of Golland Wing at $M=0.90$, $\alpha=0^\circ$.

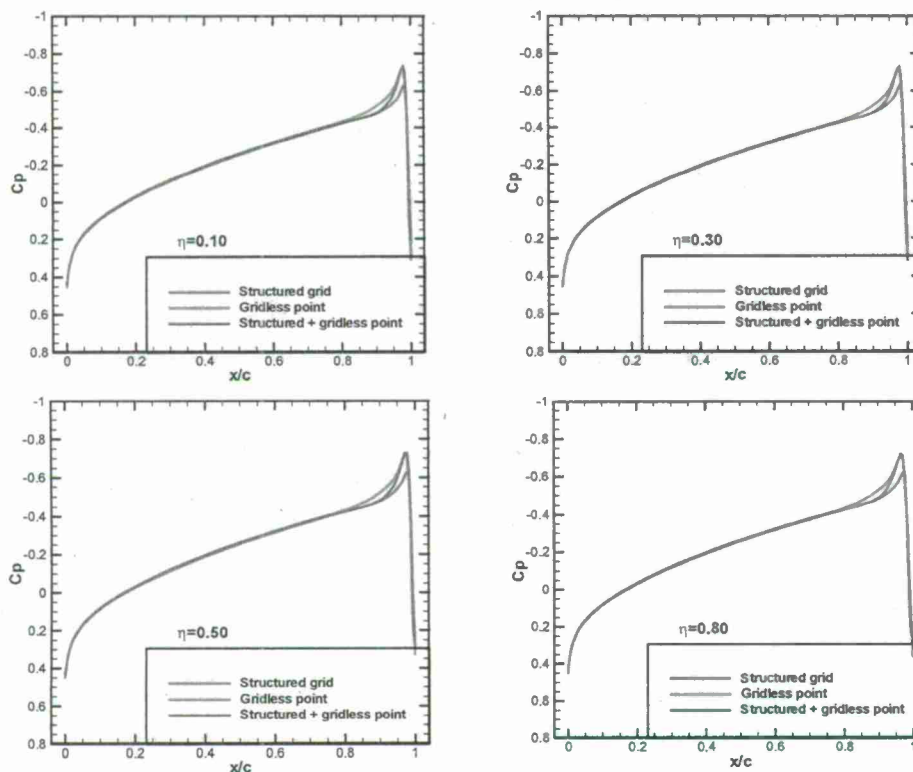


Figure 4.14(c). Pressure Distributions at Four Spanwise Locations of Golland Wing at $M=0.95$, $\alpha=0^\circ$.

4.5 GBCC3D Solver Development: Verification and Validation

The GBCC3D solver development followed after its preliminary grid cutting tool was established. We enhanced the grid cutting tool for folding wings at larger dihedral angles, and generalized it to a wider class of wing planforms. We moved ahead to apply GBCC3D on simple wing configurations for solution validation, since a GBCC3D solver has been developed. Note that the core solver of GBCC3D is a ZONA in-house code called ZONA Euler Structured grid Solver, or ZESS which is a part of ZEUS. ZEUS' explicit scheme is most suitable for it to adopt the GBCC algorithm.

The GBCC solver based on ZEUS contains two separate solvers with different grid systems; one is a structured grid system, and the other gridless system. To validate the GBCC solver, it is required to verify that each grid system works properly (Figure 4.12). Thus, we applied each solver on a given 3D wing planform, and compared the results of one against the other. This was done by adopting an OH-grid system on a Goland wing versus that by a gridless system. To verify the GBCC system works, we adopted an OH-grid + gridless system on the Folding wing and Goland wing and their results were checked against the first two (see Figures 4.12 and 4.13). When the GBCC system was verified, we then applied the Cartesian grid (a subset of structured grid solver) + gridless system (a bona fide GBCC) on a Goland wing and validated its results against that by the ZEUS/body-fitted code (see Figures 4.15-17).

For solution validation, Figures 4.15, 4.16 and 4.17 show the pressure distributions of a Goland wing respectively at three spanwise locations, $\eta = 0, 0.5$ and 0.8 . The Goland wing pressure was computed using GBCC3D for three transonic Mach numbers at $M = 0.8, 0.9$, and 0.95 . It is seen that the GBCC solutions overall compare well with the body-fitted ZEUS solutions. However, the GBCC pressure solutions seem to be slightly wiggled throughout. We believed that the solution wiggles are caused by the local coarse grids imposed. Also computing time of the GBCC is more costly than that of the body-fitted ZEUS. Future work will probably aim at improvements of the GBCC code in these aspects.

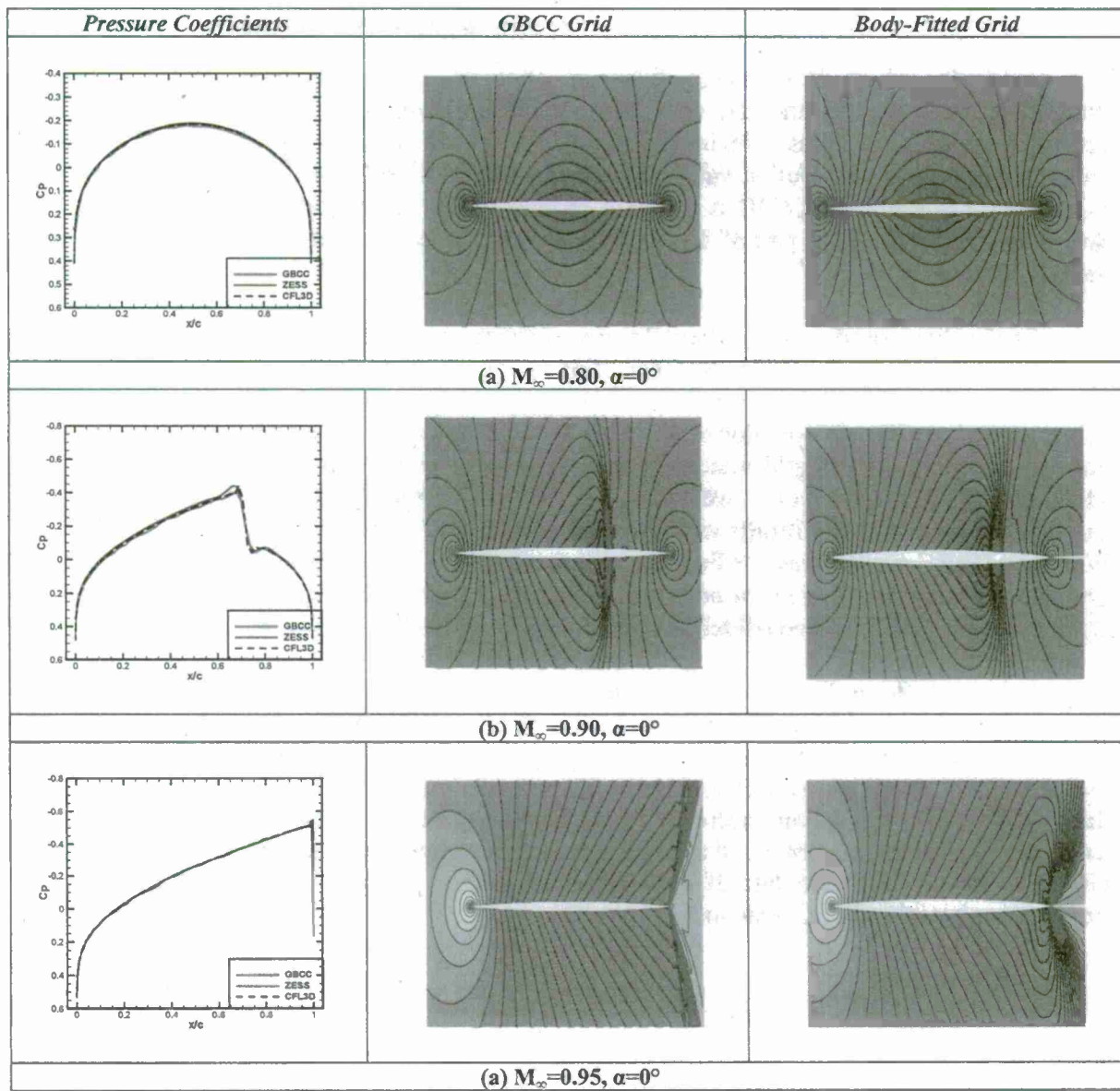
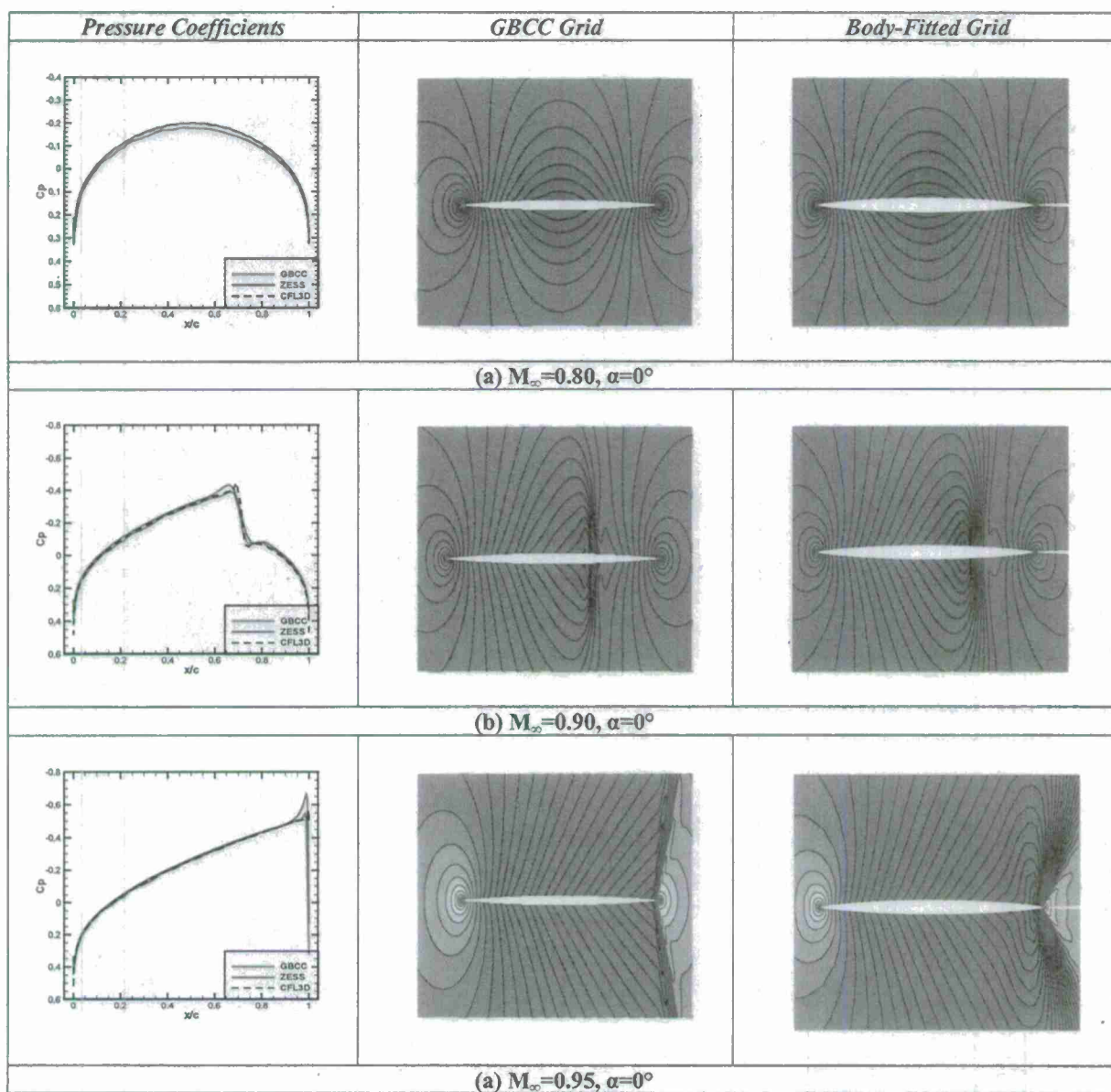
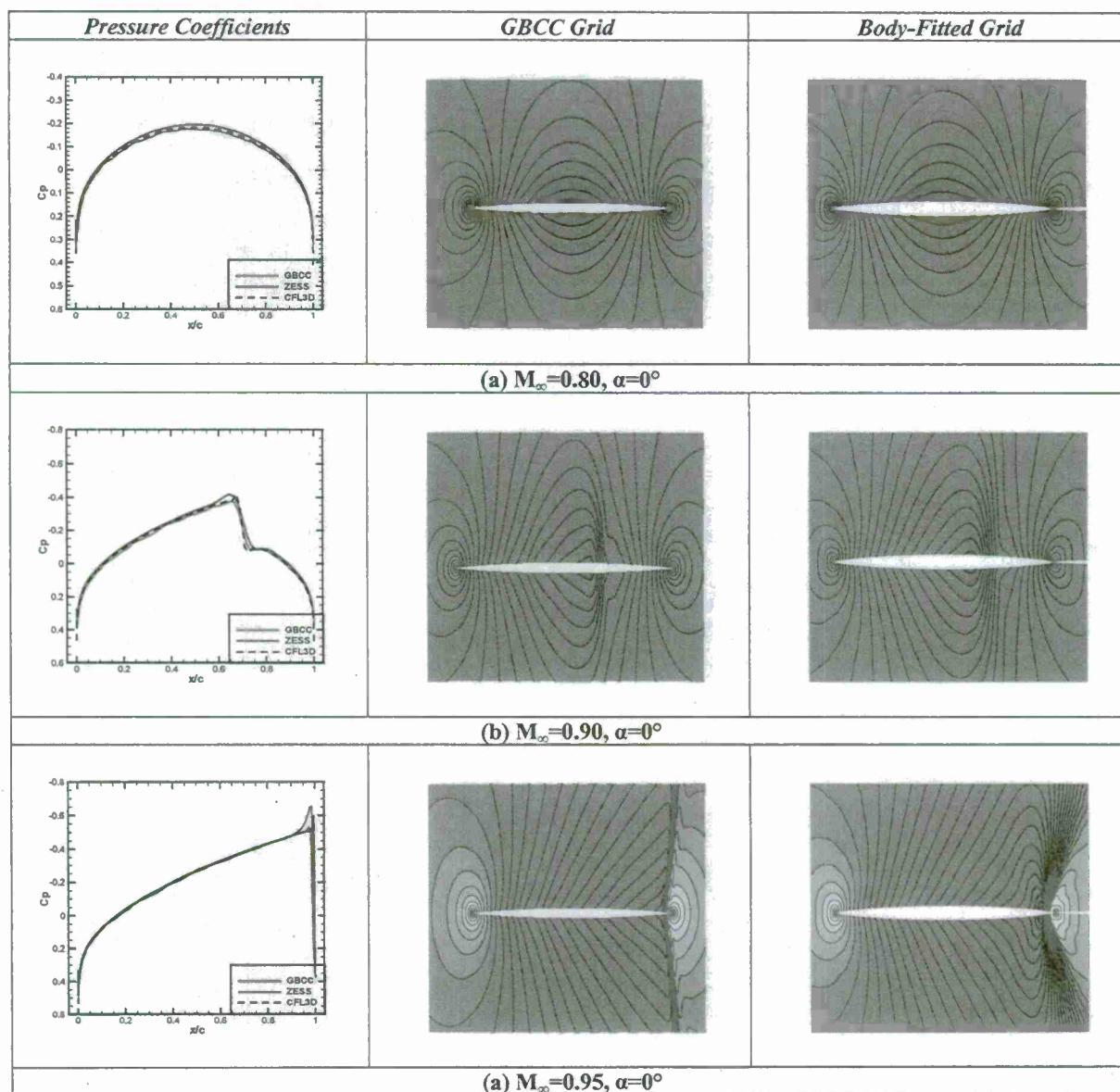


Figure 4.15. Pressure Distribution at Root Chord ($\eta=0.0$) of Golland Wing at $M_\infty=0.80, 0.90$ and 0.95 .

Figure 4.16. Pressure Distribution at Mid Chord ($\eta=0.50$) of Golland Wing at $M_\infty=0.80, 0.90$ and 0.95 .

Figure 4.17. Pressure Distribution at Near Tip Chord ($\eta=0.80$) of the Golland Wing at $M_\infty=0.80, 0.90$ and 0.95 .

4.6 Unsteady Computation

In order to solve the unsteady and aeroelastic problem, the GBCC3D code is further developed for the unsteady problem. The unsteady Euler equation in the Cartesian grid system can be expressed as:

$$\frac{\partial W}{\partial t} + \frac{\partial F}{\partial x} + \frac{\partial G}{\partial y} + \frac{\partial H}{\partial z} = 0$$

where W is the conservative variables; and where F , G , and H are the fluxes. By applying the finite volume method for each computational cell, the above equation becomes an ODE for each cell.

$$\frac{\partial W_{i,j,k}}{\partial t} + \frac{1}{V_{i,j,k}} R_{i,j,k} = 0$$

The subscript (i,j,k) notes the computational cell and $V_{i,j,k}$ is the volume for that cell. For the steady problem we solved in previous sections, the above is solved by the time marching method, e.g., Runge-Kutta multi-step method. In order to accelerate the computational process, the local time step, enthalpy damping and implicit residual smoothing are applied for the time marching process.

For the unsteady problem, the Runge-Kutta time marching is still validate if we use the same time step for the whole computational domain. But this method is time consuming with a very low efficiency. In order to solve the equation efficiently, the dual time method by Jameson is applied for the unsteady problem. In this method, a pseudo-time is implemented.

$$\frac{\partial W_{i,j,k}}{\partial \tau} + \left(\frac{\partial W_{i,j,k}}{\partial \tau} + \frac{1}{V_{i,j,k}} R_{i,j,k} \right) = \frac{\partial W_{i,j,k}}{\partial \tau} + \frac{1}{V_{i,j,k}} R^*_{i,j,k} = 0$$

The above equation is solved by the time marching method with the pseudo-time, τ . All the acceleration techniques mentioned above except for the enthalpy damping is applied to this problem. The real time derivative is discretized by the backward second finite difference method.

$$\frac{\partial W_{i,j,k}}{\partial t} \equiv \frac{W_{i,j,k}^{n+1} - 3W_{i,j,k}^n + 4W_{i,j,k}^{n-1}}{2\Delta t}$$

The superscripts for $W_{i,j,k}$ represent the variables at different time steps. Furthermore, in order to save computational time for the grid regeneration, we use the transpiration boundary condition for the unsteady computation so that the stationary grid is used in the unsteady computation.

The first case we tested was a 2D case, NACA 0012 airfoil, at a transonic condition. The coming Mach number is 0.755, the reduced frequency, $k = (\omega c) / (2U_\infty)$, is 0.0814. The airfoil takes a pitching motion around the quarter point in a sinusoidal way.

$$\alpha = \alpha_0 + \alpha_1 \sin(\omega t)$$

The mean angle of attack $\alpha_0 = 0.016^\circ$, and the amplitude of the pitching angle $\alpha_1 = 2.51^\circ$.

The comparison of the results from GBCC to the body-fitted grid is shown in Figure 4.18. The results from GBCC agree well with those from the body-fitted grid, which shows the accuracy of the current method.

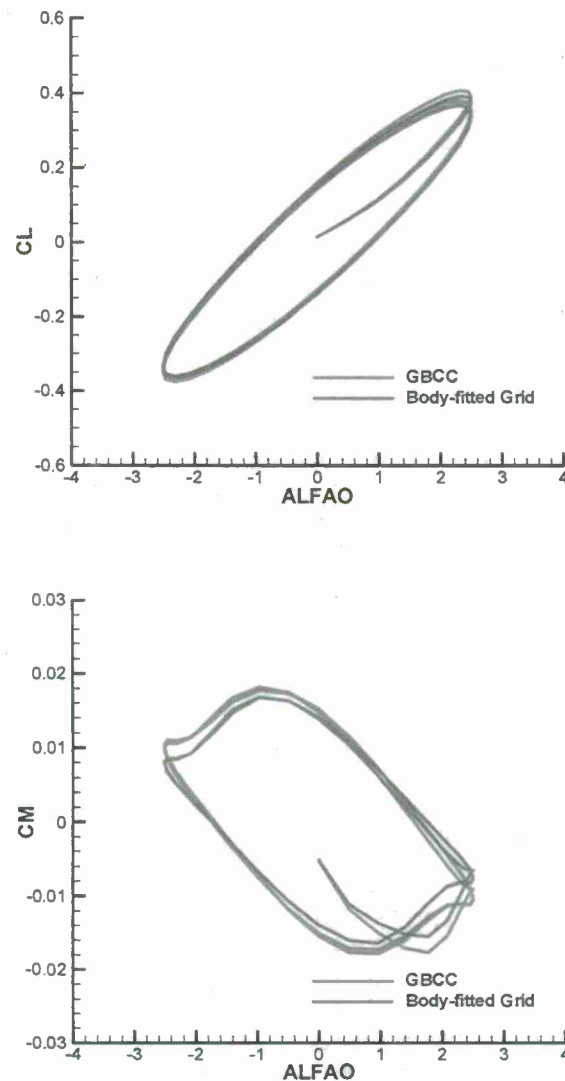


Figure 4.18. Comparison of lift and moment for NACA 0012 airfoil
 $M=0.755$, $\alpha_0 = 0.016^\circ$, $\alpha_1 = 2.51^\circ$, $k = 0.0814$, $x_m = 0.25c$

In the same way, the unsteady case for the Golland wing is computed with GBCC3D. For the Golland wing case, the computational parameters are

$$M=0.700, \alpha_0 = 0.0^\circ, \alpha_1 = 1.00^\circ, k = 0.1, x_m = 0.25$$

With the same techniques used for the 2D case, the transpiration boundary condition is applied. The comparison of the lift between the GBCC grid and body-fitted grid are shown in Figure 4.19. The results with GBCC agree well with those from the body-fitted grid.

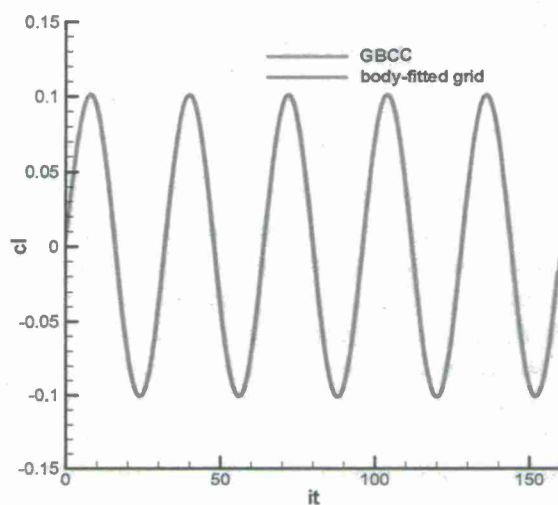


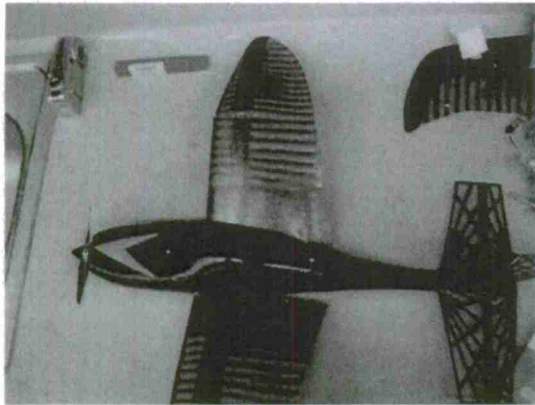
Figure 4.19 Comparison of lift and moment for goland wing
 $M=0.70, \alpha_0 = 0.0^\circ, \alpha_1 = 1.0^\circ, k = 0.10, x_m = 0.25$

Chapter 5.

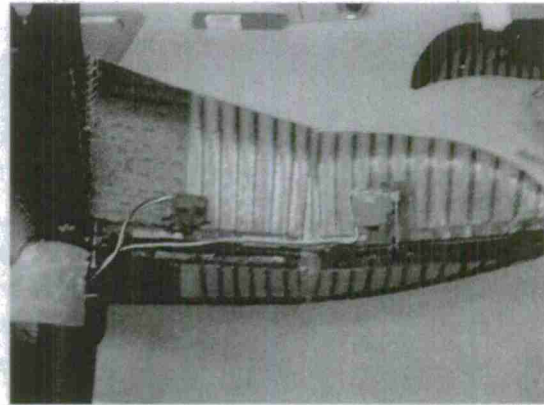
MAV MODAL TESTING, STRUCTURAL FEM AND AEROELASTIC INVESTIGATION

Summary

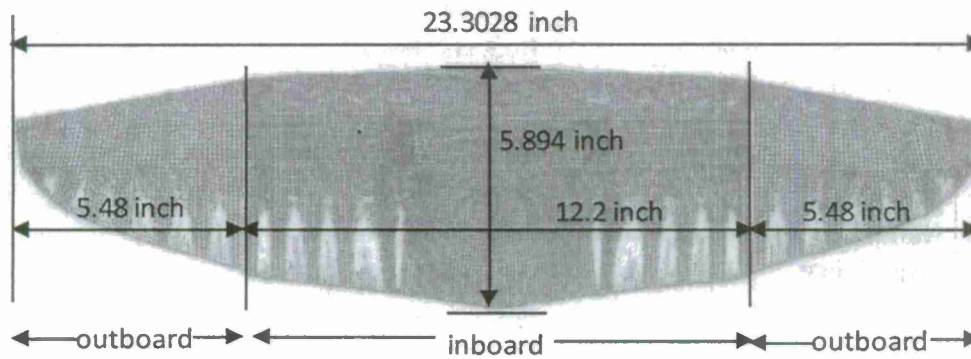
We present MAV Research & Development for the complete procedure of an aeroelastic investigation on a Gull Wing/MAV (Figure 5.1), designed and built by the University of Florida (UFL). Three major tasks were required to be performed consecutively for this morph MAV aeroelastic investigation namely: modal testing (Section 5.1), structural FEM development (Section 5.2) and aeroelastic/flutter investigation (Section 5.3). A roadmap showing these tasks and steps taken is presented in Figure 5.2. Some discrepancies were found in matching the FEM solutions with test results and possible improved measures were suggested. With modal solutions generated by the MAV FEM, ZAERO was used for Gull Wing MAV aeroelastic analysis with three wing morph (dihedral) angles namely $\Gamma = 0^\circ$, 30° , and 60° . Divergence was found for all 3 MAV configurations. With the lowest divergent speed ($\sim 83\text{fps}$ at $h = 0$) for case of $\Gamma = 30^\circ$ and highest for $\Gamma = 0^\circ$ from sea level up to $h = 12\text{Kft}$. This divergent trend with increasing dihedral Γ for an MAV has an opposite trend to that of flutter for the folding wing. We have improved the FEM model by adopting an optimization scheme to obtain more accurate material parameter values. With the improved FEM solutions the modal frequencies are largely varied from the previous ones, we re-performed the divergence/flutter analysis for the MAV.



(a) Overall View



(b) Zoomed in View of the Wing



(c) Geometry Schematics (wing only, no fuselage)
Figure 5.1. University of Florida MAV.

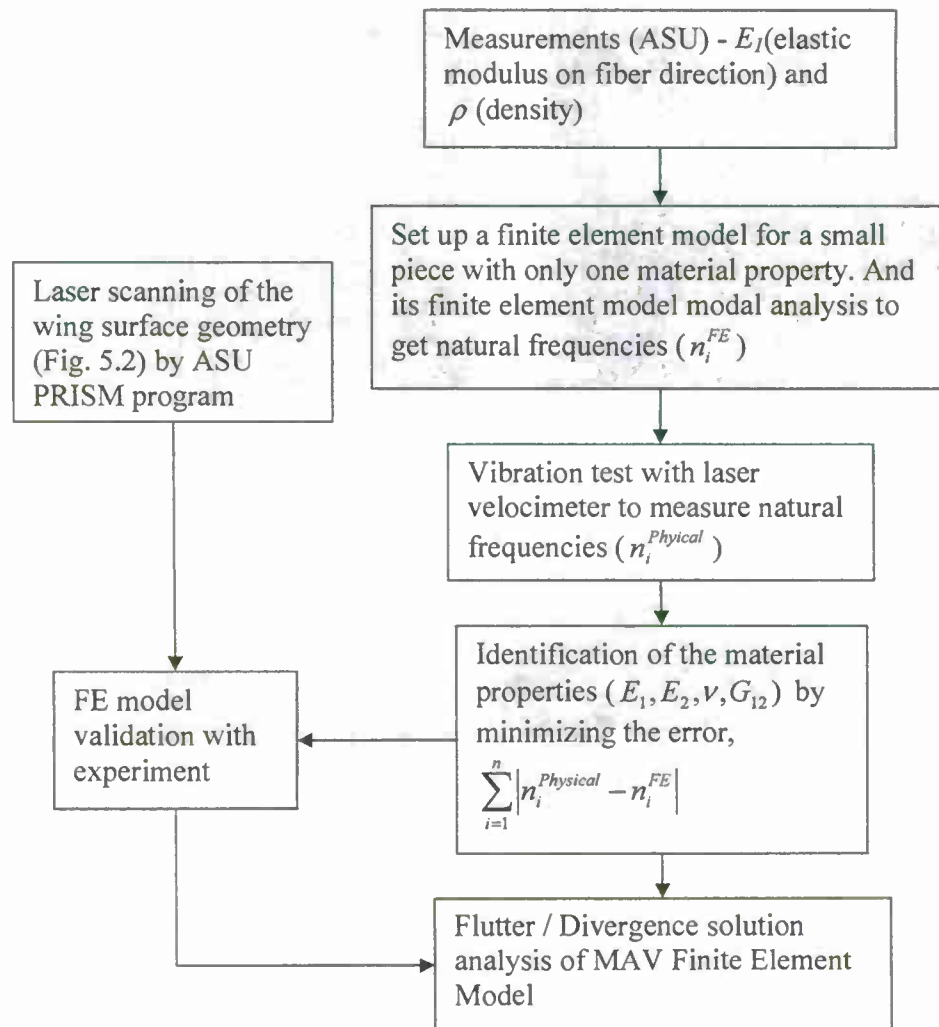


Figure 5.2. Micro Morphing Air Vehicle (MAV) Test, FEM and Aeroelastic Investigation Roadmap.

5.1 Digitization and Modal and Material Testing

Accurately recording the complex geometry of the UFL MAV was the first task accomplished in this effort. This characterization was achieved through a fine laser digitization of the set of two wings carried out by the digitization machine of ASU's Partnership for Research in Spatial Modeling (PRISM) program. This process led to a series of coordinates defining the shape, see Figure 5.3, and from which the finite element mesh could be designed.

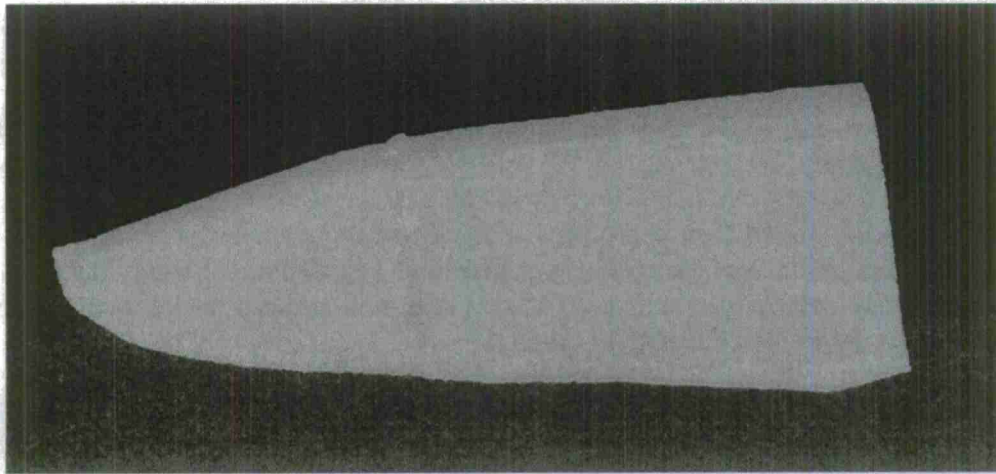


Figure 5.3. Laser Scanned Left Wing Surface.

To build a reliable finite element model of the UFL MAV, it was also necessary to obtain good estimates of the structural properties of the various materials used in its fabrication. In fact, three separate materials were identified: woven carbon fiber, unidirectional strips of carbon fibers, and fabric (kite material in orange in Figure 5.1) and pieces of those materials were cut out from the extra set of wings donated by the University of Florida.

The determination of the properties of the weave carbon fiber proved to be a particularly challenging task as this material is not isotropic but further exhibits a significant nonlinear behavior. Indeed, multiple regimes can be identified in the response vs. loading curves. At low level of excitation, the first regime exists in which the epoxy binding the fibers carries load (shear in particular). However, above a certain loading condition, the fibers slide as their tensions exceeds the load carrying capability of the epoxy. A third regime then appears in which the taut fibers lock in and start behaving as a single material. Note that (significantly) different material properties are needed in different regimes. It seemed that the vibration testing, as the operation of the MAV, would result in low stresses and strains so that the woven material would behave in the first regime. However, the stress-strain testing in ASU's Mechanical Testing Facility (IMTL) was most likely conducted in regime 2 or regimes 2 and 3. Thus, it was not clear the values obtained in these tests were appropriate for the prediction of the MAV aeroelastic behavior.

In this light, it was decided to obtain relevant values of the woven material properties in an indirect manner, i.e. to extract them from measured natural frequencies. To this end, two samples of the woven material, both nearly flat, were cut out from the extra set of wings and their modal testing was conducted. This coupon type experiment is advantageous in particular because of its simple geometry which minimizes any shape uncertainty issue. However, the small size renders the measurements sensitive to sensor attachment (e.g. mass loading) which could significantly affect the test result.

Fortunately, the ASU vibration lab utilizes two laser vibrometers, which allow very accurate measurements without any sensor attachments on small and light structures. Furthermore, by measuring and relying only the natural frequencies, any uncertainty in the loading condition during the test can be avoided. The identification of the woven material parameters was then

carried out from the measured natural frequency through an optimization process as described in Figure 5.2.

To obtain as much information about the woven material as possible, the two samples were cut differently. Specifically, as seen in Figure 5.4, the fibers of one sample were aligned with the sides of the plate while they were at 45° of these sides on the second sample. These two samples were cantilevered on one of their short sides and subjected to a small disturbance. The ensuing motion at different points was recorded using two laser velocimeters. Shown in Figure 5.5 are two scaled velocity spectra obtained in these tests and from which a set of natural frequencies were obtained for each of the rectangular samples.

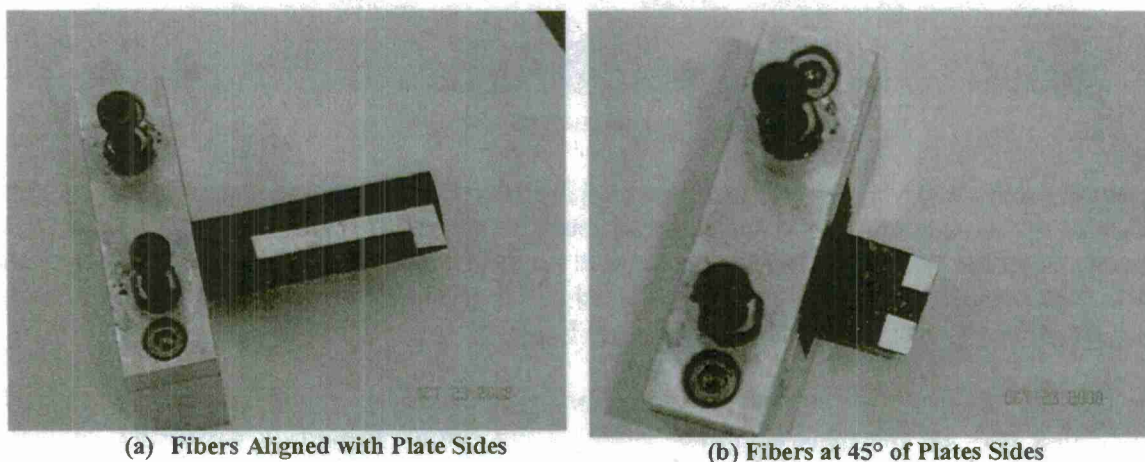


Figure 5.4. Samples of Woven Material. The White/Silver Patches are Pieces of Scattering Tape to Enhance the Strength of the Signal Received at the Collector.

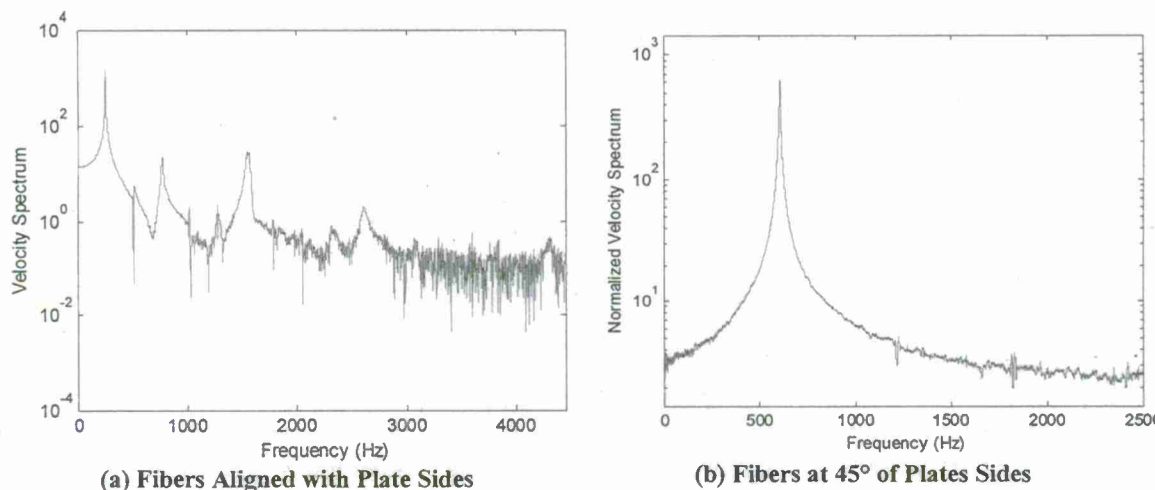


Figure 5.5. Velocity Spectra (mobilities) at the Tip of the Rectangular Samples Obtained in Free Response Test.

A similar procedure was also carried out for a thin strip of unidirectional fibers and the corresponding velocity spectrum is shown in Figure 5.6.

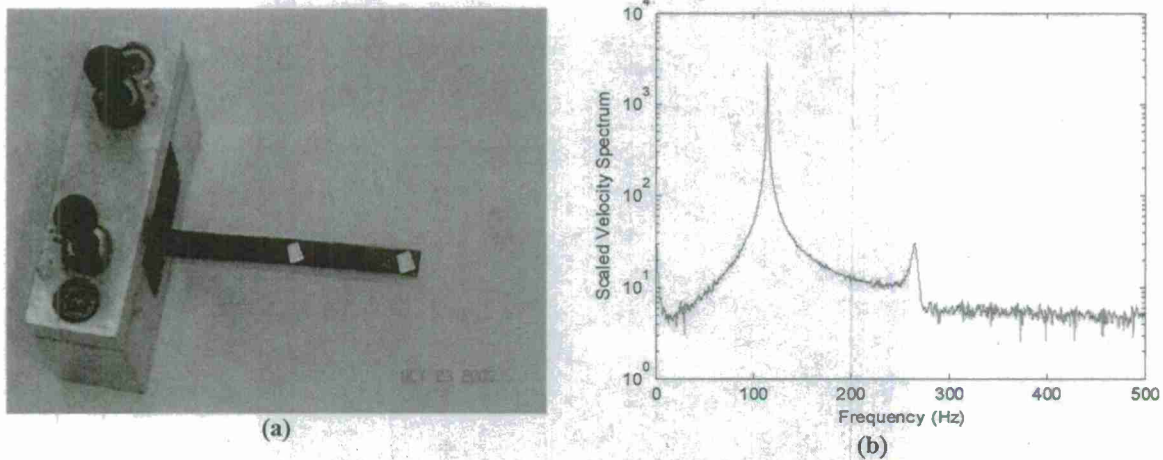


Figure 5.6. (a) Sample of Unidirectional Fibers Tested. (b) Velocity Spectrum at the Middle of the Sample.

The second part of the modal testing effort focused on the determination of the natural frequencies of one of the extra wings. This data was then used in the validation of the finite element model developed on the basis of the structural properties recovered from the earlier measurements. To perform the vibration testing, a clamp was designed and fabricated by the ASU machine shop to hold the two-wing piece at its middle, see Figure 5.7. The test piece mounted on the clamp was then installed on the shaker and tested both in free and forced response conditions with measurements obtained by a fixed laser velocimeter, see Figure 5.8.

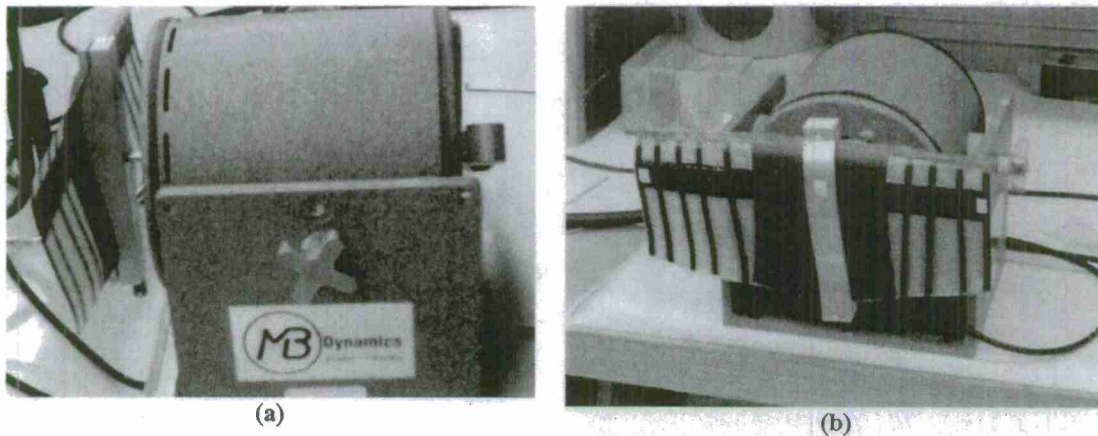


Figure 5.7. Two-Wing Test Piece Clamped and Mounted on Shaker.

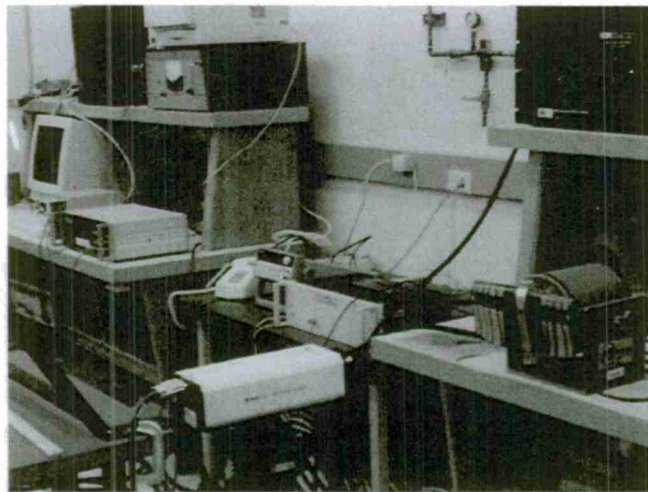
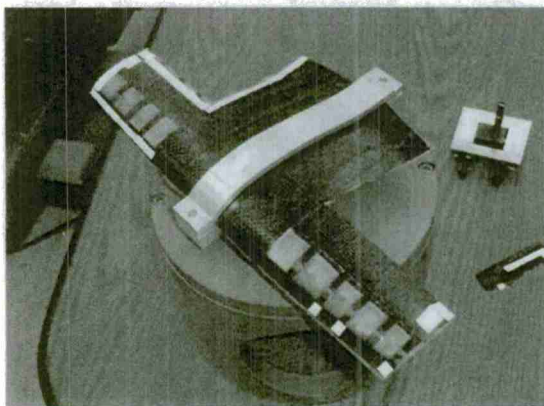
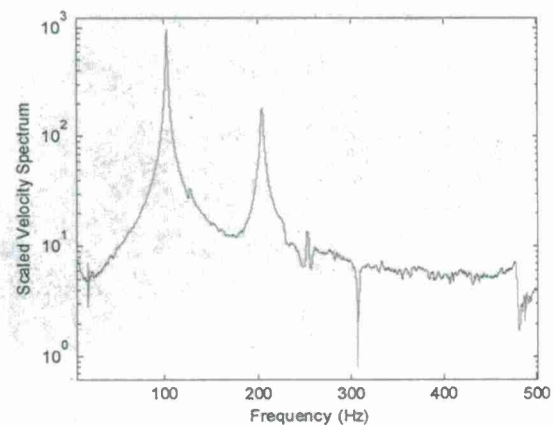


Figure 5.8. Vibration Test Setup of Two-Wing Set in ASU Vibrations Lab.

Free response tests were again conducted in which an initial deflection of the wing was performed and the motion (velocity) of one point of interest was captured using the laser velocimeter. In performing the first sets of measurements, it was recognized that the battens exhibited much lower natural frequencies than the rest of the wings and would cloud the velocity spectrum of the response and thus prevent an identification of the global wing modes involving the woven material spar and the reinforced leading edge. It was decided to cut out the section involving the kite material and batten leaving only the spar-leading edge section, see Figure 5.9(a).



(a)



(b)

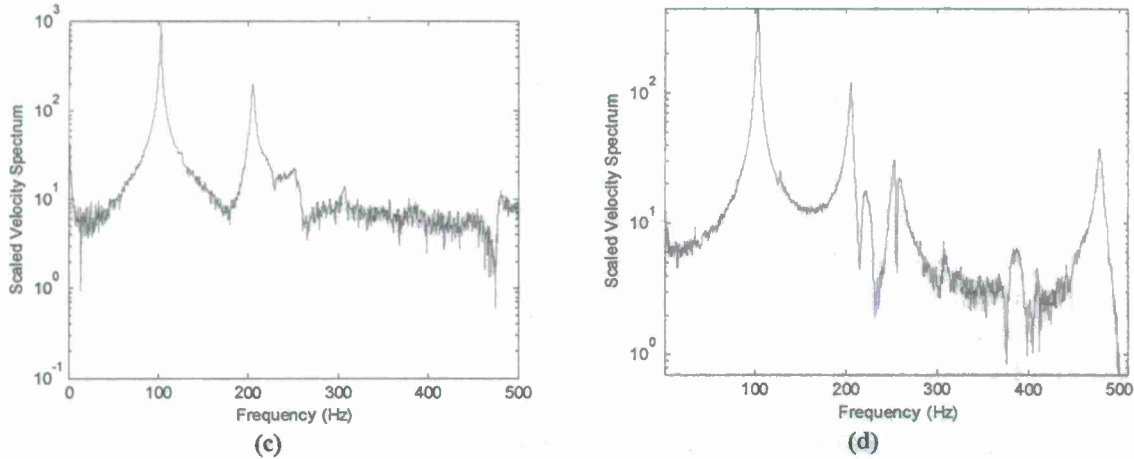


Figure 5.9 (a) Wing Model without Battens. (b)-(d) Velocity Spectra (mobility) at Three Points Along the Leading Edge. (b) Tip, (c) Point A of (a), (d) Point B of (a)

5.2 MAV Finite Element Modeling

For the finite element modeling, the geometry information and the material properties were needed. The geometry information was provided by the laser scanning which recorded the relative coordinates on the surface of the wing structure. Those coordinates are used for the finite element meshing.

The ASU IMTL conducted tensile tests on the unidirectional carbon fiber, weave carbon fiber, and fabric. Thus, the elasticity modulus on fiber direction, E_1 , for each material was given. This carbon fiber composite material was orthotropic and has the following relationship between the stress and strain.

$$\begin{Bmatrix} \varepsilon_1 \\ \varepsilon_2 \\ \gamma_{12} \\ \gamma_{1z} \\ \gamma_{2z} \end{Bmatrix} = \begin{bmatrix} \frac{1}{E_1} & -\frac{\nu_{21}}{E_2} & 0 & 0 & 0 \\ -\frac{\nu_{21}}{E_1} & \frac{1}{E_2} & 0 & 0 & 0 \\ 0 & 0 & \frac{1}{G_{12}} & 0 & 0 \\ 0 & 0 & 0 & \frac{1}{G_{1z}} & 0 \\ 0 & 0 & 0 & 0 & \frac{1}{G_{2z}} \end{bmatrix} \begin{Bmatrix} \sigma_1 \\ \sigma_2 \\ \tau_{12} \\ \tau_{1z} \\ \tau_{2z} \end{Bmatrix} \quad (5.1)$$

where, Lower index 1: fiber direction

Lower index 2: normal to the fiber direction and in-plane

Lower index z: normal to the surface

E_1 : Elasticity modulus

E_2 : Elasticity modulus

ν_{12} : Poisson's ratio

G_{12} : In-plane shear modulus

G_{1z} : Transverse shear modulus for shear in 1-Z-plane

G_{2z} : Transverse shear modulus for shear in 2-Z-plane

In this MAV FEM modeling, while considering the load and elastic deformation, the shear deformations on 2 and Z-plane and 1 and Z-plane are neglected so that the G_{1z} and G_{2z} are assumed as infinity. Therefore, only E_1, E_2, G_{12} and ν_{12} are used in the FEM modeling. The layer composition and fiber direction should also be defined. The same fiber direction as the physical model was maintained in the FEM model. For the fabric part, isotropic material properties were applied which means only E and ν are needed.

Since the only property given was E_1 , its other property values, E_1, E_2, G_{12} and ν_{12} , are derived by the analogy with other typical composite material property. In other words, the ratios among those values are kept the same for the well known composite material. This assumption might be a critical reason for the model discrepancy. However, the modal test focused on the low order natural frequencies which are mainly bending modes. Those transverse bending modes are dominated by the E_1 so that other values do not affect vibration test results as much as the E_1 does on it.

Finally the finite element model was established and compared with the modal test result. As shown in the previous chapters on experiments, the simplified wing structure is made out of the extra wing and was subjected to the vibration test. The natural frequencies were compared with the FEM modal analysis however there were some discrepancies.

To update the finite element model, a new approach was suggested. That is to decompose the structure and analyze them piece by piece. The wing structure was separated into two main components. One is unidirectional carbon fiber and the other is weave carbon fiber. Those are separately tested to measure the natural frequencies which are then used for the identification of material property.

5.2.1 Identification of Material Properties for Finite Element Modeling

• Unidirectional Carbon Fiber

Figure 5.10 is the finite element model of the small piece of the unidirectional carbon fiber which was subjected to the vibration test. As explained before, this test piece was excited and its free response was analyzed with FFT (Fast Fourier Transform). The Nyquist frequency was 500Hz. The dominant first peak is at 114.4 Hz (see Figure 5.6(b)) which didn't match the FEM model's modal analysis result, 127 Hz. In that FEM model, the material parameter values are directly given by the ASU IMTL.

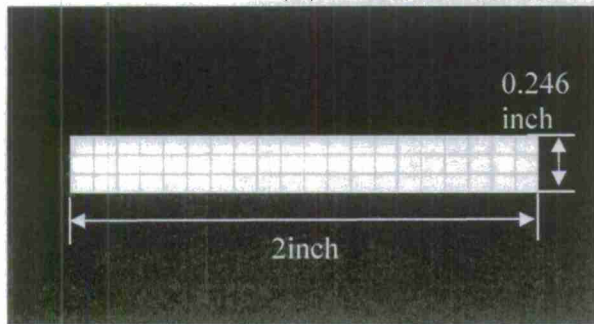
Thus, to update and identify the property, we use an error function as Eq. (5.2).

$$error = \sum_{i=1}^n |n_i^{Physical} - n_i^{FE}| \quad (5.2)$$

where, $n_i^{Physical}$: natural frequency from modal test
 n_i^{FE} : natural frequency from finite element model

This error function is minimized by adjusting the elasticity modulus E_I in the FEM model. E_I is adjusted until the first natural frequency from the modal test match the FEM model's.

Other properties are guessed at (Table 5.2) by the assumption that the typical carbon fiber material has unchanging ratios between those property values such as $E_2, G_{12}, G_{1z}, G_{2z}, \nu_{12}$.



Finite element model description

- Number of grid points: 516
- Number of quad4 elements: 62
- Boundary condition:
cantilever(clamped – free)
- Material property: table 5.2
- Composite material coordinate: the basic coordinate

Figure 5.10. Finite Element Model for the Small Piece of Carbon Fiber (uni-directional only).

Finite element model modal analysis results were compared with the analytical solution. The natural frequency of the beam with a fixed-free boundary condition can be derived analytically by Eq. (5.3) (W. D. Pilkey, 1994).

$$\omega_i(\text{rad / s}) = \frac{\lambda_i^2}{L^2} \left(\frac{EI}{\rho} \right)^{1/2} \quad (5.3)$$

where, E = Elasticity modulus
 I = moment of inertia
 ρ = mass per unit length
 L = length of the beam
 $\lambda_1 = 1.875, \lambda_2 = 4.694, \lambda_3 = 7.854$

When the first frequency is 114.4Hz, the second and third frequencies can be derived by Eq. (5.3) and those are 719.6Hz and 2016Hz. Those values are quite close to the 3rd and 4th natural frequency of the FEM model which means that most of low frequencies are dominated by only one material parameter, E_I . Thus using only one natural frequency is enough to identify the parameter.

Considering the Nyquist frequency which is 500Hz, the second mode in the modal test might be caused by the aliasing of the actual second or third modes.

Table 5.1. Natural Frequency Comparison of the FEM Model and Modal Test.

Natural frequency order	Natural frequency by Modal test experiment	Natural frequency by Finite element model
1	114.4 Hz	115.36 Hz
2	264.8 Hz	701.52 Hz
3		721.01 Hz
4		2014.89 Hz

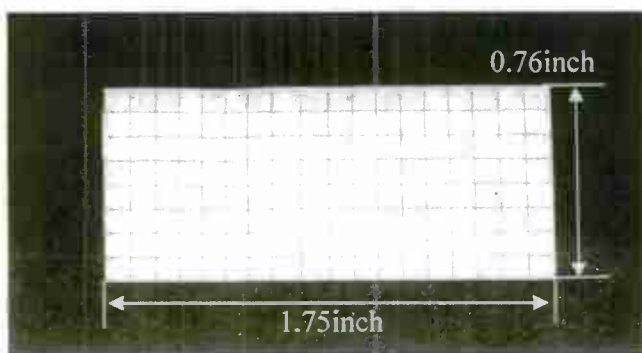
Table 5.2. Identified Material Property for Uni-Directional Carbon Fiber–Shell Element Orthotropic Material Property.

Material properties	Uni-directional carbon fiber
Young's Modulus, E_1 (PSI)	2.0E+7
E_2 (PSI)	2.0E+6
Density, ρ (Slinch/inch ³)	2.234E-4
Poisson's ratio, ν	0.28
In-plane shear modulus, G_{12} (PSI)	1.2E+6
Thickness(inch)	0.01

- Woven Carbon Fiber

Woven carbon fiber's free response is analyzed with FFT also (see Figure 5.5). The dominant first peak is at 255Hz which didn't match the FEM model's modal analysis result, 361Hz. Where, the material property is given by ASU without any updating.

Thus, to get a better model, the woven carbon fiber is modeled as two layers of uni-directional carbon fibers which are crossing at 90 degree. Each fiber has half of the original thickness. Figure 5.11 shows the finite element model of the weave carbon fiber. To minimize the error between the natural frequencies, only E_1 is adjusted. In the same way as the uni-directional carbon fiber test, other properties are also obtained (Table 5.4).



Finite element model description

- Number of grid points : 171
- Number of cquad4 elements : 144
- Boundary condition : cantilever(clamped – free)
- Material property: Table 5.4
- Composite material coordinate : the basic coordinate

Figure 5.11. Finite Element Mesh for the Woven Carbon Fiber Only.

Table 5.3. Natural Frequency Comparison of the FEM Model and Modal Test for Woven Carbon Fiber.

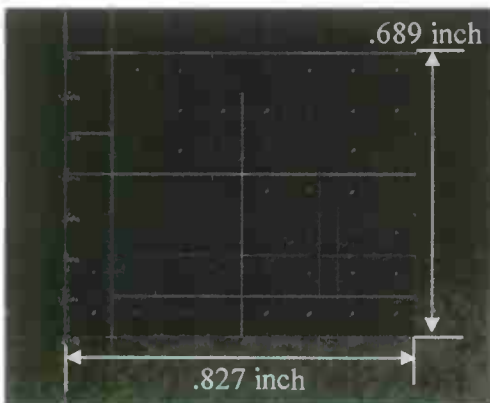
Natural frequency order	Natural frequency by Modal test experiment	Natural frequency by Finite element model
1	255 Hz	255.61 Hz
2	772 Hz	552.43 Hz
3	1544 Hz	1535.3 Hz
4	2600 Hz	2060.49 Hz

With Eq.(5.3) the natural frequencies from 2nd to 4th are derived. Those are 1604, 4494, and 8807Hz. None of them match well. It means that this test piece cannot be modeled as a beam. Moreover the E_2 is also a significant factor as E_1 .

Figure 5.12 shows the finite element model for the woven fiber whose fiber angle is 45°. The first natural frequency from the FEM model is 721Hz while the measured first natural frequency from the modal testing was 607.5Hz (see Figure 5.6(b)).

Table 5.4. Identified Material Property for Woven Type Carbon Fiber–Shell Element Orthotropic Material Property (modeled as two layers whose thickness is half of original).

Material properties	Woven type Carbon fiber
Young's Modulus, E_1 (PSI)	8.1E+6
E_2 (PSI)	8.1E+5
Density, ρ (Slinch/inch ³)	1.36E-4
Poisson's ratio, ν	0.28
In-plane shear modulus, G_{12} (PSI)	2.5E+5
Thickness(inch)	0.026



Finite element model description

- Number of grid points : 72
- Number of cquad4 elements : 56
- Boundary condition : cantilever(clamped – free)
- Material property : table 5.4
- Composite material coordinate : at a angle of 45 degree from the basic coordinate

Figure 5.12. Finite Element Mesh for the Woven Carbon Fiber with 45° Material Angle.

5.2.2 Finite Element Model

In this modeling, those fiber directions are maintained as the physical model. In Figures 5.13 and 5.14 those various colors denote the material properties and fiber direction change.

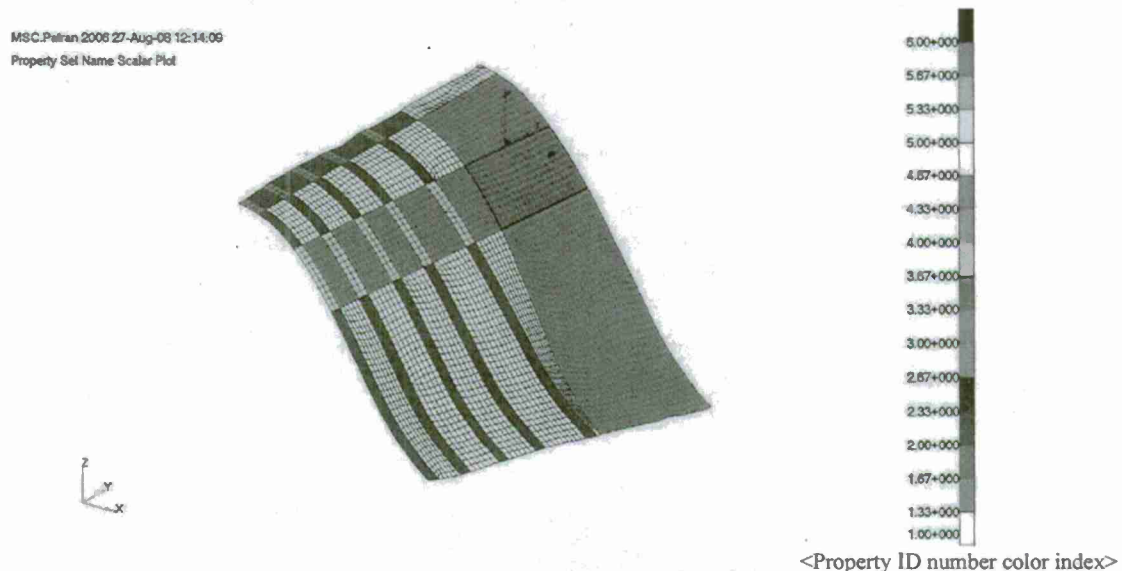


Figure 5.13. In-board Wing Finite Element Model and Distinction of Material Properties.

Figure 5.13 is the FEM model of the inboard wing. It is composed of the woven carbon fiber, uni-directional carbon fiber, and fabric (kite material).

For the material properties, we use those values which are identified by the vibration test (section 5.2). Figure 5.14 is the FEM model for the outboard wing. All 3 kinds of material, woven, uni-directional and fabric, are utilized also and the fiber direction is maintained as the physical model. These inboard and outboard wing are connected by the rigid bar elements at a grid point in-between them. And then the whole inboard and outboard wing is copied by reflection to the other side.

To see the morphing effect, the outboard wing is rotated about the inboard tip chord. As shown in Figures 5.14~5.16 with 0°, 30°, and 60° rotation of the outboard wing are modeled.

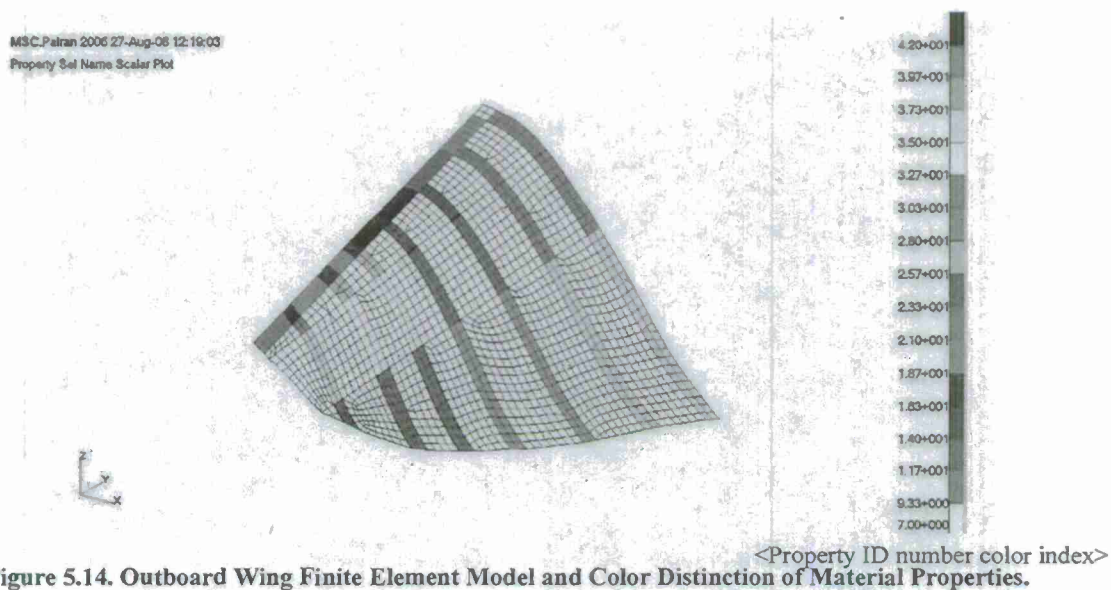


Figure 5.14. Outboard Wing Finite Element Model and Color Distinction of Material Properties.

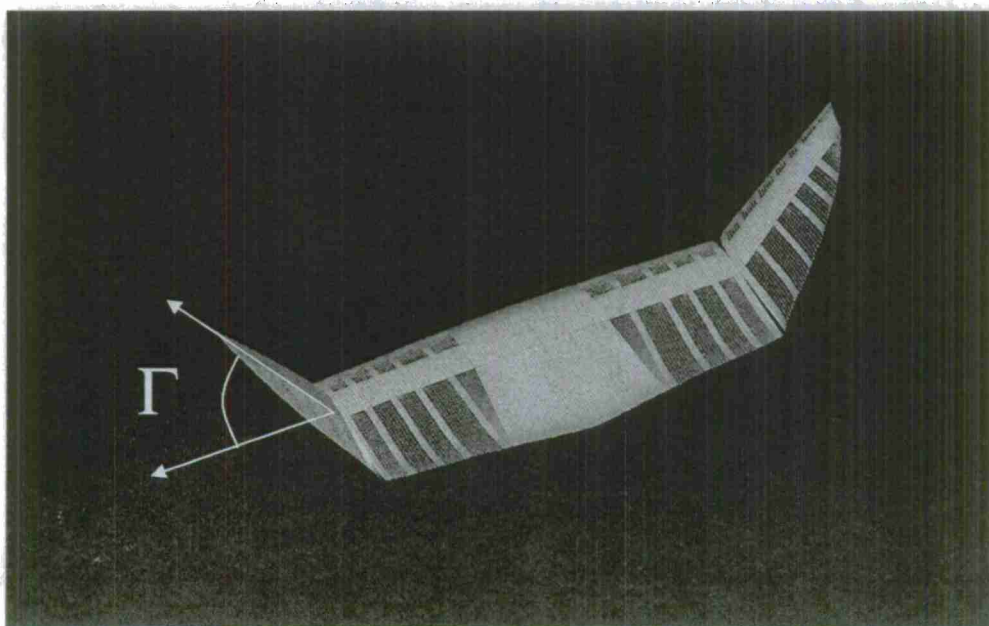


Figure 5.15. Micro Morphing Air Vehicle Finite Element Model ($\Gamma = 60^\circ$).

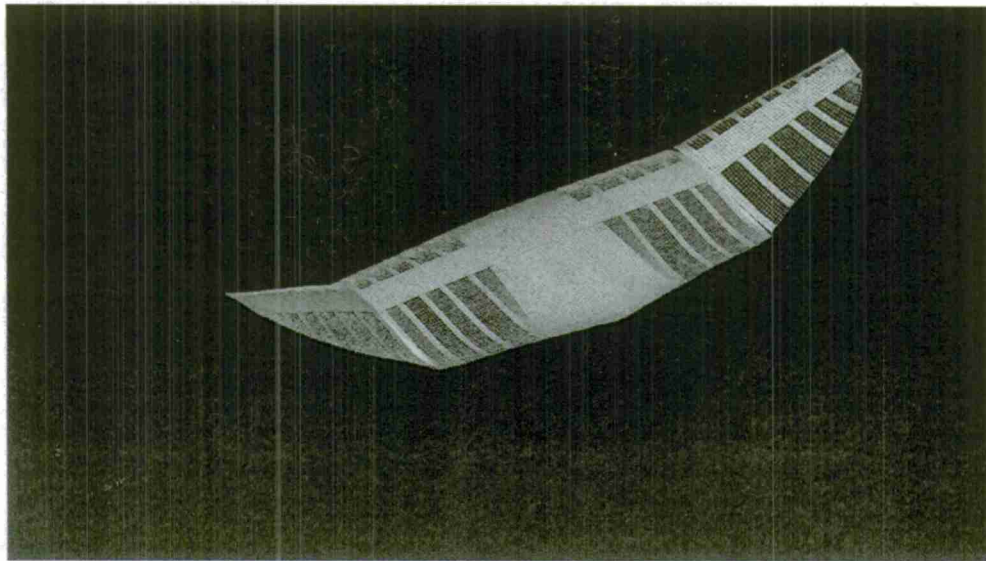


Figure 5.16. Micro Morphing Air Vehicle Finite Element Model ($\Gamma=30^\circ$).

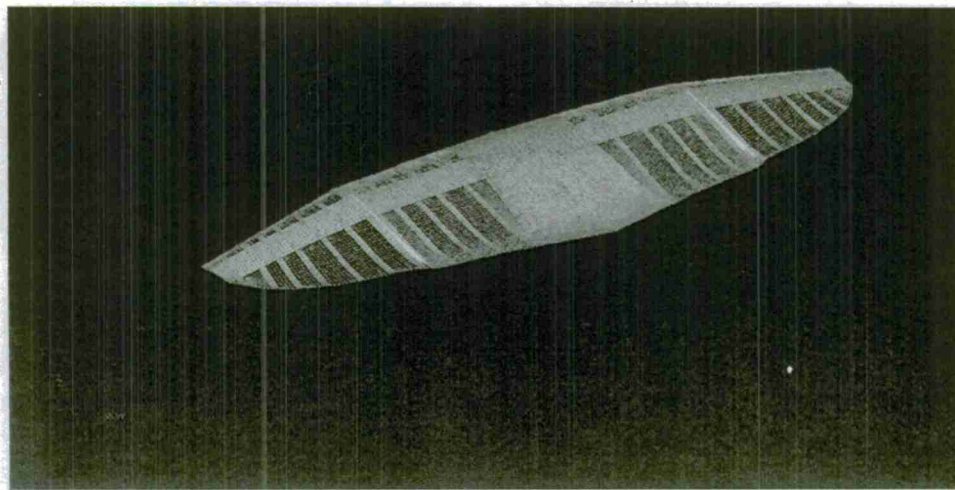


Figure 5.17. Micro Morphing Air Vehicle Finite Element Model ($\Gamma = 0^\circ$).

The above finite element model utilizes the following grid and finite elements (Table 5.5).

Table 5.5. Finite Element Model Summary (MSC.NASTRAN).

Number of grid points	10862
Number of degree of freedom	65172
Number of cquad4 elements	10570
Number of ctria3 elements	58
Number of rbe2 elements	50

The fabric part (kite material) is modeled as a membrane since it doesn't have bending rigidity. There is no pre-existing in-plane load therefore it has a lot of local modes at pretty low frequencies, which makes it difficult on the aerodynamic flutter analysis. To solve this problem, the rigid bar elements are used to prohibit it from numerous local modes.

The fabric part is composed of a single thin layer and the mass is much smaller than the composite carbon fiber layers so that its dynamic mode involvement is in a high frequency regime. Furthermore, its elastic deformation is not appreciably considered so that the FEM model directly used the measured values by the ASU IMTL. Therefore the material property for the fabric part was not participating in the identification process of the vibration test.

Table 5.6. Identified Material Property – Isotropic Material Property.

Material properties	Fabric(Kite Material)
Young's Modulus, E (PSI)	8.0E+4
Density, ρ (Slinch/inch ³)	1.013E-4
Poisson's ratio, ν	0.3
Thickness(inch)	0.002

5.2.3 Model Validation

ASU's vibration lab made the test model (see Figure 5.9(a)) out of the MAV after simplifying it by removing fabric parts. The test method and difficulties are well explained in Section 5.2. Figure 5.18 shows the finite element model of the test model. Table 5.7 shows a brief description of the finite element model. For this finite element model, the identified material properties in section 5.2.1 are used.

Figure 5.17 shows the finite element model. As shown in the Table 5.8, FFT test results show that the first natural frequency is at 102.6 Hz, and the FEM model has it at 99Hz. This 3.5% error is not bad but still has discrepancies in other frequencies as shown in the Table 5.8.

There are 3 possible causes of this discrepancy. The first one is geometry uncertainty. There is a shape difference between the FEM model and physical model which is caused by measurement error. The thickness is not constant and changing due to the irregularity in the manufacturing process.

The second cause is the boundary condition. It is very difficult to fix the axial displacement of the carbon fibers which are bonded by the epoxy which is also mentioned in the experiment. Therefore, in the physical model the corresponding degrees of freedom is released, which means it has finite stiffness. But, those displacements are fixed in the finite element model which has infinite corresponding stiffness.

The third cause is that those identified material property is not applicable all over the structure. In the process of stacking the fibers, those fibers are pressed with heat so that the material property may be altered unevenly.

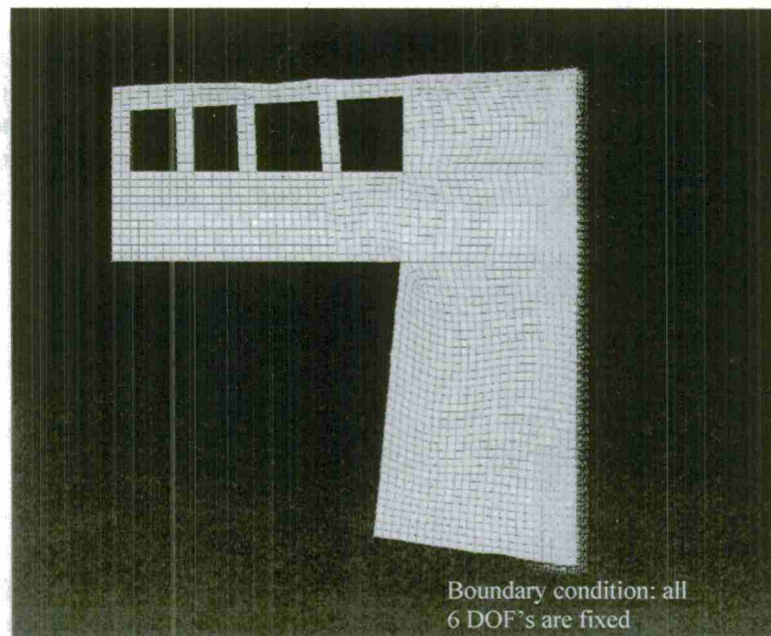


Figure 5.18. The Half of Inboard Wing Structure Without Fabric Part.
See Figure 5.9 for the Physical Model.

Table 5.7. Finite Element Model Summary (MSC.NASTRAN).

Number of grid points	2115
Number of cquad4 elements	1941
Number of ctria3 elements	3

Table 5.8. Natural Frequency Comparison of the FEM Model and Modal Test for Half Wing Structure.

Natural frequency order	Natural frequency by Modal test experiment	Natural frequency by Finite element model
1	102.6 Hz	99.00Hz
2	205 Hz	200.25 Hz
3	252.3 Hz	311.82 Hz
4	478 Hz	421.98 Hz
5		472.36 Hz

5.3 MAV Aeroelastic Investigation

Using the FEM results discussed above, divergence and flutter predictions were calculated using ZAERO. The aerodynamic model of the MAV is shown in Figure 5.19. The outboard wing section dihedral angle is denoted by Γ . Three different cases were studied: $\Gamma=0^\circ$, 30° , and 60° .

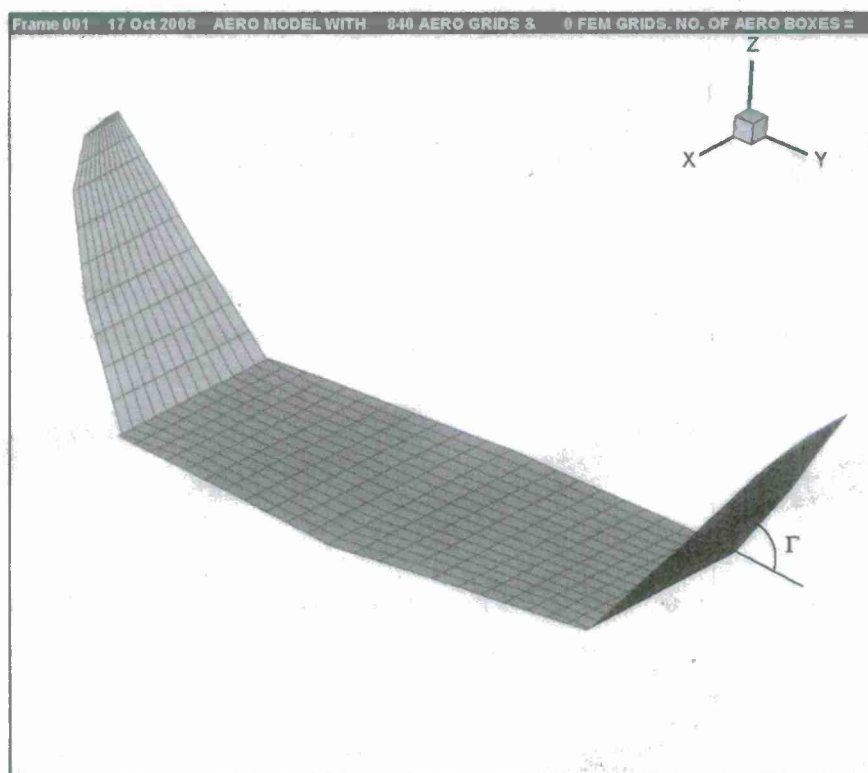
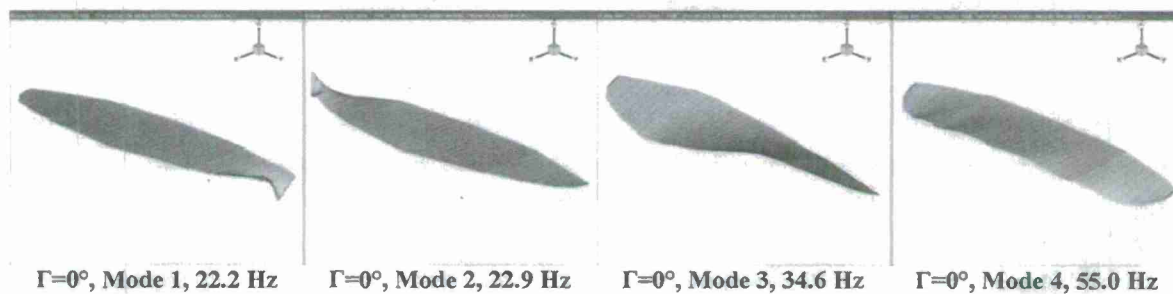


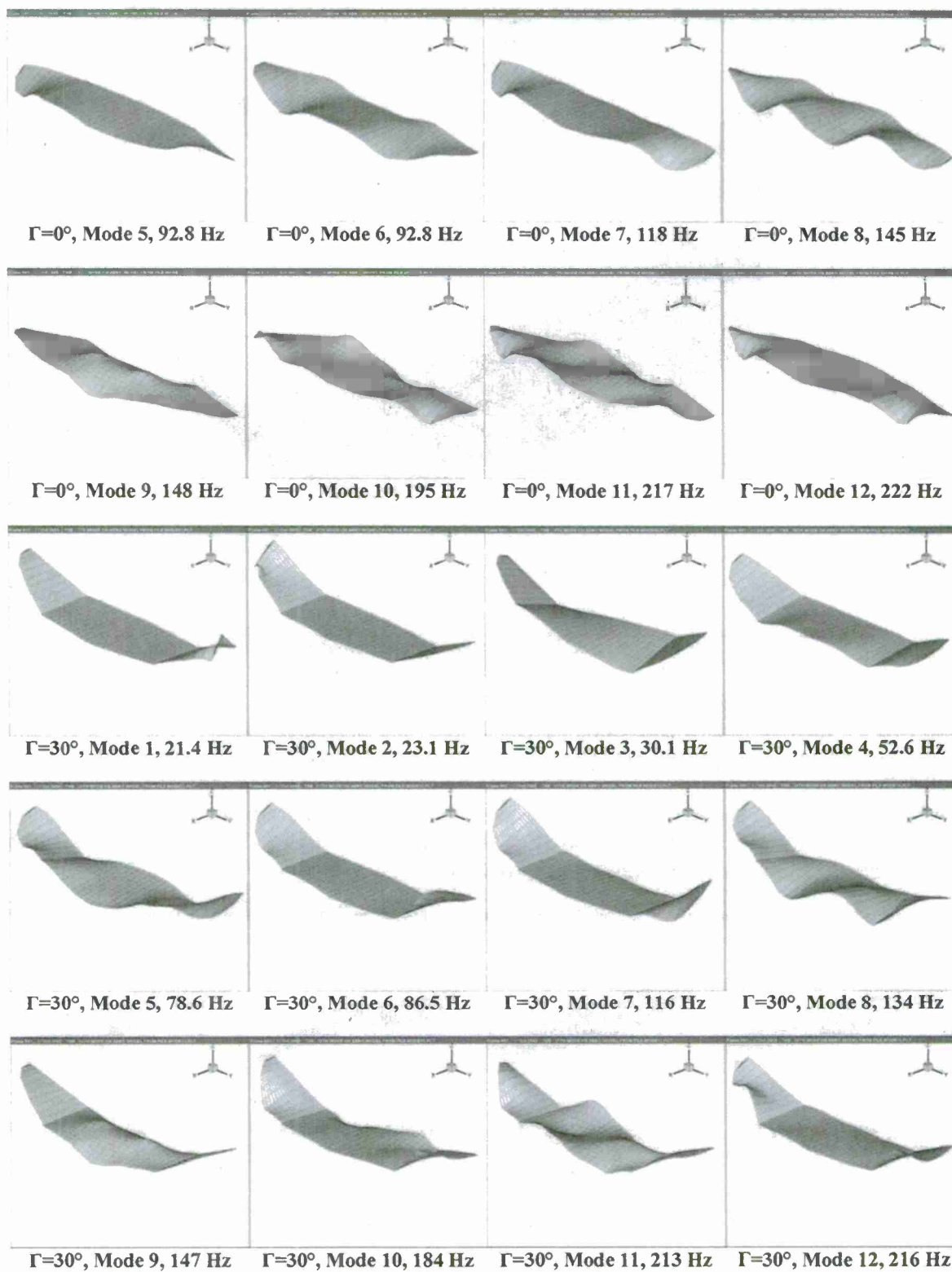
Figure 5.19. MAV Aerodynamic Model

5.3.1 MAV Structural Modes

The first 12 flexible modes calculated by NASTRAN are presented below. The infinite spline plane method was used to correlate the aerodynamic boxes and the structural grid points.

ZAERO used the generated spline matrix to calculate the displacements in the aerodynamic model, shown below in Figure 5.20, based on the NASTRAN output. Note the similarity in the first torsional bending mode for each configuration.





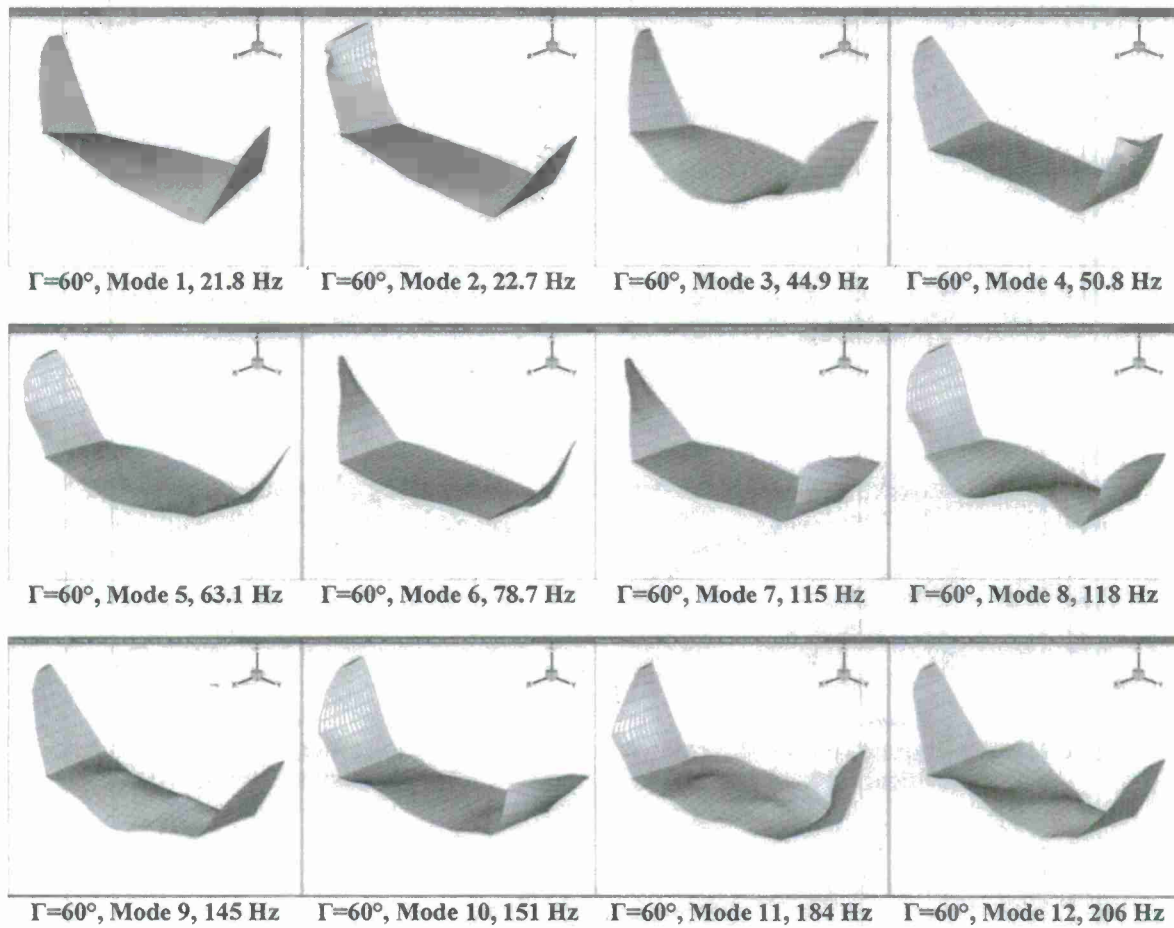


Figure 5.20. Structural Modes of MAV

5.3.2 MAV Divergence/Flutter Solutions

The ZAERO analysis for each configuration was run at a range of Mach numbers from 0.03 to 0.11. For each run, the altitude varied from -35,000 to 77,000 ft. For $M=0.1$, 14 reduced frequency values were used, ranging from 0.025 to 3. For $M=0.07$, 0.05, and 0.04, the reduced frequencies 4, 5, and 6 were added, respectively. For $M=0.03$, the reduced frequencies 7, 8, 9, 10, and 11 were added. The first 15 structural modes were included in the analysis.

Instability in the form of divergence occurs at $V=105$ to 107 ft/s for $M=0.1$ for all 3 configurations, as can be seen from Figures 5.21, 5.22, and 5.23. Here $\Gamma=60^\circ$ is the limiting case. A true flutter mode can be seen at a higher dynamic pressure for all configurations, based on the 7th structural mode, but divergence occurs well before flutter is reached.

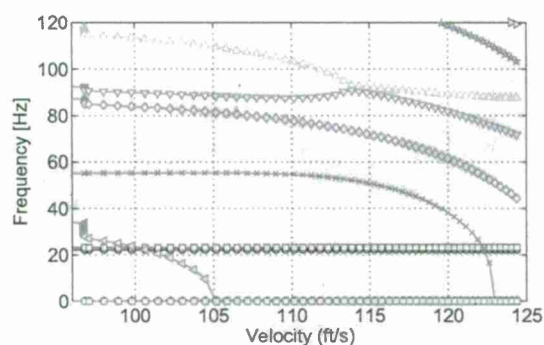


Figure 5.21. V-g Diagram of MAV Divergence/Flutter Solution, $M=0.1$, $\Gamma=0^\circ$.

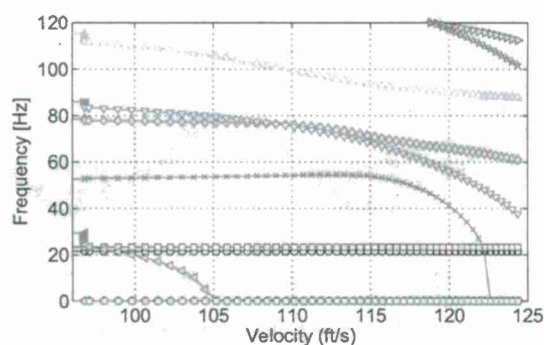


Figure 5.22. V-g Diagram of MAV Divergence/Flutter Solution, $M=0.1$, $\Gamma=30^\circ$.

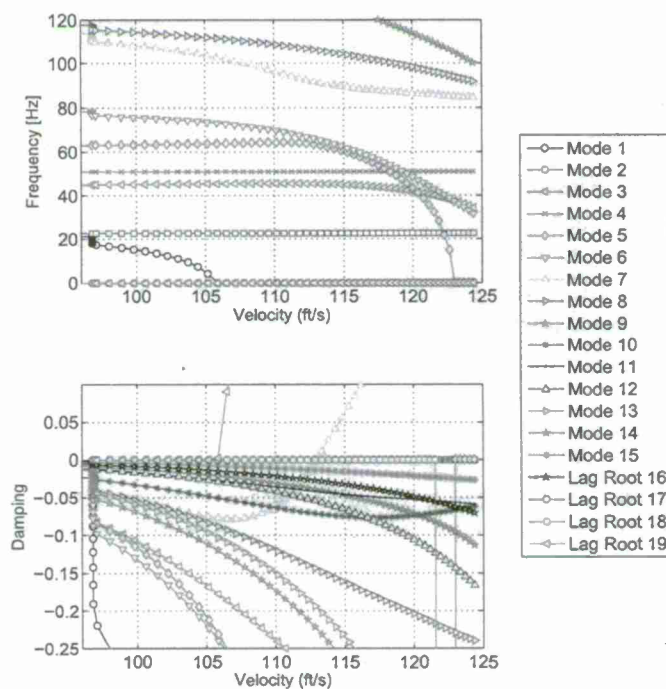


Figure 5.23. V-g Diagram of MAV Divergence/Flutter Solution, $M=0.1$, $\Gamma=60^\circ$

In Figures 5.24 and 5.25 the points at which divergence occur are compared for the 3 different configurations. At sea level, $\Gamma=30^\circ$ is the limiting case, with divergence at $M=0.075$, or 83.4 ft/s. The most stable configuration, $\Gamma=0^\circ$, diverges at $M=0.078$, or 87.4 ft/s. More configurations should be tested to find the true limiting case, as it is impossible to determine from the current data if some other value of Γ between 0° and 60° produces a lower divergence boundary. Between $M=0.095$ and 0.11 , $\Gamma=60^\circ$ becomes the limiting divergence case. This occurs between 12,000 and 20,000 ft. The divergence modes for 3 different Mach numbers are illustrated in Figure 5.26. It can be seen that the changing dihedral angle affects the divergence speed, but overall the MAV behavior changes little.

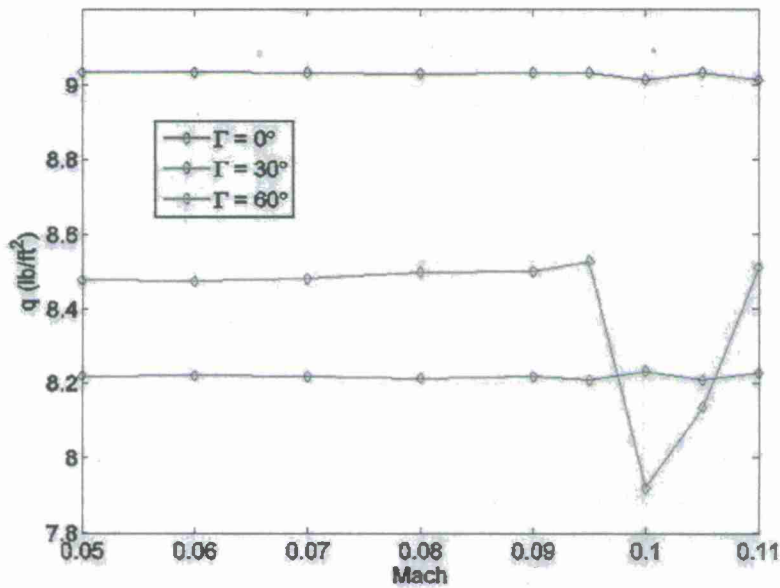


Figure 5.24. Divergence Comparison

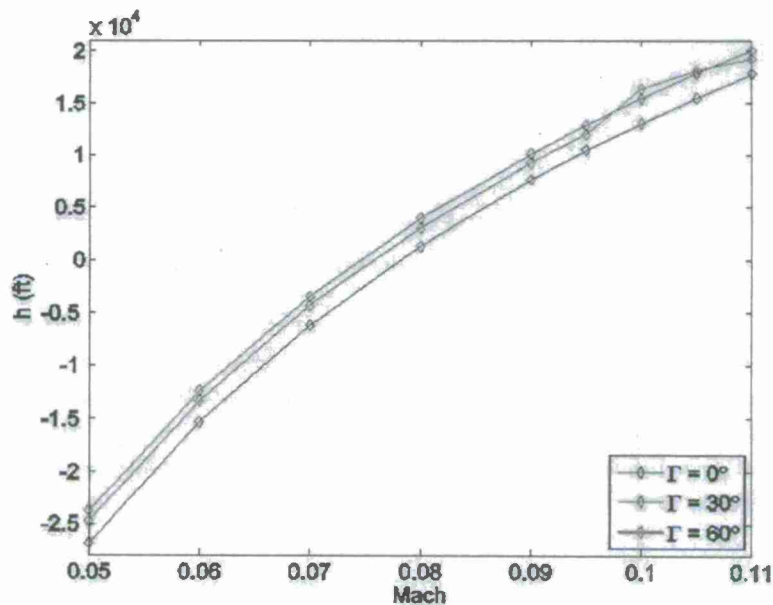


Figure 5.25. Divergence Comparison.

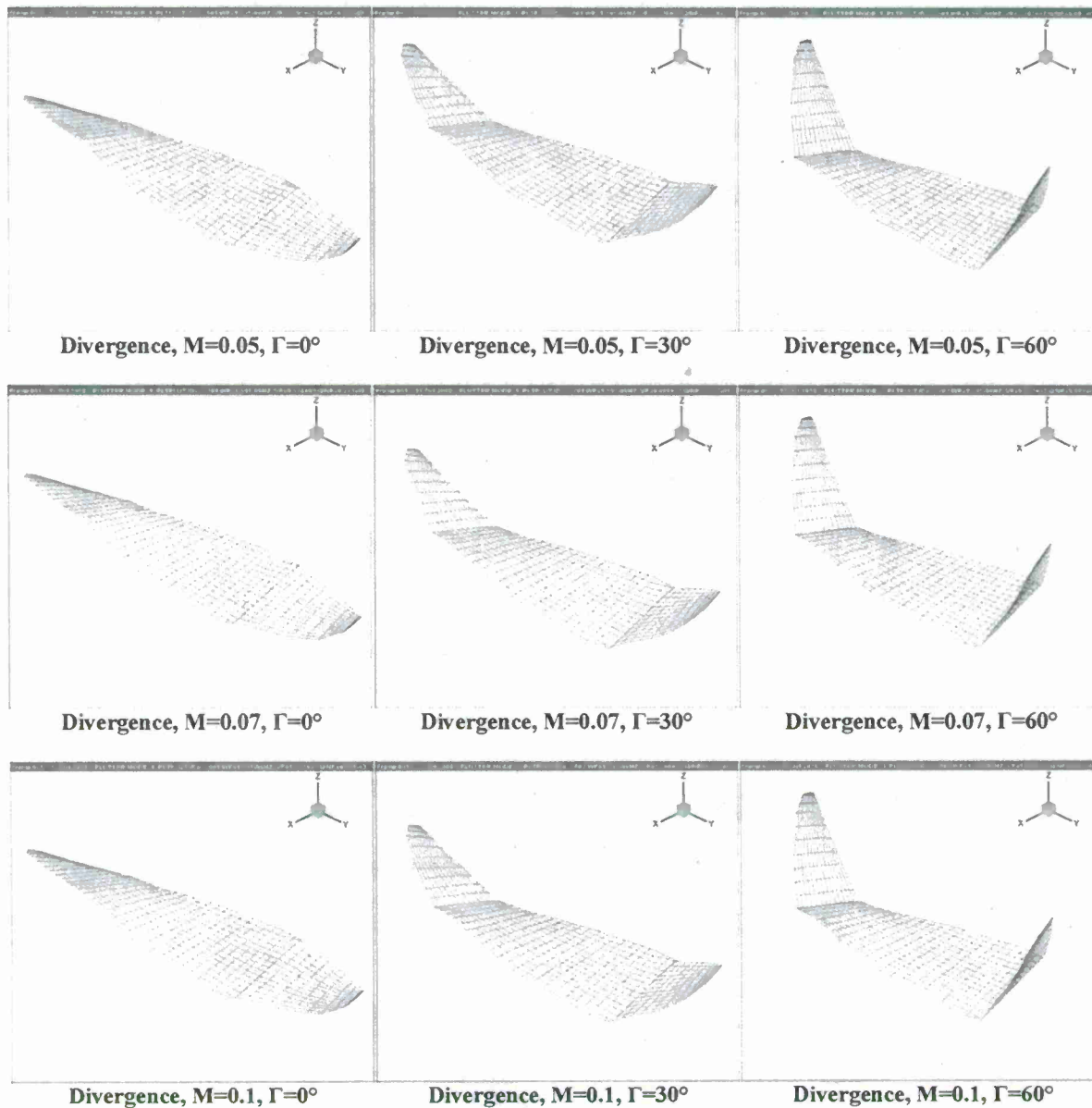


Figure 5.26. MAV Divergence Illustrations.

In Figure 5.27 the dynamic pressure at which divergence occurs is plotted as a function of the dihedral angle Γ . As opposed to the behavior shown in Figure 5.28, the divergence speed begins to drop and then reach a minimum as Γ is increased. Additionally, the variance in the instability speed is much less than in the case of the MAV. However, the configuration of the two aircrafts is quite different, and in the case of the Lockheed Martin folding wing, the instability is due to flutter instead of divergence.

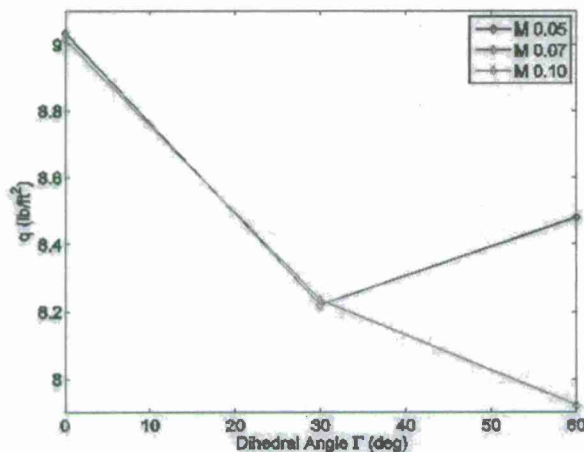


Figure 5.27. MAV Divergence Results.

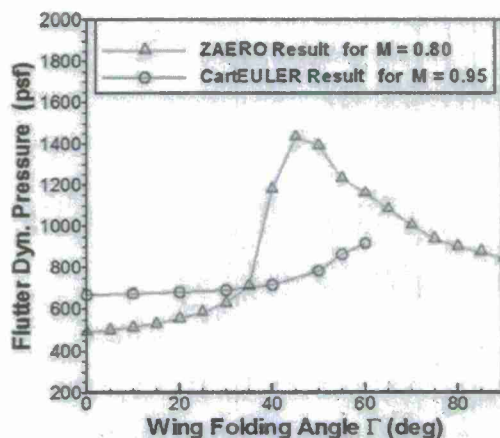


Figure 5.28. Lockheed Martin Folding Wing Flutter Results.

All instability modes are presented in Table 5.9. The divergence modes are marked by $\omega = 0$ Hz, while the flutter modes have a non-zero frequency. The divergent mode for all cases are a result of the first torsional mode, mode 3 for $\Gamma=0^\circ$ and 30° , and mode 1 for $\Gamma=60^\circ$. The flutter mode for $\Gamma=0^\circ$ is dominated by the 7th structural mode, with heavy influence from modes 4 and 6. For $\Gamma=30^\circ$, the flutter mode is dominated by the 7th structural mode, with heavy influence from modes 4 and 5. The flutter mode for $\Gamma=60^\circ$ is dominated by the 7th structural mode, with heavy influence from modes 3 and 5.

Table 5.9. Divergence/Flutter Results.

M	$\Gamma=0^\circ$			$\Gamma=30^\circ$			$\Gamma=60^\circ$		
	q (lb/ft ²)	ω (Hz)	h (ft)	q (lb/ft ²)	ω (Hz)	h (ft)	q (lb/ft ²)	ω (Hz)	h (ft)
0.05	9.04	0	-26800	8.22	0	-23750	8.48	0	-24800
0.06	9.04	0	-15300	8.22	0	-12400	8.47	0	-13300
0.07	9.03	0	-6180	8.22	0	-3480	8.48	0	-4370
							22.3	89.9	-24500
0.08	9.03	0	1340	8.21	0	3920	8.50	0	3000
				21.3	93.3	-24200	19.2	90.9	-20900
0.09	9.03	0	7660	8.22	0	10100	8.50	0	9230
	26.9	90.4	-24200	19.3	94.1	-13700	17.7	91.4	-11200
0.10	9.02	0	13100	8.23	0	15400	7.92	0	16300
	24.9	90.6	-15100	18.0	94.6	-5530	16.8	91.7	-3510

Chapter 6.

ZONA'S EULER UNSTEADY AERODYNAMIC SOLVER (ZEUS)

Summary

ZEUS is ZONA's Euler Unsteady Aerodynamic Solver that integrates the essential disciplines required for aeroelastic design/analysis. It uses an Euler equation solver as the underlying aerodynamic force generator coupled with the structural finite element modal solution to solve various aeroelastic problems such as flutter, maneuver loads, gust loads, and static aeroelastic/trim analysis. Structural nonlinearities can also be included to perform a nonlinear aeroelastic analysis.

The Euler equation solver solves the Euler equations on a Cartesian grid system using a cell-centered finite volume method with a dual-time stepping algorithm for unsteady solutions. The viscous effects are included by coupling the Euler solution with a steady boundary-layer equation. For turbulence closure, the Green's lag entrainment is employed. Because of solving the Euler equations with boundary layer coupling, the requirement of large computing resources by a Navier-Stokes code can be avoided by ZEUS. Therefore, ZEUS provides a good balance between the complete modeling of the flow physics and the computational efficiency.

We have integrated ZEUS into RETINAS replacing the OVERCAP (Overset Cartesian-Transonic Small Disturbance Theory) solver. With using ZEUS the fidelity, accuracy and computational savings have been increased which will lead to a positive impact for the key performance parameters of the Steamlined Stores Clearance (SSC) Product.

The ZEUS code has been enhanced recently; with the capability of using a body-fitted grid for modeling a body component. Automatic mesh generation was enhanced to include models with triangular surface cells, and the flow solver was updated accordingly. Preconditioning has been added for low Mach number flow computations. A vorticity confinement scheme has been implemented to improve the accuracy of solutions for high angle of attack cases.

6.1 Body-Fitted Grid for Body Modeling

For automatic mesh generation purposes, ZEUS models a body component using a straight rectangular box, and transpiring boundary-conditions are applied on the upper, lower, left and right surfaces of the box to account for the body shape effects. In order to achieve the most accurate solution, the capability of the body-fitted grid modeling for the body component was recently added to the ZEUS code.

The body-fitted mesh around a body can be automatically generated with a few parameters given. First, a 2D O-type of mesh around each body cross section was generated by solving a Laplace or Poisson equation. A final 3D mesh is obtained by smoothly connecting those 2D meshes along the X -axis and extending them beyond the leading and trailing edges of the body to the specified far-field. The 2D and 3D views of such a body-fitted mesh is shown in Figure 6.1.

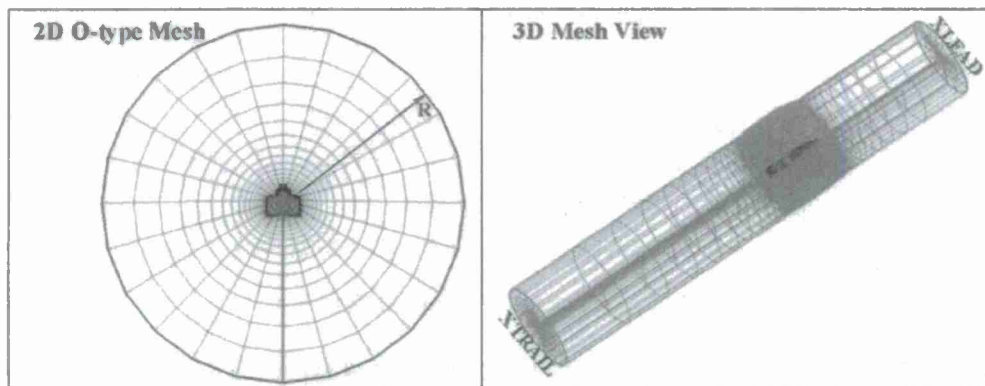


Figure 6.1. Body-Fitted Mesh Generated Around a F-18 Fuselage.

In ZEUS, we use the **BLOCK** bulk data card for the Cartesian mesh generation and the **BLOCK1** bulk data card for the body-fitted mesh generation. Unlike the **BLOCK** bulk data card that can automatically generate a Cartesian mesh containing multiple wing and body components, the O-type body-fitted mesh generated by the **BLOCK1** bulk data card must contain only one **BODY7** macroelement and cannot contain other bodies or wings. Therefore, for a wing-body configuration, if the body mesh is generated by the **BLOCK1** bulk data card, the overset mesh scheme must be used where the wing mesh (generated by a **BLOCK** bulk data card) and the body mesh have a sufficient overlapping region to allow for the communication of the flow solutions between the wing mesh (generated by **BLOCK** bulk data card) and the body mesh (generated by the **BLOCK1** bulk data card).

If a body-fitted grid is available, the exact surface boundary conditions can be applied and thus a more accurate solution is warranted. The Compact Kinetic Energy Missile (CKEM) case is used to show the accuracy of using a body-fitted grid for body modeling. The bent nose CKEM configuration has a centerbody length of 52.07 inches and a diameter of 2.214 inches. The centerbody is characterized by a 4.0-caliber, 7.0 power series nose with a cylindrical aftbody and eight wrap-around fins. The geometry of one of the wrap-around fins is depicted in Figure 6.2.

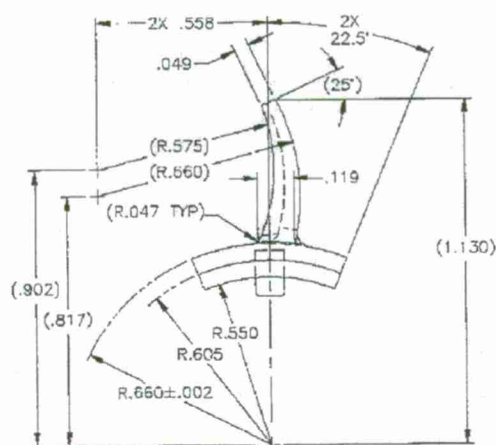


Figure 6.2. Geometry of the Wrap-Around Fin.

The maneuverability of CKEM is achieved by the bent-nose control via a single joint by which the 4.0-caliber nose is projected at an angle relative to the missile centerbody to provide a control deflection.

The overset mesh of the centerbody and the 8 fins generated by the **BLOCK1** and 8 **BLOCK** bulk data cards respectively is presented in Figure 6.3. It can be seen in the mesh projected onto the Y-Z plane, the outer boundary of the mesh of the fin does not intersect with the surface mesh of other fins due to the properly calculated entries ZBOT=-0.7 and ZTOP=0.7 specified in the **BLOCK** bulk data card. Also, in the overlapping region between the mesh of the centerbody and the mesh of the fin, the mesh size in the radial direction near the centerbody surface mesh is comparable to that of the fin along the spanwise direction. As already mentioned earlier, this mesh size in the radial direction of the centerbody is specified by the **AEFACT** bulk data card with ID=209. The comparable mesh sizes among different blocks of mesh in the overlapping region can enhance the accuracy of the flow solution interpolated by the overset mesh scheme.

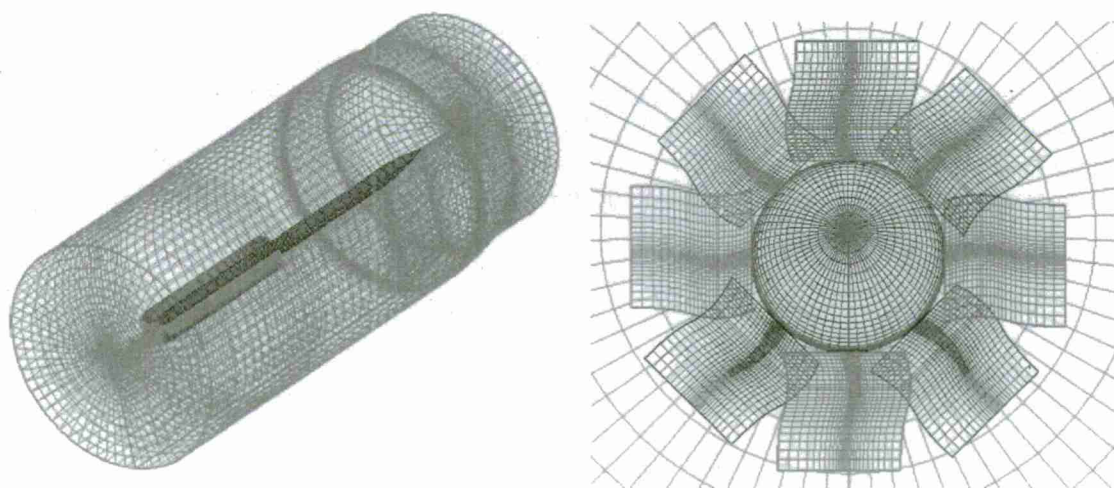


Figure 6.3. Overset Mesh for Modeling the CKEM Configuration.

The lift and moment coefficients of the CKEM configuration with a bent nose angle of 0.0° and 2.0° at a Mach number of 6.0, and angles of attack of 0° , 2.0° , 4.0° , and 6.0° , generated by the ZEUS code are compared to the wind-tunnel data as well as the results computed by the Missile DATCOM. These comparisons are shown in Figure 6.4. It can be seen that the ZEUS results compare very well with the wind-tunnel data whereas the Missile DATCOM results largely over-predicts the lift and under-predicts the moment due to its empirical-equation-based formulation. In addition, when comparing the results of the 2.0° bent nose angle to those of the 0.0° bent nose angle, the CKEM configuration with the bent nose angle of 2.0° gives a small increment of lift but significantly increases the pitch moment from those of the CKEM configuration with a bent nose angle of 0.0° at all angles of attack. This indicates that if the bent nose angle of 2.0° can be achieved by an actuator or a smart structure, the pitch moment due to the bent nose can probably provide sufficient control authority to CKEM for its stability and maneuverability.

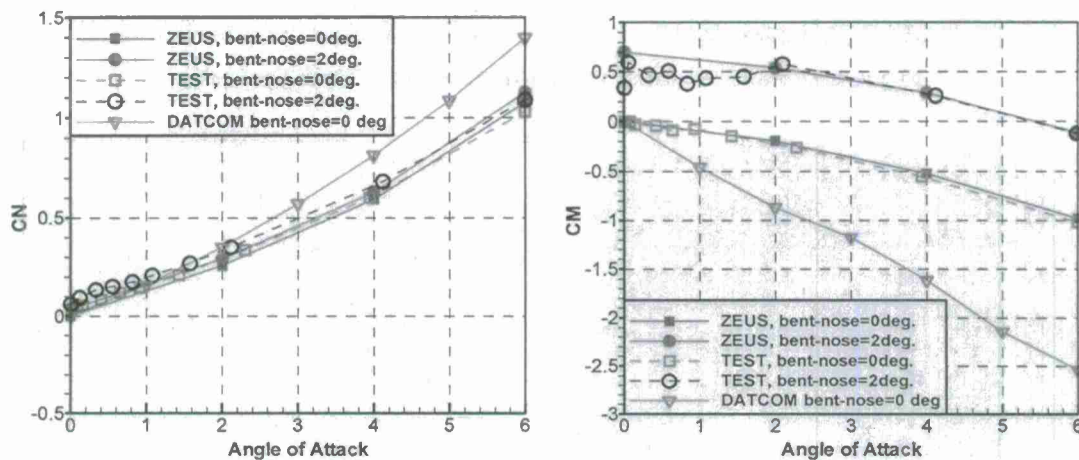


Figure 6.4. Lift and Moment Coefficients of the CKEM Configurations with Bent-Nose Angles of 0.0° , and 2.0° at a Mach number of 6.0 and at Various Angles of Attack.

6.2 Surface Mesh with Triangular Cells

The ZEUS input file is very similar to ZONA's ZAERO Software System. Based on the surface mesh specified in the input deck, ZEUS automatically generates a structural CFD mesh to be used for computation by its EULER solver. Structured mesh generation requires that the surface mesh has only quadrilateral cells. But there are cases that triangular surface cells are needed to setup the aerodynamic model, such as the Joined-Wing model shown in Figure 6.5(a) which has control surfaces with triangular cells. Figure 6.5(b) shows another unusual aerodynamic model for which traditional structural CFD mesh cannot be generated. This is a canard-wing model where the root chords of the canard and wing are concatenated with each other on the X - Y plane. In order for ZEUS to run such unusual cases, the automatic mesh generator in ZEUS has been augmented to take those triangular surface cells into account. Figure 6.6 shows the meshes on the X - Y plane for the Joined-Wing and SAAB canard-wing surface models. These meshes are kind of hybrid meshes because there are triangular cells and/or zero area cells in addition to

quadrilateral cells on the X - Y plane. Those zero volume cells are kept there in order to maintain a structural mesh.

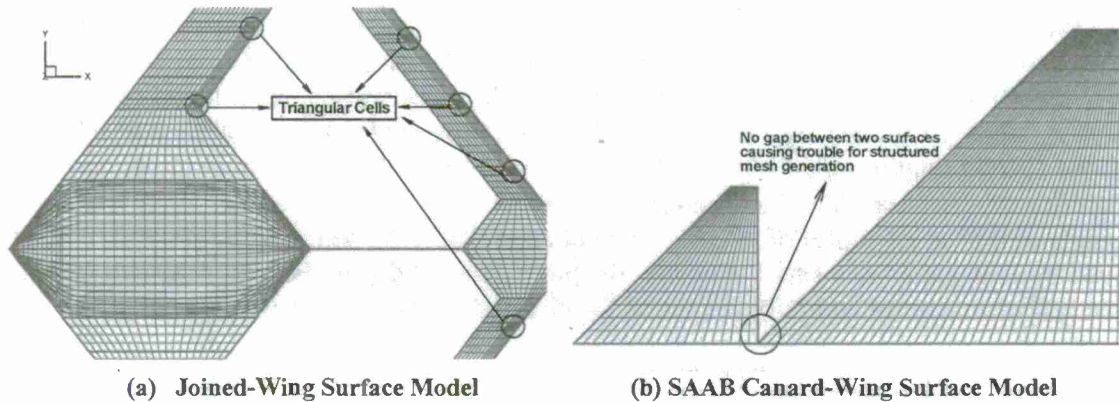


Figure 6.5. Models Causing Trouble for Structured Mesh Generation.

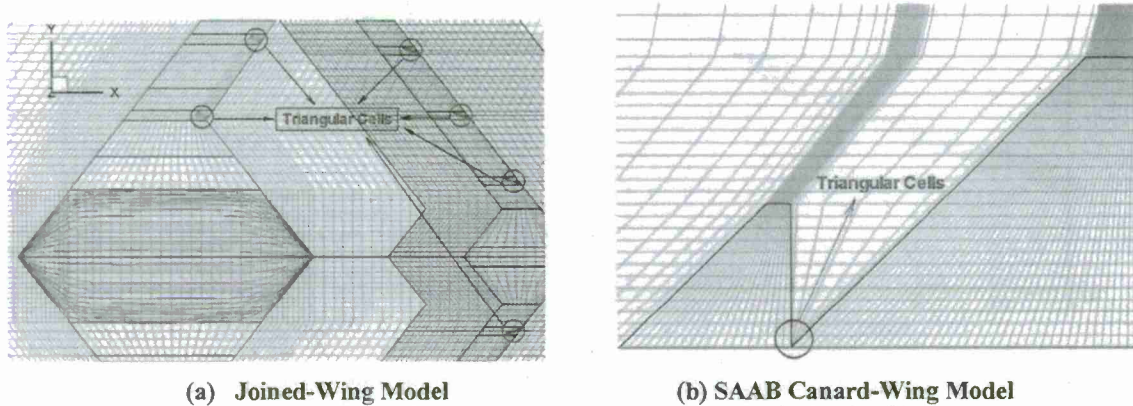


Figure 6.6. X - Y Plane View of the Hybrid CFD Meshes.

For the “hybrid” meshes ZEUS generated, the EULER solver in ZEUS has to be modified accordingly to account for those triangular cells and zero volume cells. A 1-g trim run at Mach number 0.255 has been performed for the Joined-Wing case and the resulting deformed shape with C_p contour is presented in Figure 6.7.

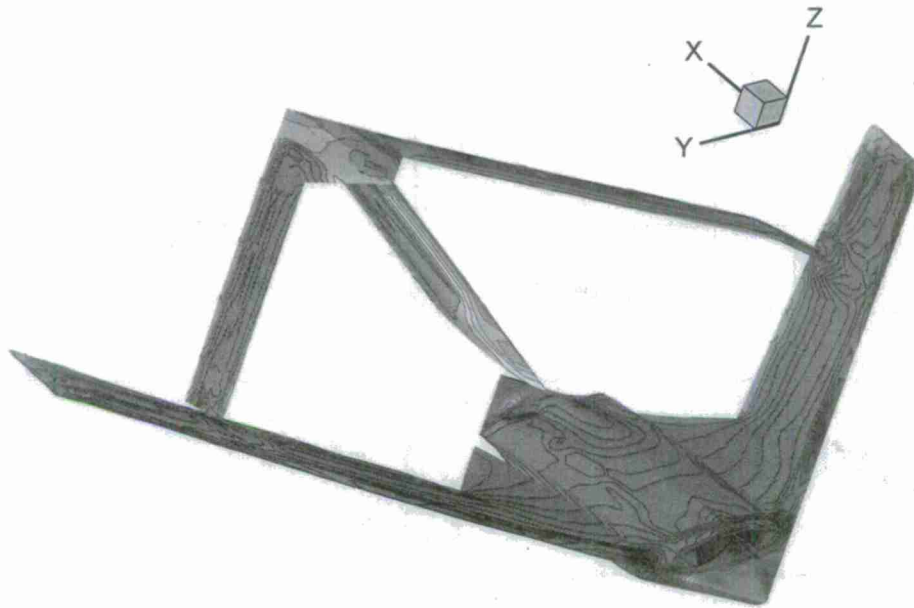


Figure 6.7. C_p Contour on Deformed Shape of the Joined-Wing Model.

The SAAB Canard-Wing model actually has a gap of 0.1 inch in Z between the canard and wing as shown in the Figure 6.8. A computational study has been performed for the SAAB model. The canard is pitching about 50% root chord while the wing is stationary. The lift on the wing is purely due to the downwash effects from the canard. Figure 6.9 shows the comparison of lift on the wing at various reduced frequencies computed by ZEUS with those of ZAERO. A good match is observed at Mach numbers 0.80 and 1.054.

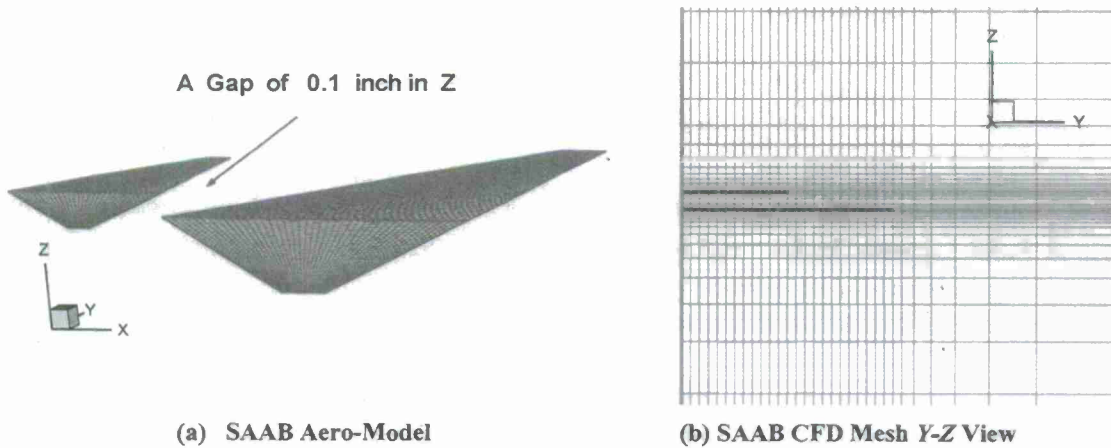


Figure 6.8. SAAB Canard-Wing Model and CFD Mesh.

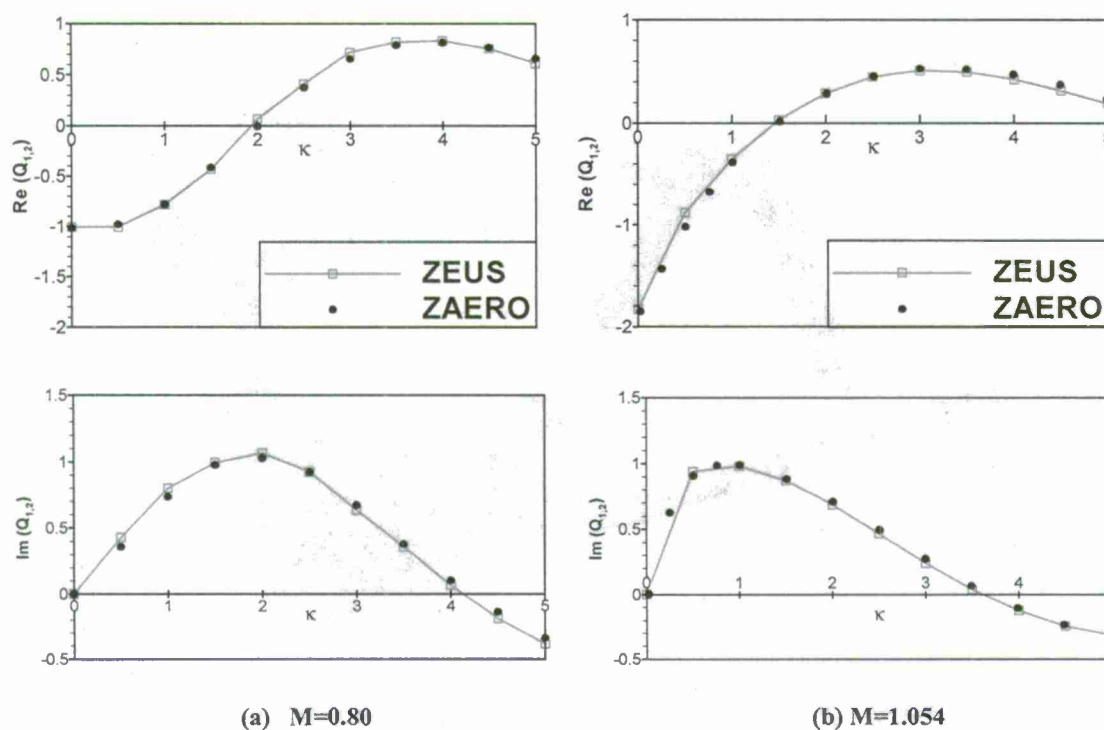


Figure 6.9. Comparison of Lift on Stationary Wing for SAAB Canard-Wing Model.

6.3 Preconditioning

It is well-known that while the Mach number is in the low subsonic range the magnitude of the flow velocity becomes small in comparison to the acoustic speed, and the convective terms of the Euler equations become stiff. We can demonstrate this with the following example. In the 3D case, we have the five eigenvalues;

$$(\Lambda_c)_{1,2,3} = V \quad (\text{convective modes})$$

$$(\Lambda_c)_{4,5} = V \pm c \quad (\text{acoustic modes})$$

Where V denotes the contravariant velocity, Λ_c are the eigenvalues of the convective flux Jacobian of Euler equation, and c is the speed of sound. The stiffness of the governing equations when marching in time is determined by the characteristic condition number. This number is defined as the ratio of the largest to the smallest eigenvalue.

$$C_N = \frac{|\Lambda_c|_{\max}}{|\Lambda_c|_{\min}} = \frac{|V| + c}{|V|} = \frac{M+1}{M}$$

The allowable local time step is limited by the fastest wave, i.e. by $(\Lambda_c)_4$. During one time step, the slowest wave moves only over a fraction of the cell width: $\Lambda_{\min} \Delta t \approx (\Lambda_{\min} / \Lambda_{\max}) h = h / C_N$.

Thus, a large condition number C_N (i.e. as M approaches zero) reduces the efficiency of the wave propagation; it slows down the convergence to a steady state. Furthermore, it can be demonstrated that schemes for compressible flows usually employ certain artificial dissipation which does not scale correctly for Mach numbers approaching zero. Thus, the accuracy of such spatial discretization suffers at low Mach numbers.

The core of ZEUS is a compressible EULER solver employing central differencing together with Jameson's artificial dissipation scheme. Therefore, the ZEUS code has difficulties converging for Mach numbers approaching zero. To resolve this problem, a preconditioning scheme is implemented in ZEUS.

Basically, we pre-multiply a proper matrix with the time derivative term of the unsteady compressible EULER equations, which alters the time evolution of the equations while retaining the same steady-state analytical equations. By doing this, we can effectively change the eigenvalues of the system to compressible flow equations and reduce the disparity in the wave speeds that cause trouble for low Mach number flow computations.

With the preconditioning scheme implemented, the ZEUS code can now run smoothly for Mach numbers as low as 0.005, which intrinsically warrants an incompressible flow condition. Figure 6.10 shows the comparison of the lift and moment coefficients computed by ZEUS with test data for a wing at incompressible flow. The wing selected is a flat plate with sweep back angle of 45° and both the aspect ratio and taper ratio equal to 1. We can see a good match for both the lift and moment coefficients at an angle of attack up to 28° .

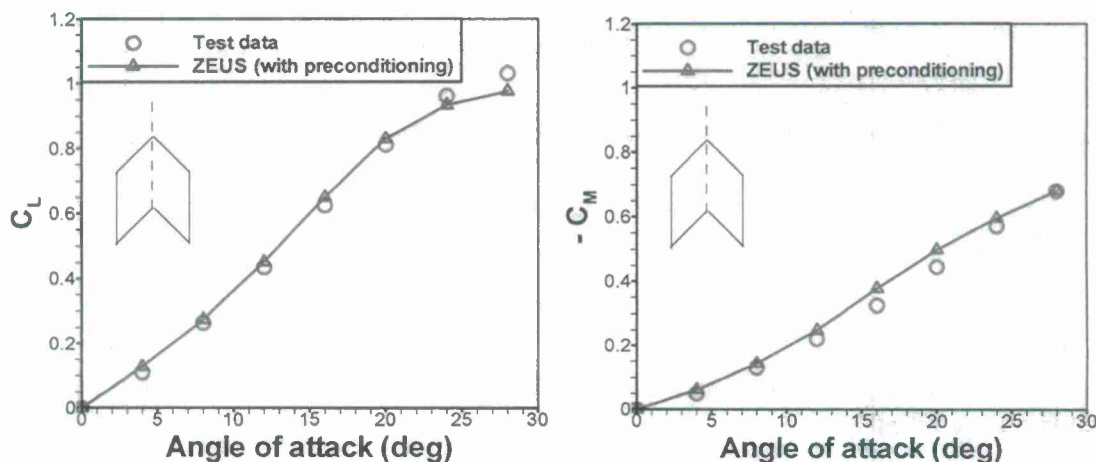


Figure 6.10. Comparison of the Lift and Moment Coefficients between ZEUS and Test Data for a Wing at Incompressible Flow.

6.4 Vorticity Confinement

At a high angle of attack, the flow is easy to separate and thus thin vortical layers or vortical filaments exist. Physically, those vortical structures often remain very thin and persist long distant of convection without significant dissipation. However, the EULER solver usually employs a somewhat coarse mesh with grid cells getting larger and larger as they become far

away from the configuration surface. The vortices could be quickly dissipated due to the numerical discretization error of the EULER solver. Without capturing the vortices properly, the flow solution obtained will be certainly detrimented. For example, the computed lift could be too different from the experimental data. Employing finer meshes can reduce this numerical dissipation but incurs longer computational time.

The so-called vorticity confinement is a method to retain those fine vortical structures without resorting to finer meshes. Basically, a source term is added to the conservation law equations and it serves as a negative dissipation mechanism to effectively convert the discretization error back into the vortex center and thus confining the vorticity.

The vorticity confinement scheme implemented in the ZEUS code is simple. The modified conservation law equations are:

$$\frac{\partial}{\partial t} \int_{\Omega} \mathbf{Q} dV + \int_{\Omega} \{\mathbf{F}(\mathbf{Q}) - \mathbf{G}(\mathbf{Q})\} \cdot \mathbf{n} dS = \int_{\Omega} \mathbf{S} dV$$

The added source term can be written as,

$$\mathbf{S} = \begin{pmatrix} 0 \\ \rho(\mathbf{f}_b)_x \\ \rho(\mathbf{f}_b)_y \\ \rho(\mathbf{f}_b)_z \\ \rho \mathbf{f}_b \cdot \mathbf{V} \end{pmatrix}$$

where \mathbf{f}_b is the body force per unit mass. This body force is defined as,

$$\mathbf{f}_b = -\varepsilon \bar{\mathbf{n}} \times \bar{\boldsymbol{\omega}}$$

$$\bar{\mathbf{n}} = -\frac{\nabla(|\bar{\boldsymbol{\omega}}|)}{|\nabla(|\bar{\boldsymbol{\omega}}|)|}$$

where ε is a confinement parameter which controls the strength of the confinement and it can be a value in the range of 0.001-0.1.

The coplanar wing-body-tail model adopted from the NACA RM L56A18 report is computed by the ZEUS code to demonstrate the effects of applying the above-mentioned vorticity confinement method. The model is a mid-wing configuration whose detailed dimension is shown in Figure 6.11. The wing has an NACA 65A004 airfoil section parallel to the plane of symmetry, 45° sweepback of 1/4-chord line, an aspect ratio of 3, and a taper ratio of 0.2.

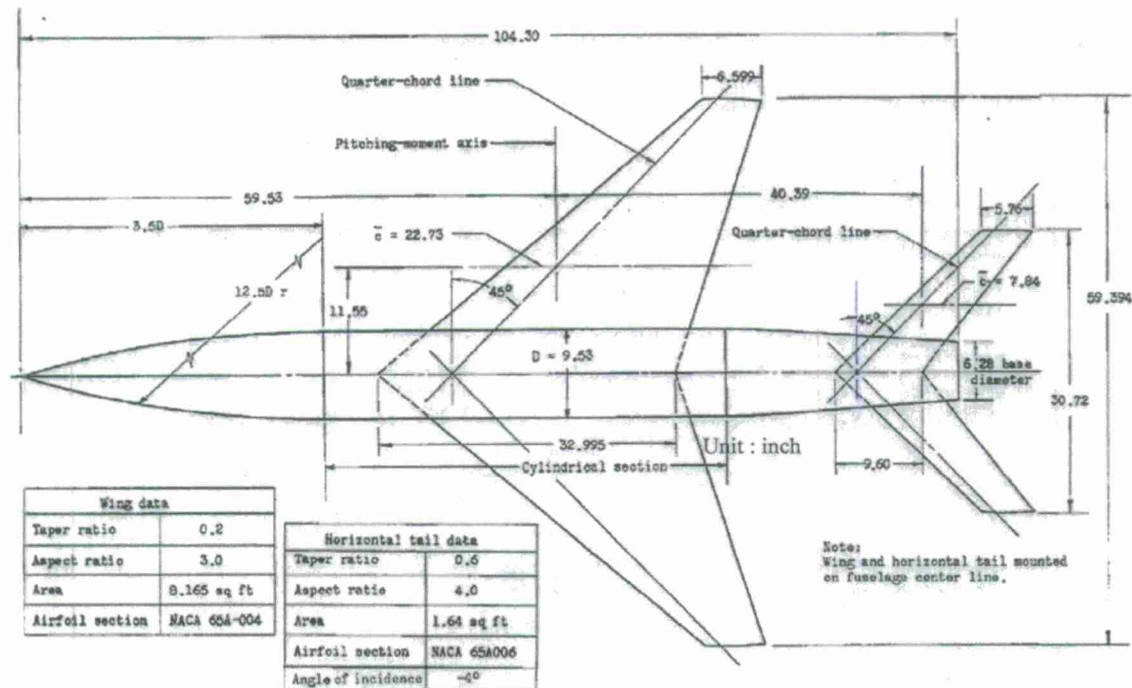


Figure 6.11. Detailed Geometry of NACA RML56A18 Wing-Body-Tail Model.

The wing is mounted in the mid-wing position on the fuselage and has no geometric incidence, dihedral, or twist. The fuselage consists of a cylindrical body of revolution having an ogival nose and a slightly boat-tailed aftbody. The horizontal tail has an aspect ratio of 4, a taper ratio of 0.6, and an NACA 65A006 airfoil section parallel to the plane of symmetry. The horizontal tail is mounted in the mid-fuselage position at an angle of incidence of -4° .

Figure 6.12 shows the ZEUS results computed with/without vorticity confinement together with the wind tunnel data. Generally speaking, the ZEUS results with vorticity confinement match better with experimental data at high angles of attacks.

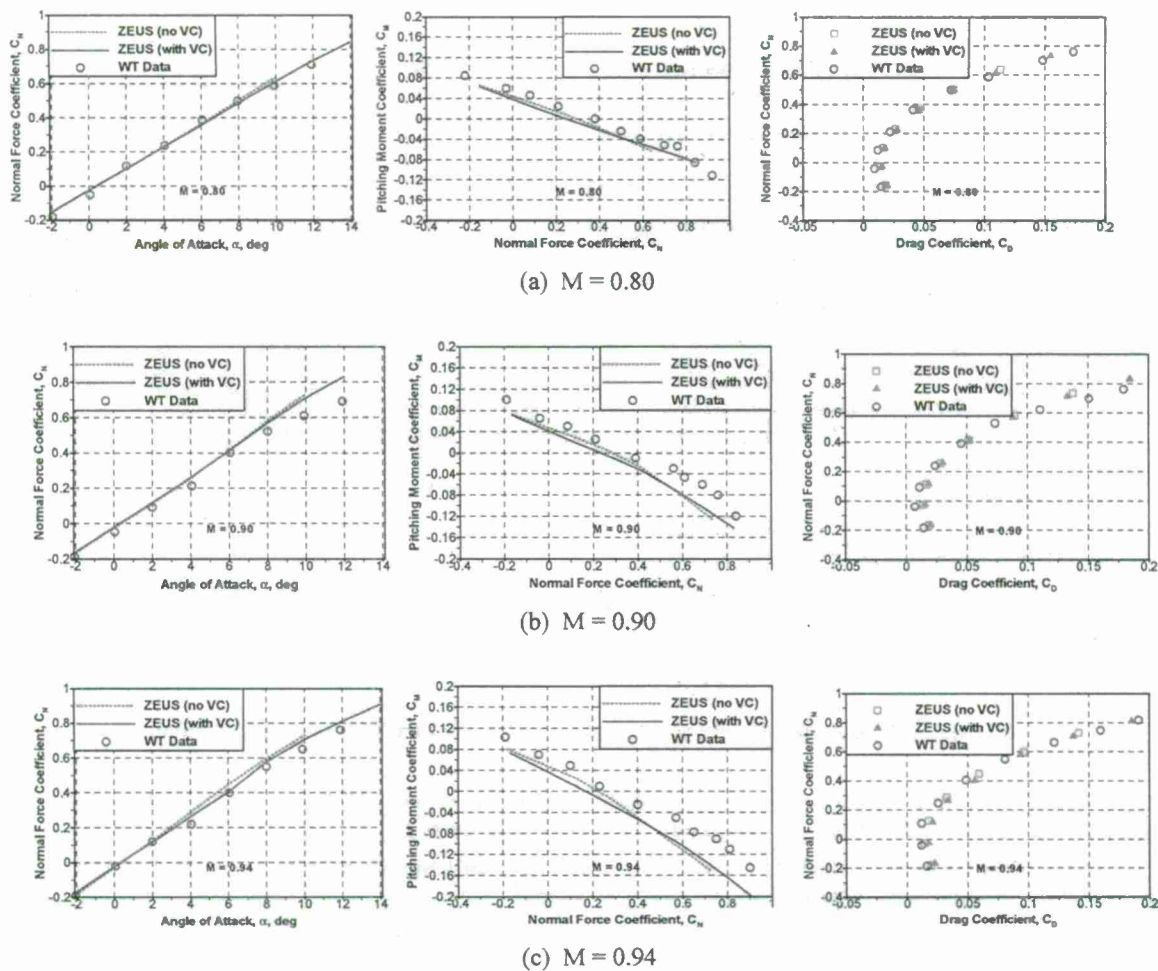


Figure 6.12. Comparison of ZEUS Results with/without Vorticity Confinement Together with Wind Tunnel Data.

Chapter 7.

Consideration of Uncertainty in the Morphing Wing

Recent investigations (e.g. [7.1]) have shown that the aeroelastic response of wings/aircraft may be quite sensitive to uncertainty in their structural properties. Given the complexity of morphing wings, it is expected that such uncertainty will indeed be present and it was thus desired to develop a framework for the estimation of its effects on the morphing wing aeroelastic response. In the present context, structural uncertainty, i.e. the lack of an exact knowledge of the structural properties of the system considered (i.e. the morphing wing here), will be simulated by the *randomization* of some of these properties. Within this global perspective, several options are available.

A first possibility is the inclusion of the random properties at the level of a detailed computational model, e.g. of a finite element model, through the modeling of one or several properties in the model, e.g. Young's modulus, Poisson's ratio, thickness (in beam and plate models), as random variables or fields. The assessment of the effects of this uncertainty on a particular response is then performed by a Monte Carlo simulation: a population of such properties are generated and the response of interest for each one is computed using the detailed computational model. This approach is quite straightforward but faces two particular challenges:

- (i) it is in general a computationally expensive effort as it requires many solutions (as many as samples in the population of properties) of the detailed model, and
- (ii) there is much information to specify in a probabilistic finite element model (or other detailed computational model) such as probability density function of the properties, especially complex when dealing with random fields, correlation information (correlation between random variables, autocorrelation function for processes and fields), etc. Yet, very little of this information may be expected to be known from measurements and thus a very large number of assumptions must be made, whose effects on the response are difficult to assess.

A second possibility is to include the uncertainty at a reduced order model level, e.g. on a modal model in linear structural dynamic problems. In such an approach, e.g. see [7.2] and [7.3], the basis functions used in the reduced order model are those associated with the "expected structure", which will be referred to here as the *mean model*. Thus, the uncertainty is only introduced in the "coefficients" of the reduced order model, e.g. the modal masses, stiffnesses, and damping for a linear structural dynamic problem. This approach typically eliminates the challenge (i) above as reduced order models run much faster than their corresponding detailed

computational models. The second challenge is also lessened by proceeding at the reduced order model level as there are fewer random variables and often no random process or field present so that the probabilistic information that must be specified is much less, but it will typically remain more than the available data. Assumptions on the probabilistic model of the coefficients of the reduced order model must accordingly still be made.

Several years ago, Soize proposed (see [7.2] and [7.3]) a very novel approach in establishing the probabilistic model of the coefficients of reduced order models. Specifically, he suggested that this probabilistic description be such that the corresponding *statistical entropy* be maximized under the constraint that available information be satisfied, i.e. the mean of the random reduced order model should reduce to the mean model, an overall measure of uncertainty should be met, as well as possible additional requirements (e.g. see [7.4]). This approach based on the maximization of the entropy has been referred to as the “nonparametric stochastic modeling” method as it does not involve the specification of parameters of specific statistical distributions used to characterize the random coefficients of the reduced order model. It is this method which will be considered here and accordingly, it is briefly reviewed below (section 7.1) before its application to the morphing wing aeroelastic system is demonstrated.

7.1 Nonparametric Stochastic Modeling

The nonparametric stochastic modeling method was first developed to assess the effects of uncertainty on the response of linear structural dynamic systems. The reduced order model used in such problems, i.e. the modal models, are characterized by mass, damping, and stiffness matrices which are from physical requirements symmetric and positive definite. Accordingly, the fundamental problem of the nonparametric methodology is the modeling of random symmetric positive definite real matrices \underline{A} such as the mass, damping, and/or stiffness matrices of linear modal models.

Then, the nonparametric approach seeks the (joint) statistical distributions of the random elements A_{ij} of \underline{A} that lead to the maximum of the statistical entropy S

$$S = - \int_{\Omega} p_{\underline{A}}(\underline{a}) \ln p_{\underline{A}}(\underline{a}) d\underline{a} \quad (7.1)$$

while satisfying constraints corresponding to available information. Note in Eq. (7.1) that $p_{\underline{A}}(\underline{a})$ is the unknown joint probability density function of the random elements A_{ij} . As such, this function must satisfy the positive everywhere and must satisfy the normalization condition

$$\int_{\Omega} p_{\underline{A}}(\underline{a}) d\underline{a} = 1 \quad (7.2)$$

which represents the first constraint.

The second constraint is that the mean of the random matrix \underline{A} should match the corresponding matrix \bar{A} of the mean model, that is $E[\underline{A}] = \bar{A}$ where $E[.]$ denotes the operation of mathematical expectation or

$$E[\underline{A}] = \int_{\Omega} \underline{a} p_{\underline{A}}(\underline{a}) d\underline{a} = \bar{A} . \quad (7.3)$$

Further, if the mean model does not exhibit any rigid body mode (i.e. \bar{A} is strictly positive definite), then it is also expected that the random matrices \underline{A} will share the same property (note that the extension of the methodology to mean models exhibiting rigid body modes has been accomplished in [7.5]). This condition is equivalent to the existence of a flat zero at zero of the probability density function of the eigenvalues of \underline{A} and can be imposed by requiring (see [7.1] and [7.2]) that

$$\int_{\Omega} \ln[\det(\underline{a})] p_{\underline{A}}(\underline{a}) d\underline{a} = v \text{ finite} \quad (7.4)$$

where the value of v will be selected so that a particular information on the level of uncertainty/variability of the matrices \underline{A} is met.

Note in Eqs (7.1)-(7.4) that Ω denotes the domain of the coefficients A_{ij} such that the matrix \underline{A} is positive definite.

The maximization of S , Eq. (7.1), under the constraints of Eqs (7.2)-(7.4) can be achieved using the Lagrange multiplier technique to yield first the joint probability density function of the elements A_{ij} , see [7.1] and [7.2]. Further observations (see [7.1] and [7.2]) then demonstrate that this joint probability density function is consistent with a particular simple simulation strategy of the random matrices \underline{A} .

Specifically, denote first by \bar{L} any decomposition, e.g. Cholesky, of \bar{A} , i.e. satisfying $\bar{A} = \bar{L} \bar{L}^T$. Then,

$$\underline{A} = \bar{L} \underline{H} \underline{H}^T \bar{L}^T \quad (7.5)$$

where \underline{H} denotes a lower triangular random matrix the elements of which are all statistically independent of each other. Moreover, its off-diagonal elements (H_{il}) are zero-mean Gaussian random variables with common variance $1/\sqrt{2\mu}$ and its diagonal elements (H_{ii}) can be obtained as $H_{ii} = \sqrt{Y_{ii}/\mu}$ where the variables Y_{ii} are Gamma distributed random variables, see Figure 7.1. The single parameter μ can be expressed in terms of the finite value v of Eq. (7.4) and thus can be used to adjust the level of uncertainty/variability in the model. It is convenient to introduce one last parameter $\lambda > 0$ through the relation:

$$\mu = \frac{n + 2\lambda - 1}{2} \quad (7.6)$$

The application of the nonparametric approach then proceeds as follows:

- (1) having obtained the mean detailed computational model (e.g. finite element model), the appropriate basis functions (e.g. modes) are selected and the mean reduced order model is obtained. From the mean matrix $\underline{\underline{A}}$, the decomposition $\underline{\underline{L}}$ is obtained from $\underline{\underline{A}} = \underline{\underline{L}} \underline{\underline{L}}^T$.
- (2) introduce a measure and level of uncertainty for the determination of the parameter λ or μ , e.g. impose the standard deviation of a particular element or eigenvalue of the random matrices $\underline{\underline{A}}$. In the analysis performed below with the morphing wing, a standard deviation of the first natural frequency of 2% of its mean model value was imposed. Another possible measure of uncertainty is the parameter δ introduced in [7.1] and [7.2] which is defined as the coefficient of variation (standard deviation divided by mean) of the Frobenius norm of the random matrices $\underline{\underline{A}}$. While there is a direct relation between δ and λ , this is not the case between other possible measure of uncertainty (e.g. the eigenvalues. In such cases, the determination of λ must proceed iteratively, i.e. a tentative value of this parameter is first selected. Then, a limited Monte Carlo analysis (with 1000 samples say) is conducted to obtain the level of uncertainty on the specified measure (e.g. standard deviation of first natural frequency) corresponding to this value of λ . The value of this parameter is then adjusted to meet the specified level of uncertainty. Performing this analysis is in fact extremely fast owing to the very simple simulation process of the matrices $\underline{\underline{A}}$.

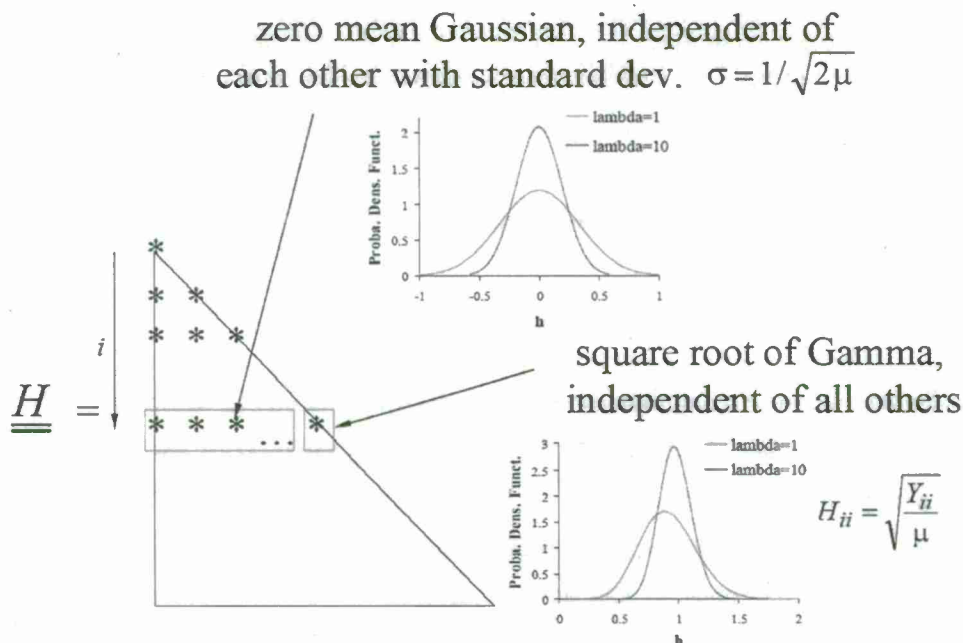


Figure 7.1. Structure of the random $\underline{\underline{H}}$ matrices (figures for $n=8$, $i=2$, and $\lambda=1$ and 10)

Since its original formulation in 2000, the nonparametric methodology has been broadly extended and validated by Soize and his group as well as by those of Mignolet and Ghanem. Extensions include the consideration of rectangular/nonpositive matrices [7.5], semipositive definite matrices [7.5], the inclusion of multiple levels of uncertainty [7.4], and random matrix fields [7.6]. Applications of the methodology have comprised linear structural dynamics (e.g. [7.2]), vibro-acoustics, aeroelasticity (e.g. [7.1]), rotordynamics [7.7] (including the joint simulation of mass and gyroscopic matrices), geometrically nonlinear structural dynamic problems [7.8], optimization under uncertainty, etc. The methodology has also been validated experimentally and has been shown to be particularly useful in validating computational models with experimental data in which uncertainty/variability with respect to the mean computational model exists.

7.2 Applications to the Morphing Wing Aeroelasticity

It was desired here to investigate the applicability of the nonparametric stochastic modeling technique for the consideration of uncertainty on the structural properties of the morphing wing. Several computational models which were used in the project will be considered and uncertainty in mass and stiffness properties will be considered.

The first application focused on the one-piece linear model of the morphing wing used in Phase I that involved the first 6 transverse modes of the structure. The uncertainty was introduced in the stiffness only and the parameter λ of the random 6x6 stiffnesses matrices was determined iteratively (see discussion above) to obtain a standard deviation of the first natural frequency equal to 2% of the mean model value.

A population of 300 such stiffnesses were generated and the aeroelastic response of each wing at a Mach of 0.95 and altitude of 18,000 ft was computed. An autoregressive modeling effort was undertaken for each of the 300 time histories of the wing response to determine the effective natural frequency and damping ratio of the random aeroelastic system. Shown in Figures 7.2 and 7.3 are the probability density functions of the response frequency and damping ratio. Note in particular that the mean wing is aeroelastically stable (with this model) at these flight conditions, there is a number of wings, albeit small (approximately 4% of them as estimated from the 300 sample), that have fluttered as indicated by the negative values of damping present in the distribution of Figure 7.3. A comparison between the time histories of the response of two wings is shown in Figure 7.4. Note the very similar behavior at small times but the growing difference induced by the aerodynamic effects.

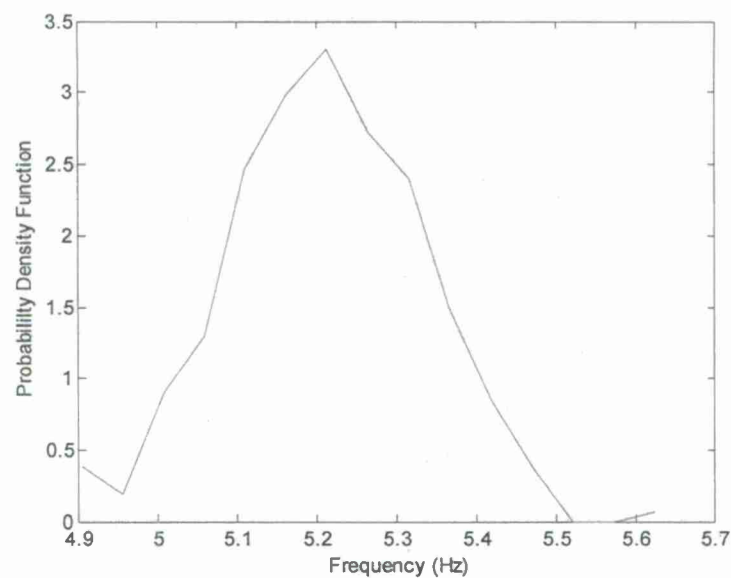


Figure 7.2. Probability density function of the random aeroelastic system response frequency, one-piece linear model, 6 modes, uncertainty in stiffness.

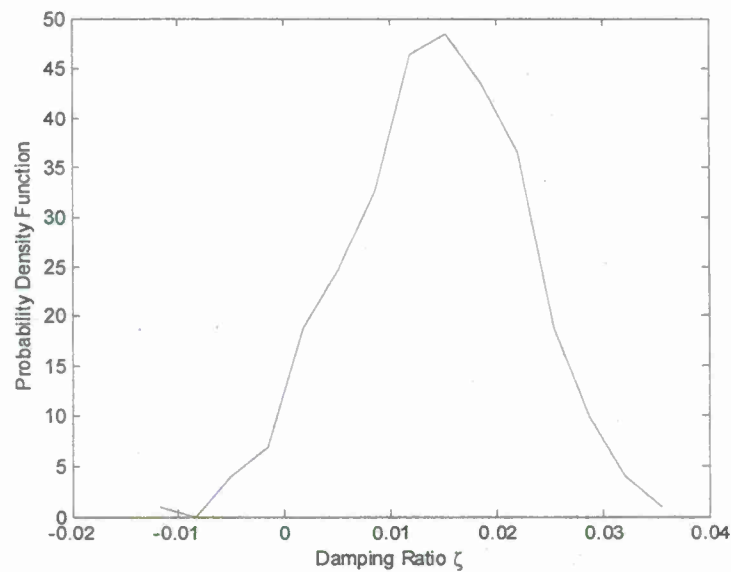


Figure 7.3. Probability density function of the random aeroelastic system response damping, one-piece linear model, 6 modes, uncertainty in stiffness.

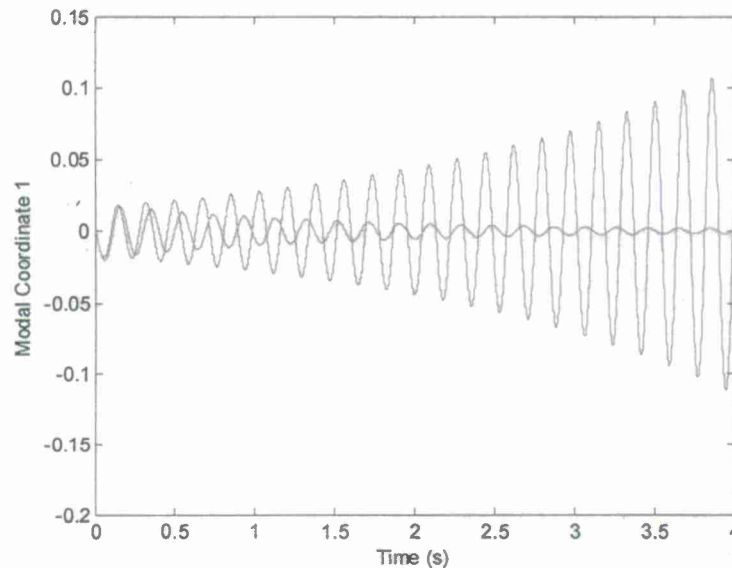


Figure 7.4. Time histories of the first modal coordinate for two different wings in the population of 300, one-piece model.

The second application of the nonparametric modeling method focused on the 2-piece linear model and uncertainty in the stiffness was again considered. Since the two wings are physically disjoint, there cannot be any topological coupling between them and thus the 13x13 stiffness matrices of the inboard and outboard wings were simulated separately from each as independent random matrices. The parameters λ were selected to achieve again a standard deviation of the first natural frequencies equal to 2% of the mean model values. As in the one-piece case, 300 set of stiffnesses were generated and the aeroelastic response of each wing at a Mach of 0.95 and altitude of 18,000 ft was computed for which the mean wing is marginally stable with this model. This data was post-processed to obtain the effective dominant frequency and associated damping ratio. The corresponding probability density functions of the frequency and damping ratio are shown in Figures 7.5 and 7.6. Note again the split of the probability density function of the damping in negative and positive values demonstrating for this flight condition that some of the wings will flutter while others will not.

Uncertainty in the stiffnesses is expected and would correspond to small variations in the elastic properties of the material used but also, and possibly more importantly, to variations in the thickness of the panels and to assembly of the wing, e.g. riveting. Variability in the thickness of the panels would also induce variations of the mass and, accordingly, it was desired next to compare the results of Figure 7.5 and 7.6 with similar ones obtained with variations of the masses.

In this regard, it should be recognized that the mass properties of the inboard and outboard wing are involved quite differently in the two-piece morphing dynamic equations. The mass properties of the inboard are only present in the corresponding mass matrix terms while those of the outboard are present everywhere, see Appendix. The inclusion of the mass uncertainty in the outboard wing would necessitate a separate treatment which was not considered here. Accordingly, only variations in the mass properties of the inboard were considered here with the same standard deviation of natural frequency (2%) and same flight conditions.

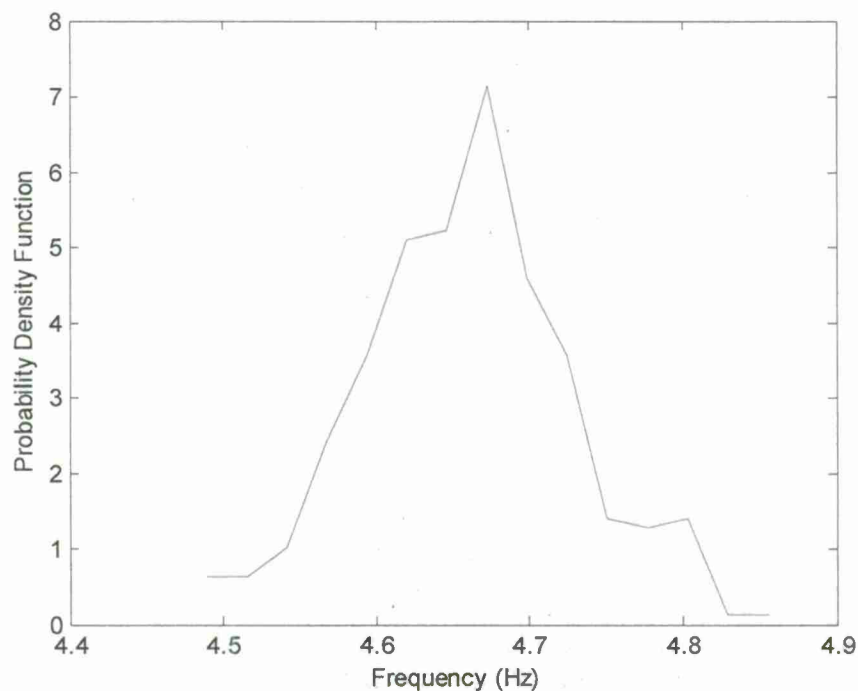


Figure 7.5. Probability density function of the random aeroelastic system response frequency, two-piece linear model, 26 modes total, uncertainty in stiffness.

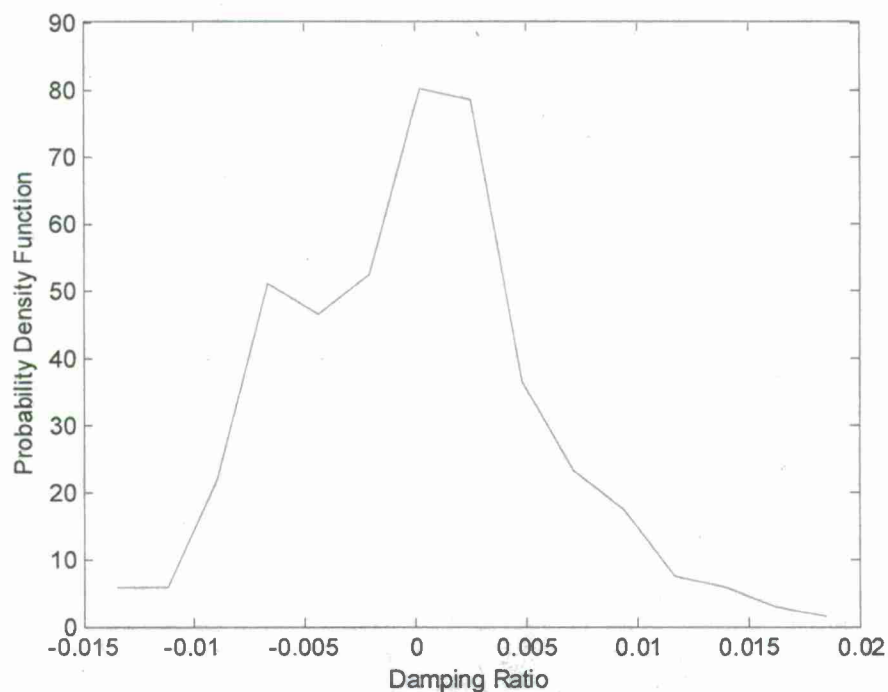


Figure 7.6. Probability density function of the random aeroelastic system response damping, two-piece linear model, 26 modes total, uncertainty in stiffness.

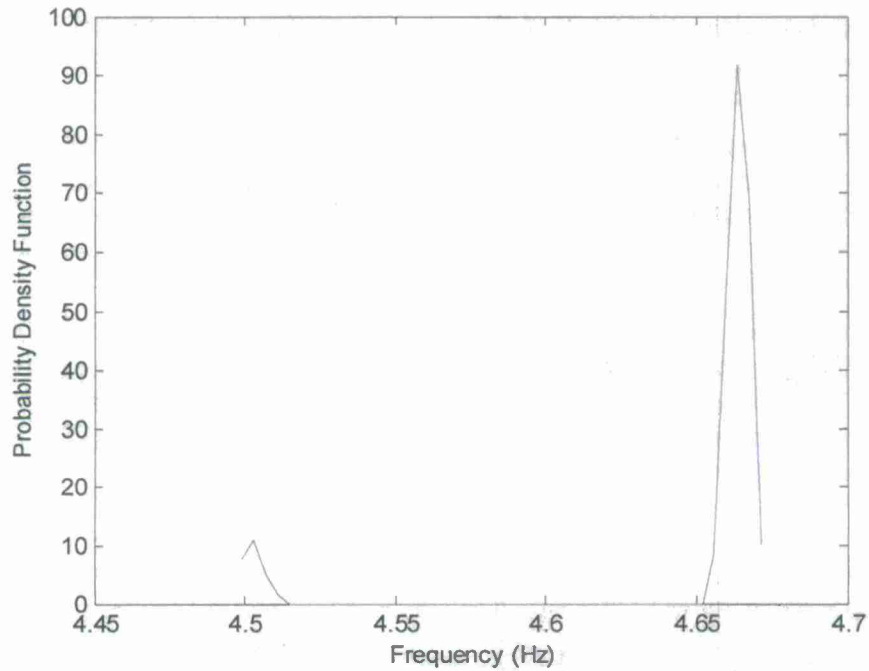


Figure 7.7. Probability density function of the random aeroelastic system response frequency, two-piece linear model, 26 modes total, uncertainty in inboard mass.

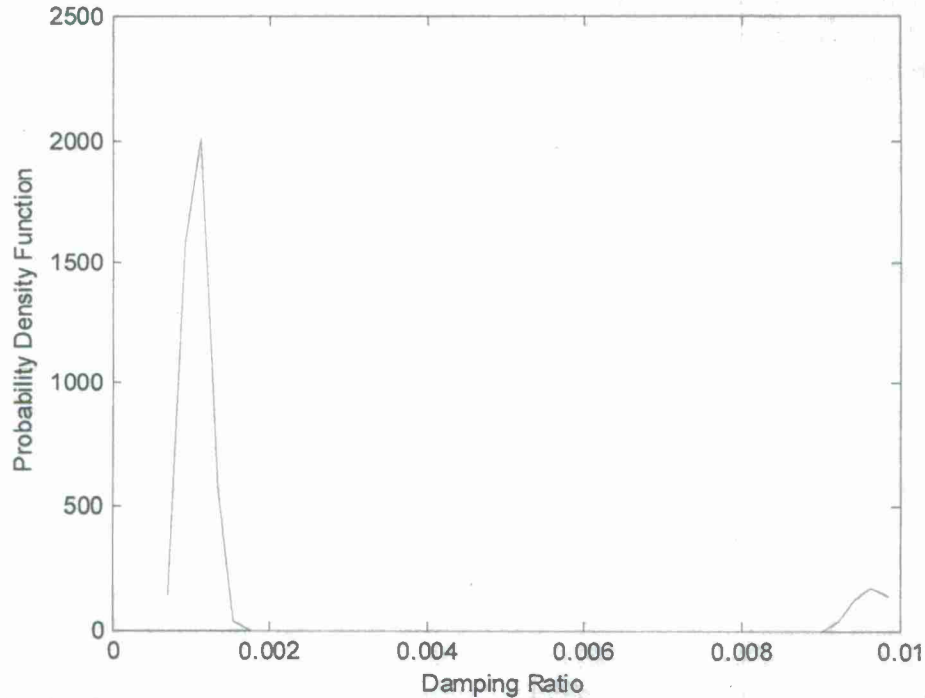


Figure 7.8. Probability density function of the random aeroelastic system response damping, two-piece linear model, 26 modes total, uncertainty in inboard mass.

Past results obtained when comparing the uncertainties in mass and stiffness in linear dynamical systems have usually demonstrated that there is little difference in the effects of these two sources of uncertainty. A rather different perspective is obtained from the present results shown in Figures 7.7 and 7.8 and their comparison with Figures 7.5-7.6. Indeed:

- (i) there were no recorded occurrence of flutter with uncertainty in inboard mass at the contrary of the uncertainty in stiffness. This observation, coupled with the usual perspective that there is only mild differences between uncertainties in mass and in stiffness suggests that the uncertain in mass of the *outboard* wing should be an important factor and will be considered in future efforts.
- (ii) the distributions of the frequency and damping ratio of Figures 7.7 and 7.8 are strongly bimodal suggesting that there are two slightly different flutter mechanisms that can take place with the occurrence of one or the other dictated by small changes of the inboard mass properties. Such an observation is unusual but has been reported before, e.g. in connection with the flutter of the Goland wing (see [7.1]).

The last application of the nonparametric methodology was on the one-piece nonlinear model used earlier. The consideration of stiffness uncertainty in geometrically nonlinear problems has been addressed extensively in [7.8] where it has been shown that the linear, quadratic, and cubic stiffness coefficients $K_{nj}^{(1)}$, $K_{njl}^{(2)}$, and $K_{njlp}^{(3)}$ can be regrouped to form a matrix $\underline{\underline{K}}_B$ which was shown [7.8] to be expected to be positive definite. In this paper, it was also recognized that negative eigenvalues could indeed occur due to difficulties in estimating accurately these stiffness coefficients, especially (see [7.9] and section 1 for discussion) when the structure is cantilevered, as the wing considered here. In accord with this earlier effort, it was in fact observed that the $\underline{\underline{K}}_B$ matrix was not positive definite. The simulation algorithm of [7.8] was then modified accordingly to split the $\underline{\underline{K}}_B$ matrix into positive and negative definite matrices, simulate with the same value of λ random positive and negative components, which were then summed to yield the final $\underline{\underline{K}}_B$ matrices. The random stiffness coefficients $K_{nj}^{(1)}$, $K_{njl}^{(2)}$, and $K_{njlp}^{(3)}$ were then extracted from these matrices as described in [7.8].

The ensemble of random stiffness coefficients $K_{nj}^{(1)}$, $K_{njl}^{(2)}$, and $K_{njlp}^{(3)}$ generated was then considered for the aeroelastic analysis at the same flight conditions as before. Owing to the long computational time involved in obtaining the final LCO level, the current Monte Carlo analysis focused only on the transient phase to assess which wing would flutter (and eventually converge to an LCO) and which one would not. The probability density functions of the frequencies and damping ratios observed during the transient phase by the population of wings are shown in Figures 7.9 and 7.10. These figures are in good agreement with those obtained in the linear model results of Figures 7.5-7.6 which is consistent with the expectation that the nonlinearity present here will not affect the stability of the wing but rather would limit the amplitude of response of those diverging, forcing them into an LCO behavior.

The various applications of the nonparametric methodology described above have well demonstrated the versatility of this approach for the consideration of structural uncertainty in aeroelastic systems including the complex morphing wing geometry investigated here.

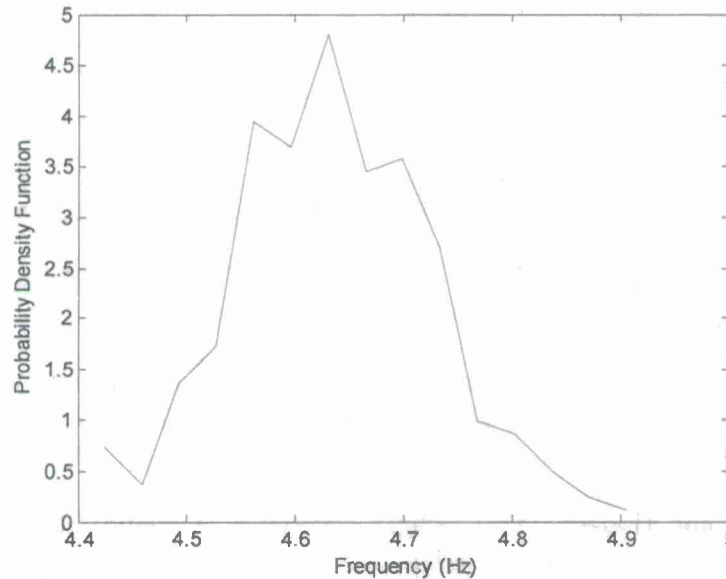


Figure 7.9. Probability density function of the random aeroelastic system response frequency, one-piece nonlinear model, 26 modes total, uncertainty in stiffnesses.

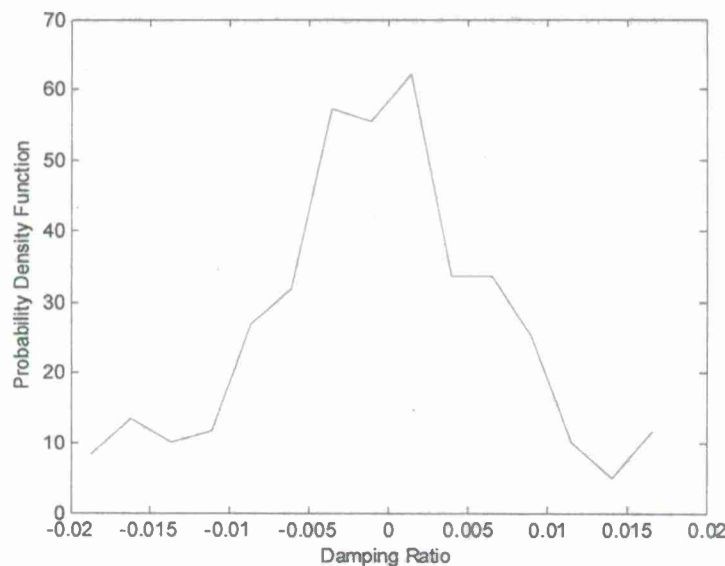


Figure 7.10. Probability density function of the random aeroelastic system response damping, one-piece nonlinear model, 26 modes total, uncertainty in stiffnesses.

Chapter 8.

REFERENCES

- [1.1] Craig, R.R. Jr., *Structural Dynamics: An Introduction to Computer Methods*, Wiley, 1981.
- [1.2] Muravyov, A.A., and Rizzi, S.A., "Determination of Nonlinear Stiffness with Application to Random Vibration of Geometrically Nonlinear Structures," *Computers and Structures*, Vol. 81, No. 15, pp. 1513–1523, 2003.
- [1.3] Kim, K., Wang, X.Q., and Mignolet, M.P., "Nonlinear Reduced Order Modeling of Functionally Graded Plates," *Proceedings of the 49th Structures, Structural Dynamics, and Materials Conference*, Schaumburg, Illinois, Apr. 7-10, 2008. AIAA Paper AIAA-2008-1873.
- [1.4] Patil, M.J., and Hodges, D.H., "Flight Dynamics of Highly Flexible Flying Wings," *Proceedings of the 2005 International Forum for Aeroelasticity and Structural Dynamics*, Munich, Germany, 2005.
- [2.1] D.H.Lee, Terrence A. Weisshaar, "Aeroelastic Studies on a Folding Wing Configuration", AIAA 2005-1996, 46th AIAA/ASME/ASCE/AHS/ASC Structures, Structural Dynamics & Materials Conference, Austin, Texas, April 2005
- [7.1] Mignolet, M.P., and Chen, P.C., "Aeroelastic Analyses with Uncertainty in Structural Properties," *Proceeding of the AVT-147 Symposium: Computational Uncertainty in Military Vehicle Design*, Athens, Greece, Dec. 3-7, 2007.
- [7.2] Soize, C., 2000, "A Nonparametric Model of Random Uncertainties on Reduced Matrix Model in Structural Dynamics," *Probabilistic Engineering Mechanics*, Vol. 15, No. 3, pp. 277-294.
- [7.3] Soize, C., 2001, "Maximum Entropy Approach for Modeling Random Uncertainties in Transient Elastodynamics," *Journal of the Acoustical Society of America*, Vol. 109, No. 5, pp. 1979-1996.
- [7.4] Mignolet, M.P., and Soize, C., 2008, "Nonparametric Stochastic Modeling of Linear Systems with Prescribed Variance Information of Several Natural Frequencies," *Probabilistic Engineering Mechanics*, Vol. 23, Nos. 2-3, pp. 267-278.
- [7.5] Soize, C., 2005, "Random Matrix Theory for Modeling Uncertainties in Computational Mechanics," *Computer Methods in Applied Mechanics and Engineering*, Vol. 194, pp. 1333-1366.
- [7.6] Soize, C., "Non-Gaussian Positive-Definite Matrix-Valued Random Fields for Elliptic Stochastic Partial Differential Operators," *Computational Methods in Applied Mechanics and Engineering*. Vol. 195, pp. 26–64, 2006.
- [7.7] Murthy, R., Mignolet, M.P., and El-Shafei, A., "Nonparametric Stochastic Modeling of Structural Uncertainty in Rotordynamic Systems," *Proceedings of the IGTI Turbo Expo '09*, Orlando, Florida, Jun. 8-12, 2009, ASME Paper GT-2009-59700. *Journal of Engineering for Gas Turbines and Power*, in press.

- [7.8] Mignolet, M.P., and Soize, C., 2008, "Stochastic Reduced Order Models for Uncertain Nonlinear Dynamical Systems," *Computer Methods in Applied Mechanics and Engineering*, Vol. 197, pp. 3951-3963.
- [7.9] Kim, K., Khanna, V., Wang, X.Q., and Mignolet, M.P., "Nonlinear Reduced Order Modeling of Flat Cantilevered Structures," *Proceedings of the 50th Structures, Structural Dynamics, and Materials Conference*, Palm Springs, California, May 4-7, 2009. AIAA Paper AIAA-2009-2492.

Chapter 9.

PERSONNEL SUPPORTED

ZONA Technology, Inc.

1. Mr. Ping-Chih Chen (PI)
2. Dr. Danny D. Liu
3. Dr. Shuchi Yang
4. Dr. Zhicun Wang
5. Dr. Zhichao "Jack" Zhang

Arizona State University

6. Dr. Marc Mignolet (University Co-PI)
7. Dr. X.Q. (Julian) Wang
8. Mr. Vishal Khanna

University of California, Irvine

9. Dr. Feng Liu (Consultant)

University of Florida

10. Sean Regisford (Consultant)

Chapter 10.

PUBLICATIONS

- **Archive Journal Papers & Dissertation**

None.

- **Proceeding Papers/Conference Presentations**

Liu, D.D., Chen, P.C., Zhang, Z., Wang, Z., Lee, D.H., Mignolet, M.P., and Liu, F., "Continuous Dynamic Simulation of Nonlinear Aerodynamic/Nonlinear Structure Interaction (NANSI) for Morphing Vehicles" *Presented at the Aerospace Flutter and Dynamics Council Meeting*, October 2007 Boston.

Liu, D.D., Wang, Z., Yang, S., Cai, C., and Mignolet, M., "Nonlinear Aeroelastic Methodology for A Membrane-on-Ballute Model with Hypersonic Bow Shock" *Presented at the Aerospace Flutter and Dynamics Council Meeting*, San Antonio, TX, May 22 – 23, 2008.

Liu, D.D., Chen, P.C., Wang, Z., Yang, S., Zhang, Z., "Aeroelastic ROM-ROM Methodology," *Presented at the Workshop on Aeroelastic Certification: Tools, Test, Decision Making*, Sedona, AZ, October 28 – 29, 2008.

Mignolet, M.P., Wang, X.Q. (Julian), Kim, K., and Khanna, V., "Reduced Order Modeling For Geometrically Nonlinear Structural Dynamic Problems," *Presented at the Workshop on Aeroelastic Certification: Tools, Test, Decision Making*, Sedona, AZ, October 28 – 29, 2008.

Liu, D.D., Chen, P.C., Mignolet, M., and Liu, F., "Morphing Wing Aeroelasticity by Continuous Dynamic Simulation using Nonlinear Aerodynamic/Nonlinear Structure Interaction (NANSI) Methodology" *Abstract submitted to AVT-168 Symposium on Morphing Vehicles*, Lisbon, Portugal. 20-24 April 2009.

Chapter 11.

INTERACTIONS/TRANSITIONS

- a) Participation/presentations at meetings, conferences, seminars, etc.
None.
- b) Consultative and advisory functions to other lab and agencies:
None.
- c) Transitions
None.

Chapter 12.

NEW DISCOVERIES, INVENTIONS, OR PATENT DISCLOSURES

None

Chapter 13.

HONORS/AWARDS

None

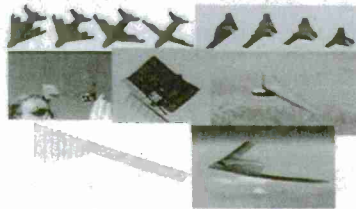
Attachment A

Continuous Dynamic Simulation of Nonlinear Aerodynamic/Nonlinear Structure Interaction (NANSI) for Morphing Vehicles

***Presented at Aerospace Flutter and Dynamics Council Meeting,
October 2007 Boston***

Continuous Dynamic Simulation of Nonlinear Aerodynamic/Nonlinear Structure Interaction (NANSI) for Morphing Vehicles

Topic #: AF06-T016, Proposal #: F064-016-0261, Contract #: FA9550-06-C-0070



Small Business:

ZONA Technology, Inc.

D.D. Liu, P.C Chen, Z. Zhang,
Z. Wang and D.H. Lee

Research Institute:

University of California, Irvine

Prof. Feng Liu

Consultant:

Prof. Marc Mignolet

Prepared AFOSR STTR Phase I Kickoff Meeting at AFOSR Base, Arlington, VA 22203, November 17, 2006

9489 E. Ironwood Square Drive, Scottsdale, AZ 85258, Tel. (480) 945-9988, Fax (480) 945-6588, E-mail: danny@zonatech.com

Phase I Technical Objectives

- Overall Objective:
 - Develop a predictive capability for the aeroelastic behavior of aircraft undergoing continuous morphing.
- Specific Objectives:
 - Develop a general methodology for the assembly of nonlinear reduced order models (ROM) of the multiple contacting substructures that provide the morphing.
 - Extend the existing 2D Gridless Boundary Condition on Cartesian grid (GBCC)/Euler method to 3D.
 - Integrate the novel nonlinear structural ROM assembly approach, the extended 3D GBCC/Euler method, and ZONA's Fluid-Structure grid interface method (BEM solver) into a new nonlinear aeroelastic methodology namely, the *Nonlinear Aerodynamics and Nonlinear Structural Interaction (NANSI) solver*.



Technical Challenges

- **CFD Grid crossover due to morphing and/or large structural deformation**
 - Morphing vehicles involve large dynamic deformation of surface geometry.
 - Conventional deforming grid methods will fail at a point when the geometry change becomes large, no matter how good the method may work for aeroelastic simulation where the change in vehicle shape is relatively small.
 - Our solution is the Gridless Boundary Condition on Cartesian grid (BGCC) method.
- **Nonlinear structural effects due to large elastic deformation**
 - In order to fully utilize the structural design of morphing aircraft, the occurrence of large elastic deformation, is expected, at least part of the time.
 - Direct coupling of a nonlinear FEM with CFD is computationally costly.
 - Our solution is the reduced order modeling (ROM) of a given FE model.
- **Morphing Dynamics using continuous approach**
 - The major difference between the aeroelastic handling of a fixed wing and a morphing wing lies in that the latter has an additional time scale due to relative motion of wing components in morphing.
 - Morphing structures involve multi-body dynamics.
 - Our solution is the *sub-structuring technique* with compatibility at interface.

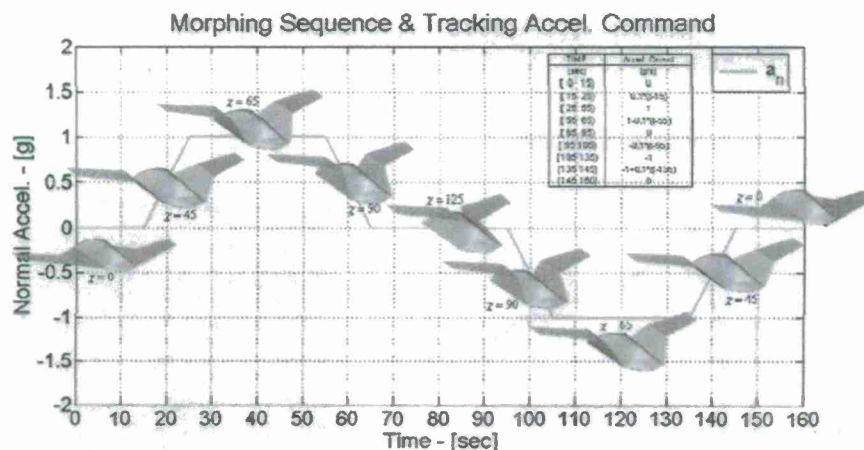


3

2022/06/08 11:17:08



Continuously Morphing Folding Wing in Time Domain



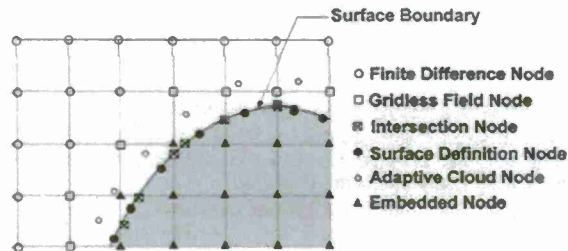
4

2022/06/08 11:17:08



Gridless Boundary Condition Treatment

- The gridless boundary method considers least squares curve fits of nodes near the surface to establish flow property gradients
- Various types of nodes are considered to obtain the fitting of flux variables near the surface boundary



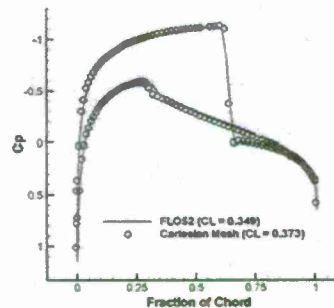
5

ZPC220NANO/Exhaust-Ducts-Prod111709 ZONA TECHNOLOGY

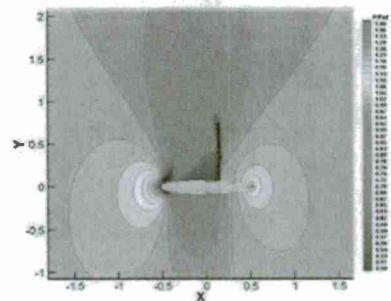
GBCC/Euler vs. Body-Fitted Grid/FLO52

- Flow Field for NACA 0012 airfoil at $M=0.8$, $\alpha=1.25^\circ$ using Boundary Gradient Method

Surface Pressure Coefficient

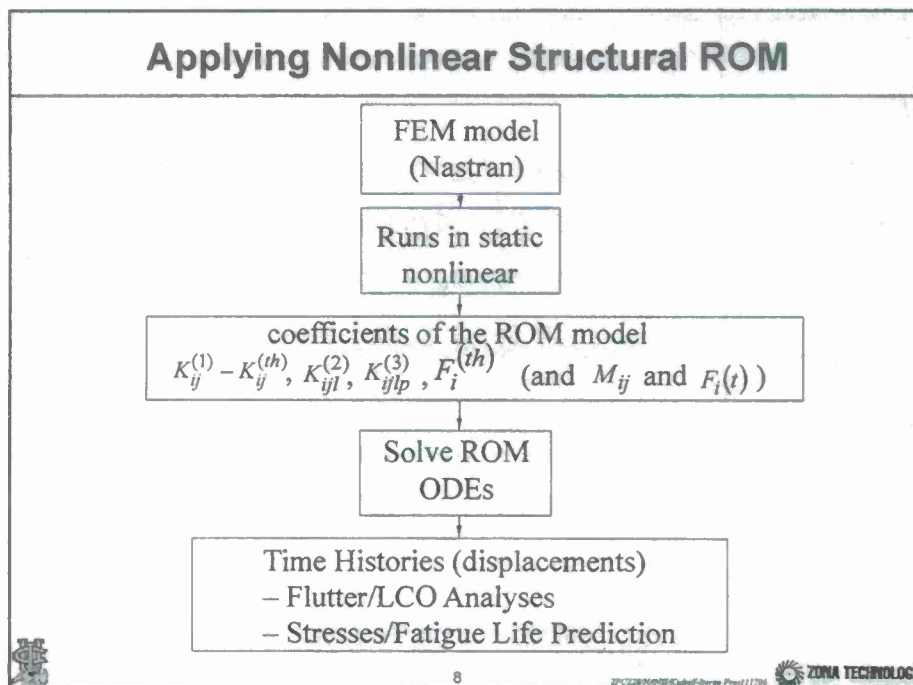
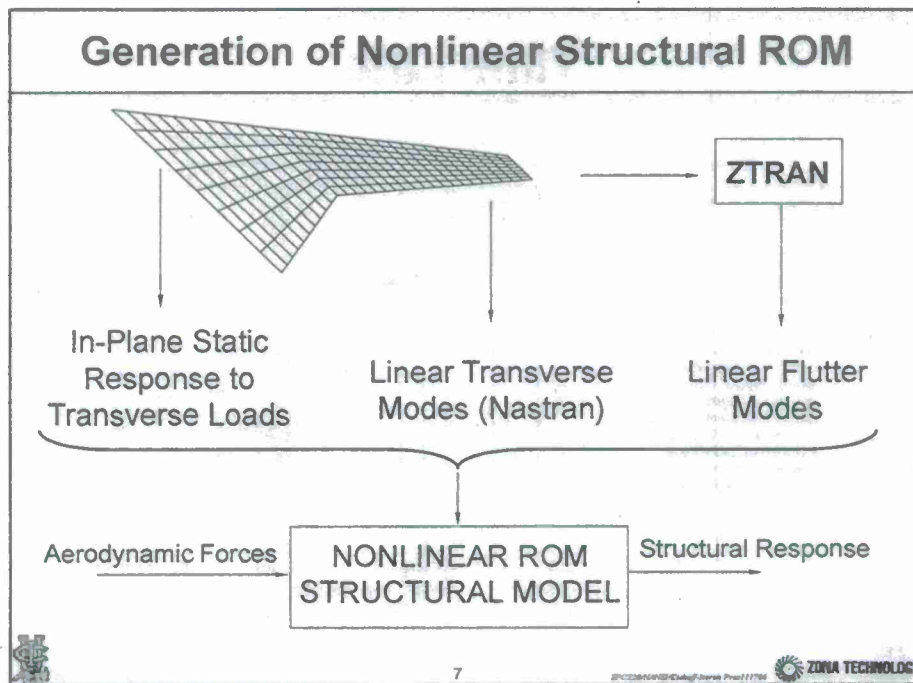


Flow Field Pressure Ratio

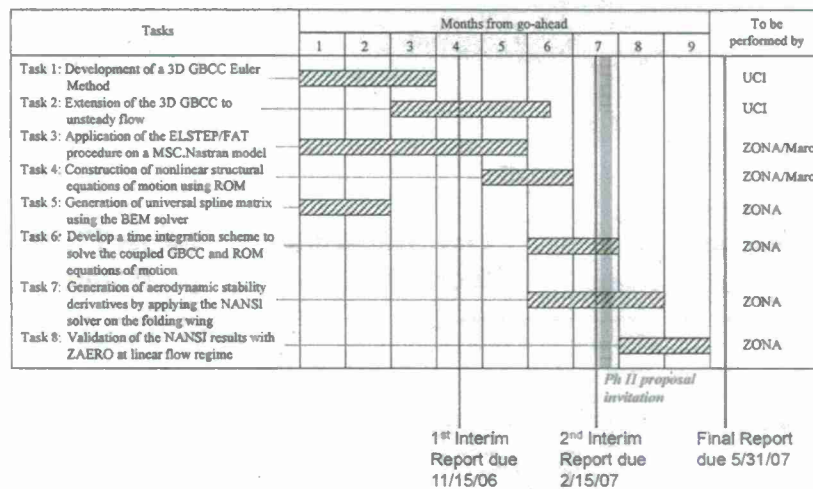


6

ZPC220NANO/Exhaust-Ducts-Prod111709 ZONA TECHNOLOGY



Time Line



9

2PC228NANSI/Kickoff/Review/Print/11/06



Gridless Boundary Condition on Cartesian Grid: the GBCC/CFD Approach for Dynamic Morphing Wings

Topic: AF06-T016, Proposal #: F064-016-0261, Contract #: FA9550-06-C-0070

Research Institute:

University of California, Irvine

Prof. Feng Liu

Prepared AFOSR STTR Phase I Kickoff Meeting at AFOSR Base, Arlington, VA 22203, November 17, 2006

9489 E. Ironwood Square Drive, Scottsdale, AZ 85258, Tel. (480) 945-8988, Fax (480) 945-8588, E-mail: danny@zonatech.com

Gridless-Boundary- conditions-Cartesian (GBCC) Grid Method

Motivation

To seek an accurate and efficient method for aeroelastic computations with minimal effort associated with grid generation and maximum flexibility in handling large structural deformation.

For this purpose, we look back at the different grid strategies



11

ZONA TECHNOLOGY

Comparison of Mesh Strategies

- Cartesian mesh
 - Earliest grid strategy for finite-difference
 - Easiest to generate
 - Lowest computational storage and operational count needed per grid point.
 - Zero grid distortion.
 - Ease in implementation of higher order schemes.
 - Does not conform to curved walls, difficult and inaccurate in the implementation of boundary conditions.



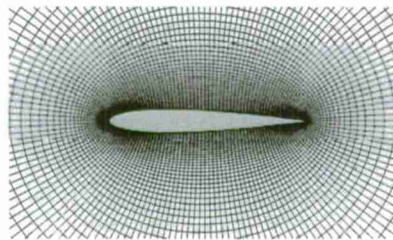
12

ZONA TECHNOLOGY

Comparison of Mesh Strategies

Structured body-fitted mesh

- Conforms to curving walls, facilitates easy and accurate implementation of boundary conditions.
- Difficult or even impossible to generate for complex geometries and topologies, even with multiple blocks, and overset grids do not offer a clean and effective solution.
- Generally non-orthogonal, skewed, stretched, adversely affecting computational efficiency and accuracy.
- Moving mesh algorithms will fail for large deformations



13

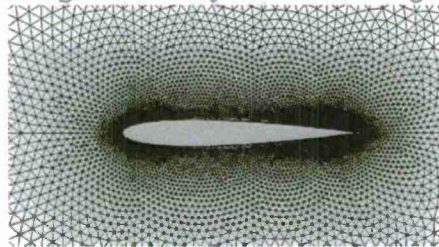
SPC2804002/Edoardo D'Amico Prof.11/708



Comparison of Mesh Strategies

Unstructured body-fitted mesh

- Conforms to curving walls, facilitates easy and accurate implementation of boundary conditions.
- Easier to generate for complex geometries compared to structured grids.
- Needs more memory and CPU time compared to a structured grid method.
- Quality of mesh is still a major issue affecting efficiency and accuracy.
- Moving mesh algorithms may still fail for large deformations.



14

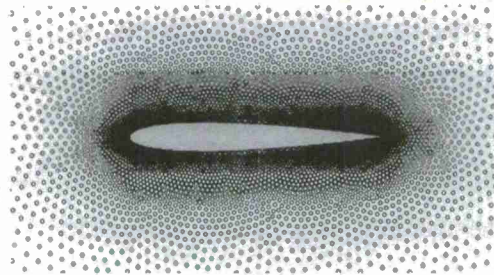
SPC2804002/Edoardo D'Amico Prof.11/708



Comparison of Mesh Strategies

Gridless/meshless

- Removes the fundamental difficulties with all previous mesh strategies: need to maintain an explicit connectivity. Instead uses clouds of nodes devoid of explicit connectivity.
- In principle, easiest to generate for any arbitrary moving/non-moving geometries.
- Uses least-squares, needs most memory and CPU time.
- In practice, accuracy sensitive to distribution of points.
- Conservation and accuracy issues with discontinuities.



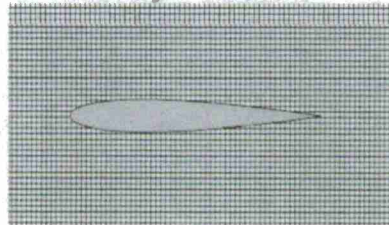
15

SPCZERNANOWSKI/Kubacki/Torres/Pratt/11706 ZONA TECHNOLOGY

Comparison of Mesh Strategies

Cartesian Grids

- Earliest grid strategy for finite-difference
- Easiest to generate.
- Lowest computational storage and operational count needed per grid point.
- Zero grid distortion.
- Ease in implementation of higher order schemes.
- Does not conform to curving walls, difficult and inaccurate in the implementation of boundary conditions.



16

SPCZERNANOWSKI/Kubacki/Torres/Pratt/11706 ZONA TECHNOLOGY

Comparison of Mesh Strategies

- The Key is: treatment of boundary conditions.
- We will distinguish two classes of applications
 - Flutter or aeroelasticity involving relatively small structural deformations
 - Aeroelastic problems involving large deformations, eg. Morphing wing.
- For the first class of applications, we propose a small perturbations boundary condition method: Euler+IBL.
- For the second class of applications, we propose a gridless boundary condition method: GBCC.

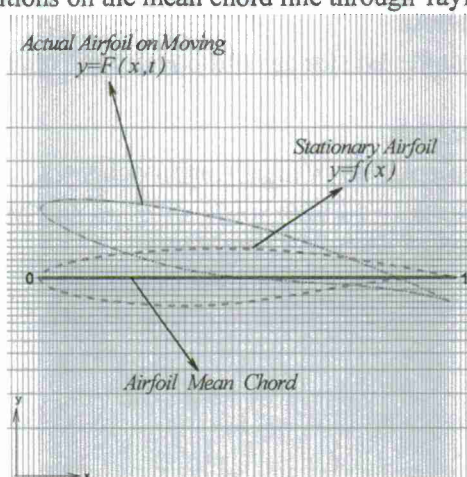


17

ZONIA TECHNOLOGY

Non-Moving Cartesian Grids Using Approximate Boundary Conditions

Boundary conditions on the actual moving airfoil is represented by boundary conditions on the mean chord line through Taylor expansions.



18

ZONIA TECHNOLOGY

EULER and EULER + IBL On Non-Moving Cartesian Grid (Replacing CAPTSD)

References:

1. Gao, C., Yang, S., Luo, S., Liu, F., and D.M. Schuster, "Calculation of Airfoil Flutter by an Euler Method with Approximate Boundary Conditions," AIAA Journal, Vol. 43, No. 2, pp. 295-305, 2005.
2. Zhang, Z., Liu, F., and Schuster, D.M., "Calculations of Unsteady Flow and Flutter by an Euler and Integral Boundary-Layer Method on Cartesian Grids," AIAA-2004-5203
3. Zhang, Z., Yang, S., Liu, F., and Schuster, D.M., "Prediction of Flutter and LCO by an Euler Method on Non-moving Cartesian Grids with Boundary-Layer Corrections," AIAA-2005-0833
4. Zhang, Z., Liu, F., and Schuster, D.M., "An Efficient Euler Method on Non-Moving Cartesian Grids with Boundary-Layer Correction for Wing Flutter Simulations," AIAA-2006-0884



GBCC Gridless Boundary Condition Cartesian Grid Method

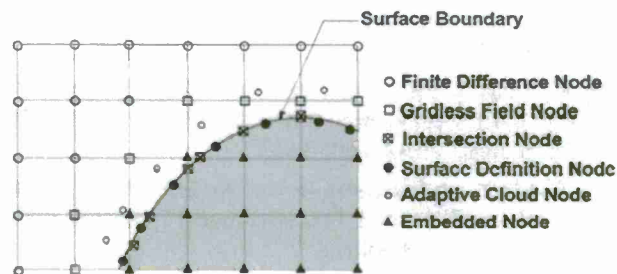
We propose the use of a non-moving Cartesian mesh with a gridless method for treating boundary conditions.

Such an approach retains all the benefits of the Cartesian mesh and eliminates issues associated with surface boundary treatment



Gridless Boundary Condition Treatment

- The gridless boundary method considers least squares curve fits of nodes near the surface to establish flow property gradients
- Various types of nodes are considered to obtain the fitting of flux variables near the surface boundary

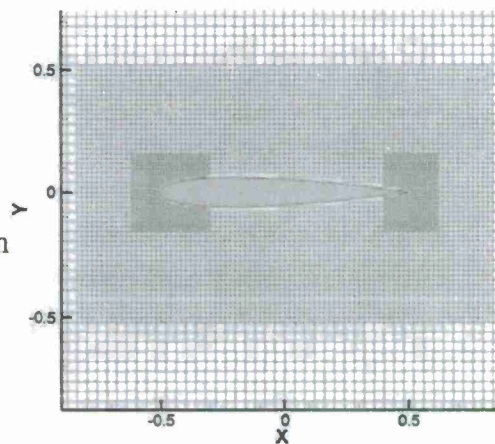


21

ZONA TECHNOLOGY

Embedded Multigrid Cartesian Mesh Topology

- This “structured” topology allows for efficient storage of grid connectivity and multigrid implementation for local grid refinement and convergence acceleration.

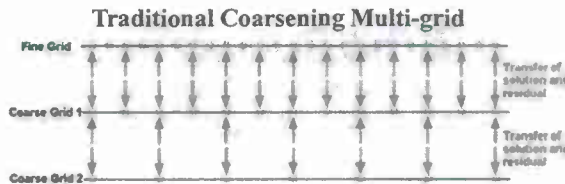


22

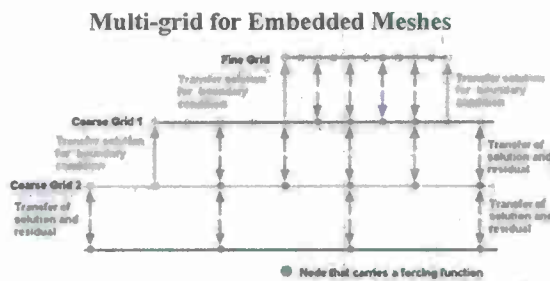
ZONA TECHNOLOGY

Multigrid for Embedded Meshes

- The implementation of multigrid for the embedded grid hierarchy considered here is slightly different from the traditional approach



- In lieu of coarsening the entire domain, multigrid acceleration is achieved using the portion of coarser grid that extends "below" a finer one



23

SPCZORNA/ISO-Kuchel-Sturm-Proz111708 ZONA TECHNOLOGY

Moving Boundary Conditions

Moving boundary conditions can be implemented either by

- Using the same small perturbation expansions as before but without the thin-wing approximation. This can be easily implemented through the use of time-dependent shape functions for the gridless boundary points namely, \tilde{y} .
- Re-calculating the locations and the associated shape functions of the gridless points around the moving boundaries. No restriction on small deformation. Since searching is needed for a small number of points and based on previous locations, the computational time needed is small.



24

SPCZORNA/ISO-Kuchel-Sturm-Proz111708 ZONA TECHNOLOGY

Details and Various Implementation of GBCC

- Kirshman, D.J., and Liu, F., "A Gridless Boundary Condition Method for the Solution of the Euler Equations on Embedded Cartesian Meshes with Multigrid," Journal of Computational Physics, Vol. 201, No. 1, pp. 119-147, Nov., 2004..
- Koh, E.P.C., Tsai, H.M., and Liu, F., "Euler Solution Using Cartesian Grid with a Gridless Least Squares Boundary Treatment," AIAA Journal, Vol. 43, No. 2, pp.246-255, 2005.
- Kirshman, D.J., and Liu, F., "Flutter Prediction by a Cartesian mesh Euler Method with Small Perturbation Gridless Boundary Conditions," Computers and Fluids, Vol. 35, no. 6, pp. 571-586, 2006.
- Luo, H., Baum J.D., and Lohner, R. "A Hybrid Cartesian Grid and Gridless Method for Compressible Flows," AIAA 2005-0492, also in J. of Computational Physics.
- Lai, K.L., Koh E.P.C., and Tsai, H.M., "Flutter Computations of Complex Configurations Using Cartesian Grids," AIAA-2006-1399.



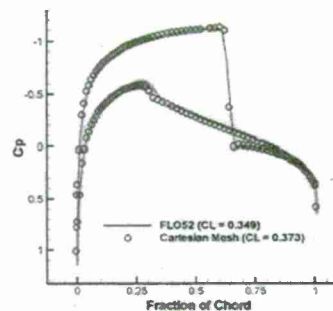
25

ZONA TECHNOLOGY

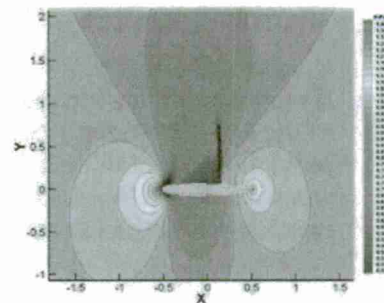
Example: Steady Transonic Flow About NACA 0012

- Flow Field for NACA 0012 airfoil at $M=0.8$, $\alpha=1.25^\circ$ using Boundary Gradient Method

Surface Pressure Coefficient



Flow Field Pressure Ratio



26

ZONA TECHNOLOGY

3D Gridless Formulation

- Euler/NS Equation: $\frac{\partial U}{\partial t} + \frac{\partial F}{\partial x} + \frac{\partial G}{\partial y} + \frac{\partial H}{\partial z} = 0$
- Least-squares shape functions can be constructed to interpolate F , G , and H , e.g.

$$F(x, y, z) = \sum_{n=1}^N \phi_n(x, y, z) F_n$$

$$\text{Thus } \frac{\partial F}{\partial x} = \sum_{n=1}^N \frac{\partial \phi_n}{\partial x} F_n$$

- Similarly we can construct $\frac{\partial G}{\partial y}$ and $\frac{\partial H}{\partial z}$
for both the inviscid and viscous fluxes



29

ZONA TECHNOLOGY

Condition for Wall Points

- Least-squares formulas are also constructed to extrapolate density and pressures from interior points to wall points.
- Zero normal velocity is enforced for the Euler equations.
- Zero velocity is enforced for the N-S equations.
- The 3D GBC method is implemented in an independent module, that can be used in any main CFD code.



30

ZONA TECHNOLOGY

Summary

- The GBCC method offers great potential for time-domain simulation of coupled nonlinear structure and nonlinear aerodynamics simulations with the best balances among computational speed, solution accuracy, and ease in handling structures with large deformation as in the case of a morphing wing.
- GBCC = Cartesian Euler +GBC. The 3D Cartesian Euler part has been developed and is called CartEuler. The GBC part is being extended from 2D to 3D as a separate module.



31

SPONSORED BY AFOSR STTR Phase I Kickoff Meeting



Nonlinear Structural Dynamics: ROM, Nonlinear FEM, and ELSTEP/FAT

Topic: AF06-T016, Proposal #: F064-016-0261, Contract #: FA9550-06-C-0070

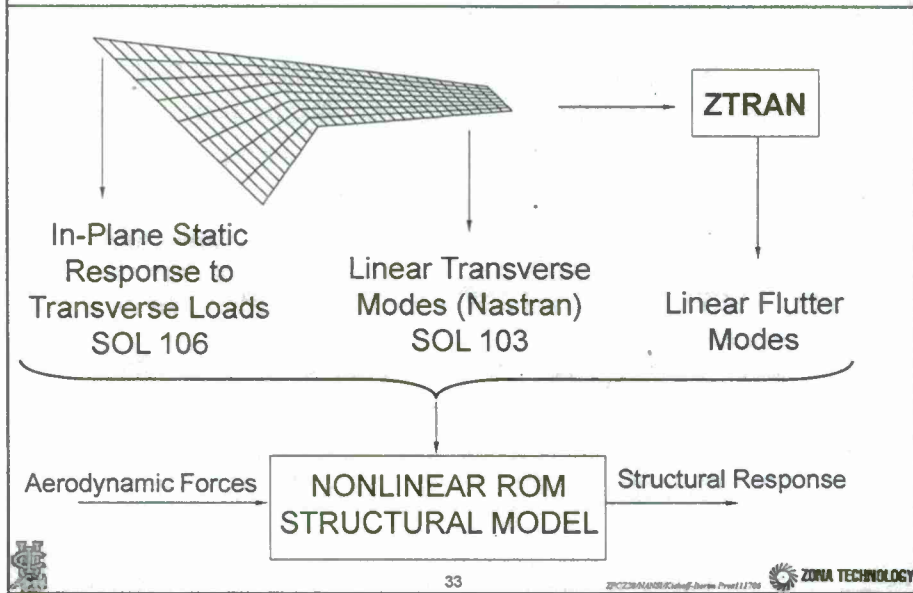
Consultant:

Prof. Marc Mignolet

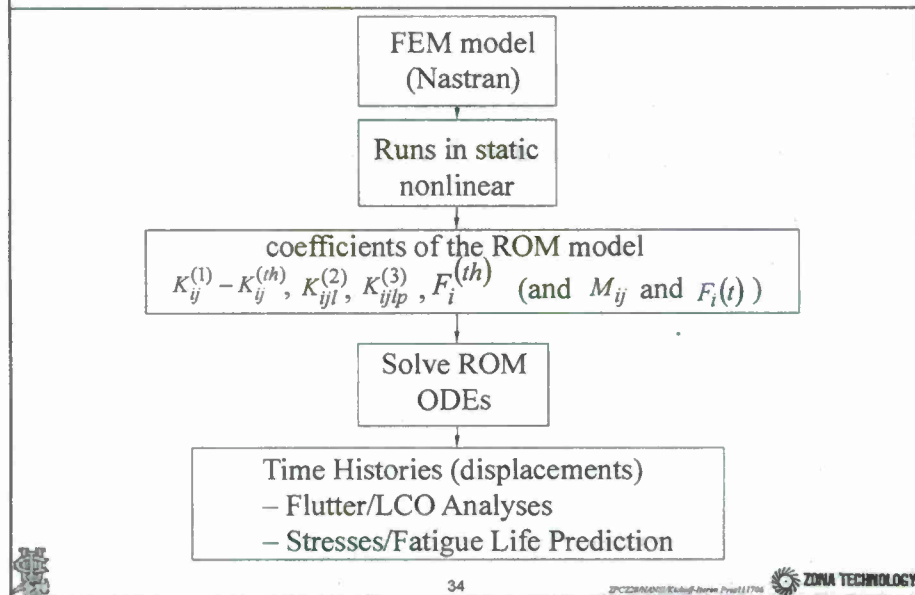
Prepared AFOSR STTR Phase I Kickoff Meeting at AFOSR Base, Arlington, VA 22203, November 17, 2006

9489 E. Ironwood Square Drive, Scottsdale, AZ 85258, Tel. (480) 945-9988, Fax (480) 945-6588, E-mail: danny@zonatech.com

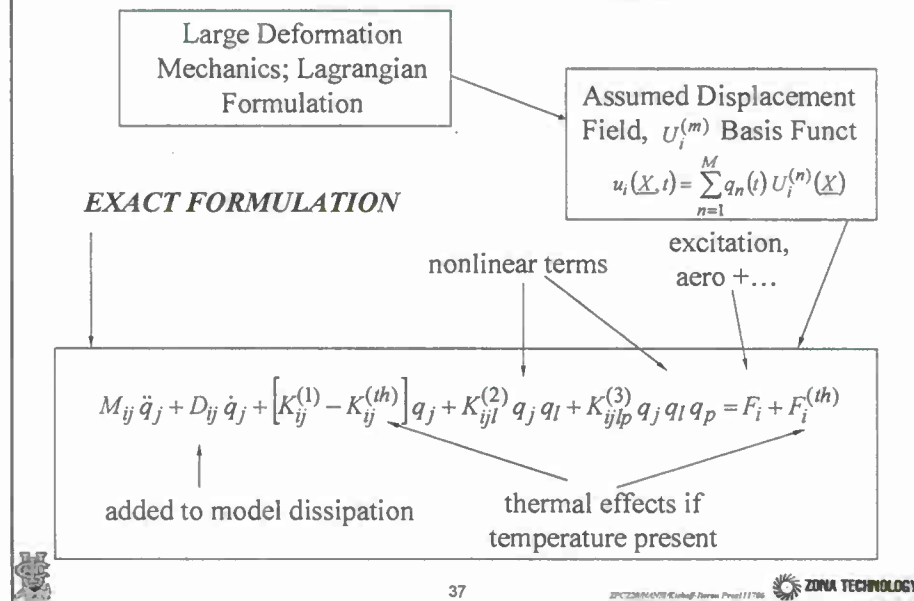
Generation of Nonlinear Structural ROM



Applying Nonlinear Structural ROM



What is ELSTEP ? Nonlinear ROM Procedure



ELSTEP Procedure

Three ingredients are necessary to obtain a reduced order model:

- (1) structure with boundary conditions, temperature, ...
- (2) basis functions $U_i^{(m)}$ (Linear modes/flutter mode, static disp.)
- (3) an approach to evaluate the coefficients of the ROM, i.e

$$K_{ij}^{(1)} - K_{ij}^{(th)}, K_{ijl}^{(2)}, K_{ijlp}^{(3)}, F_i^{(th)} \text{ (and } M_{ij} \text{ and } F_i(t) \text{)}$$

ELSTEP/FAT: ZONA/ASU code:

FEM model
of (1)
(Nastran)

+

(2)

→

(3)

solve ROM
ODEs

time histories:

- * displacements
- * velocities
- * stresses
- fatigue life



38

SPC228/NASTRAN/Elstep/Nastran/Pre111786

ZONA TECHNOLOGY

Nonlinear Structural Dynamic ROM (III)

Reduce Order Modeling (ROM) Strategy

Assume a displacement representation

$$u_i(\underline{X}, t) = \sum_{n=1}^M q_n(t) U_i^{(n)}(\underline{X})$$

$U_i^{(m)}$, $q_n(t)$ basis functions ("modal" basis, time independent satisfy the essential B.C. on $\partial\Omega_0^u$), generalized coordinates (time dependent)

Using the weak form of the equations of motion + boundary cond.

$$M_{ij} \ddot{q}_j + D_{ij} \dot{q}_j + \left[K_{ij}^{(1)} - K_{ij}^{(th)} \right] q_j + K_{ijl}^{(2)} q_j q_l + K_{ijlp}^{(3)} q_j q_l q_p = F_i + F_i^{(th)}$$

↑
added to model dissipation

thermal effects



45

ZONA TECHNOLOGY

Nonlinear Structural Dynamic ROM (IV)

General Procedure: Impose a series of static deflections and determine (e.g. from finite element model) the forces required and the stresses. Then, identify the coefficients of the reduced order model.

$$\begin{aligned} u_i &= q_j U_i^{(j)} & F_{1i} &= \left[K_{ij}^{(1)} - K_{ij}^{(th)} \right] q_j + K_{ijj}^{(2)} q_j^2 + K_{ijjj}^{(3)} q_j^3 \\ u_i &= -q_j U_i^{(j)} & F_{2i} &= -\left[K_{ij}^{(1)} - K_{ij}^{(th)} \right] q_j + K_{ijj}^{(2)} q_j^2 - K_{ijjj}^{(3)} q_j^3 \end{aligned}$$

$$K_{ijj}^{(2)} = \frac{F_{1i} + F_{2i}}{2 q_j^2}$$

$$\begin{aligned} u_i &= \hat{q}_j U_i^{(j)} & \longrightarrow & K_{ij}^{(1)} - K_{ij}^{(th)}, K_{ijjj}^{(3)} \\ \left. \begin{aligned} u_i &= q_j U_i^{(j)} + q_l U_i^{(l)} \\ u_i &= q_j U_i^{(j)} - q_l U_i^{(l)} \\ u_i &= q_j U_i^{(j)} + q_l U_i^{(l)} + q_p U_i^{(p)} \end{aligned} \right\} & \longrightarrow & K_{ilj}^{(2)}, K_{iljj}^{(3)} \\ & & & K_{iljp}^{(3)} \end{aligned}$$



46

ZONA TECHNOLOGY

Nonlinear Structural Dynamic ROM (V)

How should the basis functions $U_i^{(m)}$ be selected?

These basis functions should include the basis functions for linear motions ("linear basis", e.g. linear modes) but this is not sufficient.

Possibilities (both available in ELSTEP/FAT)

- (1) include a broad range of linear mode shapes (typically) that do not get excited in linear motions. Convergence is assured with increasing number of modes but the size of the model may be very large.
- (2) use "dual modes" (ASU/ZONA) related to AFRL companion modes

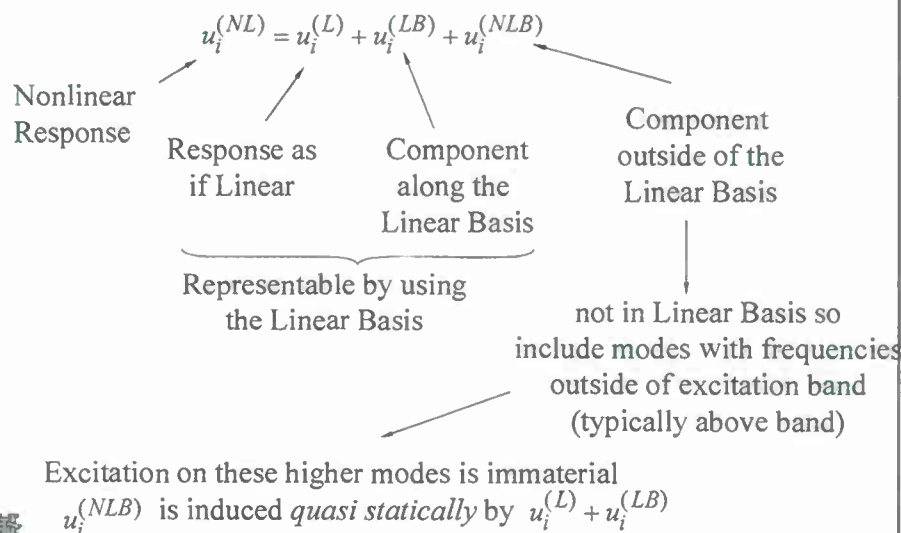


47

SPCZERNANSE Exchange Forum Press 11/706 ZONA TECHNOLOGY

Nonlinear Structural Dynamic ROM (VI)

"Dual Modes":



48

SPCZERNANSE Exchange Forum Press 11/706 ZONA TECHNOLOGY

Nonlinear Structural Dynamic ROM (VII)

Thus,

$$u_i^{(NLB)} = f(u_i^{(LB)} + u_i^{(LB)})$$

no time present in functional dependence → same as would be in static problems.

The basis to describe the component $u_i^{(NLB)}$ (i.e. the dual modes) is obtained by creating a series of “typical” static nonlinear problems such that their linear solutions would be completely included in the Linear Basis. The dual modes are then created from these solutions by eliminating the components of these nonlinear solutions in the Linear Basis.



49

ZONA TECHNOLOGY

Progress to Date

- Folding Wing Aeroelastic Analyses
- CartEuler Validation
- Flutter Solutions with Linear Structure
- Validations with ZTRAN/ZAERO
- Flutter/LCO Solutions with Nonlinear Structure
- Some Preliminary Conclusions

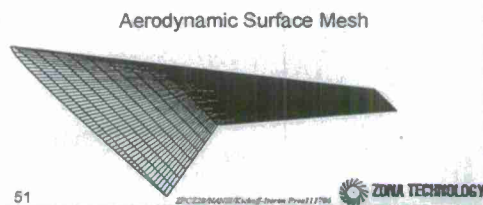
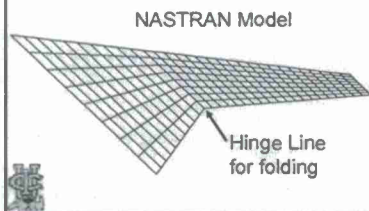
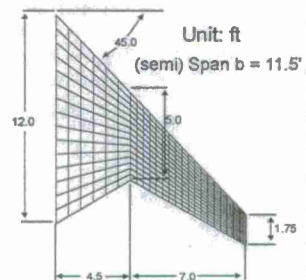


50

ZONA TECHNOLOGY

Feasibility Studies on Folding Wing

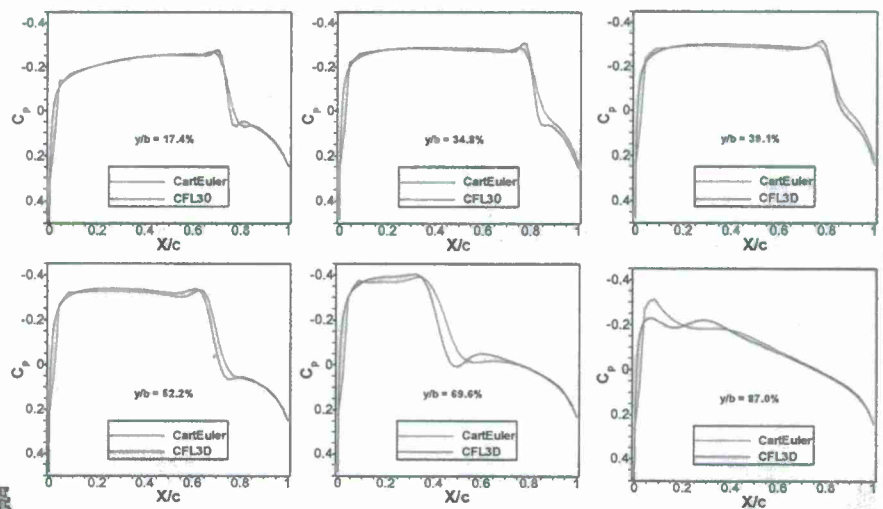
- The selected folding wing is the morphing UAV designed by Lockheed Martin Aeronautics (LM Aero).
- The structural model is a simplified plate model consisting of 240 CQUAD4 elements.
- Natural frequencies of Modes 1, 2, 3 are respectively 2.81, 10.57, 21.81 Hz
- The airfoil section is NACA64-006. The aerodynamic surface mesh consists of 49 x 25 grid points.
- Cartesian Euler Code (CartEuler) developed by the ZONA/UCI team is coupled with Nonlinear Structural ROM for nonlinear aeroelastic analysis with large elastic deformations.



51

Validation of CartEuler with CFL3D/Euler Folding Wing with NACA 0006 Section

$M = 0.95$, $\alpha = 0^\circ$, Span $b = 11.5'$

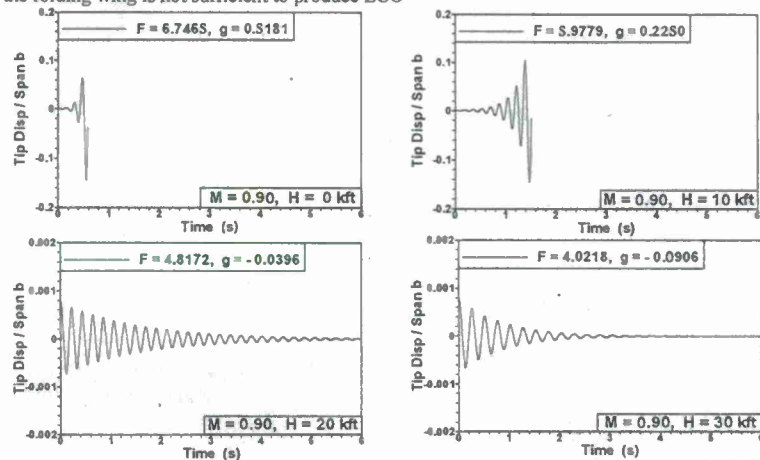


52

Aeroelastic Analysis with Linear Structures (I)

Folding Wing at $M = 0.9$, $\alpha = 0^\circ$, Span $b = 11.5'$

- According to Auto-Regressive Moving Average (ARMA) model using the damping (g) and frequency (F), flutter is determined at altitude $H = 18.4$ Kft and $F = 5.0$ Hz
- No LCO is found in the post-flutter regions, showing that the nonlinear aerodynamics alone on the folding wing is not sufficient to produce LCO



53

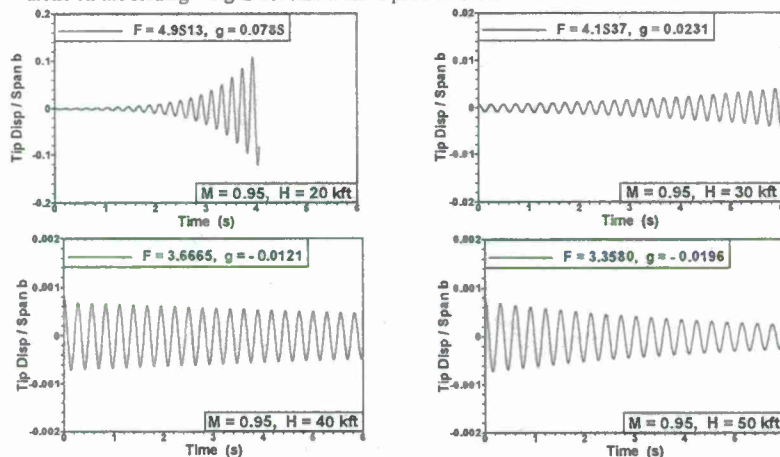
2PC23804000/Cadsoft-Inventor Pro v11.1700

ZONA TECHNOLOGY

Aeroelastic Analysis with Linear Structures (II)

Folding Wing at $M = 0.95$, $\alpha = 0^\circ$, Span $b = 11.5'$

- According to ARMA, flutter is determined at $H = 38$ Kft and $F = 3.76$ Hz
- Again, no LCO is found in the post-flutter regions, showing that the nonlinear aerodynamics alone on the folding wing is not sufficient to produce LCO



54

2PC23804000/Cadsoft-Inventor Pro v11.1700

ZONA TECHNOLOGY

Flutter Solutions with Linear Structures Validation of CartEuler with Other Methods

Folding Wing at $M = 0.9, 0.95, \alpha = 0^\circ$, Span $b = 11.5'$

- ZTRAN: Transonic Field-Panel method using steady CFL3D/Euler solution as its background flow.
- ZONA6: Linear Unsteady Panel method.

Mach Number	Flutter Altitude (Kft)			Flutter Frequency (Hz)		
	CartEuler	ZTRAN	ZONA6	CartEuler	ZTRAN	ZONA6
0.95	38.0	36.2	19.7	3.76	3.74	4.815
0.90	18.40	16.0	12.1	5.00	5.09	5.4

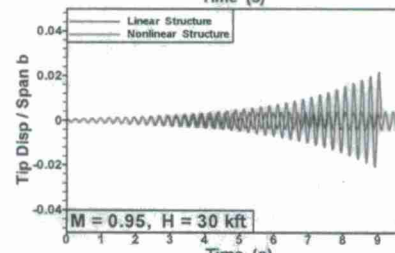
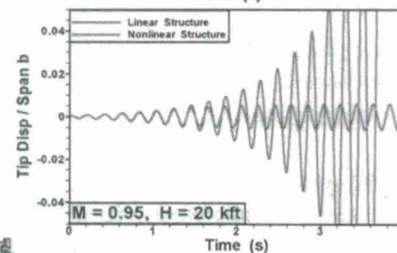
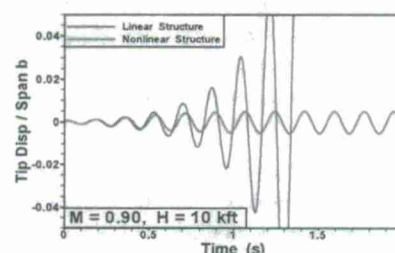
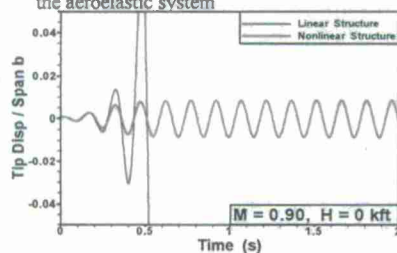


55

ZONA TECHNOLOGY

Post-Flutter Analysis with Nonlinear Structural ROM

- With Nonlinear Structural ROM, LCO in the post-flutter regions is obtained
- LCO amplitude increases as the altitude decreases
- Clearly, this LCO is mainly induced by the structural nonlinearity that provides stiffening effects to the aeroelastic system

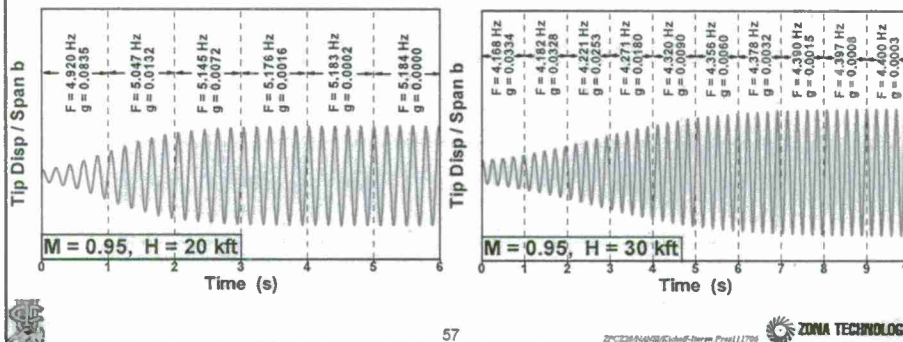


56

ZONA TECHNOLOGY

Verifying the Stiffening Effects of Nonlinear Structures

- According to ARMA calculated frequencies and damping at each second during the LCO development are shown below. Note that the frequency increases as the amplitude grows until LCO is fully developed.
- The increase of frequency verifies the stiffening effects of the nonlinear structures.



Conclusions of the Feasibility Study

- The Nonlinear Structural (NS) ROM has been successfully integrated into the CartEuler code and demonstrated with aeroelastic applications to the Folding Wing cases including large elastic deformation
 - Both M.9/M.95 cases showed LCO solutions due to Distributed Nonlinearity in Structures and Aerodynamics
- For the given CartEuler with the Nonlinear ROM, the additional computational time for large deformation analysis when compared to the aeroelastic analysis with linear structures is insignificant
- This feasibility study demonstrates that an aeroelastic analysis involved large elastic deformation for a very complex nonlinear structural finite element model is affordable
- If a reduced order model of the GBCC/CFD system is further constructed, the resulting fully ROM of the aeroelastic system could provide a nonlinear aeroelastic solution very efficiently



58

ZONA TECHNOLOGY

Tasks to be accomplished in Phase I

- *Extend the 2D GBCC Euler method to 3D GBCC Euler*
- *Implement the substructuring/nonlinear Structural ROM strategy for each wing component and the reassembly in continuous morphing*
- *Integrate the ELSTEP-generated ROM into the 3D GBCC, and lead to a high-fidelity Nonlinear Aerodynamic/Nonlinear Structural Interaction (NANSI) software system*
- *Include in ELSTEP the dynamic effects (inertia loading) onto the Folding Wing due to its continuously morphing motion*
- *Validate NANSI on the Folding Wing using*
 - *ELSTEP/Nonlinear Structural ROM modes*
 - *3D GBCC Euler vs. CartEuler*
 - *Suggested cases*
- *Documentation*



59

SPC2000/03/04/05/06/07/08/09/10/11/12/13/14/15/16/17/18 ZONA TECHNOLOGY

Phase II Plan

- *Improve the 3D GBCC/Euler method towards a production-ready NANSI software system*
- *Extend the 3D GBCC/Euler capability to include viscous effects for morphing/flapping wings, e.g. generalized vortex confinement method for separated flow, coupled with boundary layer*
- *Generalize the substructuring/nonlinear ROM strategy for various type of morphing Configurations*
- *Include in the nonlinear ROM the full dynamic/inertia effects due to morphing*
- *Obtain Flutter/LCO solutions for Continuously Morphing Folding Wing , DLR Wing (?) [NANSI - Step I]*
- *Demonstrate the NANSI capability on complex structures such as the whole aircraft finite element model of the LM Aero morphing UAV , other MAV/Flapping wings (?) [NANSI - Step II]*



60

SPC2000/03/04/05/06/07/08/09/10/11/12/13/14/15/16/17/18 ZONA TECHNOLOGY

Attachment B

Nonlinear Aeroelastic Methodology for a Membrane-on-Ballute Model with Hypersonic Bow Shock

***Presented at Aerospace Flutter and Dynamics Council Meeting,
San Antonio, TX, May 2008***

Nonlinear Aeroelastic Methodology for A Membrane-on-Ballute Model with Hypersonic Bow Shock

Danny D. Liu
Zhicun Wang
Shuchi Yang
Chunpei Cai

Marc Mignolet



Presented at the Aerospace Flutter and Dynamics Council Meeting in San Antonio, TX, May 22 – 23, 2008

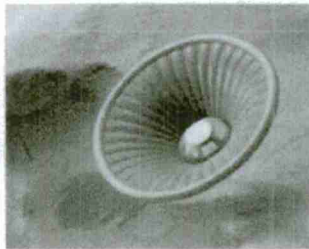
9489 E. Ironwood Square Drive, Scottsdale, AZ 85258-4578, Tel (480) 945-9988, Fax (480) 945-6588, E-mail: danny@zonatech.com

Acknowledgement

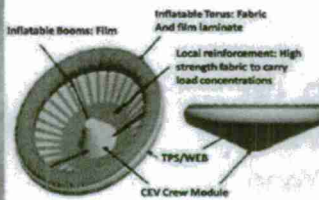
This present work is under the support of a NASA SBIR Phase I contract, with Dr. Robert Bartels as the Technical Monitor.

Different Ballute Types

• Clamped Ballute



Reentry aeroshell



A conceptual design for ballute

• Trailing/Torroid Ballute



Inflatable ballute entry

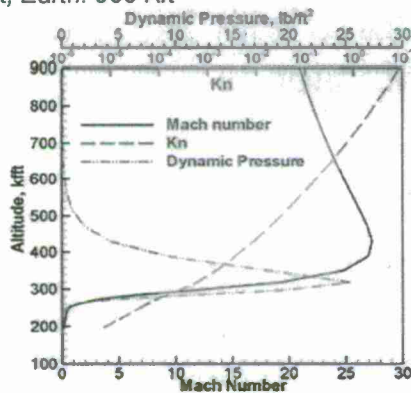
ASU

3

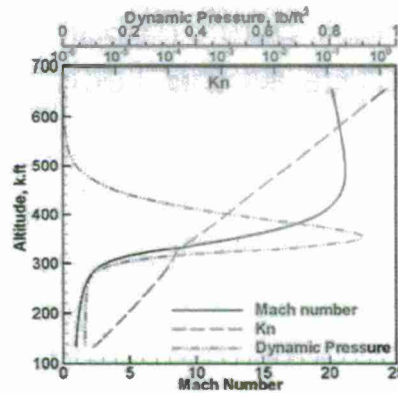
ZONA TECHNOLOGY

Earth/Mars Entry Profiles

*Parameters: ballute mass =220 lb, ballute diameter: 92 ft, Initial Mach number: 20; Gravity acceleration: Mars:10.40 ft/s², Earth 32.1740 ft/s². Initial altitude: Mars= 660 kft, Earth: 900 Kft



Earth Entry*



Martian Entry*

Knudson number: $Kn = \frac{M}{\sqrt{Re}}$ GasKinetic parameter

ASU

4

ZONA TECHNOLOGY

Overview

- Ballute aeroelastic problem requires Gaskinetic (microscopic) aerodynamics in the rarefied hypersonic flight regime
 - *Boltzmann/BGK method (time accurate) is adopted.*¹
- Ballute is an inflatable (nonlinear) structure
 - *Nonlinear structural ROM (ELSTEP) is adopted.*²
- Ballute flutter/LCO computation procedure needs to be expedited
 - *ZONA's nonlinear/linear ROM-ROM procedures are adopted.*³
- Membrane-on-Ballute with Bow-Shock is modeled first by a 2D membrane-on wedge with attached shock- thus the present study

Supported by: 1. AFOSR/Schmisseur; 2. NASA/Rizzi; 3. AFOSR/Fahroo.



5



Outline

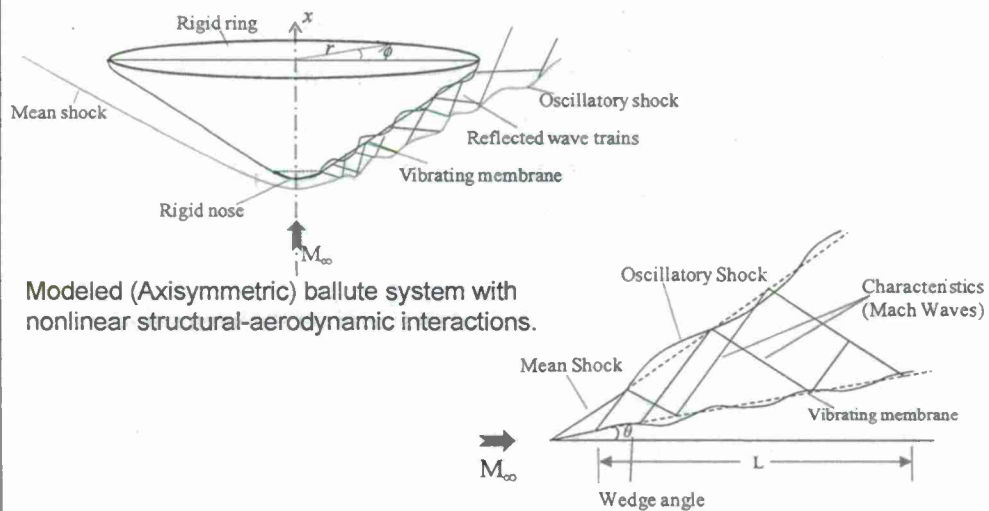
- Introduction: Ballute Systems
- Nonlinear Structural ROM (ELSTEP)
- Boltzmann Unsteady Aerodynamics: Time-Accurate BGKX
- Nonlinear Aeroelastic Static Deformation Analysis
- Aerodynamic ROM (Sys. Id. + ARMA)
- ROM/ROM Time-Domain Flutter Analysis for Undeformed/Deformed Mean Configuration
- Concluding Remarks



6



Modeled Ballute System



Modeled (Axisymmetric) ballute system with nonlinear structural-aerodynamic interactions.

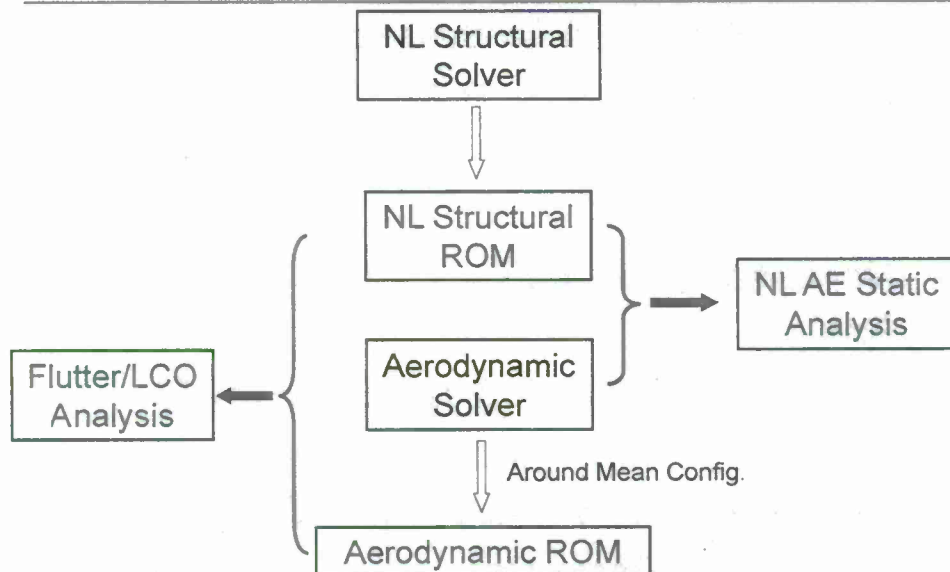
Membrane-on-wedge in hypersonic/supersonic flow.

ASU

7

ZONA TECHNOLOGY

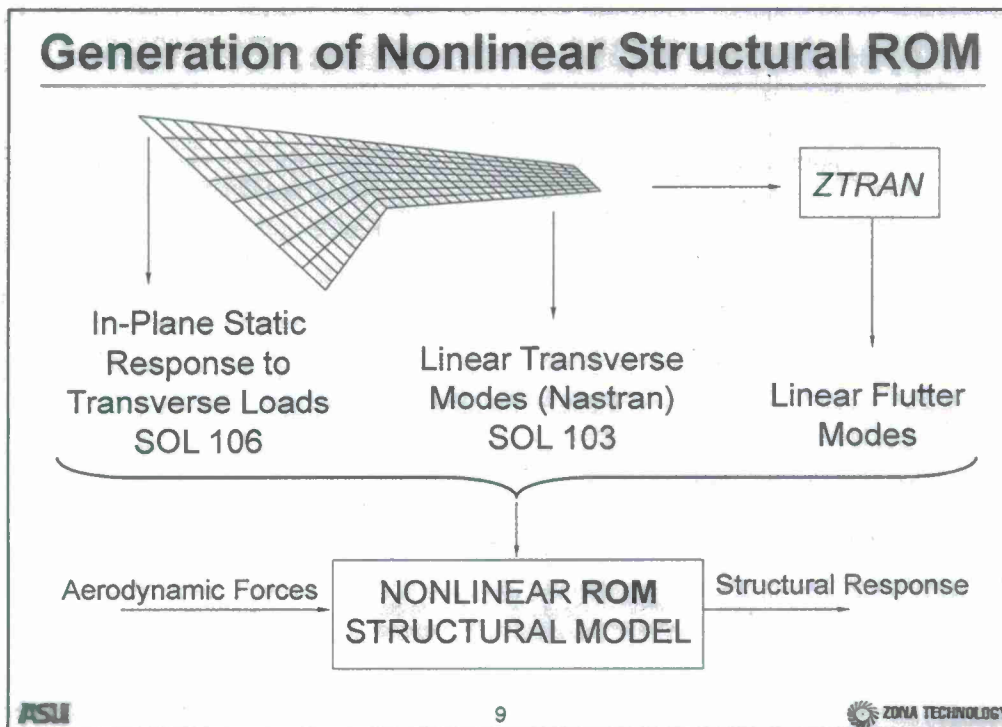
Present Nonlinear Aeroelastic Methodology



ASU

8

ZONA TECHNOLOGY

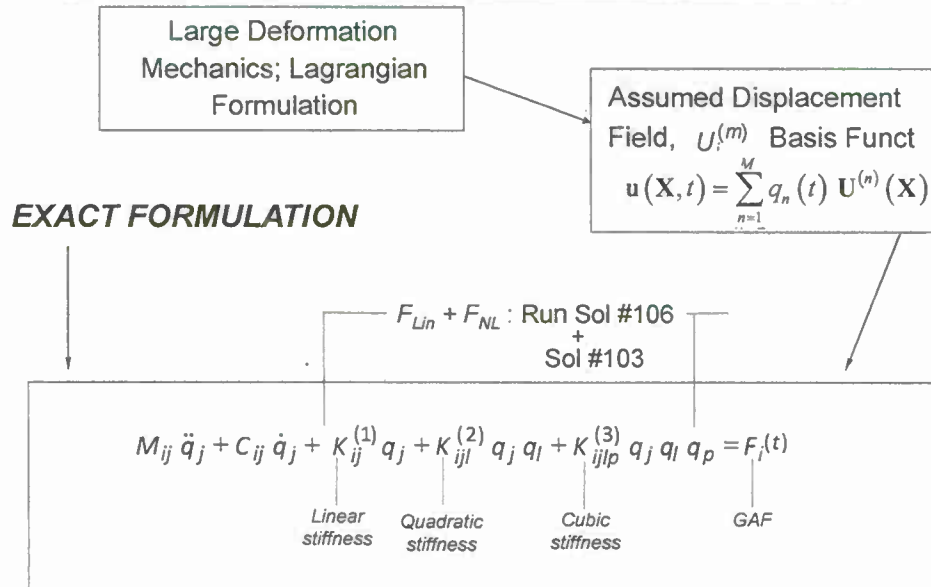


About ELSTEP/FAT

- ELSTEP/FAT = Equivalent Linearization Stiffness Evaluation Procedure/Fatigue (due to) Acoustics and Thermal Gradients
- An advancement of ELSTEP code previously developed by Steve Rizzi/NASA Langley and Alex Muravyov/MSU
- ZONA/ASU R&D efforts of ELSTEP/FAT supported under several AF/SBIR's and NASA/SBIR's from 1999 ~ 2005

ASU 10 ZONA TECHNOLOGY

Nonlinear ROM Procedure: ELSTEP

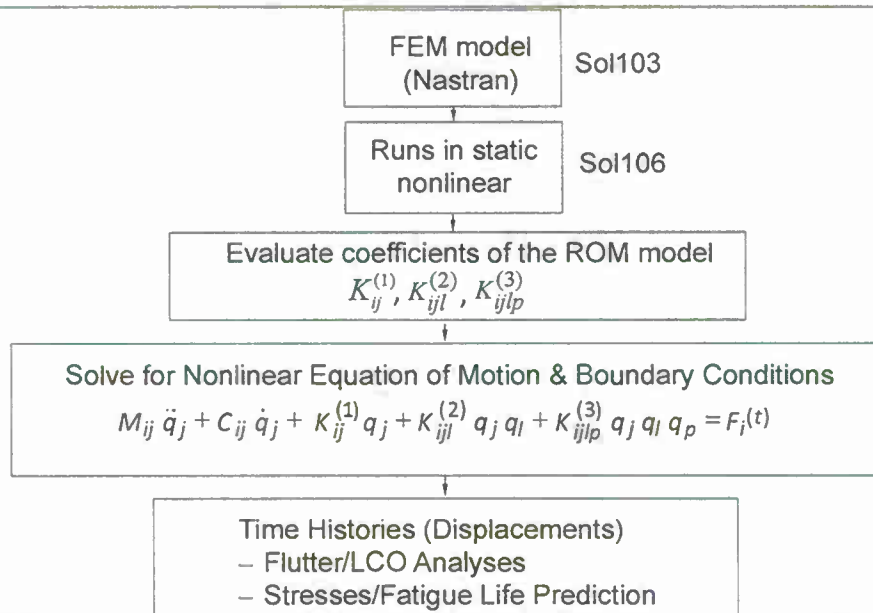


ASU

11

ZONA TECHNOLOGY

ELSTEP Nonlinear Structural ROM



ASU

12

ZONA TECHNOLOGY

Procedure to Evaluate Nonlinear Stiffness Terms

- Impose a series of static deflections and determine (e.g. from finite element model) the forces required and the stresses.
- Then, identify the coefficients of the reduced order model.

Cond. (a)

$$\mathbf{u} = q_j \mathbf{U}^{(j)} \quad (F_i)_a = K_{ij}^{(1)} q_j + K_{ijj}^{(2)} q_j^2 + K_{ijjj}^{(3)} q_j^3$$

Cond. (b)

$$\mathbf{u} = -q_j \mathbf{U}^{(j)} \quad (F_i)_b = -K_{ij}^{(1)} q_j + K_{ijj}^{(2)} q_j^2 - K_{ijjj}^{(3)} q_j^3$$

Cond. (c)

$$\mathbf{u} = \hat{q}_j \mathbf{U}^{(j)} \longrightarrow K_{ij}^{(1)}, K_{ijj}^{(3)} \text{ Inner terms}$$

$$\left. \begin{aligned} \mathbf{u} &= q_j \mathbf{U}^{(j)} + q_l \mathbf{U}^{(l)} \\ \mathbf{u} &= q_j \mathbf{U}^{(j)} - q_l \mathbf{U}^{(l)} \\ \mathbf{u} &= q_j \mathbf{U}^{(j)} + q_l \mathbf{U}^{(l)} + q_p \mathbf{U}^{(p)} \end{aligned} \right\} \longrightarrow K_{ijj}^{(2)}, K_{ilj}^{(3)}, K_{iljp}^{(3)} \text{ Cross terms}$$

ASU

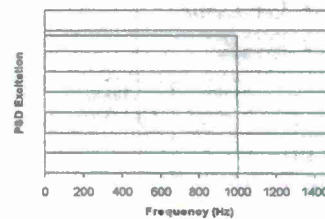
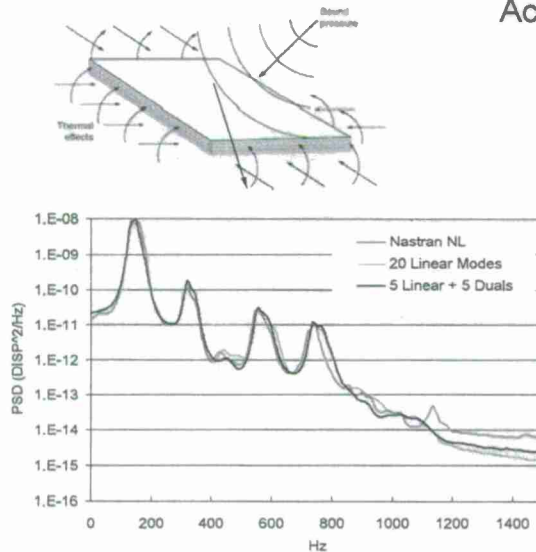
13

ZONA TECHNOLOGY

ELSTEP Past Validation

Example of Application:

Fully clamped; no temperature
Acoustic excitation 135dB



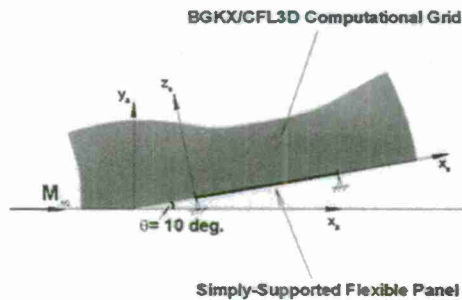
Significant nonlinearity
first peak = 154 Hz
first nat. freq. = 110 Hz

ASU

14

ZONA TECHNOLOGY

NL Structural ROM for the Membrane-on-Wedge

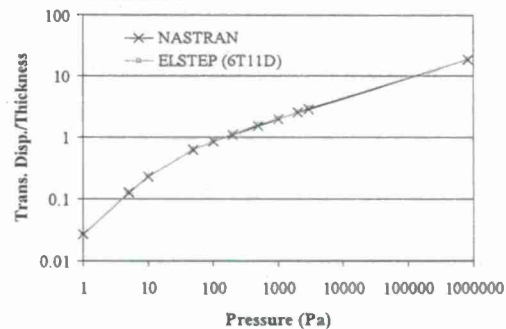


$$\Delta p = p_u - p_l$$

Assuming: $p_l = p_\infty$

$$\Delta p = p_u - p_l = q_\infty C_{p_u}$$

- The NL structural ROM for the flexible panel uses the first 6 transverse modes and 11 dual modes
- Deformation solutions under constant pressure agree excellently with Nastran nonlinear solutions



ASU

15

ZONA TECHNOLOGY

ZONA Capability of Hypersonic Flow Solvers

High level CFD methods

- CFL3D
- BGK

	NS level	Burnett Level($Kn > 0$)	Time - Accurate	Aerothermodynamics	Unsteady Motion	Local Features	Compu. Speed
CFL3D	✓	--	✓	--	Deforming mesh	Embedded Mesh	Faster
FUN3D	✓	--	✓	✓	Deforming mesh	Adaptive Mesh	Slowest
BGKX	✓	✓	✓	✓	Moving* mesh	Adaptive* Mesh	Slower

✓ = yes; -- = not available

* Under development

2D Inviscid methods

- ZPEC (Zona Perturbed Euler Characteristics)
- Piston Theory

ASU

16

ZONA TECHNOLOGY

Rarefied Hypersonics: Microscopic versus Macroscopic Approaches

- Macroscopic approaches (Continuum)
 - Flow parameters: Mach no., Reynolds no.
 - All continuum methods: Euler, N-S, etc.
- Microscopic approaches (Gaskinetic)
 - Flow parameter: Knudsen number
 - DSMC (direct simulation Monte Carlo) First-principal particle collision approach; no governing PDE
 - Boltzmann Eqn. (Integro-Differential Eqn.)

$$\left(\frac{\partial}{\partial t} + u \frac{\partial}{\partial x} \right) f = I[f_1 f_2, f'_1 f'_2]$$

- BGK Eqn. (approximation of Boltzmann)

$$\left(\frac{\partial}{\partial t} + u \frac{\partial}{\partial x} \right) f = \frac{g - f}{\tau}$$

Boltzmann/BGK vs. Classical Eqns.

- Boltzmann/BGK uses distribution function (f) as a single dependent variable with (7) independent variables (t, x_i, v_i)
- Euler/N-S have 5 prime variables (P, U, V, W, ρ) with (4) independent variables (t, x_i)
- Potential flow uses velocity potential function (Φ) as a single dependent variable with (4) independent variables (t, x_i).
- To recover solution from f and from Φ to prime variables (P, U, V, W, ρ) requires respectively to integrate f and to differentiate Φ .

BGK and BGKX Equations

- For BGK equation, the right hand side (RHS) of collision terms is simplified as one relaxation term between equilibrium state, g , and instantaneous distribution, f , and τ is the characteristic relaxation time:

$$\frac{\partial f}{\partial t} + u \frac{\partial f}{\partial x} = \frac{g - f}{\tau}, \quad \frac{1}{\tau} \sim Kn$$

- For BGKX equation, Xu adopts modern CFD kinetic flux for the left handside (LHS) terms, for the RHS, Xu replaces the relaxation time τ by a strained relaxation time τ^* , which allows for extended Knudsen number (Kn) range from 0 towards 1.0, thus covering the continuum to transient flow regime up to the order of BGKX-Burnett. Note that tackling this flow regime with DSMC would overburden its computing cost and with continuum CFD would be pushing its capability; whereas the BGKX-Burnett is a proper one.



19



Merits of the BGKX Method

- BGK eqn. is a higher level one than continuum Euler/N-S eqns.
- BGKX covers wide range of Knudsen number (Kn); it unifies continuum flow ($Kn \sim 0$) with transition flow ($0 < Kn < 1.0$).
- BGK solver is time-accurate, hence most suitable for unsteady aerodynamic applications.
- One-step computational procedure for pressure and heat flux solutions.
- Single gas distribution function, f , simplifies the flux algorithm.
- Consistent and unified procedure to handle equilibrium, equilibrium and chemically reacting flows.

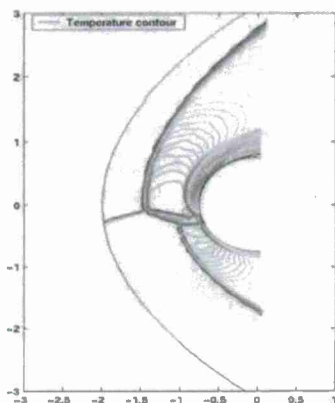
• ZONA has been supported by AFOSR/STTR on the BGKX Solver development since 2004. For publications see: Cai, C., Liu, D.D., and Xu, K., "A One-Dimensional Multi-Temperature Gaskinetic BGK Scheme for Planar Shock Wave Computation," *AIAA Journal*, Vol. 46, No. 5, May 2008.



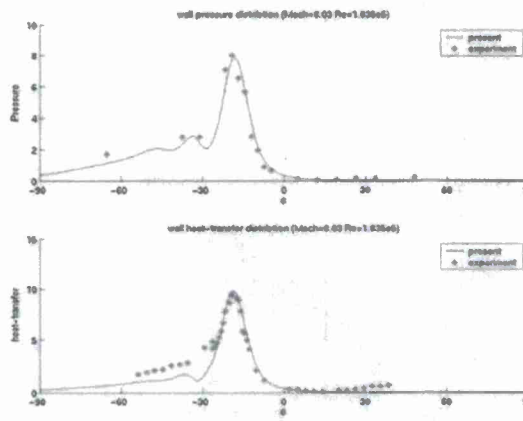
20



Shock-Shock Interaction by BGKX



Shock-shock interaction.



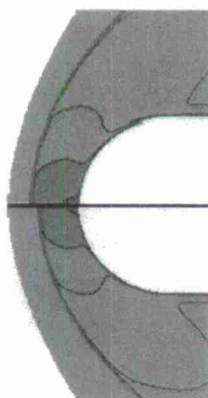
Surface pressure and heat flux distributions.

ASU

21

ZONA TECHNOLOGY

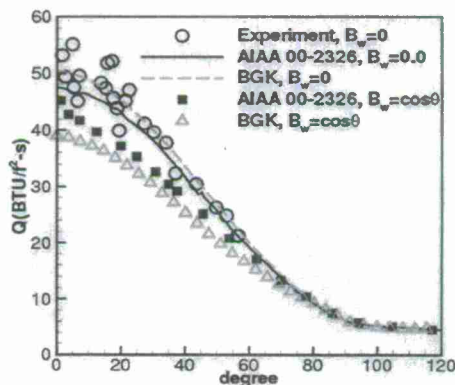
Heat-Rate Reduction by BGKX/MHD



$Ma=16.03$, $Re=1.835 \times 10^6$,
 $T_{\infty}=52.183$ K,
 $\gamma=1.4$,
 $T_{\infty}=299.444$ K

M
 12
 10
 8
 6
 4
 2
 1
 0.5
 0.1

MHD actuator effects on the shock stand off distance.



MHD actuator effects on heat flux from the cylinder.

ASU

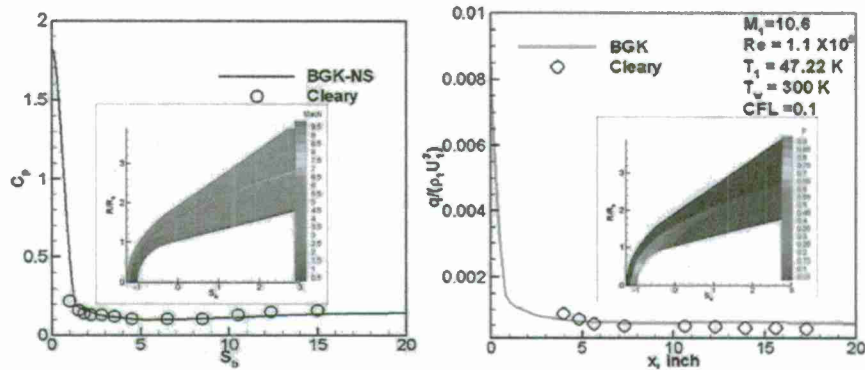
22

ZONA TECHNOLOGY

BGKX for Blunted Cone/Cylinders: Cp and Heat flux along the Surface

$Ma=10.6$, $Re=1.1e5$, $T_\infty=85R$, $R=1.1$ inch, $Pr=0.72$, $T_w=540R$.

BGK simulation results of Cp, heat flux over a spherically headed 15 degree cone.



Surface C_p and Mach number contours. Surface heat flux and pressure contours.

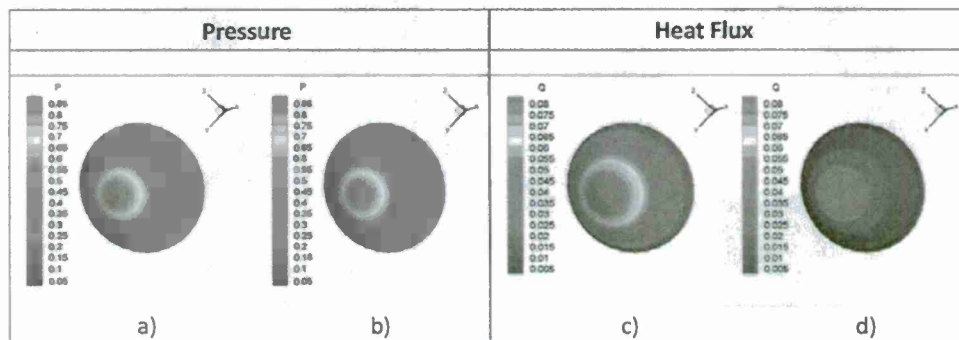
ASU

23

ZONA TECHNOLOGY

BGKX Simulation Results of a Hypersonic Flow over a Paraboloid

$M=16.03$, $T_\infty=124.93$ K, $T_w=294.4$ K



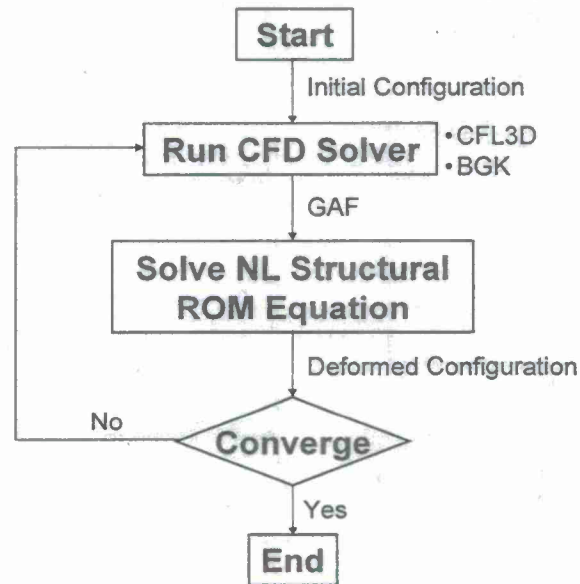
a) Pressure, $Re=1.835 \times 10^5$, b) Pressure, $Re=1.835 \times 10^4$
c) Heat Flux, $Re=1.835 \times 10^5$, d) Heat Flux, $Re=1.835 \times 10^4$

ASU

24

ZONA TECHNOLOGY

NL Aeroelastic Static Deformation

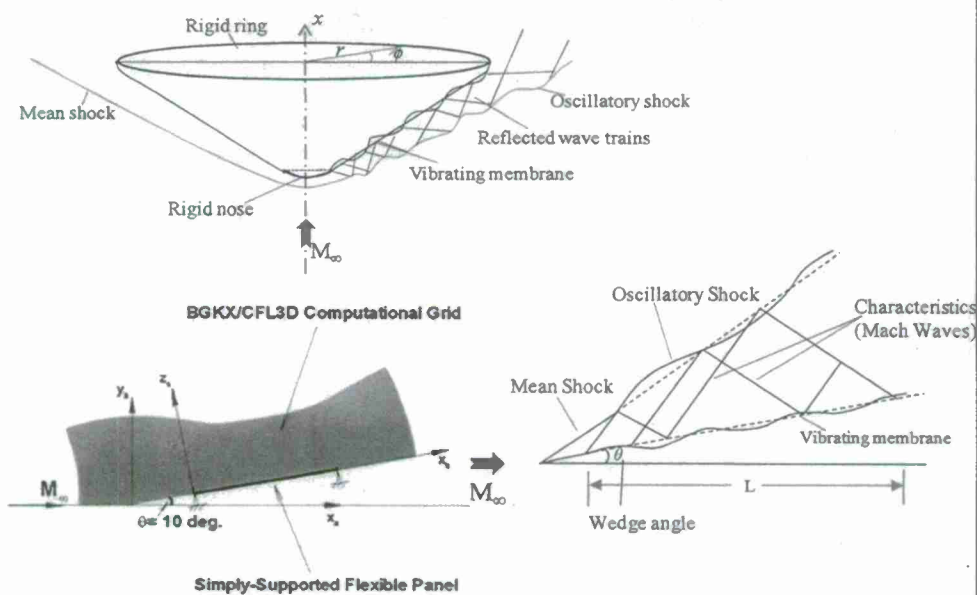


ASU

25

ZONA TECHNOLOGY

Membrane-on-Wedge

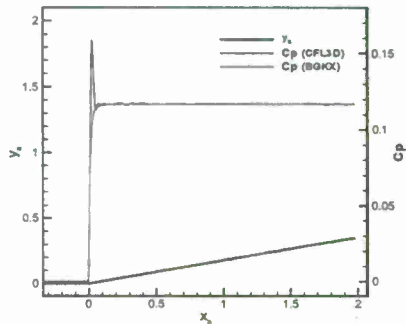


ASU

26

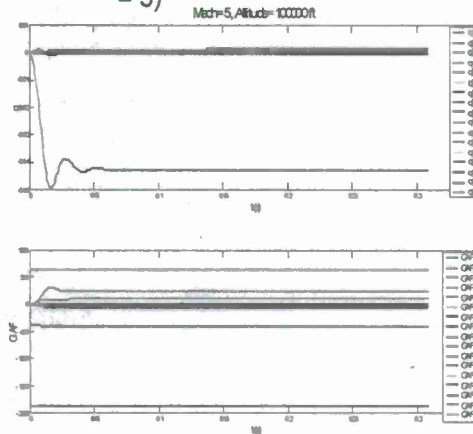
ZONA TECHNOLOGY

NL AE Static Def. Solutions for Membrane-on-Wedge



- Comparison of C_p distribution along the undeformed wedge surface by BGKX and CFL3D (Mach = 5)

- Numerical simulation process (Alt = 100 Kft, Mach = 5)

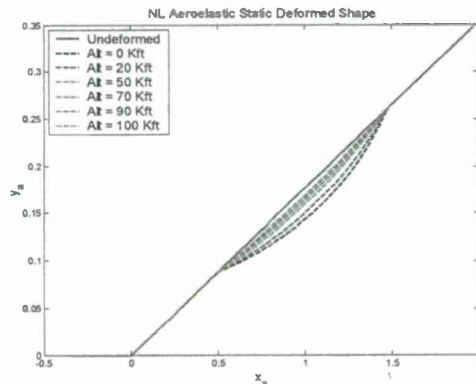


ASU

27

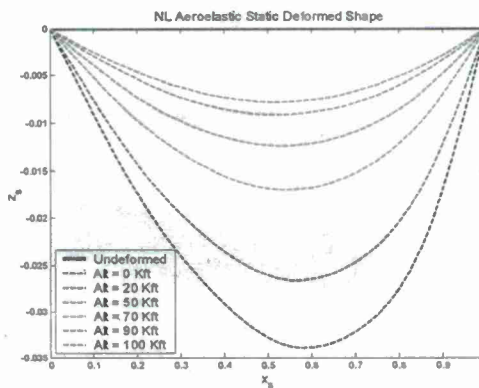
ZONA TECHNOLOGY

NL AE Static Deformed Shapes for Membrane-on-Wedge



- Nonlinear aeroelastic static deformed shapes for the flexible membrane at various altitudes represented in the aerodynamic coordinate system

- Nonlinear aeroelastic static deformed shapes for the flexible membrane at various altitudes represented in the structural coordinate system



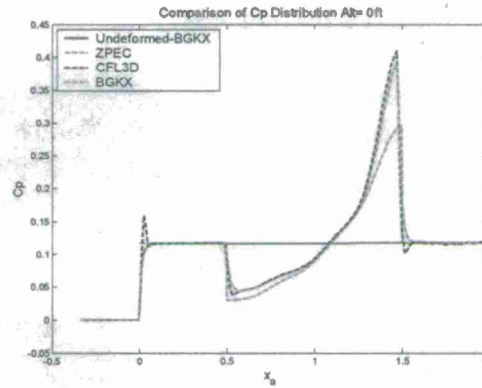
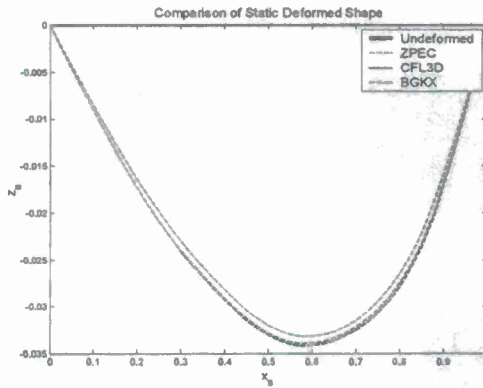
ASU

28

ZONA TECHNOLOGY

Solution Comparison Using Different Aerodynamic Solver

Mach = 5; Alt = 0 ft



- Comparison of the statically deformed shapes using various aerodynamic solvers (represented in the structural coordinate system)

- Comparison of C_p distributions along the statically deformed wedge surface using various aerodynamic solvers

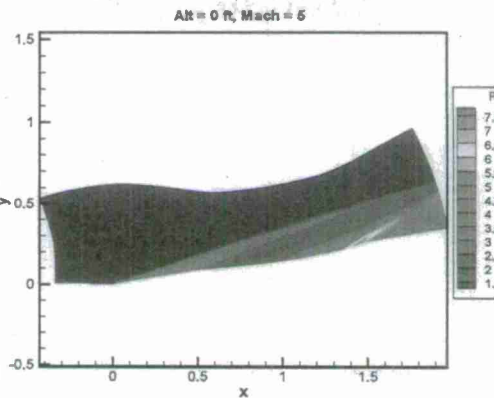
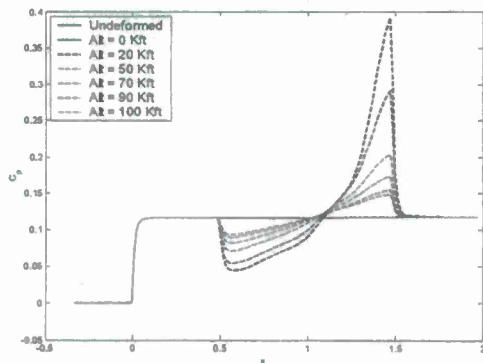
ASU

29

ZONA TECHNOLOGY

BGKX Solutions on the Statically Deformed Wedge

- C_p distribution along the deformed wedge surface (Mach = 5)



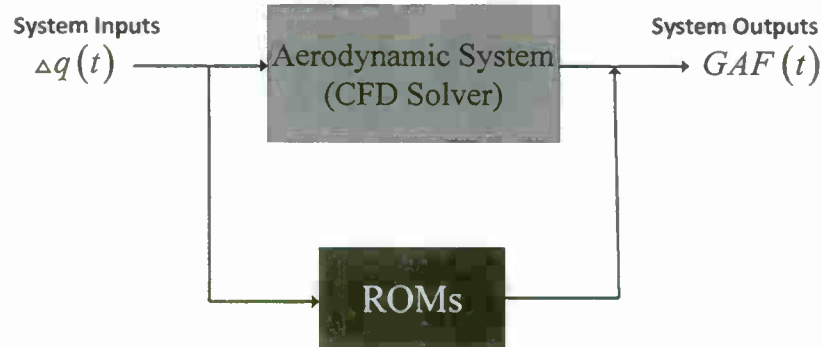
- Pressure contour plot on deformed configuration (Alt = 0 ft; Mach = 5)

ASU

30

ZONA TECHNOLOGY

Aerodynamic ROM



Linearized Equation of Motion around Statically Deformed Configuration

$$q = q_0 + \Delta q \longrightarrow M \ddot{q} + K^{(1)} q + F_{NL} = F_a$$



$$\text{Static : } K^{(1)} q_0 + F_{NL}(q_0) = \frac{1}{2} \rho V_\infty^2 \{GAF(q_0)\}$$

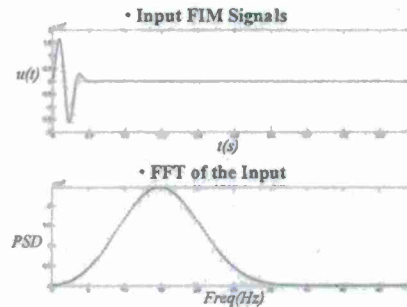
$$\text{Dynamic : } M \{\Delta \ddot{q}\} + \left(K^{(1)} + \frac{\partial F_{NL}}{\partial q} \bigg|_{q_0} \right) \{\Delta q\} = \frac{1}{2} \rho V_\infty^2 \{GAF(\Delta q)\}$$

Aerodynamic ROM Training Excitations

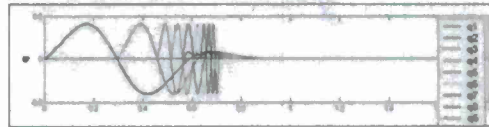
- Filter Impulsive Method (FIM) signals are chosen as excitation signals for their
 - Broader range of frequency with concentration on the frequency of interest.
 - Symmetric about zero axis.

- A FIM signal is given by:

$$u(t) = \begin{cases} Ae^{\alpha(\omega - \omega_0 - \pi)^2} \sin(\omega t - \omega_0 t_0) & \text{when } t \geq t_0 \\ 0 & \text{when } t < t_0 \end{cases}$$



- A **staggered** sequence FIM input of modal coordinates is employed.
- Each mode uses its own natural frequency as the ω .
- The lowest order goes first.



ASU

33

ZONA TECHNOLOGY

Aerodynamic ROM Approaches

- Various aerodynamic ROM methods:
 - POD/ROM-HB: Dowell (1998)
 - Volterra: Silva (1993)
 - ERA: Kim (2004)
 - POD/ROM-Time Domain: Beran (2003)
 - ARMA: ZONA* (2008)
 - NNet: ZONA
- Present approach: System Identification technique, specifically, Auto-Regressive-Moving-Average (ARMA) model.

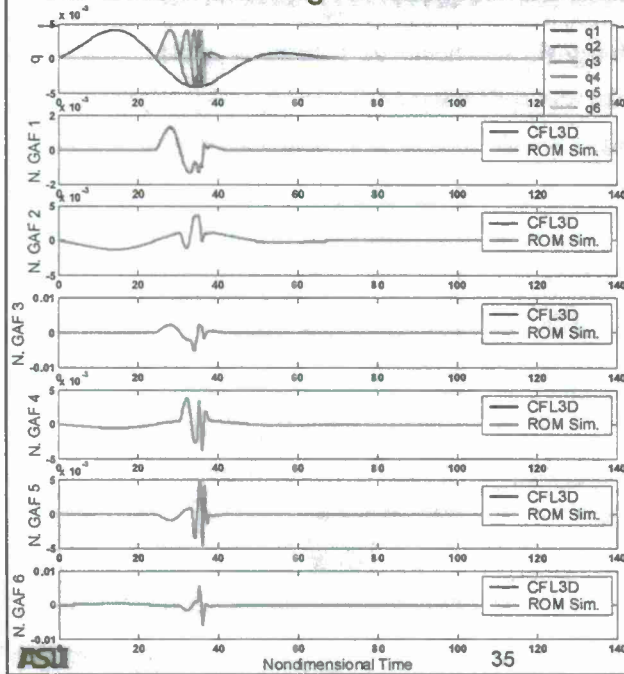
* Z. Wang, et al., "Flutter Analysis with Structural Uncertainty by Using CFD-based Aerodynamic ROM", presented in 49th AIAA/ASME/AHS/ASC SDM, 7-10 April, 2008, Schaumburg, IL

ASU

34

ZONA TECHNOLOGY

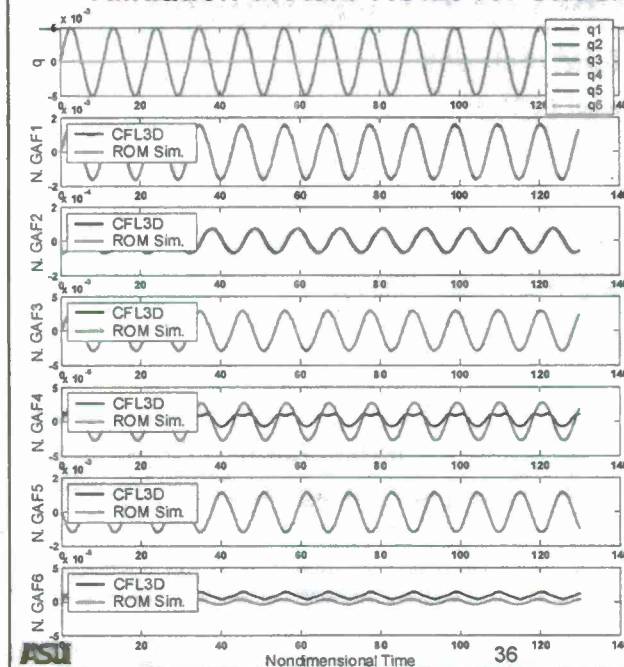
Aero ROM Training for *Undeformed Mean Wedge Configuration*



- Aero ROMs are developed for the first 6 transverse modes using CFL3D
- Staggered FIM signals are shown in the first sub-figure
- ARMA models for the 6 normalized GAF are obtained by optimization procedure using the training data set
- GAFs for the other 11 dual modes are assumed zero
- Aero ROM predictions agree well with direct CFL3D outputs

ZONA TECHNOLOGY

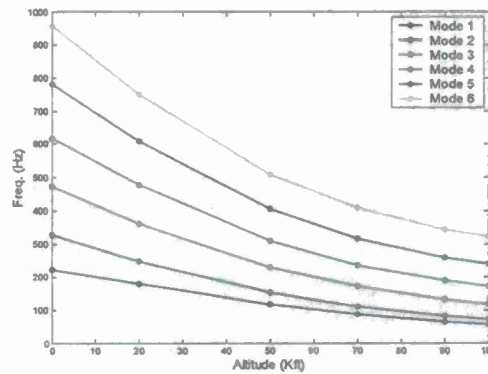
Validation of Aero ROMs for *Undeformed Mean Wedge*



- The first sub-figure is the time histories of the modal coordinates providing inputs to both the aerodynamic ROMs and the direct CFL3D solver
- Specifically, only the second modal coordinate assumes a sinusoid time history while others are kept zero.
- Aero ROM predictions agree well with direct CFL3D outputs
- The exceptions are for the fourth and sixth GAFs, but these two are very small, two-order smaller the others

ZONA TECHNOLOGY

Flutter analysis for *Deformed Mean Wedge*



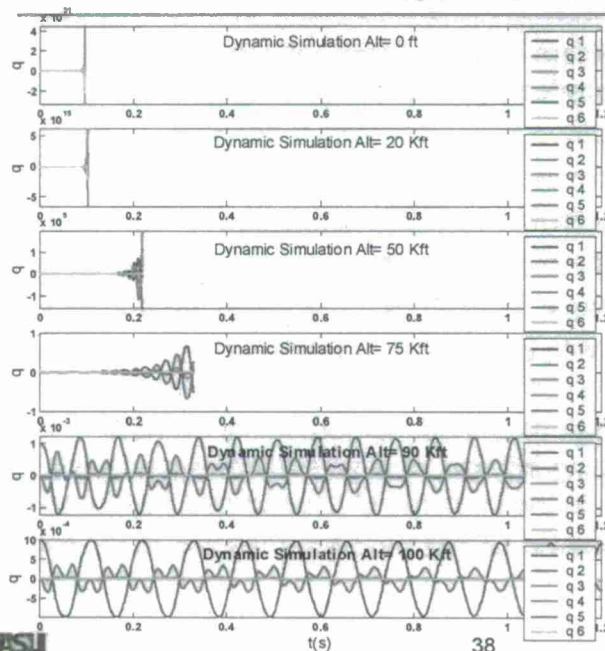
- Change of the natural frequencies around the deformed mean wedge configuration at various altitudes

ASU

37

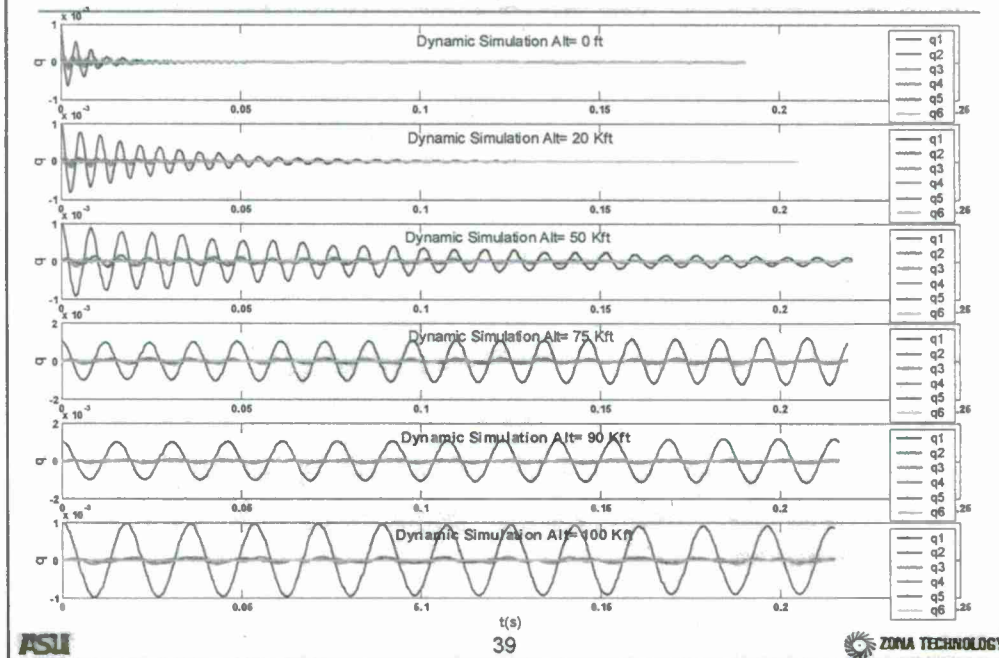
ZONA TECHNOLOGY

ROM-ROM Flutter Analysis: *Undeformed Mean Wedge*



- Conventional type of flutter analysis: linear structural EOM unchanged as altitude change
- Under our dynamic simulations, the first modal coordinate is given a small initial value; all the other initial conditions are zeros
- By varying the altitude (consequently, the free-stream speed and the dynamic pressure, i.e., the match-point methodology), one explores the decaying, near neutral, and diverging time responses.

ROM-ROM Flutter Analysis: *Deformed Mean Wedge*



Conclusions

- Ballute aeroelastic problem requires Gaskinetic (microscopic) aerodynamics in the rarefied hypersonic flight regime.
 - Boltzmann/BGK method (time accurate) is adopted
- Ballute is an inflatable (nonlinear) structure
 - Nonlinear structural ROM (ELSTEP) is adopted
- Ballute flutter/LCO computation procedure needs to be expedited
 - ZONA's nonlinear/linear ROM-ROM procedures are adopted.
- Membrane-on-Ballute with Bow-Shock is modeled first by a 2D membrane-on-wedge with attached shock-- thus the present study
- For a wedge with a mean deformed membrane, its stiffness increases with decreasing altitude, thus it becomes dynamically more stable – contrary to the outcome of undeformed membrane
- Axisymmetric membrane-on-ballute model aeroelastic study is in progress

Attachment C

Reduced Order Modeling For Geometrically Nonlinear Structural Dynamic Problems

***Presented at Workshop on Aeroelastic Certification: Tools,
Test, Decision Making, Sedona, AZ, October 2008***

REDUCED ORDER MODELING FOR GEOMETRICALLY NONLINEAR STRUCTURAL DYNAMIC PROBLEMS

Marc P. Mignolet, X.Q. (Julian) Wang,
Kwangkeun Kim, and Vishal Khanna
Arizona State University



*Ira A. Fulton School of Engineering
Department of Mechanical and Aerospace Engineering*



Why NL Structural ROM for Aeroelastic Analysis?

- Using Commercial NL FEM Code

- Loosely coupled with aero only for static aeroelastic solution.
- Closely coupled with aero (dynamic) requires FEM source code.

- Using Self-Developed NL FEM Code

- Not compatible with commercial FEM code.
- Not proven technology readily adopted by industry.

- Using NL Structural ROM

- A system identification procedure operating on commercial NL FEM code to construct the NL structural ROM
- Coupling the NL structural ROM with aerodynamics yields both static and dynamic aeroelastic solutions.
- Once NL structural ROM is obtained, aeroelastic analyses are computationally very efficient.



*Ira A. Fulton School of Engineering
Department of Mechanical and Aerospace Engineering*



APPLICATIONS:

- * Panels in large deformations (e.g., *sonic fatigue* problem)
- * wing in large deformations (e.g., LCO)
- * ...
 - _ with/without temperature field
 - _ isotropic/composite/functionally graded panel
 - _ boundary conditions (clamped, on stiffeners, cantilevered,...)
 - _ flat/curved
 - _ various shapes

BASIC ISSUES:

1. What is the form of the equations of motion?
2. How do we determine the coefficients of these equations from a finite element model?
3. What basis (“modes”) should we use to represent the motion?



Ira A. Fulton School of Engineering
Department of Mechanical and Aerospace Engineering



Large Deformation Mechanics
Lagrangian Formulation
Duhamel-Neumann medium in
undeformed configuration

Assumed Displacement
Field, $U_i^{(m)}$ Basis Funct

$$u_i(\underline{X}, t) = \sum_{n=1}^M q_n(t) U_i^{(n)}(\underline{X})$$

nonlinear terms

$$M_{ij} \ddot{q}_j + D_{ij} \dot{q}_j + \left[K_{ij}^{(1)} - K_{ij}^{(th)} \right] q_j + K_{ijl}^{(2)} q_j q_l + K_{ijlp}^{(3)} q_j q_l q_p = \bar{F}_i + F_i^{(th)} T$$

added to model dissipation

thermal effects if
temperature present

* Stresses can also be recovered $S = S_j^{(1)} q_j + S_{jl}^{(2)} q_j q_l$

* Finite element based identification procedure of the coefficients
 $K_{ij}^{(1)} - K_{ij}^{(th)}$, $K_{ijl}^{(2)}$, $K_{ijlp}^{(3)}$, $F_i^{(th)}$, $S_j^{(1)}$, $S_{jl}^{(2)}$ (and M_{ij} and $F_i(t)$)



Ira A. Fulton School of Engineering
Department of Mechanical and Aerospace Engineering



REDUCED ORDER MODEL COEFFICIENTS

Procedure: Impose a series of static deflections and determine (e.g. from finite element model) the forces required and the stresses. Then, identify the coefficients of the reduced order model.

$$\underline{u} = q_j \underline{\Psi}_j \quad F_{1i} = \overline{K}_{ij}^{(1)} q_j + \overline{K}_{ijj}^{(2)} q_j^2 + \overline{K}_{ijjj}^{(3)} q_j^3$$



*Ira A. Fulton School of Engineering
Department of Mechanical and Aerospace Engineering*



REDUCED ORDER MODEL COEFFICIENTS

Procedure: Impose a series of static deflections and determine (e.g. from finite element model) the forces required and the stresses. Then, identify the coefficients of the reduced order model.

$$\left. \begin{aligned} \underline{u} &= q_j \underline{\Psi}_j & F_{1i} &= \overline{K}_{ij}^{(1)} q_j + \overline{K}_{ijj}^{(2)} q_j^2 + \overline{K}_{ijjj}^{(3)} q_j^3 \\ \underline{u} &= -q_j \underline{\Psi}_j & F_{2i} &= -\overline{K}_{ij}^{(1)} q_j + \overline{K}_{ijj}^{(2)} q_j^2 - \overline{K}_{ijjj}^{(3)} q_j^3 \end{aligned} \right\} \rightarrow \overline{K}_{ijj}^{(2)} = \frac{F_{1i} + F_{2i}}{2 q_j^2}$$



Ira A. Fulton School of Engineering
Department of Mechanical and Aerospace Engineering



REDUCED ORDER MODEL COEFFICIENTS

Procedure: Impose a series of static deflections and determine (e.g. from finite element model) the forces required and the stresses. Then, identify the coefficients of the reduced order model.

$$\left. \begin{array}{l} \underline{u} = q_j \underline{\Psi}_j \quad F_{1i} = \overline{K}_{ij}^{(1)} q_j + \overline{K}_{ijj}^{(2)} q_j^2 + \overline{K}_{ijjj}^{(3)} q_j^3 \\ \underline{u} = -q_j \underline{\Psi}_j \quad F_{2i} = -\overline{K}_{ij}^{(1)} q_j + \overline{K}_{ijj}^{(2)} q_j^2 - \overline{K}_{ijjj}^{(3)} q_j^3 \\ \underline{u} = \hat{q}_j \underline{\Psi}_j \end{array} \right\} \rightarrow \overline{K}_{ijj}^{(2)} = \frac{F_{1i} + F_{2i}}{2 q_j^2} \quad \overline{K}_{ij}^{(1)} ; \overline{K}_{ijjj}^{(3)}$$



Ira A. Fulton School of Engineering
Department of Mechanical and Aerospace Engineering



REDUCED ORDER MODEL COEFFICIENTS

Procedure: Impose a series of static deflections and determine (e.g. from finite element model) the forces required and the stresses. Then, identify the coefficients of the reduced order model.

$$\left. \begin{aligned} \underline{u} &= q_j \underline{\Psi}_j & F_{1i} &= \overline{K}_{ij}^{(1)} q_j + \overline{K}_{ijj}^{(2)} q_j^2 + \overline{K}_{ijjj}^{(3)} q_j^3 \\ \underline{u} &= -q_j \underline{\Psi}_j & F_{2i} &= -\overline{K}_{ij}^{(1)} q_j + \overline{K}_{ijj}^{(2)} q_j^2 - \overline{K}_{ijjj}^{(3)} q_j^3 \end{aligned} \right\} \rightarrow \overline{K}_{ijj}^{(2)} = \frac{F_{1i} + F_{2i}}{2 q_j^2} \\ \underline{u} &= \hat{q}_j \underline{\Psi}_j$$

$$\left. \begin{aligned} \underline{u} &= q_j \underline{\Psi}_j + q_l \underline{\Psi}_l \\ \underline{u} &= q_j \underline{\Psi}_j - q_l \underline{\Psi}_l \\ \underline{u} &= -q_j \underline{\Psi}_j - q_l \underline{\Psi}_l \\ \underline{u} &= q_j \underline{\Psi}_j + q_l \underline{\Psi}_l + q_p \underline{\Psi}_p \end{aligned} \right\} \rightarrow \overline{K}_{ilj}^{(2)}; \overline{K}_{iljj}^{(3)}; \overline{K}_{illj}^{(3)} \\ \underline{u} &= q_j \underline{\Psi}_j + q_l \underline{\Psi}_l + q_p \underline{\Psi}_p \rightarrow \overline{K}_{iljp}^{(3)}$$



Ira A. Fulton School of Engineering
Department of Mechanical and Aerospace Engineering



BASIS (MODES) SELECTION

- * At least the mode shapes excited in the linear case
- * Any mode shape excited by internal/combination resonance
- * More basis functions to represent nonlinearity....

Example: flat structure (beam, plate) with transverse loads

Large displacement in the transverse direction induce inplane displacements that softens the nonlinear response. They/their effects must be captured for accurate transverse deflections.

Solution: use more linear modes, or use “dual modes”

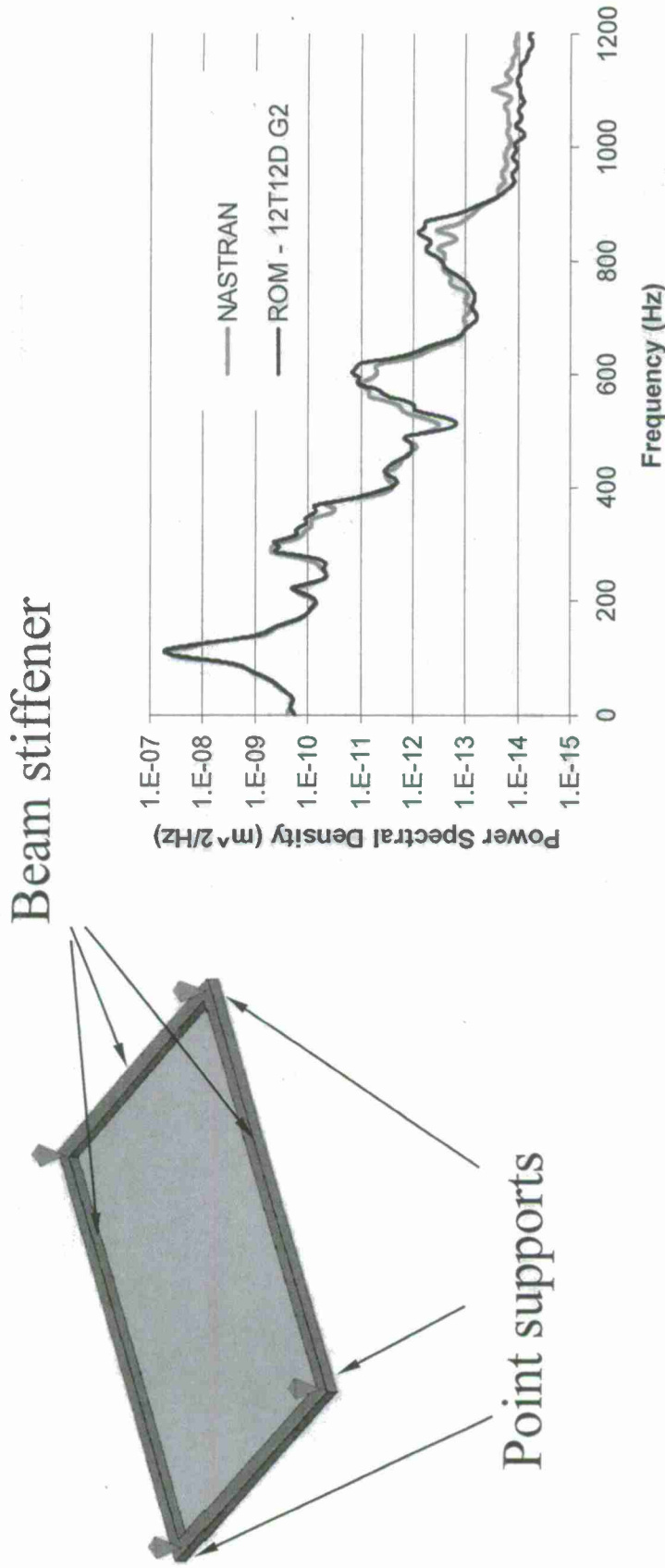
static nonlinear solutions that corresponds to typical responses of the system



*Ira A. Fulton School of Engineering
Department of Mechanical and Aerospace Engineering*



APPLICATION #1: ISOTROPIC STIFFENED PANEL



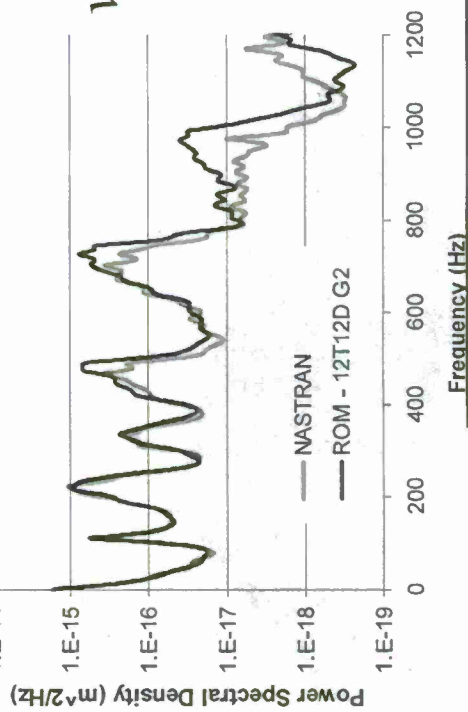
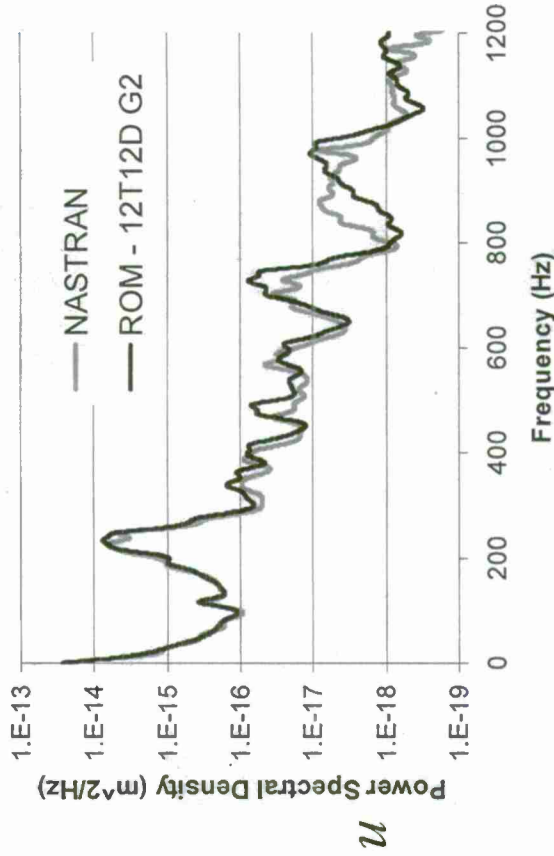
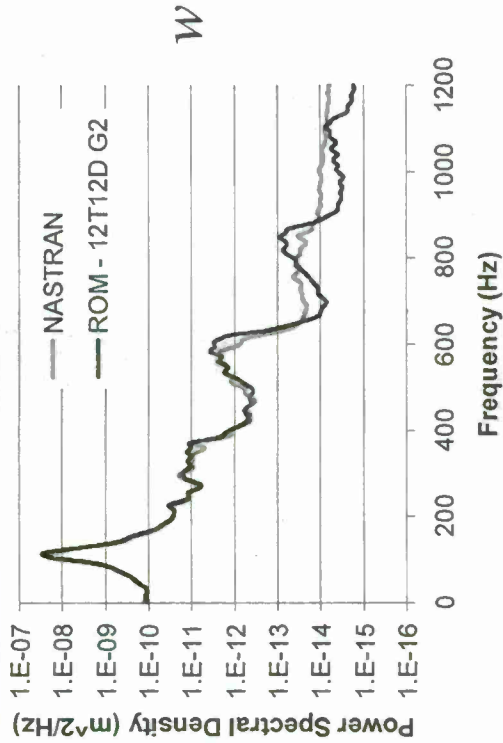
Transverse deflection at the center of isotropic (Al) plate,
random (white noise) uniform loading - $OASPL = 147dB$



*Ira A. Fulton School of Engineering
Department of Mechanical and Aerospace Engineering*



APPLICATION #1: ISOTROPIC STIFFENED PANEL



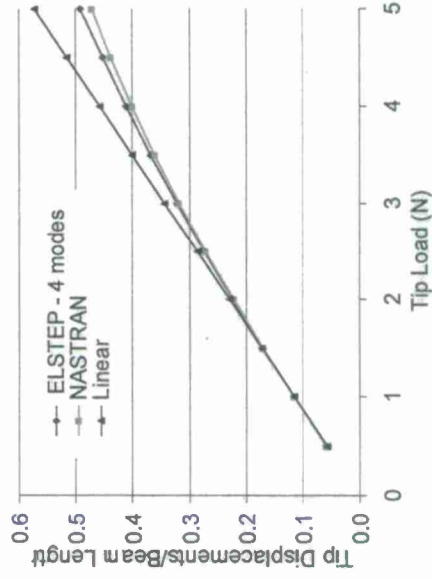
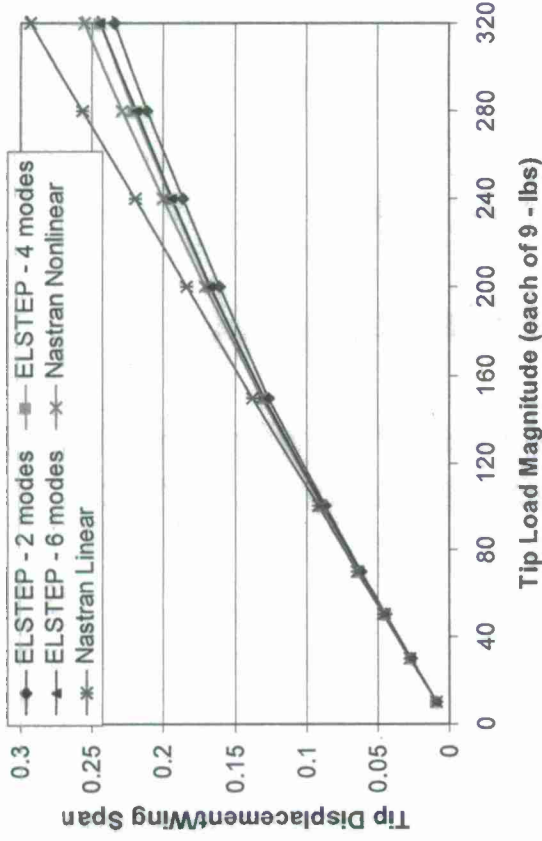
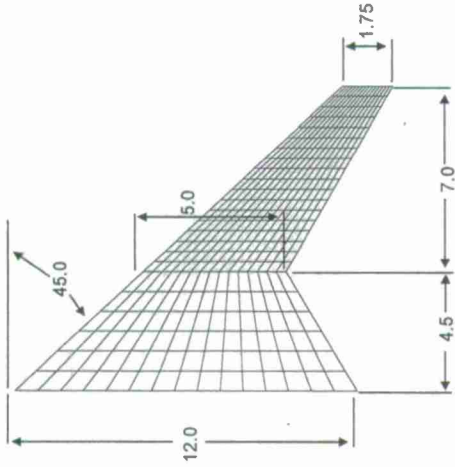
All 3 deflections at an arbitrary point of isotropic plate, random (white noise) uniform loading - $OASPL = 147dB$



Ira A. Fulton School of Engineering
Department of Mechanical and Aerospace Engineering

ASU

APPLICATION #2: WING MODELING FOR LCO



Cantilevered
Beam



Ira A. Fulton School of Engineering
Department of Mechanical and Aerospace Engineering



Attachment D

Aeroelastic ROM-ROM Methodology

***Presented at Workshop on Aeroelastic Certification: Tools,
Test, Decision Making, Sedona, AZ, October 2008***

Aeroelastic ROM-ROM Methodology

Danny D. Liu

P.C. Chen

Zhicun Wang

Shuchi Yang

Z. Zhang



ZONA TECHNOLOGY

Presented at the Aeroelastic Workshop in Sedona, AZ, October 28 – 29, 2008

9489 E Ironwood Square Dr. • Scottsdale • AZ 85258 • Tel (480) 945-9988 • Fax (480) 945-6588 • danny@zonatech.com

Aerodynamic ROM Approaches

• Various aerodynamic ROM methods

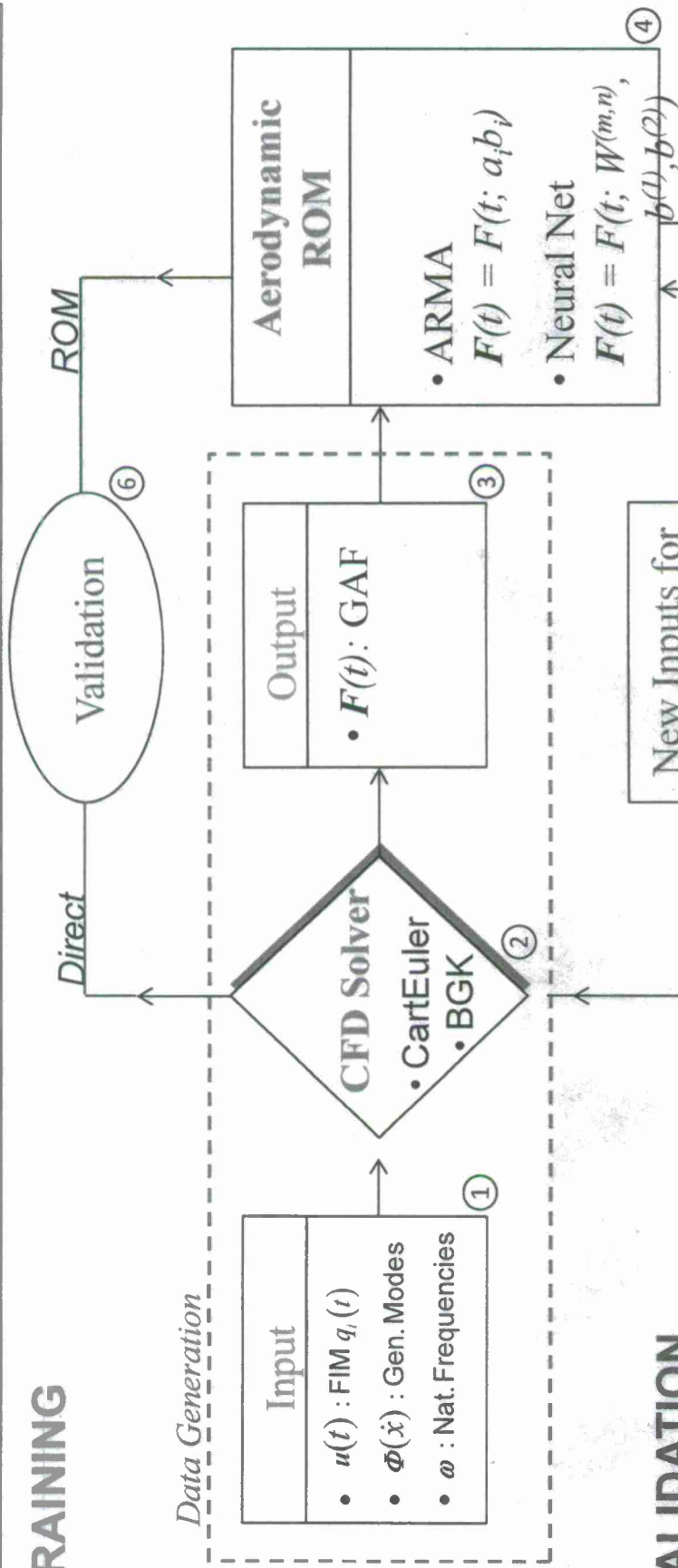
- POD/ROM-HB: Dowell (1995)
- Volterra: Silva (1993)
- ERA: Kim (2004)
- POD/ROM-Time Domain: Beran (2003)
- ARMA/N.Net: ZONA (2008)

• ZONA ROM-ROM

- Aerodynamic ROM adopts System Identify Technique to relate the generalized coordinate input to the GAF output.
- Aeroelastic ROM-ROM will dramatically reduce the computing time for flutter/LCO solutions.

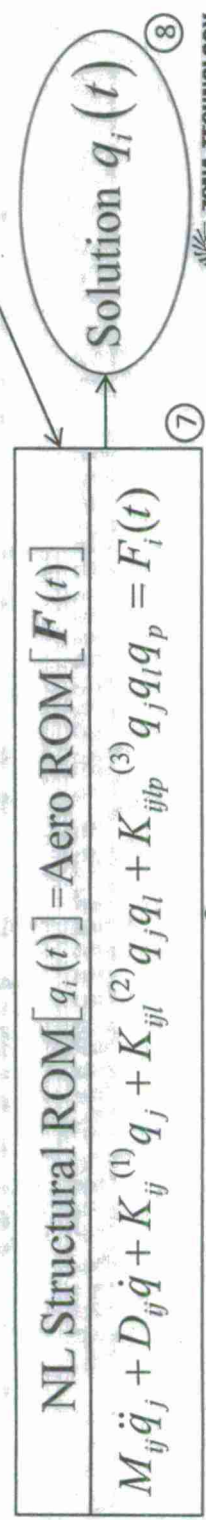
Aeroelastic ROM-ROM Roadmap

• TRAINING



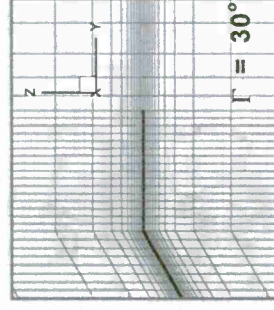
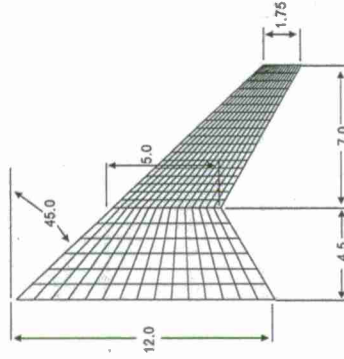
• VALIDATION

• ROM-ROM APPLICATIONS



Nonlinear Aerodynamics/Nonlinear Structure Interaction (NANSI) for Morphing Vehicles

Supported by AFOSR/AFRL under STTR Phases I and II (AF06-T016)



D.D. Liu, P.C. Chen, Z. Zhang,
Z. Wang, S. Yang, and D.H. Lee



ZONA TECHNOLOGY

Prof. Marc Mignolet



Prof. Feng Liu



Prepared for the Aerospace Flutter and Dynamics Council Meeting, Boston, MA, October 25-26, 2007

9489 E Ironwood Square Dr. • Scottsdale • AZ 85258 • Tel (480) 945-9988 • Fax (480) 945-6588 • danny@zonatech.com

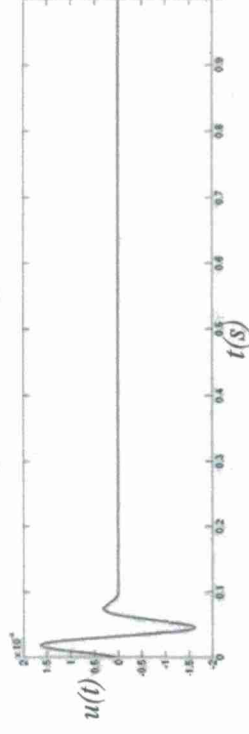
Aerodynamic ROM Input

- Filter Impulsive Method (FIM) signals are chosen as excitation signals for their
 - Broader range of frequency with concentration on the frequency of interest.
 - Symmetric about zero axis.

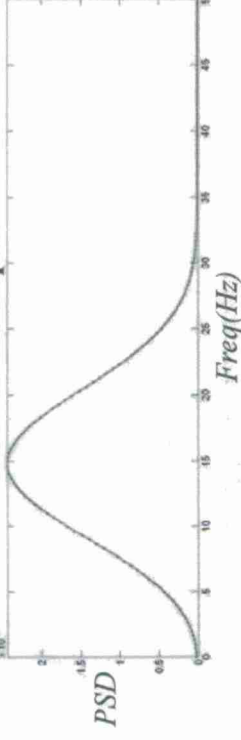
- A FIM signal is given by:

$$u(t) = \begin{cases} Ae^{\alpha_0(\omega t - \omega t_0 - \pi)^2} \sin(\omega t - \omega t_0) & \text{when } t \geq t_0 \\ 0 & \text{when } t < t_0 \end{cases}$$

• Input FIM Signals



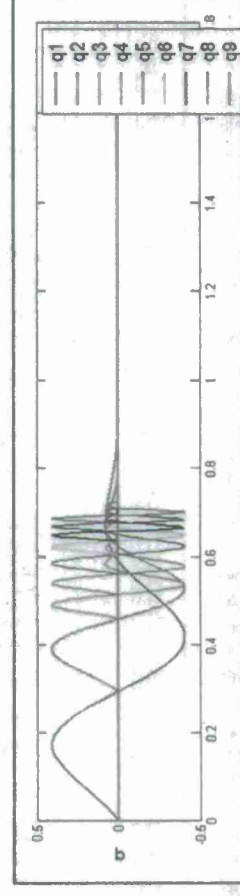
• FFT of the Input



- A **staggered** sequence FIM input of modal coordinates is employed.

- Each mode uses its own natural frequency as the ω .

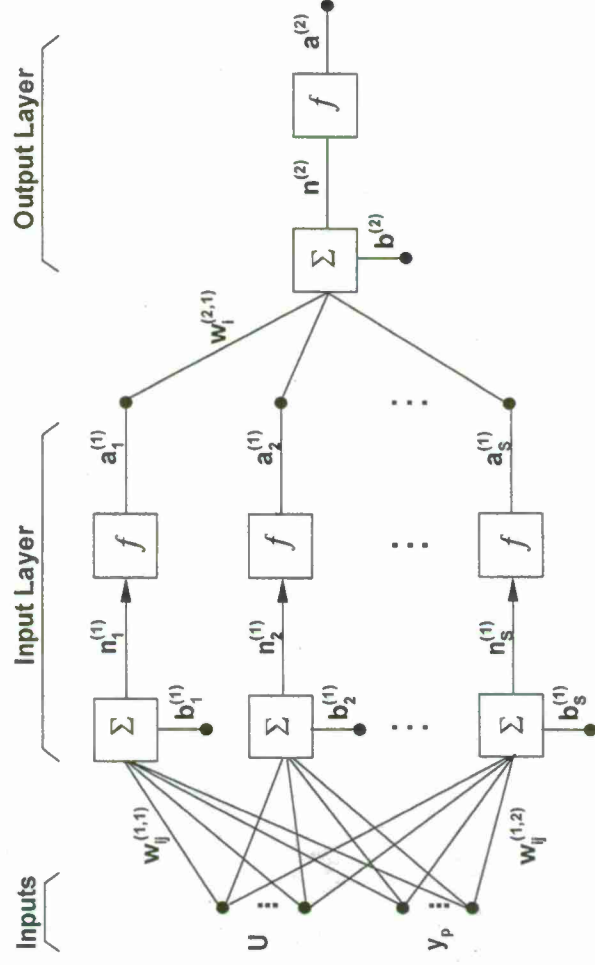
- The lowest order goes first.



Neural Net for Nonlinear Aero ROM

- The modeled plant output at time t by the neural network would be given in a concise notation as:

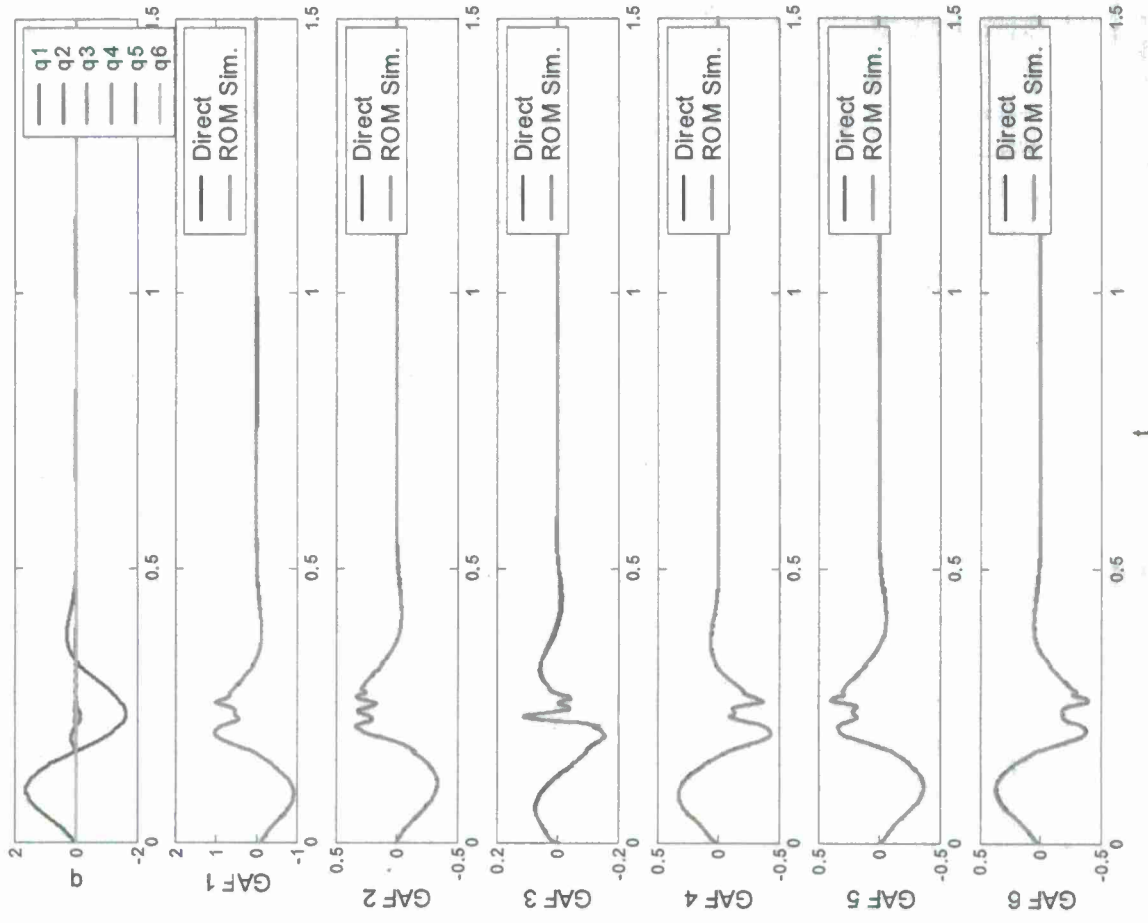
$$y(t) = a^{(2)} = W^{(2,1)} \cdot \tanh \left(W^{(1,1)} \cdot U + W^{(1,2)} \cdot y_p + b^{(1)} \right) + b^{(2)}$$



Two-layer Feed-Forward Neural Network

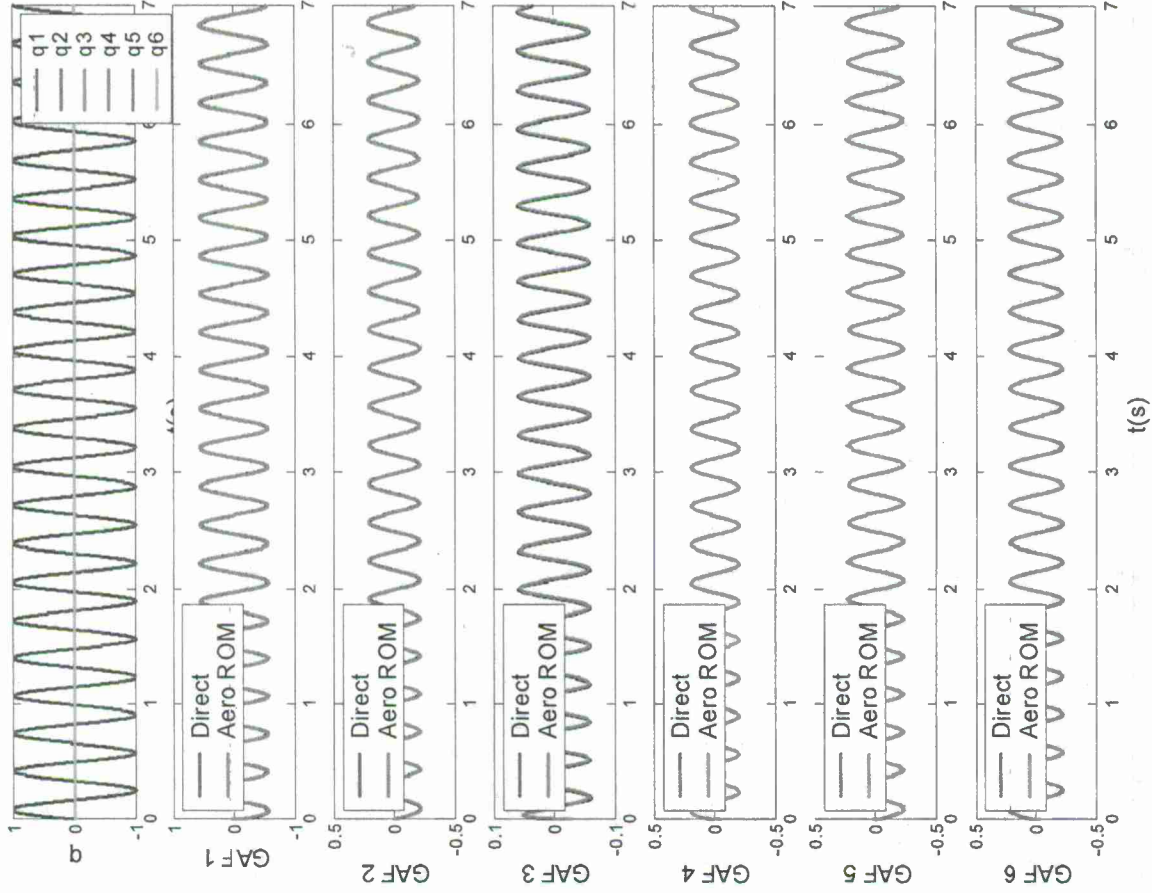
- Using the training data, an optimization procedure is implemented to search for the best parameters $W^{(1,1)}$, $b^{(1)}$, $W^{(2,1)}$ and $b^{(2)}$ by minimizing the mean square of the error between model output and targeted output or the generalized mean square error.

Aero ROM Training: Fold Wing ($\Gamma=0^\circ$)



- The nonlinear structural ROM uses the first 6 transverse modes only, therefore Aero ROMs are developed for the first 6 transverse modes only as well (Mach=0.95, AoA=0).
- Staggered FIM signals are shown in the first sub-figure with the first modal coordinate more significant.
- ARMA models for the 6 normalized GAF are obtained by optimization procedure using the training data set
- Aero ROM predictions agree well with direct CartEuler outputs

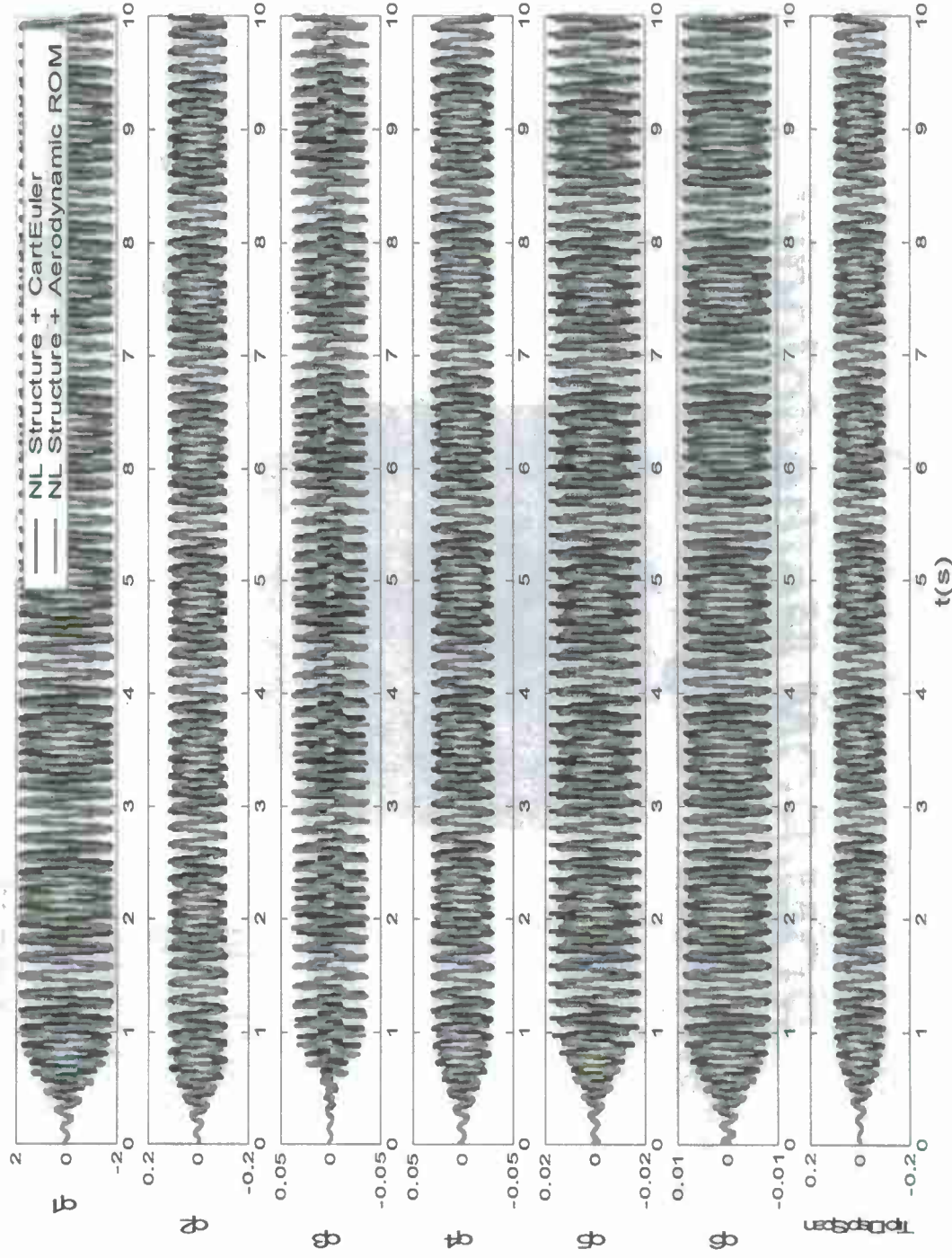
Validation of Aero ROMs: Fold Wing



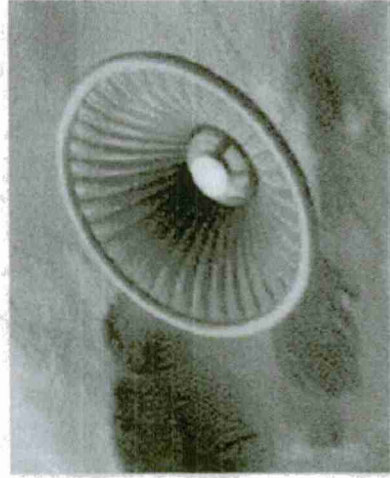
- The first sub-figure is the time histories of the modal coordinates providing inputs to both the aerodynamic ROMs and the direct CFL3D solver
- Specifically, only the first modal coordinate assumes a sinusoid time history while others are kept zero.
- Aero ROM predictions agree well with direct CartEuler outputs

ROM-ROM LCO Solutions: Fold Wing (II)

MACH = 0.95, AOA = 0 deg, Altitude = -10 Kft.



Nonlinear Aeroelastic Analysis using ROM/ROM Methodology: Membrane-on-Wedge with Attached Shock



Reentry aeroshell

Danny D. Liu
Zhicun Wang
Shuchi Yang
Chunpei Cai



ZONA TECHNOLOGY

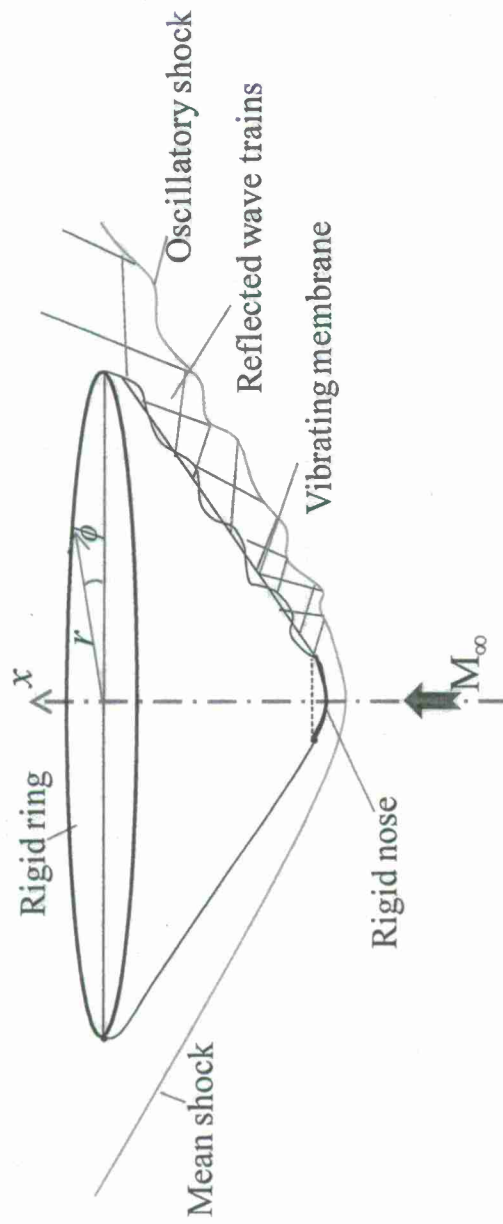
Marc Mignolet



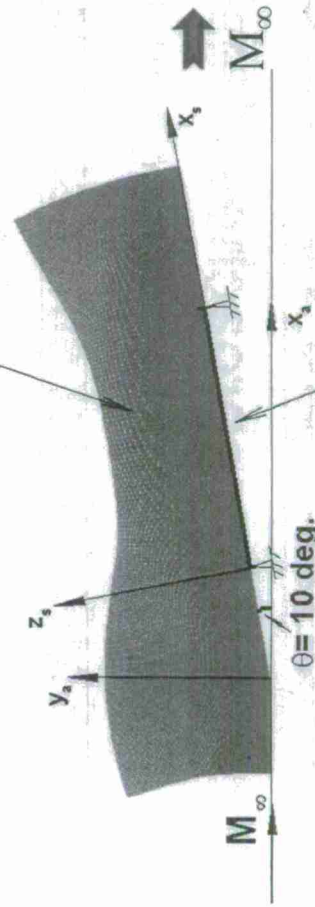
Presented at the Bifurcation & Model Reduction Techniques for Large Multi-Disciplinary Systems Meeting at the University of Liverpool 26-27 June, 2008

9489 E Ironwood Square Dr. • Scottsdale • AZ 85258 • Tel (480) 945-9988 • Fax (480) 945-6588 • danny@zonatech.com

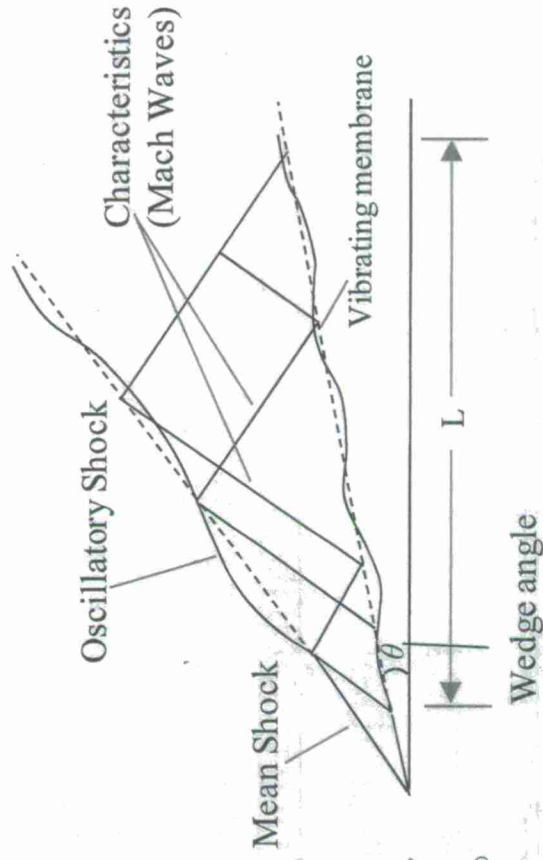
Membrane-on-Wedge



BGKX/CFL3D Computational Grid



Simply-Supported Flexible Panel



BGK- All Mach, Rarefied-to-Continuum Eqn

: Microscopic vs Macroscopic Approaches

- Microscopic approaches (Gaskinetic)
 - Flow parameter: Knudsen number
 - DSMC (direct simulation Monte Carlo)
 - Boltzmann Eqn. (Integro-Differential Eqn.)

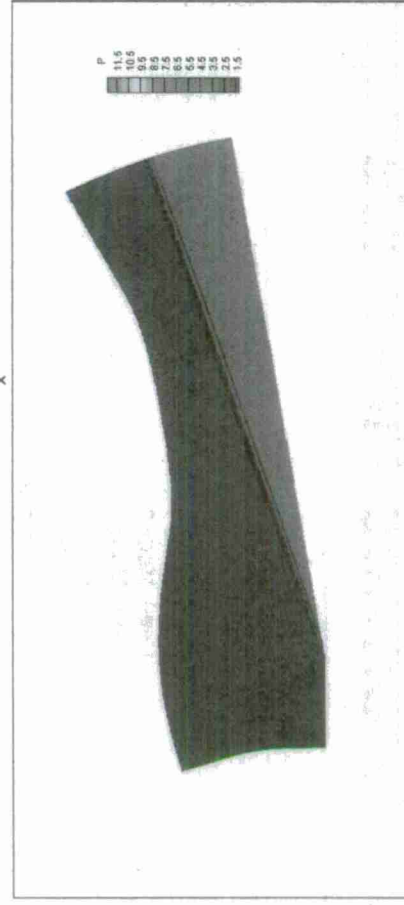
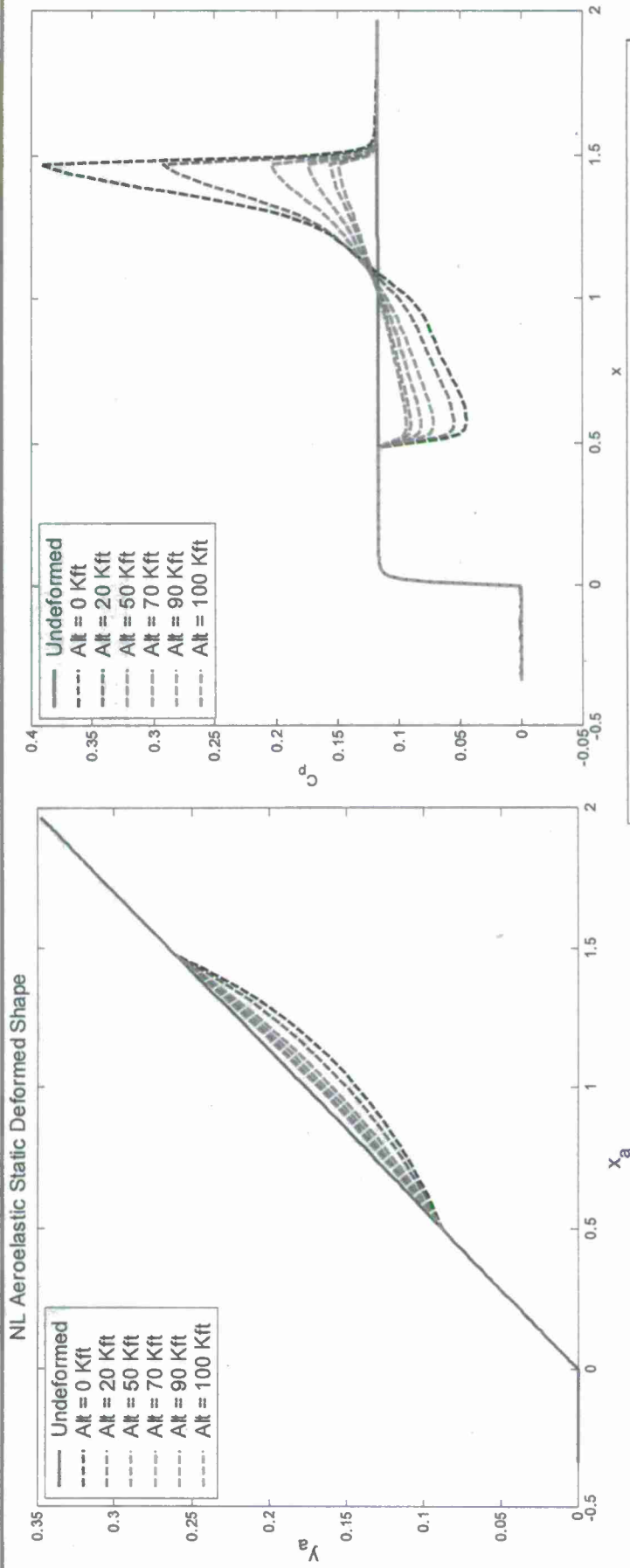
$$\left(\frac{\partial}{\partial t} + u \frac{\partial}{\partial x} \right) f = I[f_1 f_2, f_1' f_2']$$

- BGK Eqn. (approximation of Boltzmann)

$$\left(\frac{\partial}{\partial t} + u \frac{\partial}{\partial x} \right) f = \frac{g - f}{\tau}$$

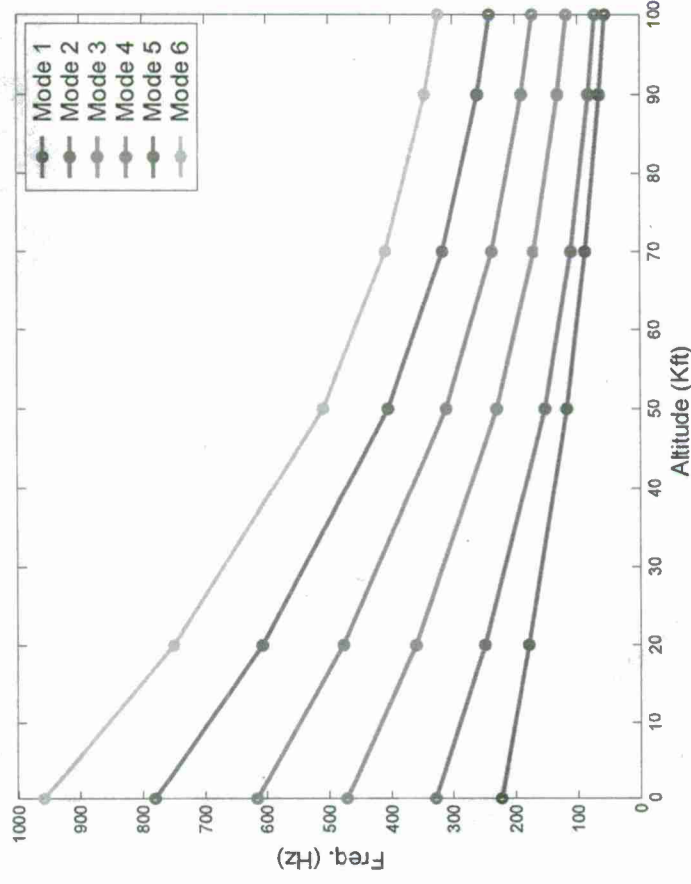
- Macroscopic approaches (Continuum)
 - Flow parameters: Mach no., Reynolds no.
 - All continuum methods: Euler, N-S, etc.

NL AE Static Deformed Shapes for Membrane-on-Wedge: BGKX Solutions @ M5.0



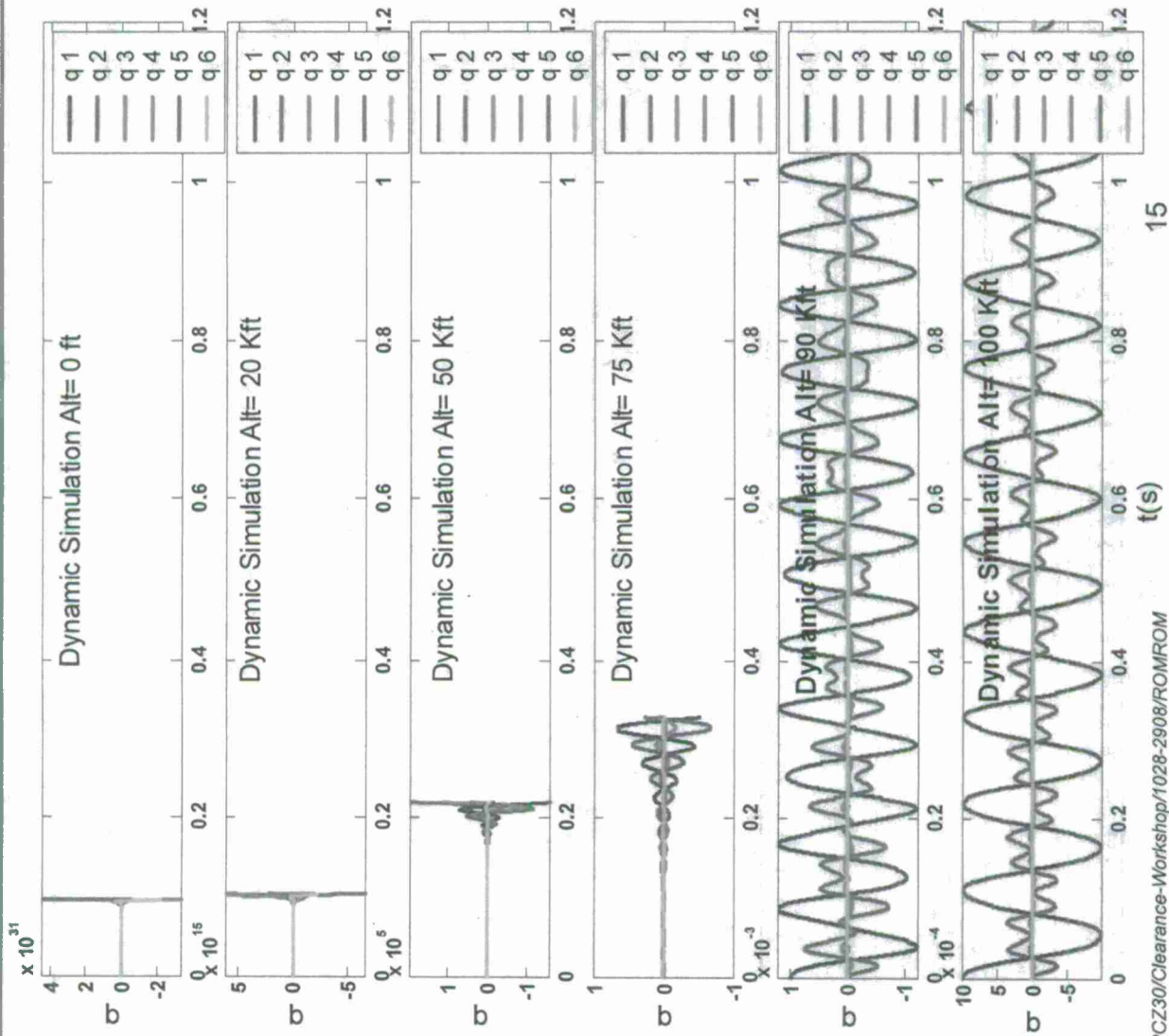
- Nonlinear aeroelastic static deformed shapes for the flexible membrane at various altitudes represented in the aerodynamic coordinate system

Linearized Stiffness for *Deformed Mean Wedge*



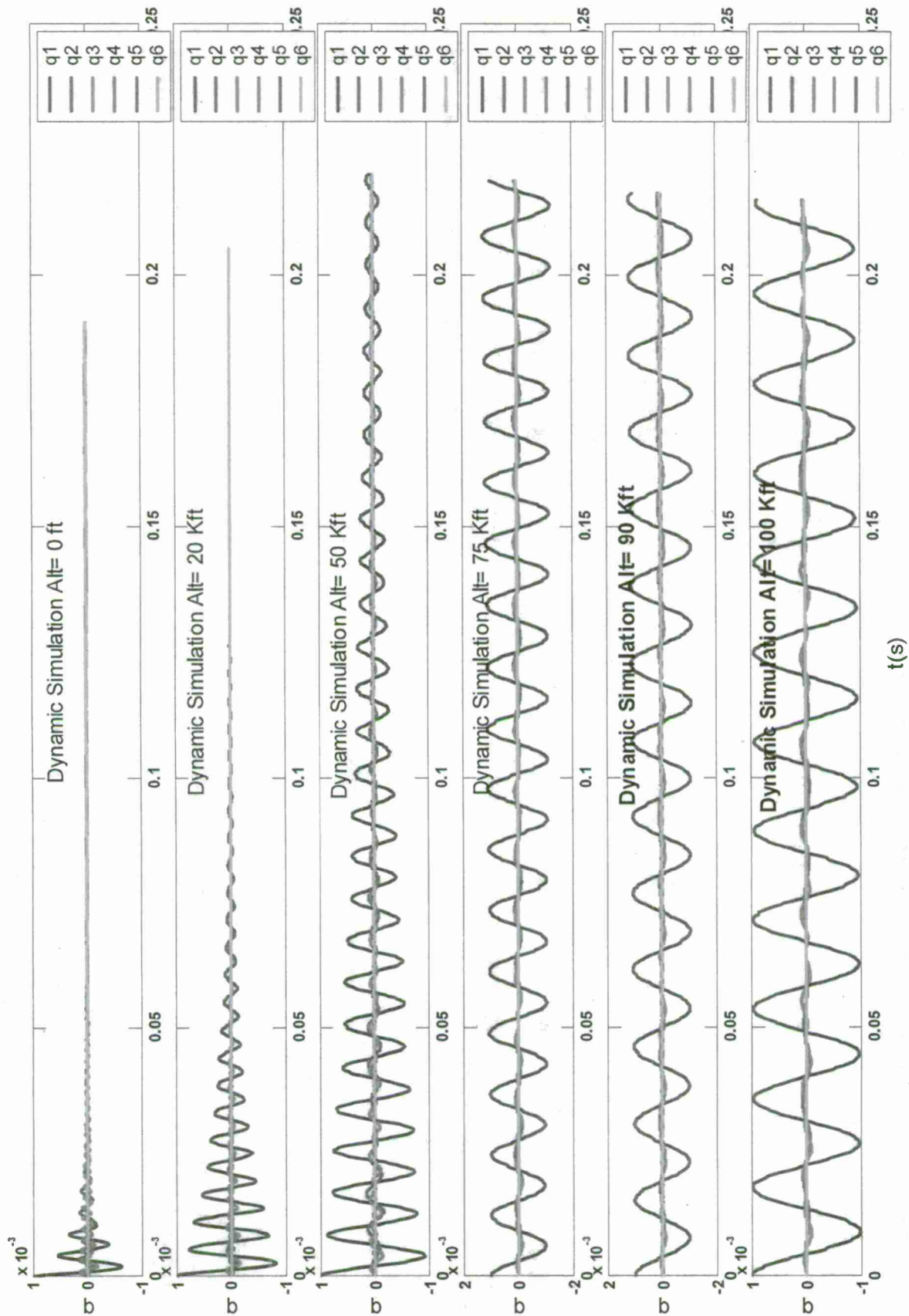
- Change of the natural frequencies around the deformed mean wedge configuration at various altitudes

ROM-ROM Flutter Analysis: Undeformed Mean Wedge



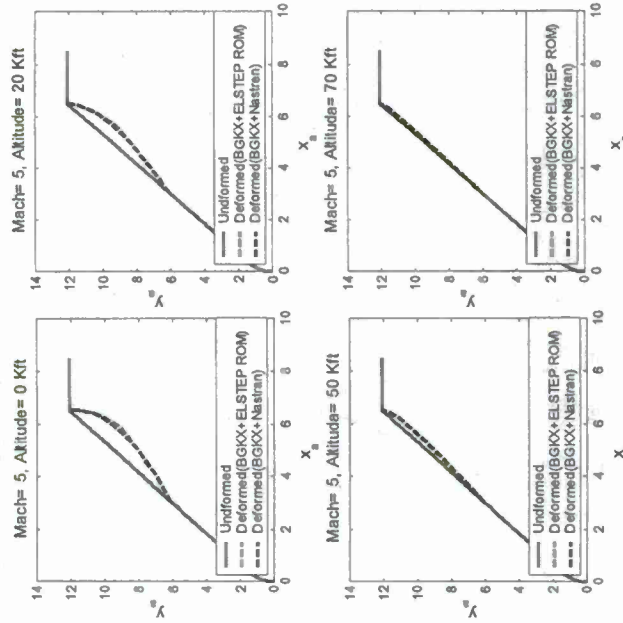
- Conventional type of flutter analysis: linear structural EOM unchanged as altitude change
- Under our dynamic simulations, the first modal coordinate is given a small initial value; all the other initial conditions are zeros
- By varying the altitude (consequently, the free-stream speed and the dynamic pressure, i.e., the match-point methodology), one explores the decaying, near neutral, and diverging time responses.

ROM-ROM Flutter Analysis: Deformed Mean Wedge



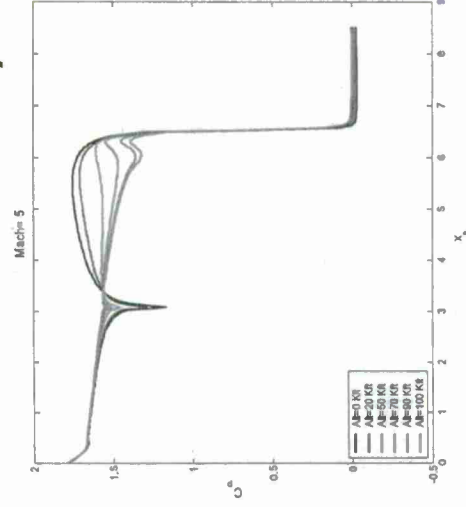
ROM-ROM on Membrane-on-Blunt Cone

Nonlinear Aeroelastic Deformed Ballute



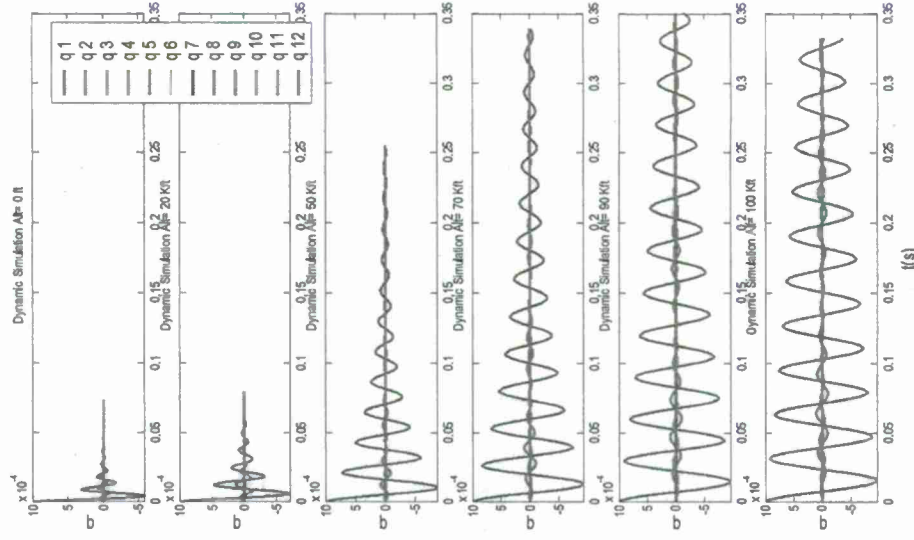
Nonlinear static deformed shape for the axisymmetric MBS at various altitudes

Deformed Ballute C_p



C_p distributions along the statically deformed axisymmetric MBS surface at various altitudes

Aeroelastic Responses of Deformed Ballute



$M=5.0 / h=SL-100K$

Aerodynamic Responses: Unsteady BGKX over Ballute



BGKX/CP: membrane-on-cone ($M_\infty = 5.0$, $\gamma = 1.4$, $k = 1.0$, $\delta = 0.10$)

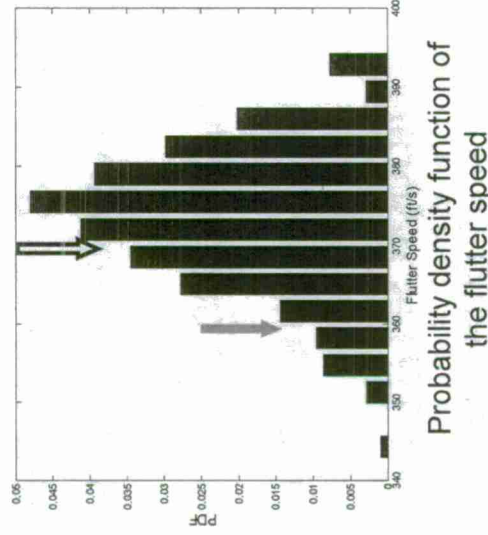
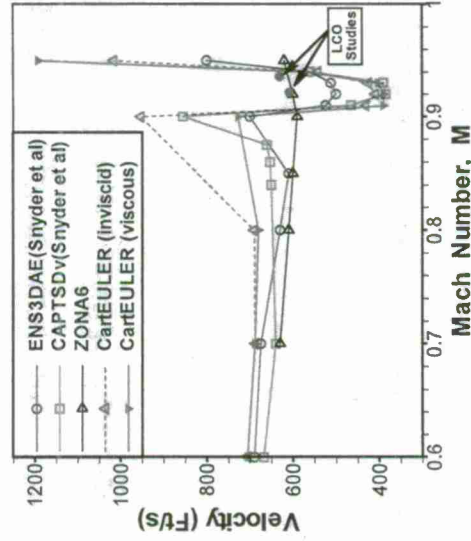
Conclusions

- Ballute aeroelastic problem requires Gaskinetic (microscopic) aerodynamics in the rarefied hypersonic flight regime.
 - Boltzmann/BGK method (time accurate) is adopted
- Ballute is an inflatable (nonlinear) structure
 - Nonlinear structural ROM (ELSTEP) is adopted
- Ballute flutter/LCO computation procedure needs to be expedited
 - ZONA's nonlinear/linear ROM-ROM procedures are adopted.
- Membrane-on-Ballute with Bow-Shock is modeled first by a 2D membrane-on-wedge with attached shock-- thus the present study

- *For a wedge with a mean deformed membrane, its stiffness increases with decreasing altitude, thus it becomes dynamically more stable – contrary to the outcome of undeformed membrane*



Flutter Analysis with Structural Uncertainty by Using CFD-based Aerodynamic ROM



Danny D. Liu
P.C. Chen



M. P. Mignolet



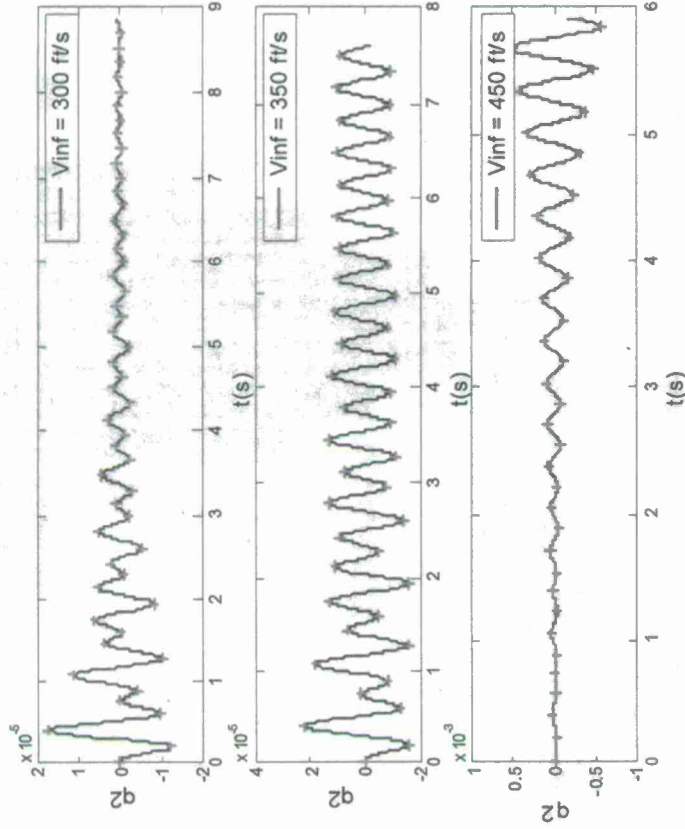
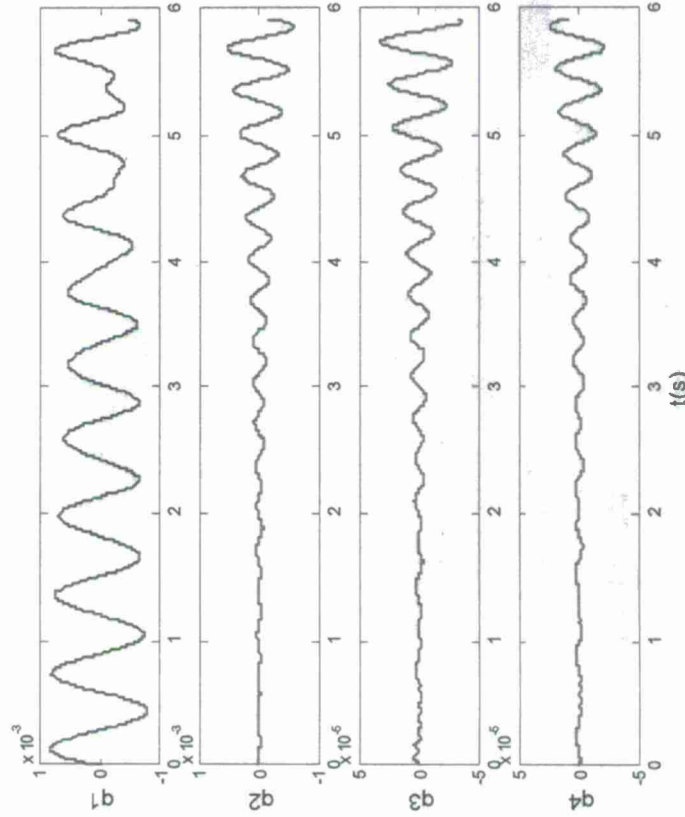
Prepared for Presentation at NATO, RTO, Advanced Methods in Aeroelasticity, Loen, Norway, May 5-8, 2008

9489 E Ironwood Square Dr. • Scottsdale • AZ 85258 • Tel (480) 945-9988 • Fax (480) 945-6588 • danny@zonatech.com

Application of ROM

Flutter Analysis on Goland Wing ($Mach = 0.92$)

- Time responses of the first four modal coordinates for the base-line Goland wing by ROM simulation at $V_{inf}=450$ ft/s



- The responses of the second mode for the base-line Goland wing using ROMs at various flight speed ($Mach=0.92$)

Transonic Flutter Uncertainty Findings

Flutter Analysis on Goland Wing (Mach = 0.92)

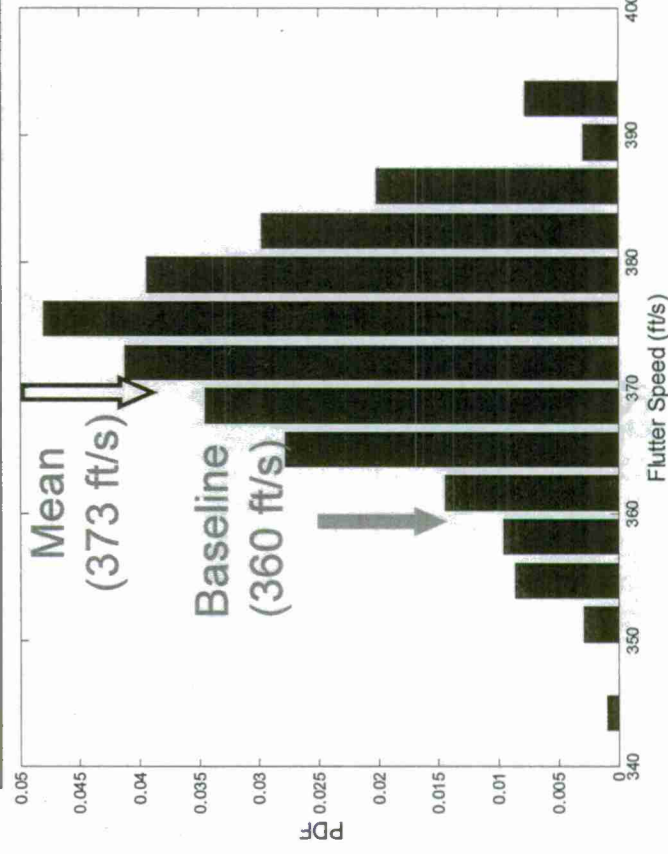
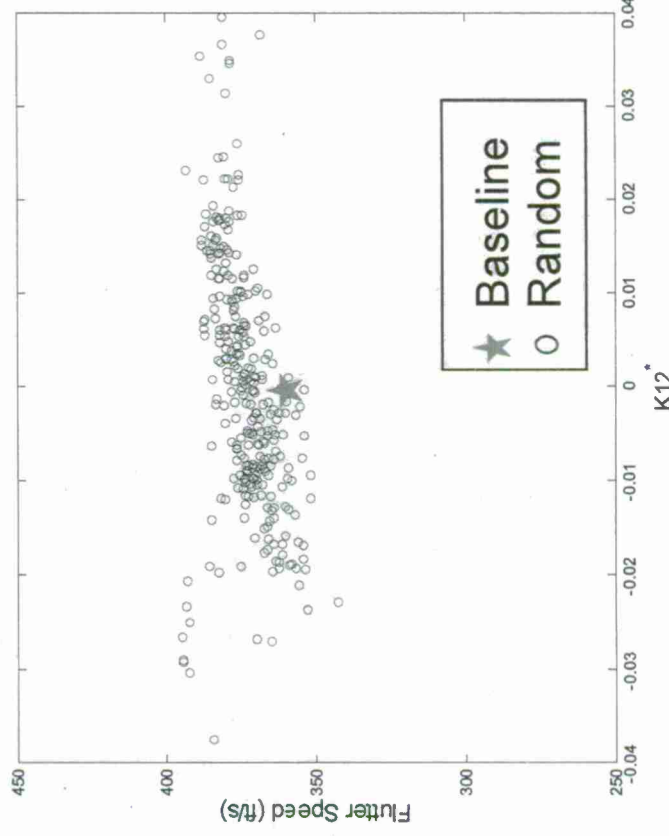
Input Data

- 1% standard deviation in the first natural frequency, 1.69Hz



Outcome

- 3.6% increase from the baseline in the mean flutter speed: 373 ft/s
- But only 2.4% standard deviation: 9 ft/s



Variations of the flutter speed

- 300 variations of the stiffness matrix

Probability density function of the flutter speed

Concluding Remarks

- Nonparametric approach directly address the uncertainty with the structural equations in the modal space. It is proven an efficient methodology for flutter analysis with structural uncertainty using CFD Aerodynamic ROM.
- *CFD-Based Aerodynamic ROM dramatically reduces CFD computing time for flutter computations from many hours to seconds.*
- Flutter uncertainty example showed: with 1% standard deviation in frequency it results in
 - Larger standard deviation in Subsonic than Transonic flutter speed (10% vs. 2.4%)
 - Smaller departure in Subsonic than Transonic mean flutter speed (-1.3% vs. 3.6%)

Fruit for Thought

How to preserve accuracy of Direct solution in Aerodynamic ROM solution?

- Problem with non-intrusive ROM as such
- System ID model structure selection
- Excitation amplitude/function effects

Overall concerns on Tools

- Modeling the structural damping for LCO
- Supersonic and Hypersonic tools



Differences among Various Aerodynamic ROMs

- Incomplete survey of various aerodynamic ROMs (Most of them, nonintrusive method)

Aero-ROM Type	System Outputs	Excitation Signal	Excitation Pattern	Frequency/ Time Domain	Linear/ Nonlinear
POD/ROM-HB (Dowell, Others)	Cp & Prime Variables	Sinusoidal	One by One	Frequency	Linear
Volterra (Silva, Others)	GAF	Impulse	One by One	Both	Both
		Step	One by One/ Staggered	Both	Both
ERA (Kim, Others)	GAF	Impulse	One by One/ Staggered	Time	Linear
POD (Beran, Others)	Cp & Prime Variables	Impulse	One by One	Time	Nonlinear
ARMA (Lai, Cowan, ZONA, Others)	GAF	3211 Multiple-Step	One by One	Time	Linear
		Gaussian-Filtered Noise	One by One	Time	Linear
		FIM	Staggered	Time	Linear
NNet (ZONA)	GAF	FIM	Staggered	Time	Nonlinear

Attachment E

***Morphing Wing Aeroelasticity by Continuous Dynamic
Simulation using Nonlinear Aerodynamic/Nonlinear Structure
Interaction (NANSI) Methodology***

Presented at NATO RTO Meeting, Lisbon, Portugal, April 2009

Morphing Wing Aeroelasticity by Continuous Dynamic Simulation using Nonlinear Aerodynamic/Nonlinear Structure Interaction (NANSI) Methodology



Dr. Danny D. Liu
Mr. P.C. Chen



Prof. Marc Mignolet



Prof. Feng Liu



Dr. Ned Lindsley
Dr. Phil Beran

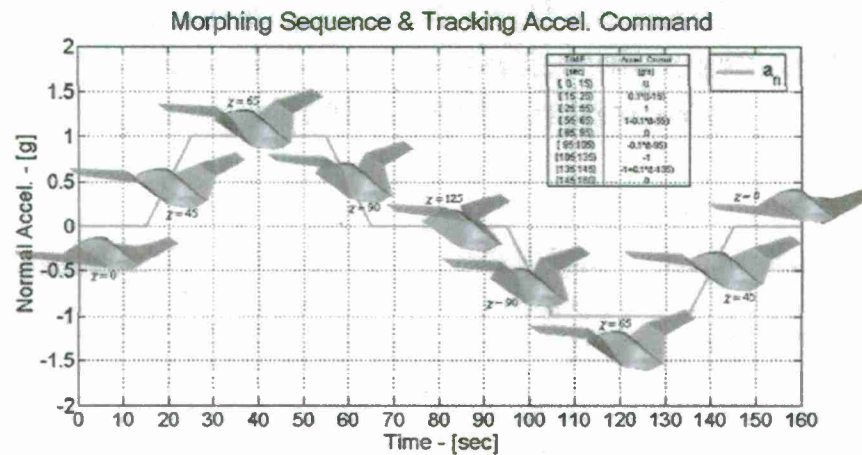
Presented at the NATO RTO Meeting in Lisbon, Portugal on April 20-24, 2009

9489 E Ironwood Square Dr. • Scottsdale • AZ 85258 • Tel (480) 945-9988 • Fax (480) 945-6588 • danny@zonatech.com

Background

- No computational tool available for transonic aeroelastic analysis of a vehicle morphing in a continuous dynamic manner
 - Currently, flutter solutions are obtained mostly using quasi-steady approach
- Study of time/configuration-varying aerodynamics, structure, and their interactions on aeroelastic stability requires proper computational methodology
 - Structural components exhibiting large deformation during morphing call for structural analysis with geometric nonlinearity
 - Transonic flow condition call for nonlinear aerodynamics
- Continuously varying configurations needs
 - Morphing structural dynamics
 - Morphing mesh for CFD
- Reduced order models (ROM) for computational efficiency
 - ROM of nonlinear structures
 - ROM of nonlinear aerodynamics
 - Coupling of aerodynamic ROM and structural ROM (ROM-ROM) for rapid nonlinear aeroelastic computations

Continuously Morphing Folding Wing in Time Domain



Approach

- Geometrically nonlinear structural dynamics of a morphing wing using sub-structuring technique
- Generation of structural ROM using ELSTEP/FAT
- Generation of aerodynamic ROM from the CartEuler code using two-layer feed-forward Neural Network
- Nonlinear aerodynamic and nonlinear structural interaction (NA NSI) for aeroelastic analysis of morphing wing
 - Coupling of structural ROM with direct CartEuler computation
 - Coupling of structural ROM with aerodynamic ROM (ROM-ROM)
- Validation on a modeled Lockheed-Martin folding wing

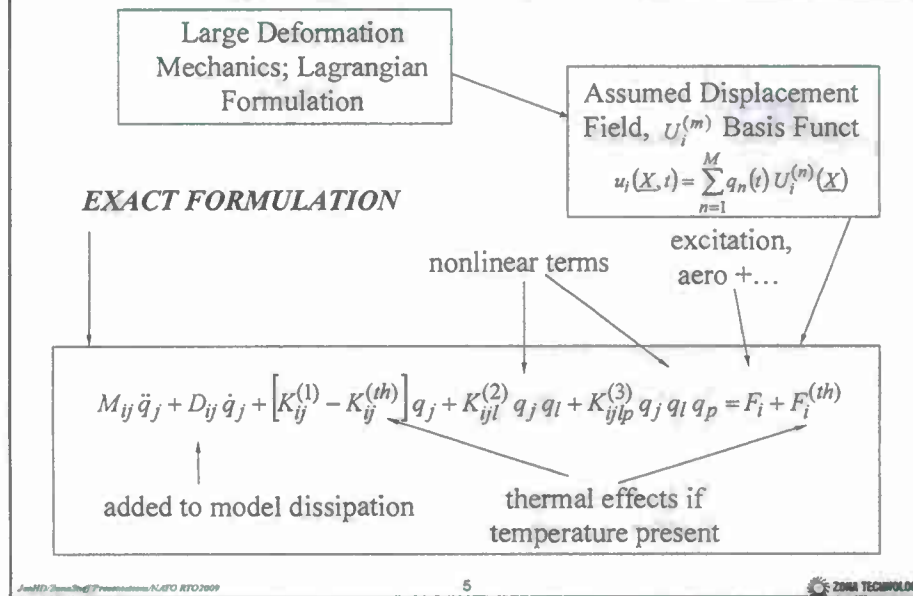


JaeHyunZhang@Presentations/NATO RTO2009

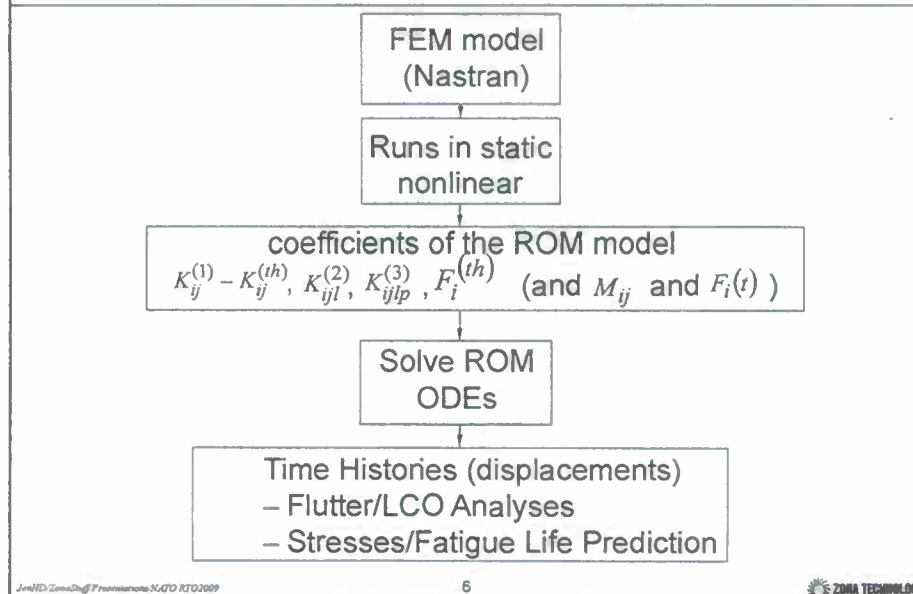
4

ZONA TECHNOLOGY

What is ELSTEP ? Nonlinear ROM Procedure

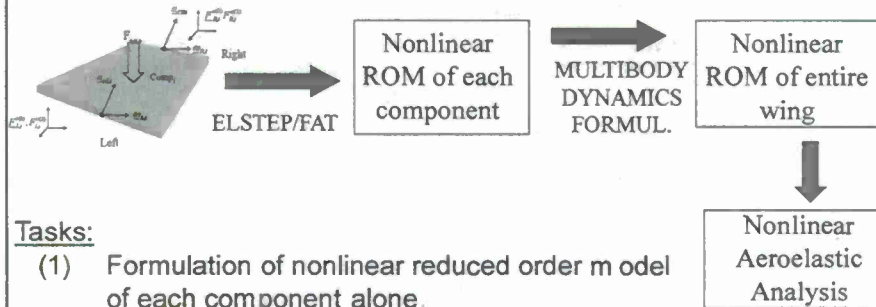


ELSTEP/FAT Operating on Nonlinear Nastran



Nonlinear Structures: Morphing Wing Dynamics

Nonlinear ROM of morphing wing development:



Tasks:

- (1) Formulation of nonlinear reduced order model of each component alone
- (2) Validations of component alone nonlinear ROMs
- (3) Assembly of component ROMs into wing ROM in large displacements
- (4) Validation of component ROM assembly (nonlinear static + linear dynamic - natural frequencies & modes)

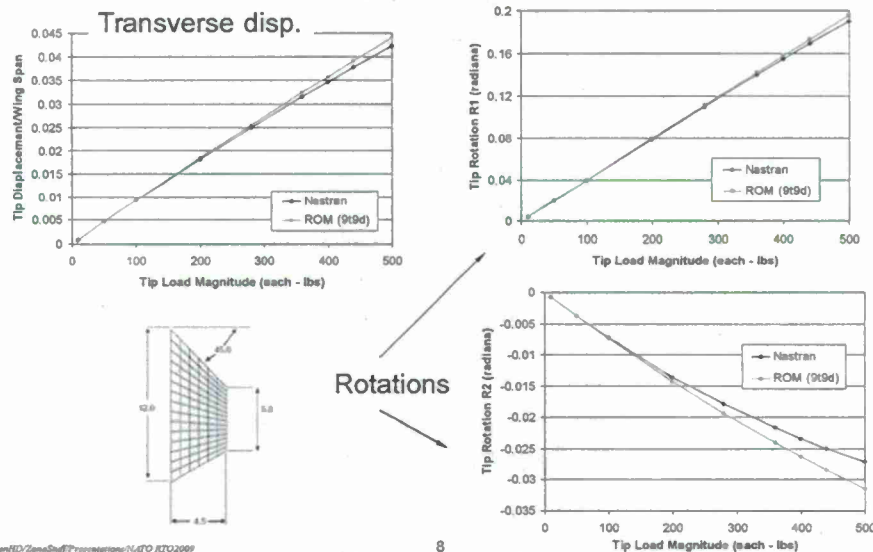
Jeroen Zama/Prof. Dr. Jeroen Zama/NATO RTO 2009

7

ZOMA TECHNOLOGY

Nonlinear Reduced Order Modeling

Validation: Wing - Inboard Alone



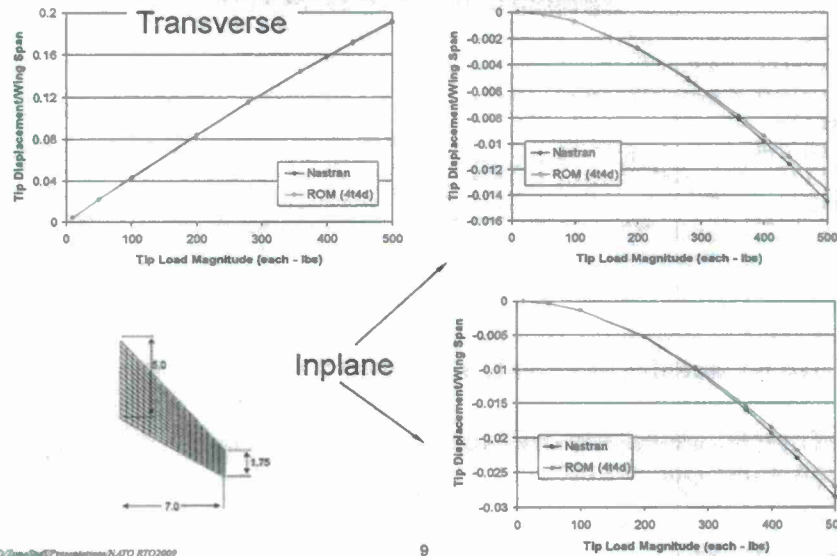
Jeroen Zama/Prof. Dr. Jeroen Zama/NATO RTO 2009

8

001

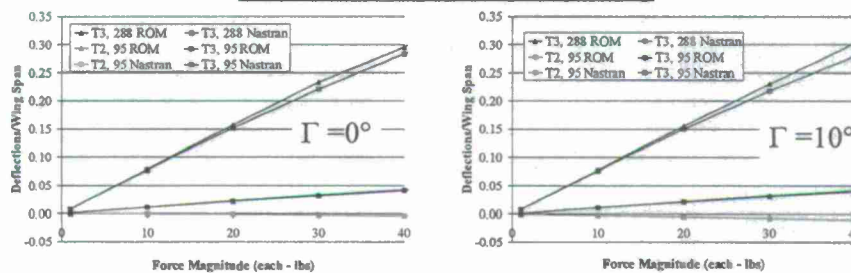
Nonlinear Reduced Order Modeling

Validation: Wing - Outboard Alone



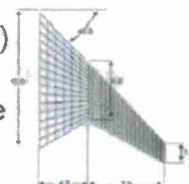
Nonlinear Static Validation of Full Wing Modeling

Validation: Entire Folding Wing



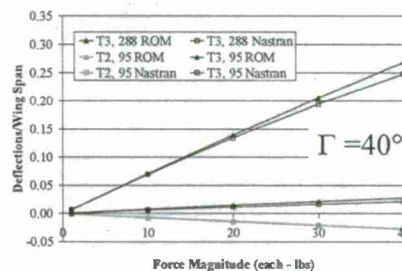
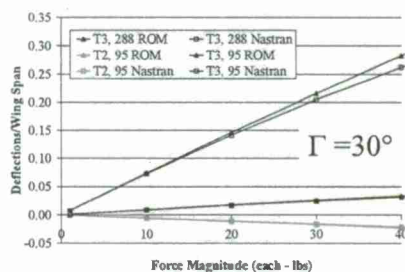
* Transverse displacement at wing tip ("T3, 288")

* Transverse/inplane displacements at hinge line ("T3,95" and "T2,95")

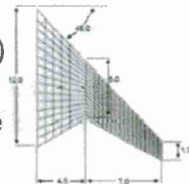


Nonlinear Static Validation of Full Wing Modeling

Validation: Entire Folding Wing



- * Transverse displacement at wing tip ("T3, 288")
- * Transverse/inplane displacements at hinge line ("T3,95" and "T2,95")



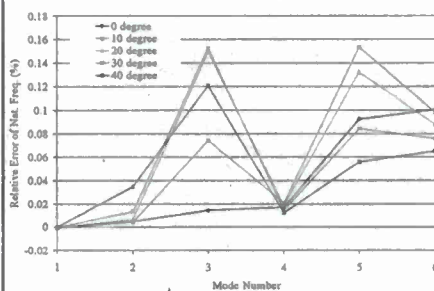
JsmHD/GamaSing/Presentations/NATO RTO2009

11

ZONA TECHNOLOGY

Linear Dynamic Validation of Full Wing Modeling

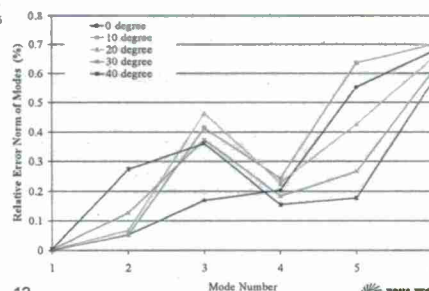
Validation: Entire Folding Wing



Natural frequencies

Modes

Prediction of full wing natural frequencies and modes at different morphing angles by substructuring vs. Nastran



JsmHD/GamaSing/Presentations/NATO RTO2009

12

ZONA TECHNOLOGY

CartEuler with Morphing Mesh

- CartEuler is ZONA's Euler Unsteady aeroelastic Solver to provide solutions for complex configurations. It uses Cartesian grid and employs boundary layer coupling.
- Cell-Centered finite volume method using Jameson's artificial dissipation scheme.
- Dual-time stepping algorithm for unsteady solution.
- Automated mesh generation scheme that requires only the surface mesh for input.
- Overset grid capability for complex configuration.
- Included ZAERO 3D spline module and Nastran modal solution importer.
- Parallel computation using OpenMP.
- Generates either time-domain aeroelastic responses or frequency-domain generalized aerodynamic forces for flutter, LCO, and static/trim aeroelastic analysis.
- Automated mesh generation scheme enables the generation of morphing mesh at each time step.

Click to Start Morphing Wing Video

NL Aeroelasticity of Continuously Morphing Folding Wing: Full-order Solutions

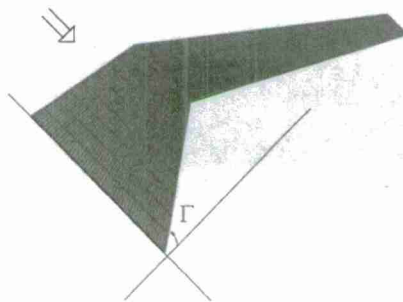
- Validation of the Substructure Model: Two-piece vs. One-piece Wings
 - 6 cases with folding-angle of 0° , 10° , 20° , 30° , 40° and 60°
 - Each case at 4 different altitudes ($H = 0$ Kft, 10Kft, 20Kft, 30Kft)
- Quasi-steady Flutter Boundary: Folding Wing
- Continuous Morphing Simulation: Folding Wing
 - Comparison of aeroelastic responses due to three different morphing schedules ($M = 0.95$, $AOA = 0^\circ$, $H = 10$ kft)
 - morphing from 0° to 60° ($M = 0.95$, $AOA = 0^\circ$, $H = 14$ kft)
 - morphing from 60° to 0° ($M = 0.95$, $AOA = 0^\circ$, $H = 14$ kft)

Jsm/HO/ZemaStg/Presentations/NATO STO2009

15

ZOMA TECHNOLOGY

Folding Wing Modeling



- One piece model
 - 6 modes for the whole wing defined in the global frame
 - Only for fixed folding angle simulation
- Two piece model
 - 13 modes each for inboard and outboard wing components
 - Additional 6 rigid-body modes for the outboard wing
 - Capable of handling continuous morphing situation

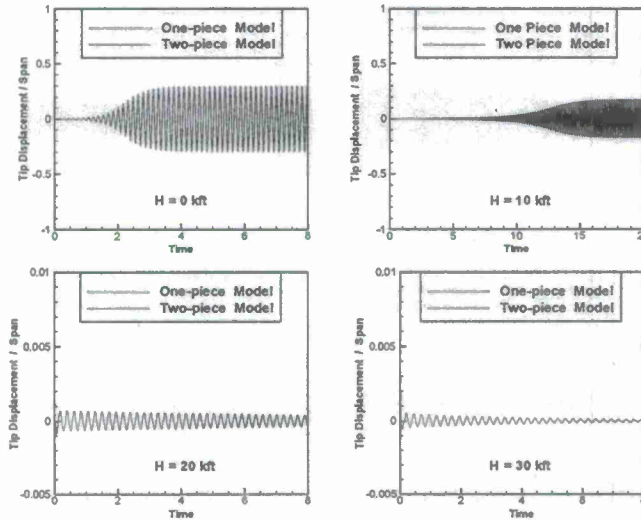
Jsm/HO/ZemaStg/Presentations/NATO STO2009

16

ZOMA TECHNOLOGY

Comparison of One-piece and Two-piece Models for Folding Wing

$M = 0.95, AOA = 0^\circ, \Gamma = 0^\circ$



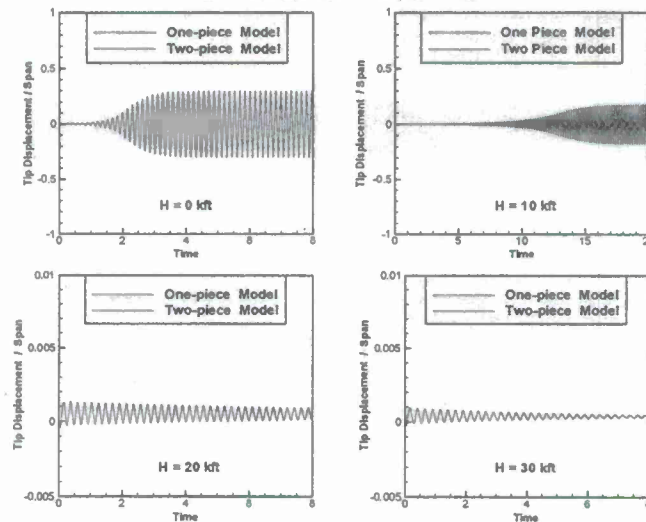
JsmFD/Zooming/Presentations/NATO RTD2009

17

ZONA TECHNOLOGY

Comparison of One-piece and Two-piece Models for Folding Wing

$M = 0.95, AOA = 0^\circ, \Gamma = 10^\circ$



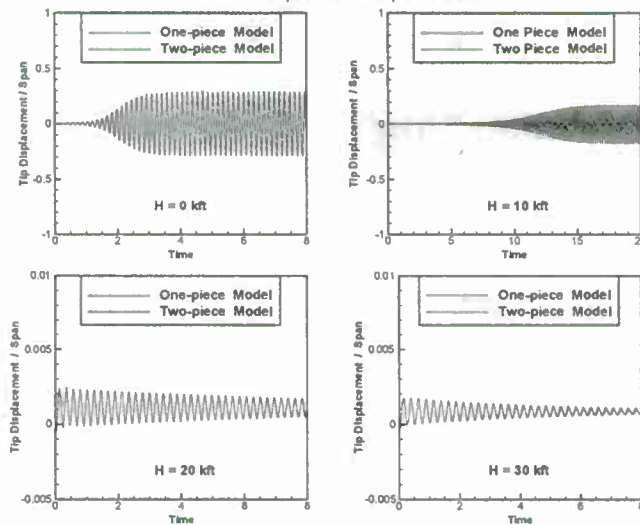
JsmFD/Zooming/Presentations/NATO RTD2009

18

ZONA TECHNOLOGY

Comparison of One-piece and Two-piece Models for Folding Wing

$M = 0.95$, $AOA = 0^\circ$, $\Gamma = 20^\circ$



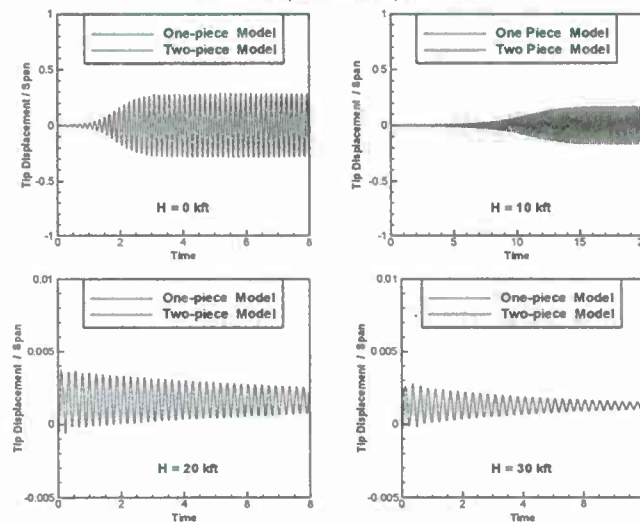
JenHD/ZonaSoft/Presentations/NATO RTO2009

19

ZONA TECHNOLOGY

Comparison of One-piece and Two-piece Models for Folding Wing

$M = 0.95$, $AOA = 0^\circ$, $\Gamma = 30^\circ$



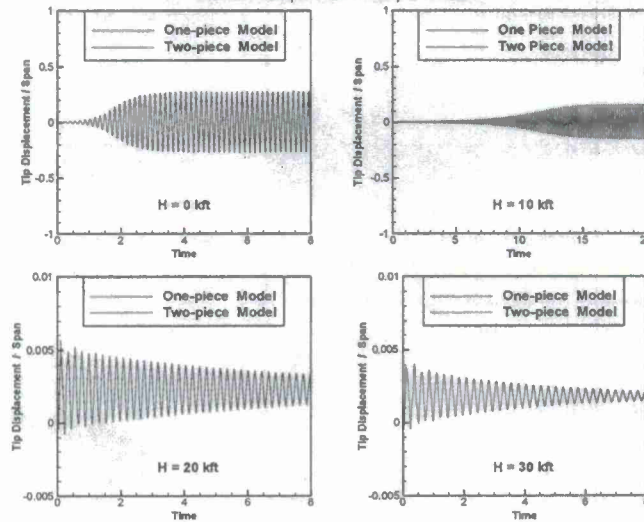
JenHD/ZonaSoft/Presentations/NATO RTO2009

20

ZONA TECHNOLOGY

Comparison of One-piece and Two-piece Models for Folding Wing

$M = 0.95$, $AOA = 0^\circ$, $\Gamma = 40^\circ$



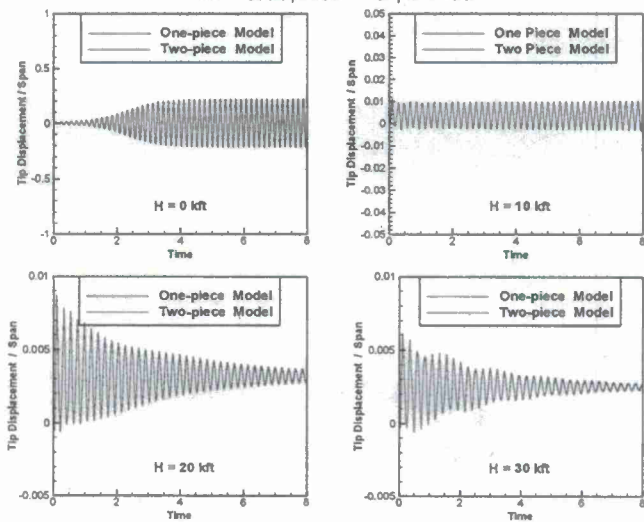
JamED/ZoneBridg/Prepresentations NATO RTG2009

21

ZONA TECHNOLOGY

Comparison of One-piece and Two-piece Models for Folding Wing

$M = 0.95$, $AOA = 0^\circ$, $\Gamma = 60^\circ$

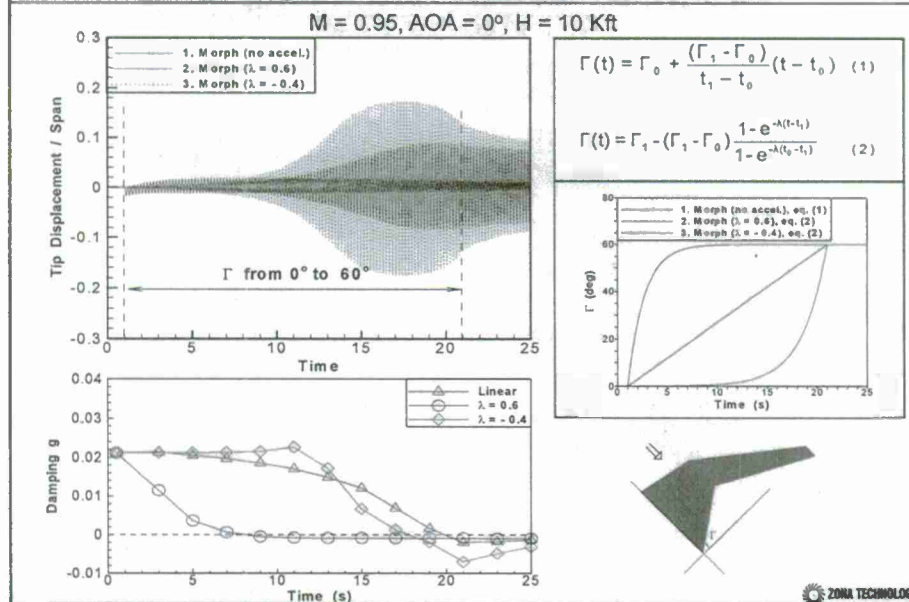


JamED/ZoneBridg/Prepresentations NATO RTG2009

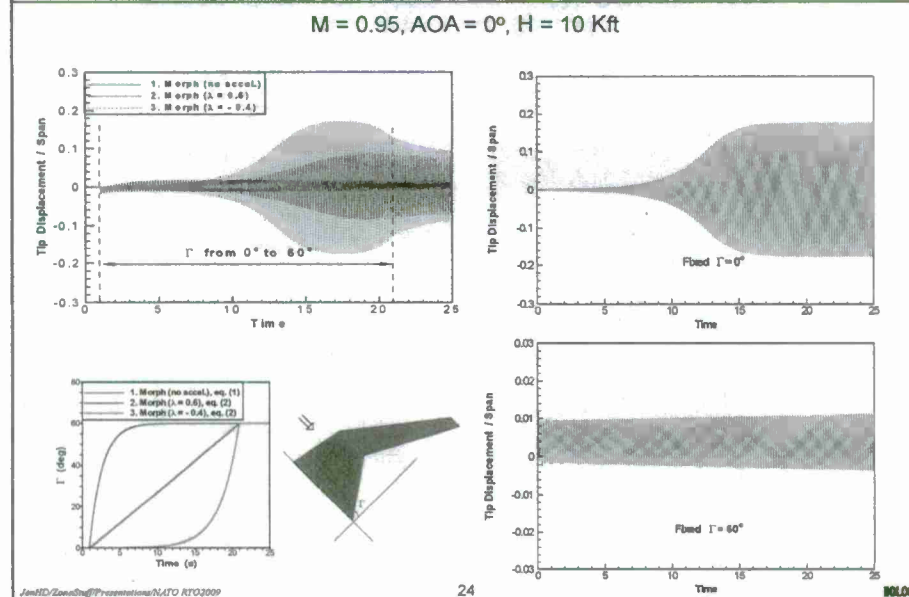
22

ZONA TECHNOLOGY

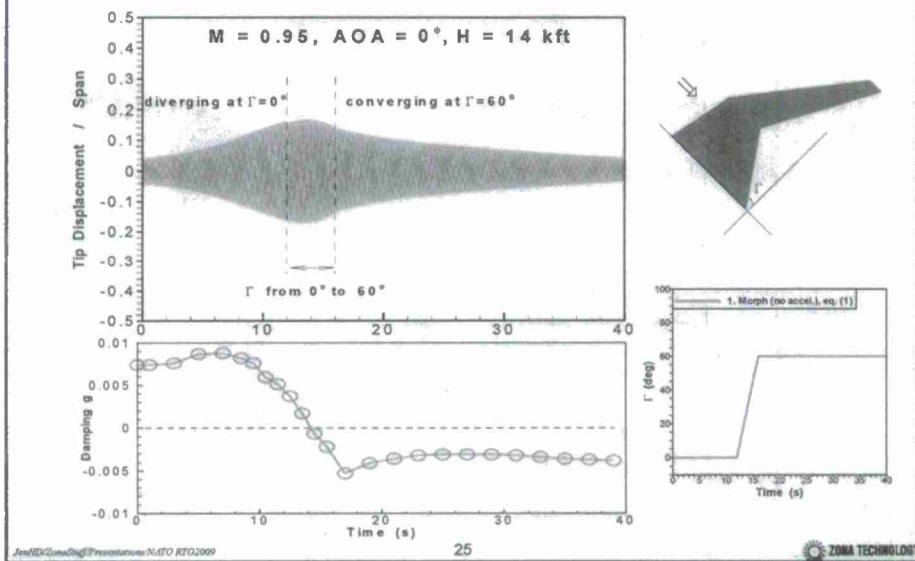
Aeroelastic Responses Due to Three Continuously Morphing Schedules: $\Gamma = 0^\circ \rightarrow \Gamma = 60^\circ$



Aeroelastic Responses Due to Three Continuously Morphing Schedules: $\Gamma = 0^\circ \rightarrow \Gamma = 60^\circ$

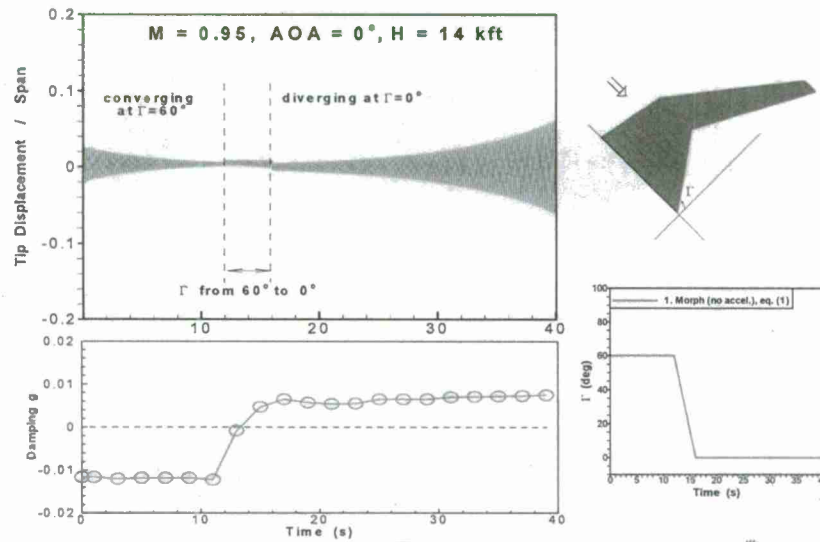


$\Gamma = 0^\circ \rightarrow \Gamma = 60^\circ$: Aeroelastic Response of Folding Wing in Continuously Morphing Motion (1)



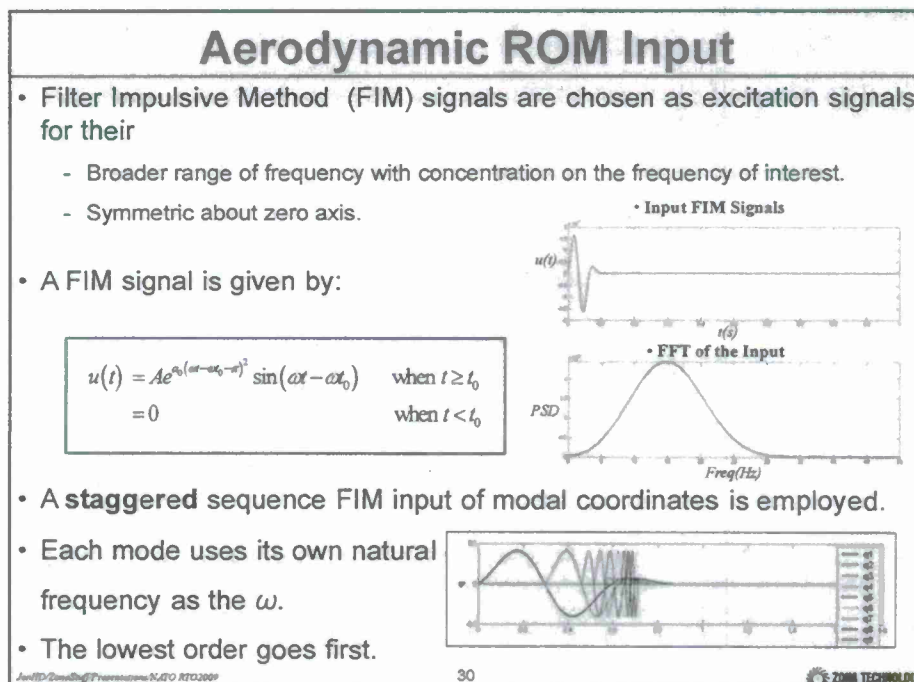
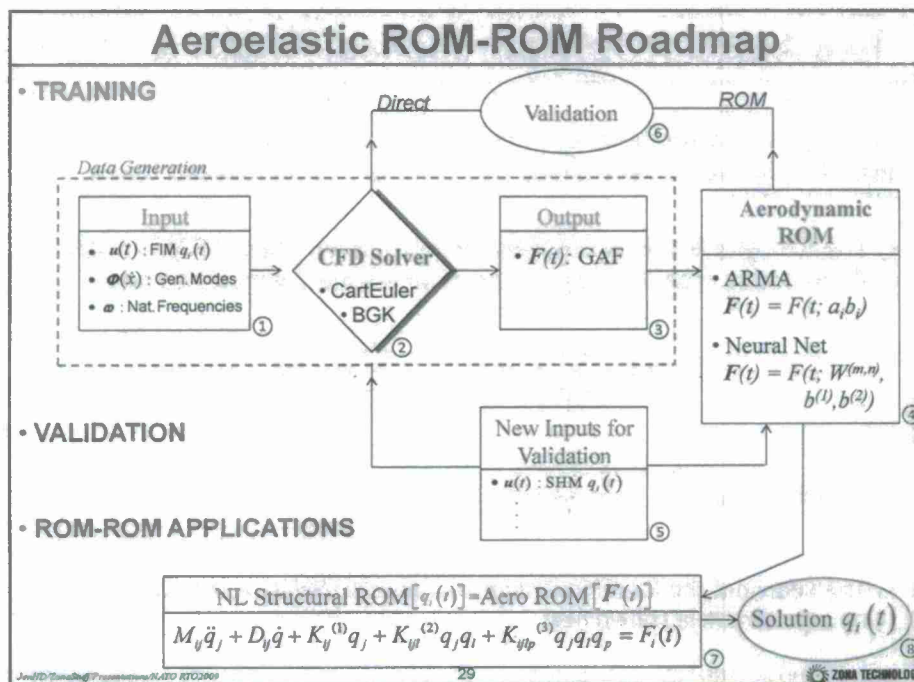
[Click to Start Folding Wing Video](#)

$\Gamma = 60^\circ \rightarrow \Gamma = 0^\circ$: Aeroelastic Response of Folding Wing in Continuously Morphing Motion (1)



Comparisons of Various Aerodynamic ROMs

Aero-ROM Type	System Outputs	Excitation Signal	Excitation Pattern	Frequency/Time Domain	Linear/Nonlinear
POD/ROM-HB (Dowell, Others)	Cp & Prime Variables	Sinusoidal	One by One	Frequency	Linear
Volterra (Silva, Others)	GAF	Impulse	One by One	Both	Both
		Step	One by One/Staggered	Both	Both
ERA (Kim, Others)	GAF	Impulse	One by One/Staggered	Time	Linear
POD (Beran, Others)	Cp & Prime Variables	Impulse	One by One	Time	Nonlinear
ARMA (Lai, Cowan, ZONA, Others)	GAF	3211 Multiple-Step	One by One	Time	Linear
		Gaussian-Filtered Noise	One by One	Time	Linear
		FIM	Staggered	Time	Linear
NNet (ZONA)	GAF	FIM	Staggered	Time	Nonlinear



Two AERO ROM Approaches: ARMA & NNET

Two types of discrete time modeling structures are used to represent the ROM between generalized coordinates and normalized GAFs.

- The first one is the autoregressive moving average (ARMA) model. By denoting y as the output, and u as the input vector, we have

$$y(t) = \sum_{i=1}^{n_a} a_i y(t-i) + \sum_{j=1}^{n_b} b_j u(t-j+1)$$

where n_a and n_b represent the order of the model.

- The second is the feed-forward neural network (NNet). A two layer neural network is shown next.

Jen-HD/ZomaSoft/Presentations/NATO_RTO2009

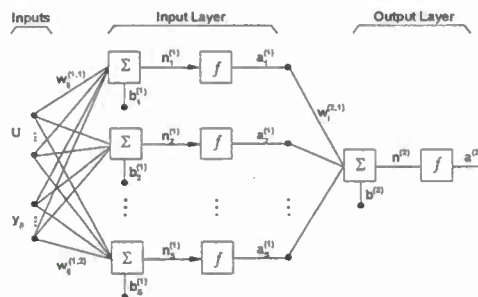
31

ZOMA TECHNOLOGY

Neural Net for Nonlinear Aero ROM

- The modeled plant output at time t by the neural network would be given in a concise notation as:

$$y(t) = a^{(2)} = W^{(2,1)} \cdot \tanh(W^{(1,1)} \cdot U + W^{(1,2)} \cdot y_p + b^{(1)}) + b^{(2)}$$



Two-layer Feed-Forward Neural Network

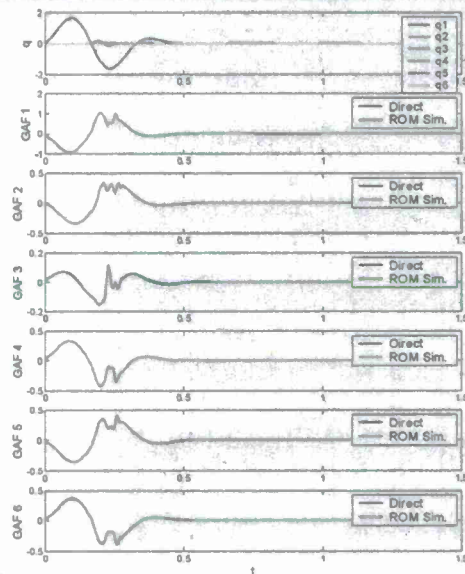
- Using the training data, an optimization procedure is implemented to search for the best parameters $W^{(1,1)}$, $b^{(1)}$, $W^{(2,1)}$ and $b^{(2)}$ by minimizing the mean square of the error between model output and targeted output or the generalized mean square error.

Jen-HD/ZomaSoft/Presentations/NATO_RTO2009

32

ZOMA TECHNOLOGY

Aero ROM Training: Folding Wing ($\Gamma=0^\circ$)



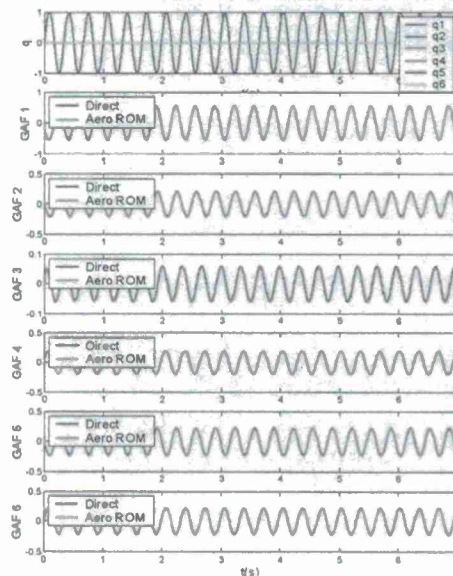
- The nonlinear structural ROM uses the first 6 transverse modes only, therefore Aero ROMs are developed for the first 6 transverse modes only as well (Mach=0.95, AoA=0).
- Staggered FIM signals are shown in the top figure with a significant first modal coordinate.
- NNet models for the 6 normalized GAF are obtained by optimization procedure using the training data set
- Aero ROM predictions agree well with direct CartEuler outputs

AmED/Summit/Presentations/NATO RTG2009

33

ZONA TECHNOLOGY

Validation of Aero ROMs: Folding Wing



- The top figure is the time histories of the modal coordinates providing inputs to both the aerodynamic ROMs and the direct CFL3D solver
- Specifically, only the first modal coordinate assumes a sinusoid time history while others are kept zero.
- Aero ROM predictions agree well with direct CartEuler outputs

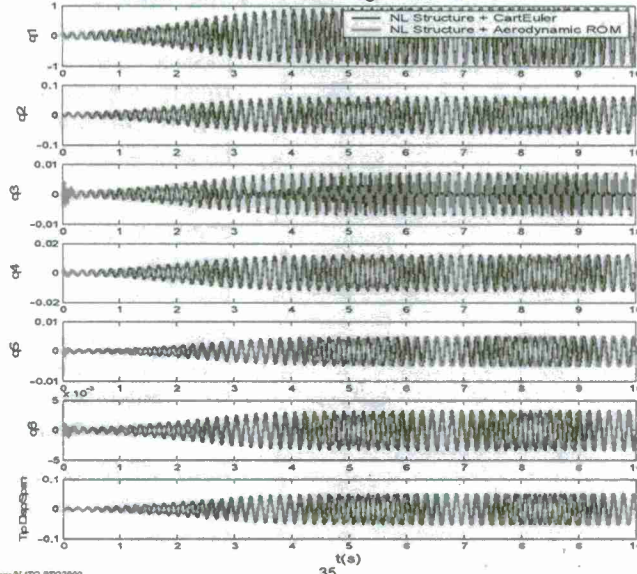
AmED/Summit/Presentations/NATO RTG2009

34

ZONA TECHNOLOGY

ROM-ROM LCO Solutions: Folding Wing (I)

Mach = 0.95, AoA = 0 deg, Altitude = 0 Kft



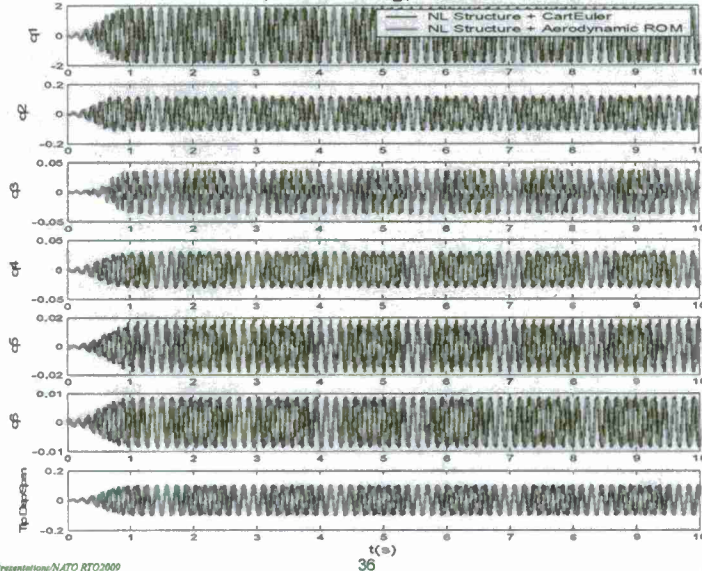
JenHD/ZonaSoft/Presentations/NATO_RTO2009

35

ZONA TECHNOLOGY

ROM-ROM LCO Solutions: Folding Wing (II)

Mach = 0.95, AOA = 0 deg, Altitude = -10 Kft.



JenHD/ZonaSoft/Presentations/NATO_RTO2009

36

ZONA TECHNOLOGY

Conclusions

- A nonlinear structural ROM procedure using ELSTEP/FAT has been developed for a rapid nonlinear aeroelastic analysis.
 - ELSTEP/FAT operates on Nastran nonlinear static analysis to generate the coefficients in the nonlinear stiffness matrices.
 - Once ROM is obtained, it can be repeatedly used for aeroelastic analysis at various flight conditions.
- The developed continuous morphing structural dynamics using sub-structuring technique
 - has been validated with structural solutions at various fixed morphing angles
 - can be combined with the nonlinear structural ROM procedure to establish a continuous morphing structural ROM
- The developed nonlinear aerodynamic ROM using Neural Network has been shown that
 - the nonlinear aerodynamic effects are fully retained when compared to the full-order solutions
 - the CPU time is reduced by two orders
- The developed nonlinear aerodynamic and nonlinear structural interaction (NANSI) procedure is
 - computational efficient for rapid aeroelastic analysis
 - applicable to the continuous morphing structure

Jianfeng.Zou@ZouaStr@Ppresentations: NATO STO/STO

37

 ZOUA TECHNOLOGY

Attachment F

Equations of Motion

The first step in obtaining the equations of motion for the entire morphing wing is to obtain the equations of motion for each of its components. In this regard, it has been argued that the hinge line should be rigid to allow for the proper rotation of the outboard wing with respect to the inboard one, see Figure F.1. Thus, the inboard and outboard wings both exhibit the same structure, i.e. rigid on one of its ends at least (both for the inboard). Then, the first step in the analysis, see section F.1, is the derivation of the equations of motion for such a component. Section F.2 will then cover the assembly of the component equations and section F.3 will discuss the linearization of the equations of motion for small deformations.

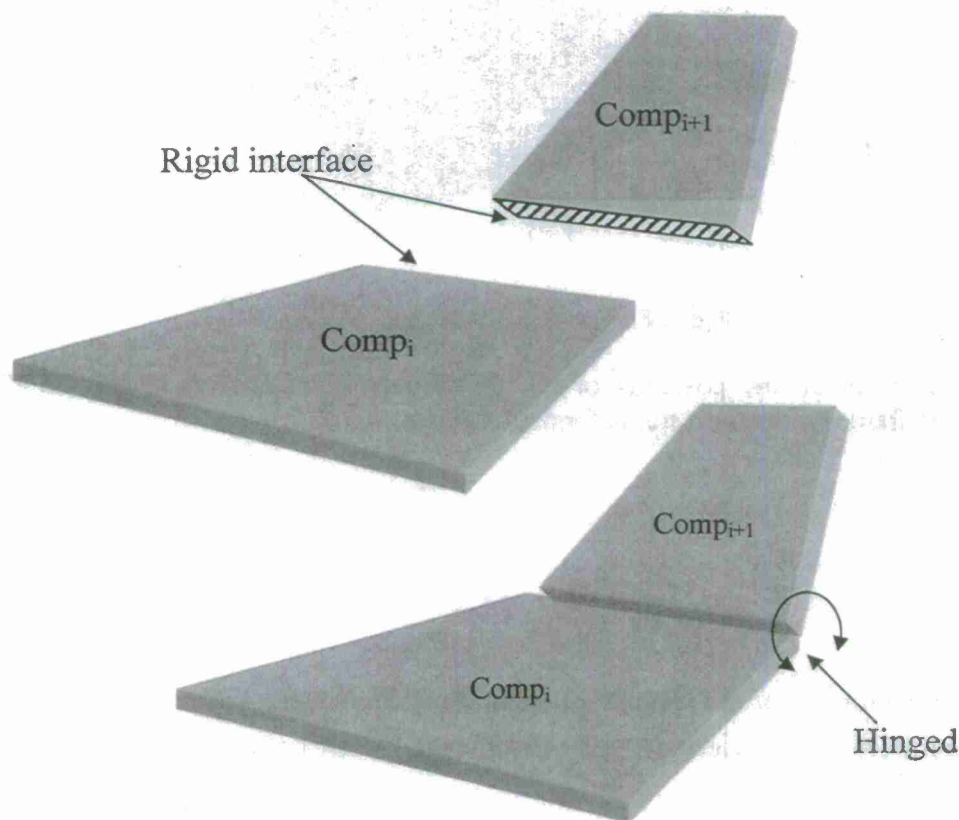


Figure F.1 Separation of the wing into components with interfaces

F.1 Equations of Motion of a Typical Component

As discussed above, a typical component will be assumed to exhibit rigid body motions as well as deformations and both large enough to prevent any linearization. The rigid body motions will be tracked through the six degrees of freedom of the rigid end and the deformations will be expressed in a modal type representation with basis functions consistent with the rigid end, e.g. exhibiting zero displacements and slopes at the rigid end for transverse motions. The deformations will be assumed to be large enough to require a general treatment using finite deformation elasticity.

The frame of reference used for the characterization of the displacement is an undeformed frame moving with the component in its rigid body motions, see Figure F.2. This frame exhibits an angular velocity $\underline{\omega}$ and an arbitrary point L of the rigid end is considered as origin of this frame.

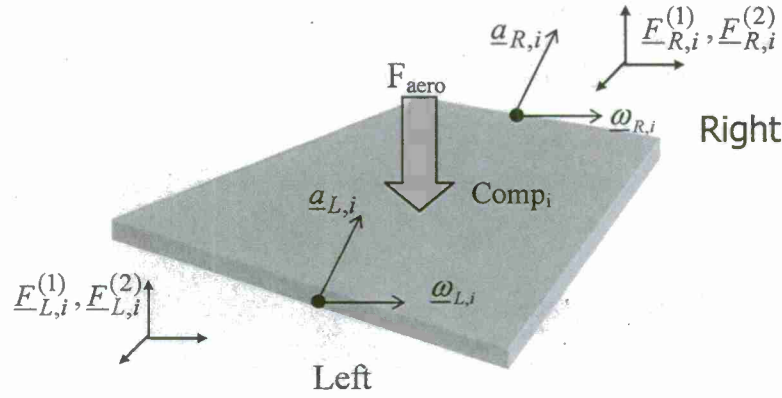


Figure F.2 Forces and kinematics of component i

Let \underline{X} and \underline{x} denote the positions of an arbitrary point of the component in the moving undeformed frame before and after deformation. Then,

$$\underline{x} = \underline{X} + \underline{u} \quad (\text{F.1})$$

where

$$\underline{u}(\underline{X}, t) = \sum_{n=1}^N q_n(t) \underline{U}^{(n)}(\underline{X}) \quad (\text{F.2})$$

is the deformation vector at the point of undeformed coordinates \underline{X} and time t . It is expressed in modal form with pre-selected basis functions $\underline{U}^{(n)}(\underline{X})$ and unknown, time-dependent generalized coordinates $q_n(t)$.

The equations of finite deformation elasticity in the undeformed moving frame of reference are

$$\frac{\partial}{\partial X_k} (F_{ij} S_{jk}) + \rho_0 b_i^0 = \rho_0 \ddot{Z}_i \quad (\text{F.3})$$

for $\underline{X} \in \Omega_0$, see [8,19-21]. In these equations, \underline{S} denotes the second Piola-Kirchhoff stress tensor, ρ_0 is the density in the reference configuration, and \underline{b}^0 is the vector of body forces, all of which are assumed to depend on the coordinates X_i of the undeformed configuration in which the structure occupies the domain Ω_0 . Further, in Eq. (F.3), the deformation gradient tensor \underline{F} is defined by its components F_{ij} as

$$F_{ij} = \frac{\partial x_i}{\partial X_j} = \delta_{ij} + \frac{\partial u_i}{\partial X_j} \quad (F.4)$$

where δ_{ij} denotes the Kronecker symbol.

Note in Eq. (F.3) that the term \ddot{Z}_i should be understood as the absolute acceleration of the particle at the undeformed location \underline{X} in the moving frame. To evaluate this acceleration, it is convenient to introduce the vector \underline{Z} of components Z_i positioning the particle with respect to an absolute frame. Then,

$$\underline{Z} = \underline{X}_L + \underline{x} = \underline{X}_L + \underline{X} + \underline{u} \quad (F.5)$$

where \underline{X}_L is the position vector of the point L in the absolute frame. Further, the second derivative in the moving frame of an arbitrary vector \underline{y} is obtained as

$$\frac{d^2 \underline{y}}{dt^2} = \frac{\partial^2 \underline{y}}{\partial t^2} + 2 \underline{\omega} \times \frac{\partial \underline{y}}{\partial t} + \underline{\omega} \times \underline{y} + \underline{\omega} \times (\underline{\omega} \times \underline{y}) \quad (F.6)$$

where $\frac{\partial \underline{y}}{\partial t}$ denotes the first derivative of \underline{y} as if the frame was not rotating, i.e. considering only the time variation of the components of \underline{y} in the frame.

With these notations and results, the absolute acceleration vector $\ddot{\underline{Z}}$ can be expressed as

$$\ddot{\underline{Z}} = \frac{d^2 \underline{Z}}{dt^2} = \ddot{\underline{X}}_L + \underline{\omega} \times \underline{X} + \underline{\omega} \times (\underline{\omega} \times \underline{X}) + \frac{\partial^2 \underline{u}}{\partial t^2} + 2 \underline{\omega} \times \frac{\partial \underline{u}}{\partial t} + \underline{\omega} \times \underline{u} + \underline{\omega} \times (\underline{\omega} \times \underline{u}) \quad (F.7)$$

where it has been recognized that $\frac{\partial \underline{X}}{\partial t} = 0$ since the vector \underline{X} does not vary with time in the rotating frame.

Combining Eq. (F.7) with Eqs (F.3) and (F.4) provides the complete governing equations for the deformations of the component.

Before addressing the approximate solution of Eqs (F.3), (F.4), and (F.7) using Eqs (F.5) and (F.2), it is appropriate to identify first the unknowns present in this representation. Clearly included in this list are the generalized coordinates $q_n(t)$ but one must also add the position vector of point L , i.e. \underline{X}_L , and the angular velocity $\underline{\omega}$ explicitly present in Eq. (F.7) but also implicitly in Eq. (F.5) as it characterizes the attitude of the rotating frame of reference in which the vectors \underline{X} and \underline{u} are defined.

In fact, to each variable on the list of unknowns is associated a distinct displacement pattern: each generalized coordinate $q_n(t)$ correspond to a particular deformation mode. Further, the unknown position vector \underline{X}_L characterizes the translational rigid body motions while the angular velocity vector $\underline{\omega}$ represents the rotational rigid body motions.

The derivation of governing equations for the variables $q_n(t)$, \underline{X}_L , and $\underline{\omega}$ will be achieved from the weak form of the field equations (F.3) and (F.7) which is (summation is implied over repeated indices)

$$\int_{\Omega_0} \rho_0 v_i \ddot{Z}_i d\underline{X} + \int_{\Omega_0} \frac{\partial v_i}{\partial X_k} (F_{ij} S_{jk}) d\underline{X} = \int_{\Omega_0} \rho_0 v_i b_i^0 d\underline{X} + \int_{\partial\Omega_0'} v_i t_i^0 ds \quad (F.8)$$

where $\partial\Omega_0'$ is the part of the boundary $\partial\Omega_0$ on which the tractions t_i^0 are given (i.e. the domain on which the aerodynamics acts) and $\partial\Omega_0''$ on which the displacements are specified (i.e. the interfaces with the other components). Finally, $v_i(\underline{X})$ denote "trial functions" which are traditionally (in a Galerkin format) selected as each of the basis functions. In the present context, this statement must be understood in the broad sense that the trial functions will be selected as each of the *displacement patterns*, i.e. deformations modes but also translational and rotational rigid body modes.

Proceeding first with the translational rigid body modes, select $v_i(\underline{X}) = \delta_{il}$, i.e. a constant displacement of unit magnitude in the l direction. Eqs (F.7) and (F.8) then yield

$$\begin{aligned} \underline{F}_L^{(1)} + \underline{F}_R^{(1)} = & - \int_{\partial\Omega_0'} \underline{F}_{aero} ds - \int_{\Omega_0} \rho_0 \underline{b}^0 d\underline{X} + m \underline{a}_L + m \dot{\underline{\omega}} \times \underline{X}_G + m \underline{\omega} \times (\underline{\omega} \times \underline{X}_G) \\ & + \ddot{q}_n \underline{mX}^{(n)} + 2 \dot{q}_n \underline{\omega} \times \underline{mX}^{(n)} + q_n [\dot{\underline{\omega}} \times \underline{mX}^{(n)} + \underline{\omega} \times (\underline{\omega} \times \underline{mX}^{(n)})] \end{aligned} \quad (F.9)$$

The second set of trial functions is obtained as the i th component of the cross-product by \underline{X} , that is $v_i(\underline{X}) = (\underline{X} \times)_i$ which describes the overall rotations (rigid body mode) of the component, that is

$$\begin{aligned} \underline{F}_L^{(2)} + \underline{F}_R^{(2)} + \underline{X}_{LR} \times \underline{F}_R^{(1)} = & - \int_{\partial\Omega_0'} \underline{X} \times \underline{F}_{aero} ds - \int_{\Omega_0} \rho_0 \underline{X} \times \underline{b}^0 d\underline{X} + m \underline{X}_G \times \underline{a}_L \\ & + I_L \dot{\underline{\omega}} + \underline{\omega} \times (I_L \underline{\omega}) - \ddot{q}_n \underline{J}^{(n)} + 2 \dot{q}_n I^{(n)} \underline{\omega} + q_n [I^{(n)} \dot{\underline{\omega}} + \underline{\omega} \times (\underline{J}^{(n)} \cdot \underline{\omega}) + \underline{\omega} \times (I^{(n)} \underline{\omega})] \end{aligned} \quad (F.10)$$

Finally, the governing equations for the flexible motions are obtained by selecting the trial function as each of the mode shape in turn, i.e. $v_i(\underline{X}) = U_i^{(n)}(\underline{X})$, to yield

$$\begin{aligned} M_{mn} \ddot{q}_n + 2(\underline{\omega} \cdot \underline{C}_{mn}) \dot{q}_n + [\dot{\underline{\omega}} \cdot \underline{C}_{mn} + \underline{\omega} \cdot (G_{mn} \underline{\omega})] q_n + \underline{mX}^{(m)} \cdot \underline{a}_L - \dot{\underline{\omega}} \cdot \underline{J}^{(m)} - \underline{\omega} \cdot (I^{(m)} \underline{\omega}) \\ + \int_{\Omega_0} \frac{\partial U_i^{(n)}}{\partial X_k} (F_{ij} S_{jk}) d\underline{X} - U^{(m)}(\underline{X}_R) \cdot \underline{F}_R^{(1)} - \frac{\partial U^{(m)}}{\partial s}(\underline{X}_R) \cdot \underline{F}_R^{(2)} - \int_{\Omega_0} \rho_0 U^{(n)} \underline{b}^0 d\underline{X} \quad (F.11) \\ = \int_{\partial\Omega_0'} \underline{U}^{(n)} \underline{F}_{aero} ds \end{aligned}$$

In the above equations, the vectors $\underline{F}_L^{(1)}$, $\underline{F}_L^{(2)}$, $\underline{F}_R^{(1)}$, $\underline{F}_R^{(2)}$ denote the total forces (superscript (1)) and moments (superscript (2)) at the 2 ends L and R with \underline{X}_{LR} the vector joining them (from L to R). Further, the quantities $\underline{a}_L = \ddot{\underline{X}}_L$, I_L , m , \underline{X}_G denote the acceleration of the point L , the mass moment of inertia of the component with respect to that point, the total mass of the component, and finally the position vector of its center of mass (undeformed) from L . Further, $\underline{mX}^{(n)}$, $\underline{J}^{(n)}$, $I^{(n)}$, \underline{C}_{mn} , and G_{mn} denote constant vectors/tensors that involve the mass distribution in the element and the mode shape(s) and are given as follows:

$$\underline{mX}^{(n)} = \int_{\Omega_0} \rho_0 \underline{U}^{(n)} d\underline{X} \quad (F.12)$$

$$\underline{J}^{(n)} = \int_{\Omega_0} \rho_0 \underline{U}^{(n)} \times \underline{X} d\underline{X} \quad (F.13)$$

$$I^{(n)} = \int_{\Omega_0} \rho_0 \left[\underline{X}^T \underline{U}^{(n)} I_3 - \underline{U}^{(n)} \underline{X}^T \right] d\underline{X} \quad (F.14)$$

$$\underline{C}_{mn} = \int_{\Omega_0} \rho_0 \underline{U}^{(n)} \times \underline{U}^{(m)} d\underline{X} \quad (F.15)$$

$$G_{mn} = \int_{\Omega_0} \rho_0 \left[\underline{U}^{(n)} \underline{U}^{(m)T} - \underline{U}^{(n)T} \underline{U}^{(m)} I_3 \right] d\underline{X} \quad (F.16)$$

Next, consider the term $\int_{\Omega_0} \frac{\partial U_i^{(n)}}{\partial X_k} (F_{ij} S_{jk}) d\underline{X}$ which characterizes the flexibility aspects of the

component. Its evaluation in terms of the generalized coordinate q_n is achieved from the modal expansion of Eq. (F.2), the definition of the deformation gradient tensor, Eq. (F.4), and assuming finally that the material is linearly elastic in the sense that the second Piola-Kirrhoff stress tensor and Green strain tensor

$$E_{ij} = \frac{1}{2} (F_{ki} F_{kj} - \delta_{ij}) \quad (F.17)$$

are linearly related, i.e.

$$S_{ij} = C_{ijkl} E_{kl} \quad (F.18)$$

Then, the flexibility term can be expressed as a 3rd order polynomial in the generalized coordinate q_n , i.e.

$$\int_{\Omega_0} \frac{\partial U_i^{(n)}}{\partial X_k} (F_{ij} S_{jk}) d\underline{X} = K_{nj}^{(1)} q_j + K_{njl}^{(2)} q_j q_l + K_{njl p}^{(3)} q_j q_l q_p. \quad (F.19)$$

Note finally that if the body forces present are limited to gravity, $\underline{b}^0 = \underline{g}$ and the relevant terms in Eq. (F.9)-(F.11) can be expressed as

$$\int_{\Omega_0} \rho_0 \underline{b}^0 d\underline{X} = m \underline{g} \quad (\text{F.20})$$

$$\int_{\Omega_0} \rho_0 \underline{X} \times \underline{b}^0 d\underline{X} = m \underline{X}_G \times \underline{g} \quad (\text{F.21})$$

$$\int_{\Omega_0} \rho_0 \underline{U}^{(n)} \cdot \underline{b}^0 d\underline{X} = m \underline{X}^{(m)} \cdot \underline{g} \quad (\text{F.22})$$

F.2 Assembly of Component Equations

Equations (F.9)-(F.16) and (F.19) provide the basic equations to be solved for each component. The structure is assembled by applying conditions on the forces and the kinematics at the interfaces. For the case of a hinge, the interface forces on the two mating components are equal and opposite in all directions, i.e. $\underline{F}_{L,i}^{(1)} = -\underline{F}_{R,i-1}^{(1)}$. For the moments, a similar condition holds, i.e. $\underline{F}_{L,i}^{(2)} = -\underline{F}_{R,i-1}^{(2)}$, but only for the two directions perpendicular to the hinge line \underline{e} , as a hinge moment exists to provide the relative rotation. Kinematically, the translations of the hinge points on the two components are equal and $\underline{\omega}_{L,i} = \underline{\omega}_{R,i-1} + \dot{\theta} \underline{e}$ where $\dot{\theta}$ is the relative angular velocity of the rotation around the hinge line.

In the specific case considered here, the wing is composed of only two components, one inboard and one outboard, see Figure F.3, for which one has:

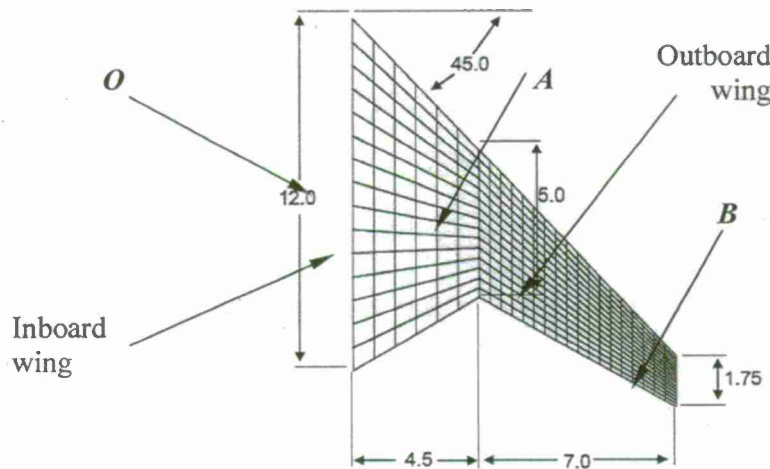


Figure F.3 Morphing wing configuration and terminology.

Inboard:Point "L" is O

$$\underline{X}_L = \underline{X}_O = \underline{0} \quad (F.23)$$

Point "R" is A

$$\underline{X}_R = \underline{X}_A \quad (F.24)$$

$$\underline{\omega} = \underline{\bar{\omega}} = \underline{\Omega}(t) = \Omega(t)\underline{E} \quad (F.25)$$

Outboard:Point "L" is A

$$\underline{X}_L = \underline{X}_A \quad (F.26)$$

Point "R" is B

$$\underline{X}_R = \underline{X}_B \quad (F.27)$$

End B is free

$$\underline{F}_B^{(1)} = \underline{F}_B^{(2)} = \underline{0} \quad (F.28)$$

$$\underline{\omega} = \underline{\bar{\omega}}_A + \dot{\theta}\underline{e}. \quad (F.29)$$

In the above equations, the point L of the inboard wing has been chosen at its hinge with the fuselage, i.e. point O , and thus does not move (as it is assumed here that there is no rigid body motion of the aircraft). The angular velocity of the inboard is given as a function of time as Ω along the fixed direction \underline{E} which coincide with the aircraft axis of symmetry. The point L of the outboard wing has been chosen at its hinge with the inboard equation, i.e. with the point A of the inboard. The acceleration of this point is expressed from the inboard angular velocity and generalized coordinates as (see Eq. (F.7))

$$\ddot{\underline{X}}_A = \dot{\underline{\bar{\omega}}} \times \underline{X}_{OA} + \underline{\bar{\omega}} \times (\underline{\bar{\omega}} \times \underline{X}_{OA}) + \frac{\partial^2 \underline{u}_A}{\partial t^2} + 2 \underline{\bar{\omega}} \times \frac{\partial \underline{u}_A}{\partial t} + \dot{\underline{\bar{\omega}}} \times \underline{u}_A + \underline{\bar{\omega}} \times (\underline{\bar{\omega}} \times \underline{u}_A). \quad (F.30)$$

where \underline{X}_{OA} and \underline{u}_A denote the undeformed position of point A from point O and the elastic deflection of point A in the inboard frame of reference. Further, $\underline{\bar{\omega}}$ denotes the angular velocity of the inboard wing with respect to O .

With these notations, the equations of motion of the morphing wing are obtained by expressing Eq. (F.9)-(F.11) for the outboard wing and Eq. (F.11) for the inboard wing, as Eqs (F.9) and (F.10) for the inboard one would only yield the values of the forces and moments to be exerted at the hinge with the fuselage located at point O . This latter information, while critical to design the hinge and motor at O , does not affect the motion of the wing which is then described by the equations

$$\begin{aligned} \underline{F}_A^{(1)} = & - \int_{\partial\Omega'_0} \underline{F}_{aero} ds - \int_{\Omega_0} \rho_0 \underline{b}^0 d\underline{X} + m \underline{a}_A + m \dot{\underline{\omega}} \times \underline{X}_G + m \underline{\omega} \times (\underline{\omega} \times \underline{X}_G) \\ & + \ddot{q}_n \underline{mX}^{(n)} + 2 \dot{q}_n \underline{\omega} \times \underline{mX}^{(n)} + q_n \left[\dot{\underline{\omega}} \times \underline{mX}^{(n)} + \underline{\omega} \times (\underline{\omega} \times \underline{mX}^{(n)}) \right] \end{aligned} \quad (F.31)$$

$$\begin{aligned} \underline{F}_A^{(2)} = & - \int_{\partial\Omega'_0} \underline{X} \times \underline{F}_{aero} ds - \int_{\Omega_0} \rho_0 \underline{X} \times \underline{b}^0 d\underline{X} + m \underline{X}_G \times \underline{a}_A + I_A \dot{\underline{\omega}} + \underline{\omega} \times (I_A \underline{\omega}) \\ & - \ddot{q}_n \underline{J}^{(n)} + 2 \dot{q}_n I^{(n)} \underline{\omega} + q_n \left[I^{(n)} \dot{\underline{\omega}} + \underline{\omega} (\underline{J}^{(n)} \cdot \underline{\omega}) + \underline{\omega} \times (I^{(n)} \underline{\omega}) \right] \end{aligned} \quad (\text{F.32})$$

$$\begin{aligned} M_{mn} \ddot{q}_n + 2(\underline{\omega} \underline{C}_{mn}) \dot{q}_n + [\dot{\underline{\omega}} \underline{C}_{mn} + \underline{\omega} (G_{mn} \underline{\omega})] q_n + m \underline{X}^{(m)} \cdot \underline{a}_A - \dot{\underline{\omega}} \underline{J}^{(m)} - \underline{\omega} (I^{(m)} \underline{\omega}) \\ + K_{nj}^{(1)} q_j + K_{nj}^{(2)} q_j q_l + K_{njlp}^{(3)} q_j q_l q_p - \int_{\Omega_0} \rho_0 \underline{U}^{(n)} \cdot \underline{b}^0 d\underline{X} = \int_{\partial\Omega'_0} \underline{U}^{(n)} \underline{F}_{aero} ds \end{aligned} \quad (\text{F.33})$$

$$\begin{aligned} \bar{M}_{mn} \ddot{\bar{q}}_n + 2(\bar{\underline{\omega}} \bar{\underline{C}}_{mn}) \dot{\bar{q}}_n + [\dot{\bar{\underline{\omega}}} \bar{\underline{C}}_{mn} + \bar{\underline{\omega}} (\bar{G}_{mn} \bar{\underline{\omega}})] \bar{q}_n - \dot{\bar{\underline{\omega}}} \bar{\underline{J}}^{(m)} - \bar{\underline{\omega}} (\bar{I}^{(m)} \bar{\underline{\omega}}) + \bar{K}_{nj}^{(1)} \bar{q}_j \\ + \bar{K}_{nj}^{(2)} \bar{q}_j \bar{q}_l + \bar{K}_{njlp}^{(3)} \bar{q}_j \bar{q}_l \bar{q}_p + \bar{\underline{U}}^{(m)} (\underline{X}_{OA}) \cdot \underline{F}_A^{(1)} + \frac{\partial \bar{\underline{U}}^{(m)}}{\partial s} (\underline{X}_{OA}) \cdot \underline{F}_A^{(2)} - \int_{\bar{\Omega}_0} \bar{\rho}_0 \bar{\underline{U}}^{(n)} \cdot \bar{\underline{b}}^0 d\underline{X} \\ = \int_{\partial\bar{\Omega}'_0} \bar{\underline{U}}^{(n)} \underline{F}_{aero} ds \end{aligned} \quad (\text{F.34})$$

with $\underline{a}_A = \ddot{\underline{X}}_A$, Eq. (F.30), and where an overbar $\bar{\quad}$ has been used to refer to quantities of the inboard wing, consistently with Eq. (F.25), (F.29), and (F.30).

It remains to discuss the determination of the angular velocity of the outboard wing frame of reference (i.e. defining the rotational rigid body motions of that wing) as specified by Eq. (F.29). In this equation, $\underline{\omega}_A$ refers to the angular velocity of the rigid part of hinge attached to the inboard which differs from $\underline{\omega}$ by the flexible rotations of the inboard wing seen at its point A on the hinge. Denoting this flexible component by $\underline{\omega}_A^{Flex}$, one has

$$\underline{\omega} = \underline{\omega}_A + \dot{\underline{\theta}} \underline{e} = \underline{\omega} + \underline{\omega}_A^{Flex} + \dot{\underline{\theta}} \underline{e}. \quad (\text{F.35})$$

At this point, it only remains to address the determination of the angular velocity $\underline{\omega}_A^{Flex}$ and of the rotation (angles) of the hinge line \underline{e} created by the deformations of the inboard wing. A formal approach to achieve this task can be developed by an analysis of the hinge line motion in a frame of reference exhibiting three rotations ψ , ϕ , and γ (e.g. Euler's angles). Specifically, using the representation of Eq. (F.2), the velocity of several points H on the hinge line could first be obtained as

$$\underline{V}_H = \dot{\underline{X}}_L + \underline{\omega} \times \underline{X}_{LH} + \frac{\partial \underline{u}}{\partial t} + \underline{\omega} \times \underline{u} = \underline{\omega} \times \underline{X}_{OH} + \frac{\partial \underline{u}}{\partial t} + \underline{\omega} \times \underline{u} \quad (\text{F.36})$$

where the second equality results from Eq. (F.23) and the displacement \underline{u} is that of point H . Next, recognize that the part of the hinge on the inboard wing is also a rigid body but with angular velocity $\underline{\omega}_A$. Then, the velocity of the same points of the hinge as in Eq. (F.36) can also be expressed as

$$\underline{V}_H = \dot{\underline{X}}_A + \underline{\omega}_A \times \underline{X}_{AH} \quad (F.37)$$

where \underline{X}_{AH} is the relative position vector of the point H on the hinge with respect to its point A . Forcing the equality of the velocities \underline{V}_H of Eq. (F.36) and (F.37) at, at least 3 different points H_1, H_2, H_3 , would give a set of equations to evaluate $\underline{\omega}_A$ for each position. Having admitted a frame of reference specific to the hinge line and described by the rotations ψ, ϕ , and γ , the angular velocity $\underline{\omega}_A$ would appear as a linear combination of terms involving $\dot{\psi}, \dot{\phi}$, and $\dot{\gamma}$ in fact yielding a set of three nonlinear differential equations for these angles that can be integrated to yield the specific attitude of the hinge line and its current angular velocity. This process cannot be applied to a pure hinge line as all the points of this line will have a similar direction \underline{X}_{AH} ; it is thus not possible to capture the component of $\underline{\omega}_A$ along that direction. The solution to this difficulty is to add one or several artificial points to the hinge that are not on the line itself, effectively making the hinge a true 3-dimensional body.

The above process was not implemented in the final program because (i) of the magnitude of the deformations obtained, which led still to small rotations, and (ii) the known difficulties in proceeding with the above scheme. Rather, a simpler, approximate approach was adopted that relies on the rotations R_1, R_2 , and R_3 of the finite element basis functions which were treated as angles. That is, consistently with Eq. (F.2), these rotations stacked in the vector \underline{R} were determined as

$$\underline{R}(\underline{X}, t) = \sum_{n=1}^N \bar{q}_n(t) \underline{U}_R^{(n)}(\underline{X}) \quad (F.38)$$

where $\underline{U}_R^{(n)}(\underline{X})$ denotes the components of the finite element basis functions along the rotations. Finally, the angular velocity associated with the deformations was obtained as

$$\underline{\omega}^{Flex}(\underline{X}, t) = \sum_{n=1}^N \dot{\bar{q}}_n(t) \underline{U}_R^{(n)}(\underline{X}). \quad (F.39)$$

In particular, $\underline{\omega}_A^{Flex}$ was determined from Eq. (F.39) using any point on the hinge line.

In the desired morphing strategy, the outboard wing was to remain horizontal at all times while rotating around an axis parallel to the axis of the body. Thus, without deformations of the inboard, there would be no rigid body rotation of the outboard wing, i.e.

$$\dot{\theta} = -\Omega \quad (F.40)$$

$$\underline{e} = \underline{E} \quad (F.41)$$

Assuming that Eq. (F.40) would continue to hold with deformations, i.e. that the step motor used at the inboard-outboard hinge line would be programmed to give the same rotation as the one placed at the fuselage-inboard wing hinge line, Eq. (F.35) can then be rewritten as

$$\underline{\omega} = \underline{\omega}_A + \dot{\underline{e}} = \Omega(\underline{E} - \underline{e}) + \underline{\omega}_A^{Flex}. \quad (F.42)$$

F.3 Linearized Equations of Motion

The procedure described in the above sections leads to rather complex nonlinear differential equations and it was desired to implement a linearized strategy for both comparison but also more extensive computational investigations. This linearization was performed for the specific morphing configuration and strategy chosen in the investigation. That is, with Eq. (F.42) which indicates that $\underline{\omega}$ is of first order in the deformations.

This property leads to notable simplifications of Eqs (F.31)-(F.34) which become

$$\underline{F}_A^{(1)} = - \int_{\partial\Omega_0'} \underline{F}_{aero} ds - \int_{\Omega_0} \rho_0 \underline{b}^0 d\underline{X} + m \underline{a}_A + m \underline{\omega} \times \underline{X}_G + \ddot{q}_n m \underline{X}^{(n)} \quad (\text{F.43})$$

$$\underline{F}_A^{(2)} = - \int_{\partial\Omega_0'} \underline{X} \times \underline{F}_{aero} ds - \int_{\Omega_0} \rho_0 \underline{X} \times \underline{b}^0 d\underline{X} + m \underline{X}_G \times \underline{a}_A + I_A \underline{\dot{\omega}} - \ddot{q}_n \underline{J}^{(n)} \quad (\text{F.44})$$

$$M_{mn} \ddot{q}_n + \underline{mX}^{(m)} \cdot \underline{a}_A - \underline{\dot{\omega}} \cdot \underline{J}^{(m)} + K_{nj}^{(1)} q_j - \int_{\Omega_0} \rho_0 \underline{U}^{(n)} \cdot \underline{b}^0 d\underline{X} = \int_{\partial\Omega_0'} \underline{U}^{(n)} \underline{F}_{aero} ds \quad (\text{F.45})$$

and, for the inboard wing,

$$\begin{aligned} & \overline{M}_{mn} \ddot{\overline{q}}_n + 2(\underline{\omega} \cdot \underline{C}_{mn}) \dot{\overline{q}}_n + [\underline{\dot{\omega}} \cdot \underline{C}_{mn} + \underline{\omega} \cdot (\underline{G}_{mn} \underline{\omega})] \overline{q}_n - \underline{\dot{\omega}} \cdot \underline{J}^{(m)} - \underline{\omega} \cdot (\underline{I}^{(m)} \underline{\omega}) + \overline{K}_{nj}^{(1)} \overline{q}_j \\ & + \underline{U}^{(m)} (\underline{X}_{OA}) \cdot \underline{F}_A^{(1)} + \frac{\partial \underline{U}^{(m)}}{\partial s} (\underline{X}_{OA}) \cdot \underline{F}_A^{(2)} - \int_{\overline{\Omega}_0} \overline{\rho}_0 \underline{U}^{(n)} \cdot \underline{b}^0 d\underline{X} = \int_{\partial\overline{\Omega}_0'} \underline{U}^{(n)} \underline{F}_{aero} ds \end{aligned} \quad (\text{F.46})$$

Attachment G

Nonlinear Reduced Order Modeling of Flat Cantilevered Structures

***Presented at the Structural Dynamics and Materials
Conference April 2009***

NONLINEAR REDUCED ORDER MODELING OF FLAT CANTILEVERED STRUCTURES

Kwangkeun Kim^{*}, Vishal Khanna[#], X. Q. Wang[†], and Marc P. Mignolet[‡]

Arizona State University, Tempe, AZ 85287-6106, USA

ABSTRACT

The focus of this investigation is on the development and validation of structural dynamic reduced order models for the geometrically nonlinear response of flat cantilevered structures, e.g. beams and plates. The specificities of cantilevered structures, as compared to those supported all around, are first highlighted. On this basis, extensions of existing reduced order modeling strategies are presented which provide a complete representation of the structural response, i.e., including both transverse and inplane displacement fields. Next, this methodology is successfully applied, first to a simple beam model and then to a flat wing both of which subjected to transverse loads. Finally, the response of a beam under combined transverse and inplane loads as well as its postbuckling behavior are also shown to be also accurately predicted by the reduced order model.

INTRODUCTION

The formulation and validation of dynamic reduced order models (ROM) of geometrically nonlinear structures has received significant attention in the past few years in the context of beams, plates, and shells representative of aircraft panels, see for example [1-9]. These reduced order models represent a natural extension of modal models used in linear structural dynamic analyses to geometrically nonlinear structures. That is, the response of the structure is expressed in a modal expansion-type representation,

i.e., as a linear combination of time-invariant, spatially varying basis functions weighted by time-dependent modal coordinates. Then, using a Galerkin approach (or weak formulation), it was shown, e.g. see [9], that the modal coordinates satisfy a set of second order differential equations nonlinear only in the stiffness terms which consist of linear, quadratic, and cubic polynomials of the modal coordinates. Interestingly, the *form* of these equations (i.e. the cubic nonlinearity) is obtained independently of the basis functions selected but their *coefficients* (the linear, quadratic, and cubic stiffness coefficients) do depend on the basis selected.

The key aspects in formulating such nonlinear reduced order models are thus (i) the selection of the basis functions, and (ii) the evaluation of the coefficients of the cubic stiffness nonlinearity. In the limit of small motions, the nonlinear reduced order model should reduce naturally to a modal model and thus the nonlinear basis should completely include its linear counterpart, i.e. the set of linear modes significantly excited.

This is however not enough and a complete representation of the structural response requires additional basis functions. As a simple proof, consider the response to transverse loads of a flat, symmetric beam or plate subjected to a purely transverse loading. In the linear, infinitesimal case, the decoupling of the inplane and transverse modes implies that only the latter ones are necessary and no inplane motion takes place. However, finite deformations can only occur with a stretching of the beam or plate and, accordingly, with inplane deformations. Thus, the nonlinear basis required for a full representation must include both transverse linear modes and functions describing the inplane motions.

In light of these comments, one can broadly separate the recent investigations [1-9] into two distinct groups: those which have relied on a full modeling of the response [2,4-6,9] and those in which the basis functions necessary to complement the linear modes are treated as "hidden" and implicitly condensed in the model, leaving only the modal coordinates associated with the linear modes as sole unknowns [1,3,7,8]. The

^{*}Postdoctoral Fellow, Department of Mechanical and Aerospace Engineering. Currently, Research Engineer at ZONA Technology, Scottsdale, AZ.

[#]Research Assistant, Department of Mechanical and Aerospace Engineering.

[†]Faculty Research Associate, Department of Mechanical and Aerospace Engineering.

[‡]Professor, Department of Mechanical and Aerospace Engineering, Associate Fellow, AIAA.

recovery of the full response is achieved after solving for these coordinates through the use of the "companion modes" which characterize the "hidden" part of the model.

Once the basis has been selected, the estimation of the stiffness coefficients is achieved from a series of static nonlinear responses of a full finite element model, either by imposing the displacements and determining the necessary forces [2,4-6,9] using the algorithm of [2] (as modified in [4,5,9]) or by proceeding in reverse with the displacements induced by a series of loading cases [1,3,7,8].

The reduced order models obtained in the recent literature have several key advantages over full finite element models. Most notably, they represent a compact and accurate representation of the response (both displacements and strains/stresses) which is typically computationally expedient (owing to the small number of degrees of freedom involved) but also, and maybe more importantly, easily integrable with other computational solvers, e.g. computational fluid dynamics (CFD) codes, as demonstrated in [10]. Note furthermore that the reduced order modeling techniques described in [1-9] are generic, i.e. applicable in principle to a broad class of structures, not only to the panel like structures considered in these investigations.

These observations suggest that reduced order models will be particularly convenient in multi-physics problems leading to large responses, one of which is the post flutter limit cycle oscillations of wings and other lifting surfaces.

NONLINEAR REDUCED ORDER MODELING

A reduced order model (ROM) is defined here as a modal-like representation of the displacement field u_i as

$$u_i(\underline{X}, t) = \sum_{n=1}^M q_n(t) U_i^{(n)}(\underline{X}) \quad i = 1, 2, 3 \quad (1)$$

where \underline{X} denotes the coordinates of a point (in the undeformed configuration), $U_i^{(n)}(\underline{X})$ are specified, constant basis functions satisfying the boundary conditions also in the undeformed configuration, and $q_n(t)$ are the time variable generalized coordinates.

The derivation of the governing (ordinary differential) equations for the generalized coordinates $q_n(t)$ can be performed in a Galerkin format. That is, the error obtained by introducing Eq. (1) in the equations of finite elasticity expressed in the undeformed configuration will be made orthogonal to the set of

basis functions $U_i^{(n)}(\underline{X})$. A key issue in this derivation is the clarification of the concept of linear elasticity. Specifically, two notable options are possible. The first one assumes that the stress and strain tensors in the undeformed configuration are linearly related, i.e.

$$\underline{S}_{ij} = \underline{C}_{ijkl} \underline{E}_{kl} \quad (2)$$

where \underline{S} and \underline{E} denote the second Piola-Kirchhoff stress tensor and the Green strain tensor, respectively, and \underline{C} is a fourth order elasticity tensor function in general of the undeformed coordinates \underline{X} . Note that summation over repeated indices is implicitly assumed. An alternative formulation can be derived by assuming a similar relation between the corresponding deformed configuration tensors, i.e.

$$\underline{\sigma}_{ij} = \hat{\underline{C}}_{ijkl} \underline{e}_{kl} \quad (3)$$

where $\underline{\sigma}$ and \underline{e} are the Cauchy stress and Almansi strain tensors and $\hat{\underline{C}}$ is also a fourth order elasticity tensor but dependent on the deformed coordinates \underline{x} . The undeformed stress and strain tensors are obtained from their deformed counterparts from the pull back operations (e.g., see [11,12])

$$\underline{S} = J \underline{F}^{-1} \underline{\sigma} \underline{F}^{-T} \quad \text{and} \quad \underline{E} = \underline{F}^T \underline{e} \underline{F} \quad (4)$$

where the components F_{ij} of the deformation gradient tensor \underline{F} are

$$F_{ij} = \frac{\partial x_i}{\partial X_j} = \delta_{ij} + \frac{\partial u_i}{\partial X_j} \quad (5)$$

with δ_{ij} the Kronecker symbol and $\underline{u} = \underline{x} - \underline{X}$. Note finally that J denotes the Jacobian of the transformation $\underline{x} = \underline{x}(\underline{X})$, i.e. $J = \det(\underline{F})$.

Combining Eqs (2)-(4), it is readily seen that it is not possible for both sets elements \underline{C}_{ijkl} and $\hat{\underline{C}}_{ijkl}$ to be independent of the deformations, i.e. of F_{ij} .

Equivalently, the two linear elasticity definitions, Eqs (2) and (3), are not compatible and different displacement fields will be obtained by assuming one or the other law.

In keeping with the expansion of Eq. (1) in the undeformed configuration, the linear elasticity condition of Eq. (2) will be assumed here and it leads (e.g. see [9]) to the governing equations

$$M_{ij} \ddot{q}_j + D_{ij} \dot{q}_j + K_{ij}^{(1)} q_j + K_{ijl}^{(2)} q_j q_l + K_{ijlp}^{(3)} q_j q_l q_p = F_i \quad (6)$$

where following standard practice, a damping term $D_{ij} \dot{q}_j$ has been added to collectively represent various dissipation mechanisms.

In Eq. (6), M_{ij} denotes the elements of the mass matrix, $K_{ij}^{(1)}$, $K_{ijl}^{(2)}$, $K_{ijlp}^{(3)}$ are the linear, quadratic, and cubic stiffness coefficients and F_i are the pulled back modal forces. Note that it is sufficient to consider $p \geq l \geq j$. Although integral expressions for these components can be derived, e.g. see [13], it is easier to identify/evaluate them directly from the finite element model. Specifically, denoting by Φ_i the vector of displacements at the finite element degrees of freedom corresponding to $U_i^{(n)}(X)$, one finds directly that

$$M_{ij} = \Phi_i^T M_G \Phi_j \quad \text{and} \quad F_i = \Phi_i^T \underline{F}(t) \quad (7), (8)$$

where M_G is the global mass matrix and $\underline{F}(t)$ is the vector of forces pulled back to the undeformed configuration.

The determination of the stiffness parameters is more complex and 2 distinct methods have been proposed to achieve this task. In the first one, the evaluation procedure of [2], as modified in [4,5,9], the coefficients $K_{ij}^{(1)}$, $K_{ijl}^{(2)}$, and $K_{ijlp}^{(3)}$ are determined from the computed modal forces necessary to induce a certain ensemble of prescribed static displacement fields of the structure. In the second approach, see [1,3,7,8], the stiffness coefficients are determined from the computed static displacements induced by prescribed forces.

CANTILEVERED STRUCTURES PROPERTIES

As stated in the introduction, the nonlinear reduced order modeling approach briefly reviewed in the previous section has primarily been used in connection with beams and panels supported on two opposite sides or more. A reason for this bias in applications is certainly the much stronger nonlinearity encountered in structures with multiple sides supported as compared to those which are cantilevered. This situation is depicted in Fig. 1 presenting the peak static transverse displacement induced by a uniform load for an isotropic steel beam, either cantilevered or clamped-clamped, of properties given in Table 1.

In assessing the nonlinearity of these 2 displacement vs. load curves, note that the displacement of the cantilevered beam is normalized by the beam length as opposed to the clamped-clamped response normalized by the much smaller beam thickness.

A different perspective on the same issue can be obtained from the stiffness coefficients $K_{ij}^{(1)}$, $K_{ijl}^{(2)}$, and $K_{ijlp}^{(3)}$ corresponding to the two sets of boundary

Table 1. Cantilevered Beam Properties

Beam Length	0.2286 m
Cross-section Width	0.0127 m
Cross-section Thickness	$7.75 \cdot 10^{-4}$ m
Mass per unit length	7875 kg/m^3
Young's Modulus	205,000 MPa
Shear Modulus	80,000 MPa

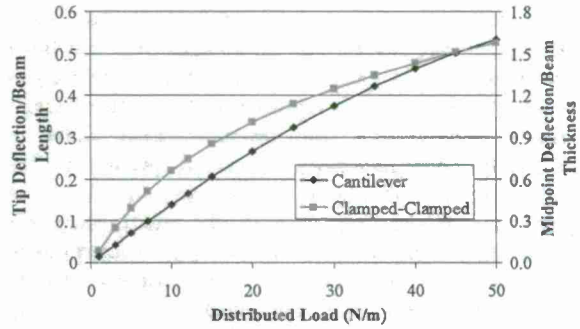


Figure 1. Peak static transverse displacement vs. uniform load magnitude, cantilevered and clamped-clamped beams.

conditions. Consider for simplicity a reduced order model involving only 1 transverse mode and 1 inplane mode (the dual modes of [9] are selected here). Then, note that the linear decoupling of these 2 motions implies first that $K_{12}^{(1)} = K_{21}^{(1)} = 0$, $M_{12} = M_{21} = 0$, and $D_{12} = D_{21} = 0$. Further, the symmetry of the system in the transverse direction implies that a switch of sign of the transverse forces leads to change of sign of the transverse displacement but leaves unchanged the inplane motions. Thus,

$$K_{111}^{(2)} = K_{212}^{(2)} = K_{122}^{(2)} = 0$$

and

$$K_{1112}^{(3)} = K_{1222}^{(3)} = K_{2111}^{(3)} = K_{2122}^{(3)} = 0.$$

A final reduction of the model is achieved by assuming, as MSC. Nastran does (in SOL 106 and SOL 400), that there is no nonlinearity associated with the inplane motions. Then, $K_{1122}^{(3)} = K_{2222}^{(3)} = K_{2112}^{(3)} = 0$ also and the final reduced order model is

$$M_{11}\ddot{q}_1 + D_{11}\dot{q}_1 + K_{11}^{(1)}q_1 + K_{112}^{(2)}q_1q_2 + K_{1111}^{(3)}q_1^3 = F_1 \quad (9)$$

and

$$M_{22}\ddot{q}_2 + D_{22}\dot{q}_2 + K_{22}^{(1)}q_2 + K_{211}^{(2)}q_1^2 = F_2 \quad (10)$$

The nonzero stiffness coefficients $K_{11}^{(1)}$, $K_{22}^{(1)}$, $K_{112}^{(2)}$, $K_{211}^{(2)}$, and $K_{1111}^{(3)}$ are presented in Tables 2 and 3.

Table 2. Cantilevered beam ROM coefficients

$K_{11}^{(1)}$	$K_{22}^{(1)}$	$K_{112}^{(2)}$	$K_{211}^{(2)}$	$K_{1111}^{(3)}$	$\hat{K}_{1111}^{(3)}$
6.10 10^3	3.10 10^9	2.18 10^{11}	1.09 10^{11}	7.64 10^{12}	1.24 10^8

Table 3. Clamped-clamped beam ROM coefficients

$K_{11}^{(1)}$	$K_{22}^{(1)}$	$K_{112}^{(2)}$	$K_{211}^{(2)}$	$K_{1111}^{(3)}$	$\hat{K}_{1111}^{(3)}$
2.47 10^5	7.26 10^{10}	1.65 10^{12}	8.26 10^{11}	5.88 10^{13}	4.00 10^{13}

Comparing these two tables reveals that:

- (i) the coefficient $K_{1111}^{(3)}$ is smaller for the cantilevered configuration than for the clamped-clamped one
- (ii) as importantly, the inplane transverse coupling terms $K_{112}^{(2)}$ and $K_{211}^{(2)}$ are significantly larger in magnitude for the cantilevered configuration than for the clamped-clamped one.

These two facts induce the much smaller nonlinearity of the cantilevered configuration. The role of the inplane-transverse coupling terms in lowering the effective nonlinearity is best visualized by noticing that the inplane generalized coordinate q_2 can be obtained from Eq. (10) as

$$q_2 = -\frac{K_{211}^{(2)}}{K_{22}^{(1)}} q_1^2 \quad (11)$$

since the present loading is static and is only transverse, i.e. $F_2 = 0$. Introducing Eq. (11) into Eq. (9) yields

$$M_{11}\ddot{q}_1 + D_{11}\dot{q}_1 + K_{11}^{(1)} q_1 + \hat{K}_{1111}^{(3)} q_1^3 = F_1 \quad (12)$$

where

$$\hat{K}_{1111}^{(3)} = K_{1111}^{(3)} - \frac{K_{211}^{(2)} K_{112}^{(2)}}{K_{22}^{(1)}}. \quad (13)$$

The values of the coefficients $\hat{K}_{1111}^{(3)}$ for the two configurations, also given in Tables 2 and 3, are consistent with the trends of Fig. 1.

Note further that $\hat{K}_{1111}^{(3)}$ is only $1.6 \cdot 10^{-5}$ of $K_{1111}^{(3)}$ so that the stiffening induced by the pure transverse term $K_{1111}^{(3)}$ is almost completely negated by the softening induced by the inplane motions. This situation is of particular concern from a numerical point of view as the coefficients $\hat{K}_{1111}^{(3)}$ must remain positive to ensure

a stiffening behavior. The generalization of this stability condition when there are multiple modes is presented in [13] and is expressed through the positive definiteness of symmetric matrix, referred to as \underline{K}_B , which combines the linear, quadratic, and cubic stiffness coefficients.

Unfortunately, numerical experimentation with the beam of properties given by Table 1 has demonstrated that a lack of positive definiteness of \underline{K}_B occurs with as few as 3 transverse and 3 inplane modes. Such a n unstable model is thus not only unphysical but it also leads to a poor matching of the response predicted by a nonlinear full finite element model.

CONDENSED REDUCED ORDER MODELS

In view of the aforementioned problems, a modified modeling approach was formulated to circumvent the issue of accuracy. The basic idea of this revised formulation is not to identify separately the large stiffening (i.e., $K_{1111}^{(3)}$ in the above simple example),

and softening terms ($K_{112}^{(2)}$ and $K_{211}^{(2)}$) but rather to estimate the net stiffening effect directly ($\hat{K}_{1111}^{(3)}$).

Practically, this strategy requires that the model be constructed solely in terms of the transverse deflections, i.e. with the inplane motions "condensed", e.g. Eq. (12) for the one-mode model. In fact, such condensed models have already been introduced and shown to be successful in a broad range of cases, e.g. see [1,3,7,8]. As with the "full" reduced order model, i.e. including both transverse and inplane displacements, the stiffness parameters of the condensed ROM can be obtained by either of the two approaches described above. The evaluation procedure of [2,4,5,9] was chosen here but was modified to reflect the condensation or unobservability of the inplane displacements. Specifically, as required in the methodology, an ensemble of displacement field were prescribed and the necessary forces determined. However, in keeping with the condensation of the inplane motions, only the transverse displacements were prescribed with inplane motions free to occur. In the Nastran terminology, the required transverse displacements were enforced by SPCD commands.

The first example of validation focused on the cantilevered beam of rectangular cross section with properties given in Table 1 and subjected to a static tip load. A series of static nonlinear solution (SOL106) were performed to obtain the evolution of the tip deflection as a function of the applied load magnitude. This data is presented in Fig. 2 for deflections up to 1/2 of the beam length. Also presented on this figure are the

deflections predicted under a linear model and those obtained by using a four transverse mode model nonlinear ROM with condensed inplane motions. As expected, the agreement of the condensed ROM is excellent at relatively small deflection levels, and in fact very good until 40%-50% of the beam length (the error is 4.5% for a deflection nearly equal to 1/2 of the beam length).

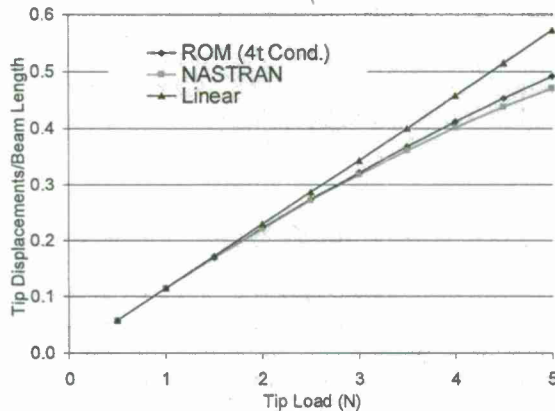


Figure 2. Tip transverse deflection vs. load, beam model. Full Nastran and 4-mode condensed reduced order model ("ROM (4t Cond.)").

The second validation example focused on the flat, aluminum wing model of Fig. 3 modeled with CQUAD4 elements 1.15" thick. Shown in Fig. 4 is the corresponding tip deflection vs. load (assumed uniformly distributed along the tip boundary) estimated from static Nastran solutions. Also presented on these figures are the deflections predicted under a linear model and those obtained by using two, four, and six transverse mode models in the above condensed ROM procedure. Clearly, convergence of the model is achieved in four to six modes and the accuracy is very good until a tip transverse deflection equal to 35% of the wing span (the error is approximately 6%).

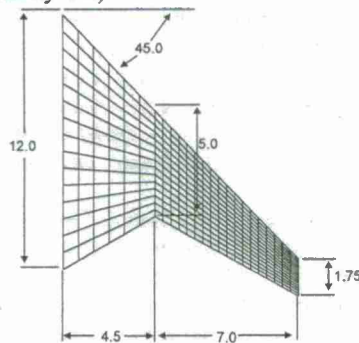


Figure 3. Flat wing example (dimensions in feet)

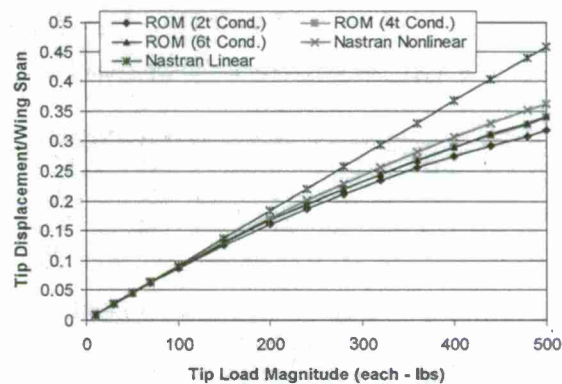


Figure 4. Tip transverse deflection vs. load, wing model of Fig. 1. Full Nastran and 2-, 4-, and 6-mode condensed reduced order models ("ROM(Nt Cond.)").

DECONDENSED REDUCED ORDER MODELS

The results of Figs 2 and 4 are very significant as they provide the first stable and accurate nonlinear reduced order models of cantilevered structures. Nevertheless, the condensation of the inplane displacements entails limitations which are best revealed in the simplified analysis of Eqs (9)-(12). Specifically, the derivation of Eq. (12) from Eqs (9) and (10) required the following assumptions

- (i) there be no inplane forces (i.e., $F_2=0$ in the 1 mode model),
- (ii) the problem is static or the inplane inertia and damping effects can be neglected, and
- (iii) there is no nonlinearity in the inplane displacements or such nonlinearity can be neglected.

Of these 3 assumptions, the first one is probably the most immediate and significant limitation as it prevents for example the buckling and postbuckling analyses. The neglect of the inertia terms may also not be valid and will be assessed in more details in the validation section.

To eliminate the above 3 limitations, it was decided to recover a "full" reduced order model, i.e. with inplane motions represented, from the condensed model to avoid the numerical accuracy issues discussed earlier. This process is referred to here as "decondensation" since the inplane displacements initially condensed are reverted to as observed variables.

The first step in this approach is the generalization of the 2 mode analysis of Eq. (9)-(12). To this end, separate the governing equations (6) into those corresponding to transverse and inplane modes as

$$M_{ij}^{(t)} \ddot{q}_j^{(t)} + D_{ij}^{(t)} \dot{q}_j^{(t)} + K_{ij}^{(1t)} q_j^{(t)} + K_{ijl}^{(2t)} q_j^{(t)} q_l^{(t)} + K_{ijlp}^{(3t)} q_j^{(t)} q_l^{(t)} q_p^{(t)} = F_i^{(t)} \quad (14)$$

$$M_{ij}^{(i)} \ddot{q}_j^{(i)} + D_{ij}^{(i)} \dot{q}_j^{(i)} + K_{ij}^{(1i)} q_j^{(i)} + K_{ijl}^{(2i)} q_j^{(i)} q_l^{(i)} = F_i^{(i)} \quad (15)$$

in which it has been assumed that the structure is symmetric in the transverse direction and that there is no nonlinearity of the inplane motions, i.e. assumption (ii).

In Eqs. (14) and (15), $q_j^{(i)}$ and $q_j^{(t)}$ denote the generalized coordinates associated with the inplane (superscript (i)) and transverse (superscript (t)) motions. Assuming that there are no forces in the inplane direction (assumption (i)) and that the frequencies of the excitation bandwidth are small with respect to the inplane mode frequencies (quasi-static inplane response or assumption (iii)), Eq. (15) can be directly solved for the inplane displacements in terms of their transverse counterparts as

$$q_j^{(i)} = -[K^{(1i)}]_{js}^{-1} K_{srl}^{(2i)} q_r^{(t)} q_l^{(t)}. \quad (16)$$

Introducing Eq. (16) in Eq. (14) leads to the transverse only set of equations

$$M_{ij} \ddot{q}_j^{(t)} + D_{ij} \dot{q}_j^{(t)} + K_{ij}^{(1t)} q_j^{(t)} + \hat{K}_{ijlp}^{(3t)} q_j^{(t)} q_l^{(t)} q_p^{(t)} = F_i^{(t)} \quad (17)$$

where

$$\hat{K}_{ijlp}^{(3t)} = K_{ijlp}^{(3t)} - K_{ijr}^{(2t)} [K^{(1t)}]_{rs}^{-1} K_{slp}^{(2t)}. \quad (18)$$

In fact, Eqs (17) and (18) are the desired generalizations of Eqs (12) and (13).

The decondensation problem is thus to create a full model of the form of Eqs (14) and (15) from the condensed one of Eqs (17) and (18) while maintaining the stability of the final model. Clearly, there is not enough information to do so and thus a two step approach was formulated as follows.

(a) A condensed model is first developed providing the tensor $\hat{K}_{ijlp}^{(3t)}$.

(b) A full, inplane and transverse, model is then developed using the approach of [2,4,5,9], giving estimates of the various tensors of Eqs (17) and (18) and in particular $K_{ij}^{(1t)}$, $K_{ijr}^{(2t)}$, and $K_{slp}^{(2t)}$ but the tensor $K_{ijlp}^{(3t)}$ obtained by this approach is not used further. Rather, the cubic stiffness tensor $K_{ijlp}^{(3t)}$ of Eq. (17) is obtained from Eq. (18) as

$$K_{ijlp}^{(3t)} = \hat{K}_{ijlp}^{(3t)} + K_{ijr}^{(2t)} [K^{(1t)}]_{rs}^{-1} K_{slp}^{(2t)}. \quad (19)$$

Note that selecting the cubic stiffness tensor $K_{ijlp}^{(3t)}$ according to Eq. (19) assures that the system will remain stable as the condensation of the decondensed model recovers the original condensed model which is stable.

The validation of this full reduced order modeling approach was achieved first on the cantilevered beam subjected to a uniform pressure and shown in Figs 5 and 6 are the comparisons of the tip displacement obtained by Nastran, the condensed reduced order model, and the full reduced order model. A similar comparison is shown in Fig. 7 and 8 when an additional, compressive inplane force at the tip also exists of magnitude equal to 10% of the total transverse load applied. In all cases, it is found that the full reduced order model performs extremely well over a broad range of tip deflections, exceeding those expected in practice.

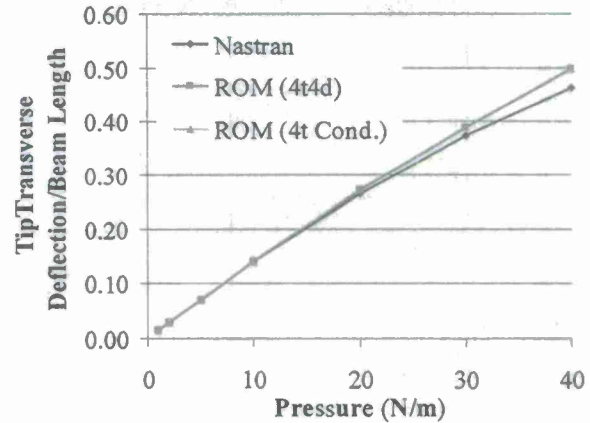


Figure 5. Tip transverse deflection vs. load, beam model. Full Nastran, 4-mode condensed ("4t Cond."), and 4 transverse - 4 dual modes ("4t4d") reduced order models ("ROM").

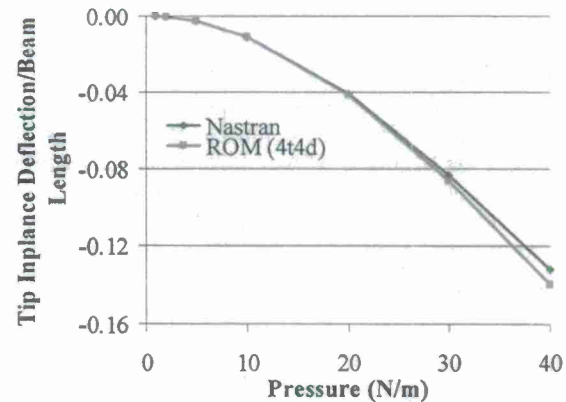


Figure 6. Tip inplane deflection vs. load, beam model. Full Nastran and 4 transverse - 4 dual modes reduced order model ("ROM(4t4d)").

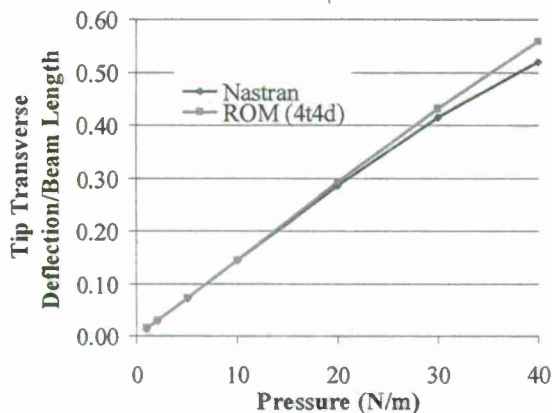


Figure 7. Tip transverse deflection vs. load, beam model. Full Nastran and 4 transverse - 4 dual modes reduced order model ("ROM(4t4d)"), 10% inplane compressive tip load.

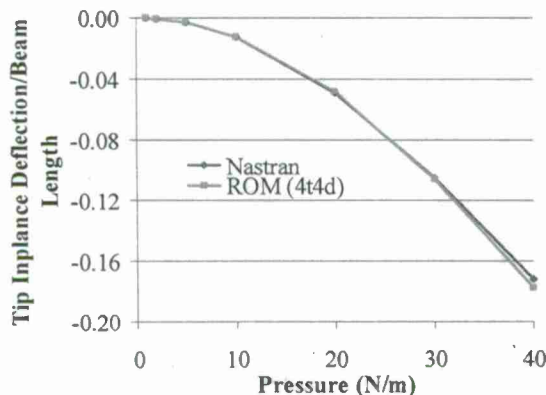


Figure 8. Tip inplane deflection vs. load, beam model. Full Nastran and 4 transverse - 4 dual modes reduced order model ("ROM(4t4d)"), 10% inplane compressive tip load.

Having successfully validated the decondensed reduced order model in static situations, it was desired next to assess its predictive capabilities in dynamic situations. To this end, a random excitation, white noise in the frequency domain $[0, 600]$ Hz, was applied in the transverse direction without axial load. Two different excitation levels were considered corresponding to standard deviations of 6, 24, and 48 N/m. To permit a close comparison between the Nastran and ROM results, a simple Rayleigh damping model was adopted, i.e. for which the damping matrix is $D = \alpha M + \beta K$ with $\alpha = 1.60/s$ and $\beta = 1.24E-5s$. This selection led to damping ratios between 0.6% and 2.1% on the first four transverse modes.

The power spectrum of the tip displacement in the transverse and axial directions are shown in Fig. 9 and

10 for the former and latter excitation case, respectively, for both Nastran SOL 400 and the 4 transverse - 4 dual decondensed reduced order model. Note the near perfect matching between the Nastran and reduced order model predictions over the entire frequency range of excitation and for both cases.

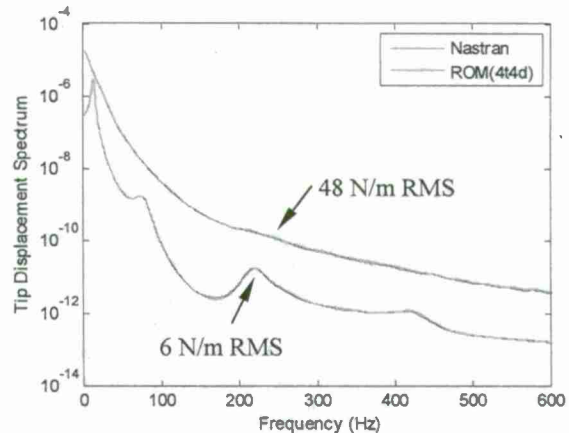


Figure 9. Power spectra of the random tip transverse response Full Nastran and 4 transverse - 4 dual modes reduced order model ("ROM(4t4d)").

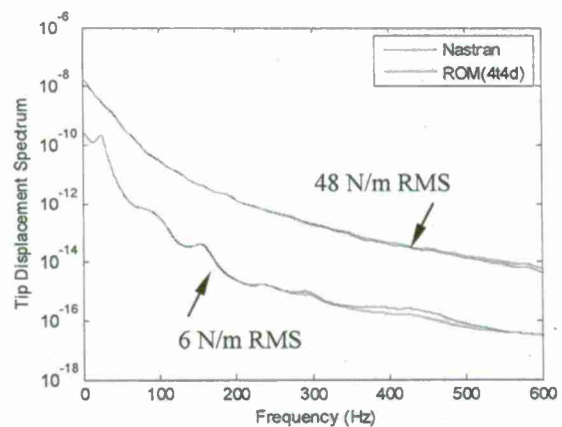


Figure 10. Power spectra of the random tip inplane response Full Nastran and 4 transverse - 4 dual modes reduced order model ("ROM(4t4d)").

Interestingly, the two corresponding standard deviations of the transverse tip displacement are not in the ratio 1 to 8 as the excitation as might have been construed from the near linearity of the static displacement vs. load of Fig. 1. These standard deviations are 0.0062, 0.0132, and 0.0192 m or 2.7%, 5.8%, and 8.5% of the beam length. In fact, the shape of the transverse displacement spectra, even at the lowest excitation level, clearly suggest the presence of nonlinearity.

To better understand these seemingly different results, similar response computations were also carried out with the 4-mode condensed reduced order model. These results, e.g. see Fig. 11, demonstrate indeed that the

condensed model behaves nearly linearly. This observation is further supported by the standard deviations of the tip transverse displacements which were found to be 0.0228, 0.0912, and 0.15514 m or 10%, 39.9%, and 67.9%. Thus, the condensed model is nearly linear until the largest load case.

As expected by construction, see Fig. 11, the condensed model predictions match their decondensed counterparts (and the Nastran results) in the zero frequency limit but deviate otherwise demonstrating that the increased nonlinearity observed in the dynamic case as opposed to the static one originates from the inertia and damping terms of the inplane motions. These results indicate that the consideration of condensed models of cantilevered structures may reflect well their static nonlinear behavior but may not be appropriate in dynamic conditions.

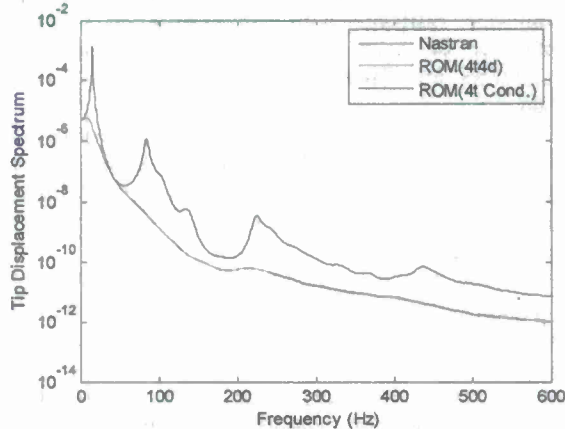


Figure 11. Power spectra of the random tip transverse response, 24N/m RMS excitation. Full Nastran, 4 transverse - 4 dual modes reduced order model ("ROM(4t4d)"), and 4 transverse condensed reduced order model ("ROM(4t Cond.)").

The last validation of the reduced order modeling strategy with the decondensation procedure focused on the prediction of the buckling tip load and of the post-buckling deflection of the beam. The Nastran buckling load was obtained using SOL 105 and was found to be 5.00lbs. The estimate of this load from the reduced order model was obtained under similar linear static assumptions, i.e. the inplane equations Eq. (15) were solved first to yield

$$q_j^{(i)} = [K^{(1i)}]_{ji}^{-1} F_i^{(i)} N \quad (20)$$

where $F_i^{(i)}$ denote the inplane modal forces associated with a unit tip force while N is the unknown magnitude of this force. Introducing the above expression in the transverse equations, Eq. (14), and

further linearizing leads in the static case to the condition

$$K_{ij}^{(1i)} q_j^{(i)} = (-N) \left\{ K_{ijl}^{(2i)} [K^{(1i)}]_{lp}^{-1} F_p^{(i)} \right\} q_j^{(i)} \quad (20)$$

which is recognized as a generalized eigenvalue problem in which $-N$ is the eigenvalue. This process led to the estimate of 5.01lbs for the tip load.

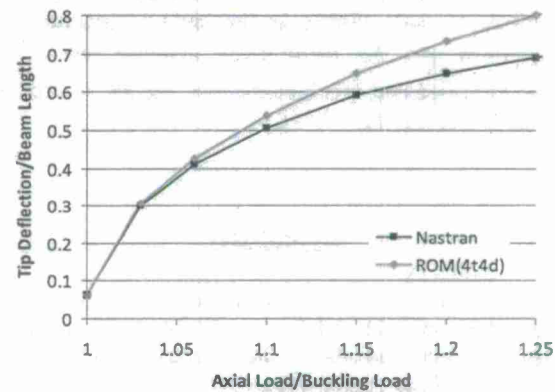


Figure 12. Post buckling tip transverse deflection vs. axial only load. Full Nastran and 4 transverse - 4 dual modes reduced order model ("ROM(4t4d)").

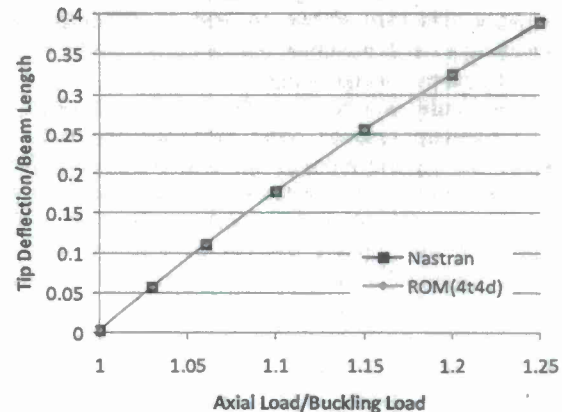


Figure 13. Post buckling tip inplane deflection vs. axial only load. Full Nastran and 4 transverse - 4 dual modes reduced order model ("ROM(4t4d)").

Given this very good matching of the buckling load, an analysis of the post-buckling behavior was undertaken. That is, the tip load was increased past its buckling value and the static displacement of the beam tip in both transverse and inplane directions was computed by both NASTRAN SOL 106 and the 8-mode reduced order model. These results are shown in Fig. 12 and 13. It is clearly seen that the reduced order model accurately captures the post buckling behavior for transverse deflections as large as 40%-50% of the beam length. For larger deflections, a steadily growing

difference with the Nastran results is observed, similarly to Figs 2 and 5-8. This difference with Nastran is rooted in the specification in the reduced order model of the linearly elastic behavior between the *undeformed* stress and strain tensors. This is in contrary to Nastran which specifies a similar property between the *deformed* stress and strain tensors. As discussed in Eqs (2)-(5), this difference becomes increasing more visible as the level of deformation increases and the deformation gradient tensor \underline{F} becomes less and less identity-like, exactly as seen in Figs 2, 5-8, and 12.

SUMMARY

The focus of this investigation was on the development and validation of structural dynamic reduced order models for the geometrically nonlinear response of flat cantilevered structures, e.g. beams and plates. It was first observed that the static displacement vs. load curves of cantilevered structures exhibit a rather weak nonlinearity as compared to those for structures supported on all sides. This property was then shown to lead to difficulties in obtaining a stable nonlinear reduced order model using recently proposed algorithms.

This difficulty was resolved through the introduction of a two-step reduced order modeling approach in which the inplane motions are first condensed, then reintroduced in a "decondensation" stage. This process led to a reduced order model exhibiting both transverse and inplane degrees of freedom that is applicable for all loading conditions: transverse forces, inplane forces or combination thereof.

This reduced order modeling approach was assessed primarily on a cantilevered beam model subjected first to static transverse alone, transverse-inplane, and inplane alone (buckling and post buckling) loads. In all cases, an excellent agreement with the corresponding Nastran results was observed for transverse displacements up to 40%-50% of beam length. Above that limit, it was demonstrated that the difference between the reduced order model and Nastran results originates from a difference in the definition of the linearly elastic behavior, which is stated between the undeformed stress and strain tensors in the reduced order model and the deformed ones in Nastran.

An assessment of the reduced order model under dynamic transverse loads was also carried out with the same success and demonstrated the need to include the inplane inertia and damping terms in the model for an accurate prediction of the response.

ACKNOWLEDGEMENTS

The financial support of this work by the STTR contract SA9550-08C-0004 to ZONA Technology and ASU from the Air Force Office of Scientific Research with Drs F. Fahroo and P. Beran as grant monitors is gratefully acknowledged.

REFERENCES

1. McEwan, M.I., Wright, J.R., Cooper, J.E., and Leung, A.Y.T., "A combined Modal/Finite Element Analysis Technique for the Dynamic Response of a Nonlinear Beam to Harmonic Excitation," *Journal of Sound and Vibration*, Vol. 243, pp. 601-624, 2001.
2. Muravyov, A.A., and Rizzi, S.A., "Determination of Nonlinear Stiffness with Application to Random Vibration of Geometrically Nonlinear Structures," *Computers and Structures*, Vol. 81, pp. 1513-1523, 2003.
3. Hollkamp, J.J., Gordon, R.W., and Spottswood, S.M., "Nonlinear Modal Models for Sonic Fatigue Response Prediction: A Comparison of Methods," *Journal of Sound and Vibration*, Vol. 284, pp. 1145-1163, 2005.
4. Mignolet, M.P., Radu, A.G., and Gao, X., "Validation of Reduced Order Modeling for the Prediction of the Response and Fatigue Life of Panels Subjected to Thermo-Acoustic Effects," *Proceedings of the 8th International Conference on Recent Advances in Structural Dynamics*, Southampton, United Kingdom, Jul. 14-16, 2003.
5. Radu, A., Yang, B., Kim, K., and Mignolet, M.P., "Prediction of the Dynamic Response and Fatigue Life of Panels Subjected to Thermo-Acoustic Loading," *Proceedings of the 45th Structures, Structural Dynamics, and Materials Conference*, Palm Springs, California, Apr. 19-22, 2004. Paper AIAA-2004-1557.
6. Przekop A., and Rizzi S.A., "Nonlinear Reduced Order Random Response Analysis of Structures with Shallow Curvature," *AIAA Journal* Vol. 44 (8), pp. 1767-1778, 2006.
7. Gordon R.W., and Hollkamp, J.J., "Reduced-Order Modeling of the Random Response of Curved Beams using Implicit Condensation," *AIAA-2006-1926*, 2006.
8. Spottswood, S.M., Hollkamp, J.J., and Eason, T.G., "On the Use of Reduced-Order Models for a Shallow Curved Beam Under Combined Loading," *Proceedings of the 49th Structures, Structural Dynamics, and Materials Conference*, Schaumburg, Illinois, Apr. 7-10, 2008. AIAA Paper AIAA-2008-1873.
9. Kim, K., Wang, X.Q., and Mignolet, M.P., "Nonlinear Reduced Order Modeling of Functionally Graded Plates," *Proceedings of the 49th Structures*,

Structural Dynamics, and Materials Conference, Schaumburg, Illinois, Apr. 7-10, 2008. AIAA Paper AIAA-2008-1873.

10. Kim, K., Kim, Y.C., Mignolet, M.P., Liu, D.D., Chen, P.C., Lee, D.H., "Random Aeroelastic Response Due to Strong Hypersonic Unsteady-Wave/Shock Interaction with Acoustic Loads," *Proceedings of the 48th Structures, Structural Dynamics, and Materials Conference*, Honolulu, Hawaii, Apr. 23-26, 2007. AIAA Paper AIAA-2007-2014.

11. Fung, Y.C., and Tong, P., *Classical and Computational Solid Mechanics*, World Scientific, River Edge, New Jersey, 2001.

12. Bonet, J., and Wood, R.D., *Nonlinear Continuum Mechanics for Finite Element Analysis*, Cambridge University Press, Cambridge, 1997.

13. Mignolet, M.P., and Soize, C., "Stochastic Reduced Order Models for Uncertain Geometrically Nonlinear Dynamical Systems," *Computer Methods in Applied Mechanics and Engineering*, Vol. 197, 2008, pp. 3951-3963.

Attachment H

Nonlinear Reduced Order Modeling of Flat Cantilevered Structures

A P.h.D Thesis by V. Khanna, December 2009

Nonlinear Reduced Order Modeling of Flat Cantilevered Structures

P.h.D. Thesis

by

V. Khanna

December 2009

ABSTRACT

Reduced order (or modal) models are a standard tool in linear structural dynamics but their development and use in the context of nonlinear problems has only been initiated in the last decade. The advantages of these reduced order models include not only the computational speed in the determination of the response but also, and more importantly maybe, the ease with which these models can be coupled to other physics codes, e.g. aerodynamics, heat transfer. Much of the applications to date have focused on clamped structures, especially those modeling aircraft panels.

The focus of the present investigation is on the development and validation of structural dynamic reduced order models for the geometrically nonlinear response of flat cantilevered structures, e.g. beams and plates. The specificities of cantilevered structures, as compared to those supported all around, are first highlighted. On this basis, extensions of existing reduced order modeling strategies are presented which provide a complete representation of the structural response, i.e., including both transverse and inplane displacement fields. Next, this methodology is successfully applied, first to a simple beam model and then to a flat wing both of which subjected to transverse loads. Finally, the response of a beam under combined transverse and inplane loads as well as its postbuckling behavior are also shown to be also accurately predicted by the reduced order model.

To my parents.

ACKNOWLEDGMENT

I would like to express my deepest thanks to Dr. Marc P. Mignolet for his unique stewardship and guidance that has not only brought about the successful completion of this work but also made this course of graduate study a memorable experience. I am also grateful to Dr. Aditi Chattopadhyay, Dr. Joseph K. Davidson and Dr. Henry Sodano for serving on my committee.

My heartfelt thanks to Dr. Julian X.Q.Wang for his vital inputs, and our fruitful discussions, which were key to my progress. Thanks to Dr. Kwangkeun Kim for his fundamental work towards this research topic. And special thanks to Kringan Saha and Javier Avalos for their camaraderie which made this graduate study a thoroughly enjoyable experience.

TABLE OF CONTENTS

	<u>Page</u>
1. INTRODUCTION	H-1
2. REDUCED ORDER MODELING.....	H-3
2.1 GENERAL FORMULATION.....	H-3
2.2 CANTILEVER STRUCTURES PROPERTIES	H-6
2.3 CODNESED REDUDED ORDER MODELS	H-10
2.4 DECONDENSED REDUCED ORDER MODEL	H-13
3. VALIDATION CASE	H-15
3.1 STATIC TRANSVERSE LOAD.....	H-16
3.2 STATIC TRANSVERSE AND STATIC INPLANE LOAD.....	H-17
3.3 DYNAMIC TRANSVERSE LOAD.....	H-21
3.4 DYNAMIC TRANSVERSE AND STATIC INPLANE LOAD.....	H-23
3.5 BUCKLING LOAD PREDICTION.....	H-26
4. CONCLUSIONS.....	H-28
REFERENCES	H-29

LIST OF TABLES

	<u>Page</u>
1. Beam Properties	H-7
2. Cantilevered Beam ROM Coefficients	H-8
3. Clamped-Clamped Beam ROM Coefficients	H-8

LIST OF FIGURES

	<u>Page</u>
1. Deformed –Unreformed Configuration	H-3
2. Peak Static Transverse Displacements vs. Uniform Load Magnitude for the Cantilever and Clamped-Clamped Beam	H-7
3. Tip Transverse Deflection vs. Static Load, Beam Model. Full Nastran and 4-Mode Condensed Reduced Order Model (“ROM (4t Cond.)”)	H-11
4. Aluminum Wing Model and Discretization.....	H-12
5. Tip Transverse Deflection vs. Static Transverse Load. Full Nastran and 2-, 4-, and 6-Mode Condensed Reduced Order Models (“ROM (Nt Cond.)”).....	H-13
6. Tip Transverse Deflection vs. Static Load, Beam Model. Full Nastran, 4-Mode Condensed (“4t Cond.”), and Transverse – 4 Dual Modes (“4t4d”) Reduce Order Models (“ROM”).....	H-16
7. Tip Inplane Deflection vs. Static Load, Beam Model. Full Nastran and 4 Transverse – 4 Dual Modes Reduced Order Model (“ROM(4t4d)”)	H-16
8. Tip Transverse Deflection vs. Static Load, Beam Model. Full Nastran and 4-Transverse – 4 Dual Modes Reduced Order Model (“ROM(4t4d)”), 20% Inplane Compressive Tip Load.....	H-17
9. Tip Inplane Deflection vs. Static Load, Beam Model. Full Nastran and 4-Transverse – 4 Dual Modes Reduced Order Model (“ROM(4t4d)”), 20% Inplane Compressive Tip Load.....	H-17
10 Tip Transverse Deflection vs. Static Load, Beam Model. Full Nastran and 4-Transverse – 4 Dual Modes Reduced Order Model (“ROM(4t4d)”), 20% Inplane Tensile Tip Load	H-18
11. Tip Inplane Deflection vs. Static Load, Beam Model. Full Nastran and 4-Transverse – 4 Dual Modes Reduced Order Model (“ROM(4t4d)”), 20% Inplane Tensile Tip Load	H-18
12. Tip Transverse Deflection vs. Static Load, Beam Model. Full Nastran and 4-Transverse – 4 Dual Modes Reduced Order Model (“ROM(4t4d)”), 40% Inplane Compressive Tip Load.....	H-19
13. Tip Inplane Deflection vs. Static Load, Beam Model. Full Nastran and 4-Transverse – 4 Dual Modes Reduced Order Model (“ROM(4t4d)”), 40% Inplane Compressive Tip Load.....	H-19

14. Tip Transverse Deflection vs. Static Load, Beam Model. Full Nastran and 4-Transverse – 4 Dual Modes Reduced Order Model (“ROM(4t4d)”), 40% Inplane Tensile Tip Load.....	H-20
15. Tip Inplane Deflection vs. Static Load, Beam Model. Full Nastran and 4-Transverse – 4 Dual Modes Reduced Order Model (“ROM(4t4d)”), 40% Inplane Tensile Tip Load.....	H-20
16. Power Spectra of the Random Tip Transverse Response Full Nastran and 4 Transverse – 4 Dual Modes Reduced Order Model (“ROM(4t4d)”)	H-21
17. Power Spectra of the Random Tip Inplane Response Full Nastran and 4 Transverse – 4 Dual Modes Reduced Order Model (“ROM(4t4d)”)	H-22
18. Power Spectra of the Random Tip Transverse Response, 24N/m RMS Excitation. Full Nastran, 4 Transverse – 4 Dual Modes Reduced Order Model (“ROM(4t4d)”), and 4 Transverse Condensed Reduced Order Model (“ROM(4t Cond.)”)	H-23
19. Power Spectra of the Random Tip Transverse Response Full Nastran and “Decondensed” Reduced Order Model (“ROM(4t4d)”) for 40% Static Inplane Buckle Load	H-24
20. Power Spectra of the Random Tip Inplane Response Full Nastran and “Decondensed” Reduced Order Model (“ROM(4t4d)”) for 40% Static Inplane Buckle Load	H-24
21. Power Spectra of the Random Tip Transverse Response Full Nastran and “Decondensed” Reduced Order Model (“ROM(4t4d)”) for 80% Static Inplane Buckle Load	H-25
22. Power Spectra of the Random Tip Inplane Response Full Nastran and “Decondensed” Reduced Order Model (“ROM(4t4d)”) for 80% Static Inplane Buckle Load	H-25
23. Post Buckling Tip Transverse Deflection vs. Axial Only Load. Full Nastran and Transverse – 4 Dual Modes Reduced Order Model (“ROM(4t4d)”)	H-26
24. Post Buckling Tip Inplane Deflection vs. Axial Only Load. Full Nastran and Transverse – 4 Dual Modes Reduced Order Model (“ROM(4t4d)”)	H-27

1. INTRODUCTION

The next generation of air vehicles will continue to exhibit the trends of lighter, more flexible, and yet higher loaded wings and bodies. This situation is clear from projects such as the High Altitude Long Endurance and planned hypersonic vehicles. These trends have already and will continue to result in structures which respond in a geometrically nonlinear (i.e., large deflection) manner to the deterministic and random dynamic loads. This non-linearity implies in particular a transverse – in-plane coupling that is not accounted for in linear analyses which typically over-predict, sometimes significantly, the response. Certainly, finite element formulations of these structural dynamic problems are available but the corresponding computations can be quite lengthy, especially when assessing the fatigue life of these structures to random dynamic loads. Further, these nonlinear models are not easy to couple to existing codes that predict the aerodynamics and/or the heat transfer aspects, as would be desirable for the required coupled multi-physics, aero-thermo-elastodynamic, analyses of these structures in their harsh environments.

An attractive alternative to detailed finite element models are reduced order models (ROM) which have received significant attention in the past few years in the context of beams, plates, and shells representative of aircraft panels, see for example (McEwan 2001; Muravyov 2003; Hollkamp 2005; Mignolet 2005; Radu 2004; Prezkop 2006; Gordon 2006; Spottswood 2008; Kim 2008). These reduced order models represent a natural extension to nonlinear structures of the modal models used in linear structural dynamic analyses. Specifically, the response of the structure is expressed in a modal expansion-type representation, i.e., as a linear combination of time-invariant, spatially varying basis functions weighted by time-dependent modal coordinates. Then, using a Galerkin approach (or weak formulation), it was shown, e.g. see (Kim 2008), that the modal coordinates satisfy a set of second order differential equations nonlinear only in the stiffness terms which consist only of linear, quadratic, and cubic polynomials of the modal coordinates. Interestingly, the cubic form of these nonlinear equations is obtained independently of the basis functions selected, but their coefficients (the linear, quadratic, and cubic stiffness coefficients) do depend on the basis selected.

The remaining important aspects in formulating such nonlinear reduced order models are thus: (i) the selection of the basis functions, and (ii) the evaluation of the coefficients of the cubic stiffness nonlinearity. In the limit of small motions, the nonlinear reduced order model should reduce naturally to a modal model and thus the nonlinear basis should completely include its linear counterpart, i.e. the set of linear modes significantly excited.

This is however not enough and a complete representation of the structural response requires additional basis functions. As a simple proof, consider the response to transverse loads of a flat, symmetric beam or plate subjected to a purely transverse loading. In the linear, infinitesimal case, the decoupling of the inplane and transverse modes implies that only the latter ones are necessary and no inplane motion takes place. However, finite deformations can only occur with

a stretching of the beam or plate and, accordingly, with inplane deformations. Thus, the nonlinear basis required for a full representation must include both transverse linear modes and functions describing the inplane motions.

In light of these comments, one can broadly separate the recent investigations (McEwan 2001; Muravyov 2003; Hollkamp 2005; Mignolet 2005; Radu 2004; Prezkop 2006; Gordon 2006; Spottswood 2008; Kim 2008) into two distinct groups: those which have relied on a full modeling of the response (Muravyov 2003; 2005; Radu 2004; Prezkop 2006 ; Kim 2008) and those in which the basis functions necessary to complement the linear modes are treated as “hidden” and implicitly condensed in the model, leaving only the modal coordinates associated with the linear modes as sole unknowns (McEwan 2001; Hollkamp 2005; Prezkop 2006; Spottswood 2008). The recovery of the full response is achieved after solving for these coordinates through the use of the “companion modes” which characterize the “hidden” part of the model.

Once the basis has been selected, the estimation of the stiffness coefficients is achieved from a series of static nonlinear responses of a full finite element model, either by imposing the displacements and determining the necessary forces (Muravyov, 2003; Mignolet, 2003; Radu 2004; Prezkop, 2006; Kim, 2008) using the algorithm of (Muravyov 2003) (as modified in (Mignolet 2005; Radu 2004 ; Kim 2008)) or by proceeding in reverse with the displacements induced by a series of loading cases (McEwan 2001; Hollkamp 2005; Gordon 2006; Spottswood 2008).

The reduced order models obtained in the recent literature have several key advantages over full finite element models. Most notably, they represent a compact and accurate representation of the response (both displacements and strains/stresses) which is typically computationally expedient (owing to the small number of degrees of freedom involved) but also easily integrable with other computational solvers as demonstrated in (Kim, 2007). Note furthermore that the reduced order modeling techniques described in (McEwan 2001; Muravyov 2003; Hollkamp 2005; Mignolet 2005; Radu 2004; Prezkop 2006; Gordon 2006; Spottswood 2008; Kim 2008).are generic, i.e. applicable in principle to a broad class of structures, not only to the panel like structures considered in these investigations. Implicit method of convergence is used Newton-Raphson, which requires the evaluation of Jacobian matrix at every time step. Though computation is expensive but advantage comes in the evaluation of the natural frequencies around other deformed-states.

These observations suggest that reduced order models will be particularly convenient in multi-physics problems leading to large responses, one of which is the post flutter limit cycle oscillations of wings and other lifting surfaces.

2. REDUCED ORDER MODELING

2.1 GENERAL FORMULATION

A ROM is defined here as a modal-like representation of the displacement field u_i as

$$u_i(\underline{X}, t) = \sum_{n=1}^M q_n(t) U_i^{(n)}(\underline{X}) \quad i = 1, 2, 3 \quad (1)$$

where \underline{X} denotes the coordinates of a point (in the undeformed configuration), $U_i^{(n)}(\underline{X})$ are specified, constant basis functions satisfying the boundary conditions also in the undeformed configuration, and $q_n(t)$ are the time variable generalized coordinates.

The derivation of the governing (ordinary differential) equations for the generalized coordinates $q_n(t)$ can be performed in a Galerkin format. That is, the error obtained by introducing Equation (1) in the equations of finite elasticity expressed in the undeformed configuration will be made orthogonal to the set of basis functions $U_i^{(n)}(\underline{X})$. A key issue in this derivation is the clarification of the concept of linear elasticity. Consider an arbitrary linearly elastic (i.e. with a linear relation between the Green strain and second Piola-Kirchhoff stress tensors) structure undergoing large deformations. The position vector of a point of the structure will be denoted by \underline{X} in the reference configuration and as \underline{x} in the deformed one so that the displacement vector is $\underline{u} = \underline{x} - \underline{X}$ (as shown in Figure 1).



Figure 1 Deformed - Unreformed Configuration

Associated with the displacement field \underline{u} are deformations which are characterized by the Green strain tensor $\underline{\underline{E}}$ of components

$$E_{ij} = \frac{1}{2} (F_{ki} F_{kj} - \delta_{ij}) \quad (2)$$

where the components F_{ij} of the deformation gradient tensor $\underline{\underline{F}}$ are

$$F_{ij} = \frac{\partial x_i}{\partial X_j} = \delta_{ij} + \frac{\partial u_i}{\partial X_j} \quad (3)$$

with δ_{ij} the Kronecker symbol and $\underline{u} = \underline{x} - \underline{X}$. Note finally that J denotes the Jacobian of the transformation $\underline{x} = \underline{x}(\underline{X})$, i.e. $J = \det(\underline{F})$. Now working with the stress and strain tensors in the undeformed configuration, and assuming they are linearly related, i.e.

$$S_{ij} = \sum_{kl} C_{ijkl} E_{kl} \quad (4)$$

Where \underline{S} denote the second Piola-Kirchhoff stress tensor and \underline{C} is a fourth order elasticity tensor function in general of the undeformed coordinates \underline{X} satisfying the symmetry conditions

$$C_{ijkl} = C_{jikl} = C_{ijlk} \quad (5)$$

as well as

$$C_{ijkl} = C_{klij} \quad (6)$$

An alternative formulation can be derived by assuming a similar relation between the corresponding deformed configuration tensors, i.e.

$$\sigma_{ij} = \sum_{kl} \hat{C}_{ijkl} e_{kl} \quad (7)$$

where $\underline{\sigma}$ and \underline{e} are the Cauchy stress and Almansi strain tensors and $\hat{\underline{C}}$ is also a fourth order elasticity tensor but dependent on the deformed coordinates \underline{x} .

The undeformed stress and strain tensors are obtained from their deformed counterparts from the pull back operations (e.g., see (Fung, 2001; Bonet, 1997))

$$\underline{S} = J \underline{F}^{-1} \underline{\sigma} \underline{F}^{-T} \quad \text{and} \quad \underline{E} = \underline{F}^T \underline{e} \underline{F} \quad (8)$$

Combining Equations (2)-(7), it is readily seen that it is not possible for both sets elements C_{ijkl} and \hat{C}_{ijkl} to be independent of the deformations, i.e. of F_{ij} . Equivalently, the two linear elasticity definitions, Equations (2) and (6), are not compatible and different displacement fields will be obtained by assuming one or the other law.

The linear elasticity condition of Equation (2) will be assumed here. The equation of motion of the structure is then given by (e.g. see (Fung, 2001)).

$$\frac{\partial}{\partial X_k} \left(\sum_j F_{ij} S_{jk} \right) + \rho_0 b_i^0 = \rho_0 \ddot{u}_i \quad \text{for } \underline{X} \in \Omega_0 \quad (9)$$

where $\rho_0(\underline{X})$ represents the density in the reference configuration and is positive over the $\underline{X} \in \Omega_0$ and \underline{b}^0 is the vector of body forces, all of which are assumed to depend on the coordinates X_i and be expressed in the reference configuration in which the structure occupies the domain Ω_0 . The boundary conditions are

$$\underline{u} = \underline{0} \quad \text{for } \underline{X} \in \partial\Omega_0'' \quad (10)$$

and

$$F_{ij} S_{jk} n_k^0 = t_i^0 \quad \text{for } \underline{X} \in \partial\Omega_0' \quad (11)$$

where domain Ω_0 is composed of two parts, $\partial\Omega_0''$ on which the displacements are specified and $\partial\Omega_0'$ represents the tractions t_i^0 .

Thus the weak formulation of the geometric nonlinear elastodynamic problem is to determine the displacement field \underline{u}

$$\int_{\Omega_0} \rho_0 v_i \ddot{u}_i d\underline{X} + \int_{\Omega_0} \frac{\partial v_i}{\partial X_k} (F_{ij} S_{jk}) d\underline{X} = \int_{\Omega_0} \rho_0 v_i b_i^0 d\underline{X} + \int_{\partial\Omega_0'} v_i t_i^0 ds \quad (12)$$

where the integral is over the whole domain Ω_0 and v_i satisfying the equation. Also $\underline{v} = \underline{v}(\underline{X})$ denotes the vector function of \underline{X} that is sufficiently differentiable and such that

$$\underline{v} = \underline{0} \quad \text{on } \partial\Omega_0''.$$

The weak form of equation is then substituted with Equation (1) to obtain the final governing equations (e.g. see (Kim, 2008))

$$M_{ij} \ddot{q}_j + D_{ij} \dot{q}_j + K_{ij}^{(1)} q_j + K_{ijl}^{(2)} q_j q_l + K_{ijlp}^{(3)} q_j q_l q_p = F_i \quad (13)$$

where following standard practice, a damping term $D_{ij} \dot{q}_j$ has been added to collectively represent various dissipation mechanisms. In the above equation M_{ij} denotes the elements of the

mass matrix, $K_{ij}^{(1)}$, $K_{ijl}^{(2)}$, $K_{ijlp}^{(3)}$ are the linear, quadratic, and cubic stiffness coefficients and F_i are the pulled back modal forces. Note that it is sufficient to consider $p \geq l \geq j$. Although integral expressions for these components can be derived, e.g. see (Kim, 2008), it is easier to identify/evaluate them directly from the finite element model. Specifically, denoting by $\underline{\varphi}_i$ the vector of displacements at the finite element degrees of freedom corresponding to $U_i^{(n)}(\underline{x})$, one finds directly that

$$M_{ij} = \underline{\varphi}_i^T M_G \underline{\varphi}_j \quad (14)$$

and

$$F_i = \underline{\varphi}_i^T \underline{F}(t) \quad (15)$$

where M_G is the global mass matrix and $\underline{F}(t)$ is the vector of forces pulled back to the undeformed configuration.

The determination of the stiffness parameters is more complex and two distinct methods have been proposed to achieve this task. In the first one, the evaluation procedure of (Muravyov, 2003), as modified in (Mignolet, 2003; Radu, 2004; Kim, 2008), the coefficients $K_{ij}^{(1)}$, $K_{ijl}^{(2)}$, and $K_{ijlp}^{(3)}$ are determined from the computed modal forces necessary to induce a certain ensemble of prescribed static displacement fields of the structure. In the second approach, see (McEwan, 2001; Hollkamp 2005; Radu, 2004, Gordon, 2006), the stiffness coefficients are determined from the computed static displacements induced by prescribed forces.

2.2 CANTILEVER STRUCTURES PROPERTIES

The nonlinearity in the cantilever beams are much stronger as compared to beams with two or more supports. The nonlinear reduced order modeling approach, as explained previously has been used for beams and panels supported on two opposite sides or more. The comparison between the multiple supported and cantilevered structures could be better understood with the quantitative comparison below. For the two sample models with same dimensions and discretization, we can compare the deflections by applying a static uniformly distributed load in the transverse direction. Both of the beams are isotropic in nature, one is clamped at both ends and the other is cantilevered. The Figure 2 compares the peak static transverse displacements and Table 1 gives the properties of the structure.

Table 1 Beam Properties

Beam Length	0.2286 m
Cross-Section Width	0.0127 m
Cross-Section Thickness	$7.75 \cdot 10^{-4}$ m
Mass Per Unit Length	7875 kg/m ³
Young's Modulus	205,000 MPa
Shear Modulus	80,000 MPa
Number of Nodes	41

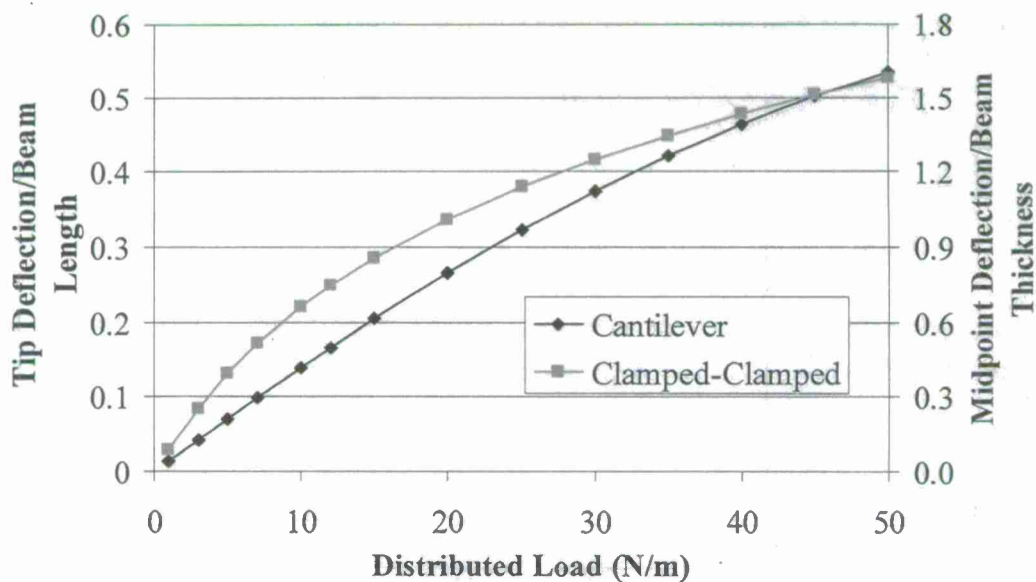


Figure 2 Peak Static Transverse Displacements vs. Uniform Load Magnitude for the Cantilever and Clamped-Clamped Beam

Note that to better distinguish the behavior of these beams, the displacement vs. the load curve, is plotted with displacement of the cantilever beam normalized by the beam length as opposed to the clamped-clamped response normalized by the much smaller beam thickness.

The same comparison can be addressed by seeking the stiffness coefficients of the two models for respective boundary conditions and comparing them. For simplicity a reduced order model involving only one transverse and one inplane mode (the dual modes of (Kim, 2008) are selected here). The various linear, quadratic and cubic stiffness coefficients are represented as $K_{ij}^{(1)}$, $K_{ijl}^{(2)}$, and $K_{ijlp}^{(3)}$ respectively. The linear decoupling of these transverse and the inplane motions implies first that $K_{12}^{(1)} = K_{21}^{(1)} = 0$, $M_{12} = M_{21} = 0$, and $D_{12} = D_{21} = 0$. Further, the symmetry of the system in the transverse direction implies that a switch of sign of the transverse forces leads to change of sign of the transverse displacement but leaves unchanged the inplane motions. Thus,

$$K_{111}^{(2)} = K_{212}^{(2)} = K_{122}^{(2)} = 0$$

and

$$K_{1112}^{(3)} = K_{1222}^{(3)} = K_{2111}^{(3)} = K_{2122}^{(3)} = 0$$

A final reduction of the model is achieved by assuming, as MSC. Nastran does (in SOL 106 and SOL 400), that there is no nonlinearity associated with the inplane motions. Then, $K_{1122}^{(3)} = K_{2222}^{(3)} = K_{2112}^{(3)} = 0$ also and the final reduced order model is

$$M_{11}\ddot{q}_1 + D_{11}\dot{q}_1 + K_{11}^{(1)}q_1 + K_{112}^{(2)}q_1q_2 + K_{1111}^{(3)}q_1^3 = F_1 \quad (16)$$

and

$$M_{22}\ddot{q}_2 + D_{22}\dot{q}_2 + K_{22}^{(1)}q_2 + K_{211}^{(2)}q_1^2 = F_2 \quad (17)$$

representing the equations for transverse and inplane respectively. The nonzero stiffness coefficients $K_{11}^{(1)}$, $K_{22}^{(1)}$, $K_{112}^{(2)}$, $K_{211}^{(2)}$, and $K_{1111}^{(3)}$ are presented in Tables 2 and 3.

Table 2 Cantilevered Beam ROM Coefficients

$K_{11}^{(1)}$	$K_{22}^{(1)}$	$K_{112}^{(2)}$	$K_{211}^{(2)}$	$K_{1111}^{(3)}$	$\hat{K}_{1111}^{(3)}$
$6.10 \cdot 10^3$	$3.10 \cdot 10^9$	$2.18 \cdot 10^{11}$	$1.09 \cdot 10^{11}$	$7.64 \cdot 10^{12}$	$1.24 \cdot 10^8$

Table 3 Clamped-Clamped Beam ROM Coefficients

$K_{11}^{(1)}$	$K_{22}^{(1)}$	$K_{112}^{(2)}$	$K_{211}^{(2)}$	$K_{1111}^{(3)}$	$\hat{K}_{1111}^{(3)}$

2.47 10 ⁵	7.26 10 ¹⁰	1.65 10 ¹²	8.26 10 ¹¹	5.88 10 ¹³	4.00 10 ¹³
----------------------	-----------------------	-----------------------	-----------------------	-----------------------	-----------------------

Comparing the two tables above reveals that: The cubic coefficient $K_{111}^{(3)}$ is smaller for the cantilevered configuration then for the clamped-clamped one.

The inplane transverse coupling terms $K_{112}^{(2)}$ and $K_{211}^{(2)}$ are significantly larger in magnitude for the cantilevered configuration then for the clamped-clamped one.

These two facts induce the much smaller nonlinearity of the cantilever configuration. The role of the inplane-transverse coupling terms in lowering the effective nonlinearity is best visualized by noticing that the inplane generalized coordinate q_2 can be obtained from Equation (17) as

$$q_2 = -\frac{K_{211}^{(2)}}{K_{22}^{(1)}} q_1^2 \quad (18)$$

since the present loading is static and is only transverse, i.e. $F_2=0$. Introducing Equation (18) into Equation (16) yields

$$M_{11}\ddot{q}_1 + D_{11}\dot{q}_1 + K_{11}^{(1)} q_1 + \hat{K}_{111}^{(3)} q_1^3 = F_1 \quad (19)$$

where

$$\hat{K}_{111}^{(3)} = K_{111}^{(3)} - \frac{K_{211}^{(2)} K_{112}^{(2)}}{K_{22}^{(1)}} \quad (20)$$

The values of the coefficients $\hat{K}_{111}^{(3)}$ for the two configurations, also given in Tables 2 and 3, are consistent with the trends of Figure 1.

Note, $\hat{K}_{111}^{(3)}$ is only $1.6 \cdot 10^{-5}$ of $K_{111}^{(3)}$ so that the stiffening induced by the pure transverse term $K_{111}^{(3)}$ is almost completely negated by the softening induced by the inplane motions. This situation is of particular concern from a numerical point of view as the coefficients $\hat{K}_{111}^{(3)}$ must remain positive to ensure a stiffening behaviour. This also raises the issue of numerical accuracy obtained for deriving the coefficients of stiffness, as they require to be accurate to 5th decimal place. The generalization of this stability condition when there are multiple modes is presented in (Mignolet, 2008) and is expressed through the positive definiteness of symmetric matrix, referred to as $\underline{\underline{K}}_B$, which combines the linear, quadratic, and cubic stiffness coefficients.

Unfortunately, numerical experimentation with the beam of properties given by Table 1 has demonstrated that a lack of positive definiteness of $\underline{\underline{K}}_B$ (see (Kim, 2008)) occurs with as few as

3 transverse and 3 inplane modes. Such a model is thus not only unphysical but it also leads to a poor matching of the response predicted by a nonlinear full finite element mode.

2.3 CODNESED REDUED ORDER MODELS

Condensed as the name implies refers to the model that gets constructed with degree of freedoms of the inplane motions “condensed” but solely based on the transverse deflection. In contrast to the full model that includes both transverse and inplane displacements, the condensed model would be represented by only Equation (19) for the one mode model. The idea of this formulation is to represent the net stiffening effect ($\hat{K}_{111}^{(3)}$) rather than evaluating large stiffening (i.e., $K_{111}^{(3)}$ in the above simple example), and softening terms ($K_{112}^{(2)}$ and $K_{211}^{(2)}$) separately, as done in the example above. As with the full reduced order model, the stiffness parameters of the condensed ROM can be obtained by either of the two approaches described earlier. The evaluation procedure of (Muravyov, 2001; Mignolet, 2003; Radu, 2004; Kim, 2008) was chosen here but was modified to reflect the condensation or unobservability of the inplane displacement. Thus the change is so made that it reflects the condensation of the inplane motions, only the transverse displacements were prescribed with inplane motions free to occur. This is carried out, as per the methodology, by ensemble of displacement field prescribed and the necessary forces determined.

Revisiting the equation of motion of the model, we have,

$$M_{ij}\ddot{q}_j + D_{ij}\dot{q}_j + K_{ij}^{(1)}q_j + K_{ijl}^{(2)}q_jq_l + K_{ijlp}^{(3)}q_jq_lq_p = F_i$$

with static displacement fields as,

$$u_i(\underline{X}, t) = \sum_{n=1}^M q_n(t) U_i^{(n)}(\underline{X}) \quad i = 1, 2, 3$$

Having known the traction $\partial\Omega'_0$ with different $q_n(t)$ through set of NASTRAN runs we can estimate the stiffness terms as follows. Now to find the unknowns in the equation we apply set of combination of modal forces on the system and observe the response (see (Muravyov, 2003)). For evaluation of $K_{ijl}^{(1)}$, $K_{ijj}^{(2)}$ and $K_{ijjj}^{(3)}$ which could be just solved for as F_i^n is known. Further the calculation of $K_{ijl}^{(2)}$, $K_{ijll}^{(3)}$ and $K_{ijll}^{(3)}$ for $l \neq j$ is solved for by application of combination of generalized coordinates q_j and q_l .

$$u_i^{(n)}(\underline{X}) = q_l U_i^{(n)}(\underline{x}) + q_j U_i^{(n)}(\underline{x}) \quad n = 1, 2, 3 \quad (21)$$

could generate the same. Lastly combination of all three could result in determination of $K_{ijlp}^{(3)}$.

The ROM model forms the basis of the decondensed ROM, which includes inplane (dual) modes to the existing transverse modes. Thus the response of the ROM model should just be applicable to static loads and the consideration would provide a reliable and fast perspective of the response. Applied in the following validation models is a static transverse load which generates close to 50% deflection at the tip for the cantilever model.

The first validation case is same as presented in the above discussion with material properties given in Table 1 and subjected to static load only, in transverse direction. The Figure 3 represents the results for series of nonlinear Nastran solution (SOL106), performed to obtain the evolution of the tip deflection as a function of the applied load magnitude. It also includes deflection predicted under linear model and those using a four transverse mode model nonlinear ROM with condensed inplane motion. The data presented is for deflections up to 1/2 of the beam length. As expected, the agreement of the condensed ROM is excellent at relatively small deflection levels and the fact very good until 40%-50% of the beam length (the error is 4.5% for a deflection nearly equal to 1/2 of the beam length).

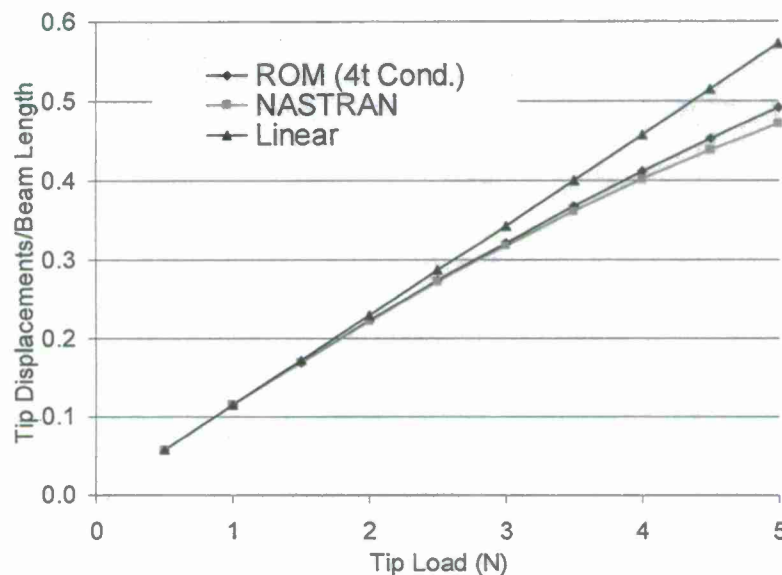


Figure 3 Tip Transverse Deflection vs. Static Load, Beam Model. Full Nastran and 4-Mode Condensed Reduced Order Model ("ROM (4t Cond.)")

The second validation example focused on the flat, aluminum wing model of Figure 4 modeled with CQUAD4 elements 1.15" thick. Shown in Figure 5 is the corresponding tip deflection vs. load (assumed uniformly distributed along the tip boundary) estimated from static Nastran solutions.

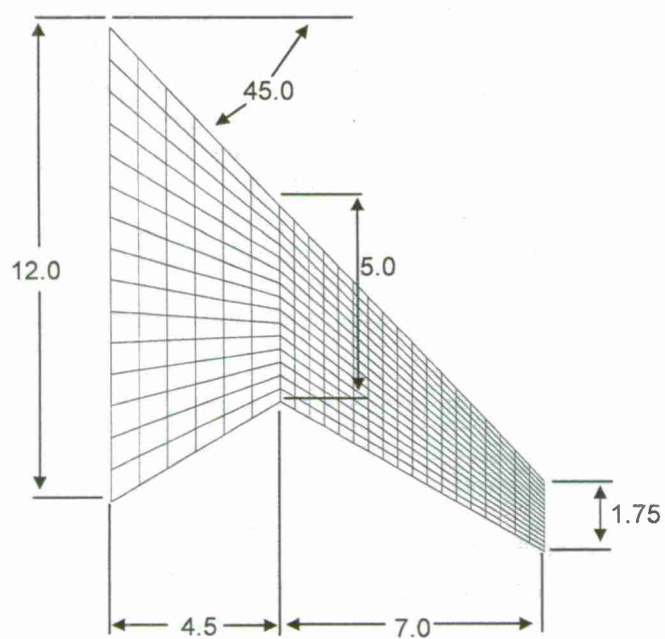
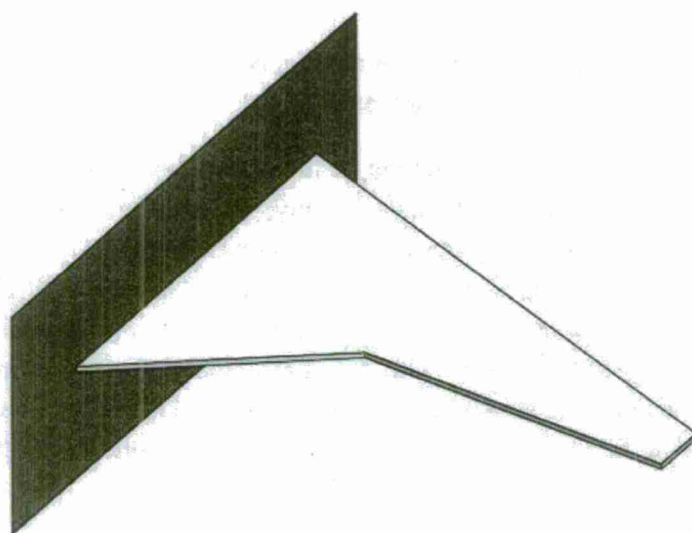


Figure 4 Aluminum Wing Model and Discretization

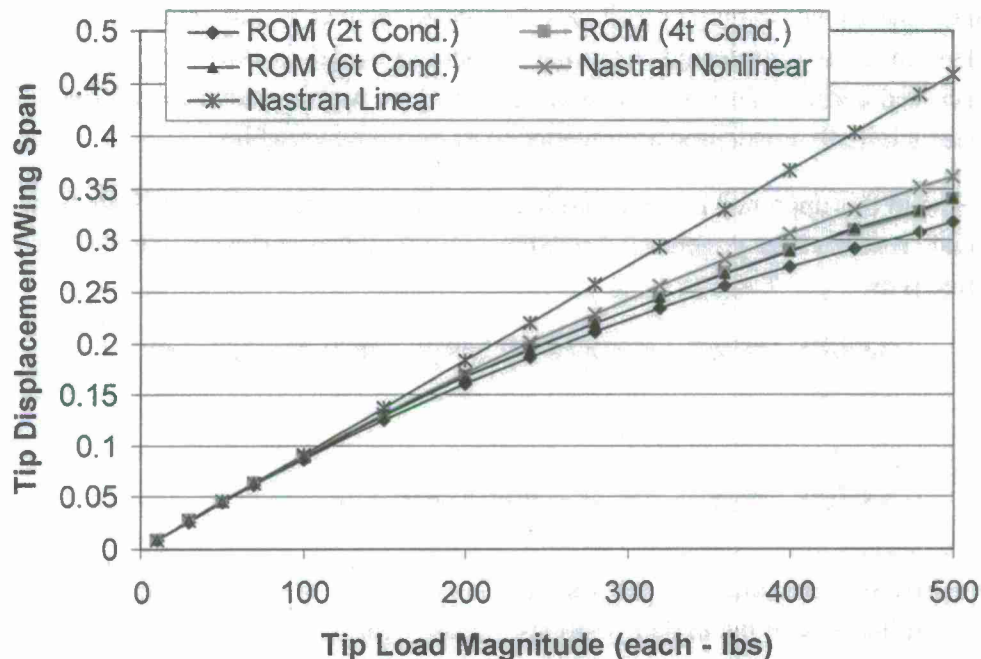


Figure 5 Tip Transverse Deflection vs. Static Transverse Load. Full Nastran and 2-, 4-, and 6-Mode Condensed Reduced Order Models ("ROM (Nt Cond.)")

Also presented on these figures are the deflections predicted under a linear model and those obtained by using two, four, and six transverse mode models in the above condensed ROM procedure. Clearly, convergence of the model is achieved in four to six modes and the accuracy is very good until a tip transverse deflection equal to 35% of the wing span (the error is approximately 6%).

2.4 DECONDENCED REDUCE ORDER MODEL

The results presented above are very significant and the corresponding reduced order models do provide an excellent basis for post flutter LCO analyses, for example. Nevertheless, the condensation of the inplane displacements entails limitations which are best revealed in the simplified analysis of Equations (16)-(19). Specifically, the derivation of Equation (19) from Equations (16) and (17) required the following assumptions:

- (i) there be no inplane forces (i.e., $F_2=0$ in the 1 mode model),
- (ii) the problem is static or the inplane inertia and damping effects can be neglected, and
- (iii) there is no nonlinearity in the inplane displacements or such nonlinearity can be neglected.

Of these 3 assumptions, the first one is probably the most significant limitation as it prevents for example the buckling and postbuckling analyses.

To eliminate the above 3 limitations, it was decided to recover a “full” reduced order model, i.e. with inplane motions represented, from the condensed model to avoid the numerical accuracy issues discussed earlier. This process is referred to here as “decondensation” since the inplane displacements initially condensed are reverted to as observed variables.

The first step in this approach is the generalization of the 2 mode analysis of Equations (16)-(19). To this end, separate the governing Equation (6) into those corresponding to transverse and inplane modes as:

$$M_{ij}^{(t)} \ddot{q}_j^{(t)} + D_{ij}^{(t)} \dot{q}_j^{(t)} + K_{ij}^{(1t)} q_j^{(t)} + K_{ijl}^{(2t)} q_j^{(t)} q_l^{(t)} + K_{ijlp}^{(3t)} q_j^{(t)} q_l^{(t)} q_p^{(t)} = F_i^{(t)} \quad (22)$$

and

$$M_{ij}^{(i)} \ddot{q}_j^{(i)} + D_{ij}^{(i)} \dot{q}_j^{(i)} + K_{ij}^{(1i)} q_j^{(i)} + K_{ijl}^{(2i)} q_j^{(i)} q_l^{(i)} = F_i^{(i)} \quad (23)$$

in which it has been assumed that the structure is symmetric in the transverse direction and that there is no nonlinearity of the inplane motions, i.e. assumption (ii).

In Equations (22) and (23), $q_j^{(i)}$ and $q_j^{(t)}$ denote the generalized coordinates associated with the inplane (superscript (i)) and transverse (superscript (t)) motions. Assuming that there are no forces in the inplane direction (assumption (i)) and that the frequencies of the excitation bandwidth are small with respect to the inplane mode frequencies (quasi-static inplane response or assumption (iii)), Equation (23) can be directly solved for the inplane displacements in terms of their transverse counterparts as:

$$q_j^{(i)} = -[K^{(1i)}]_{js}^{-1} K_{srl}^{(2i)} q_r^{(t)} q_l^{(t)} \quad (24)$$

Introducing Equation (24) in Equation (22) leads to the transverse only set of equations:

$$M_{ij}^{(t)} \ddot{q}_j^{(t)} + D_{ij}^{(t)} \dot{q}_j^{(t)} + K_{ij}^{(1t)} q_j^{(t)} + \hat{K}_{ijlp}^{(3t)} q_j^{(t)} q_l^{(t)} q_p^{(t)} = F_i^{(t)} \quad (25)$$

where

$$\hat{K}_{ijlp}^{(3t)} = K_{ijlp}^{(3t)} - K_{ijr}^{(2t)} [K^{(1t)}]_{rs}^{-1} K_{slp}^{(2t)} \quad (26)$$

In fact, Equations (25) and (26) are the necessary generalizations of Equations (19) and (20).

The decondensation problem is thus to create a full model of the form of Equations (22) and (23) from the condensed one of Equations (25) and (26) while maintaining the stability of the final model. Clearly, there is not enough information to do so and thus a two step approach was formulated as follows.

(a) A condensed model is first developed providing the tensor $\hat{K}_{ijlp}^{(3t)}$.

(b) A full, inplane and transverse, model is then developed using the approach of (Muravyov, 2003; Mignolet, 2003; Radu, 2004; Kim, 2008), giving estimates of the various tensors of Equations (25) and (26) and in particular $K_{ij}^{(1t)}$, $K_{ijr}^{(2t)}$, and $K_{slp}^{(2t)}$ but the tensor $K_{ijlp}^{(3t)}$ obtained by this approach is not used further. Rather, the cubic stiffness tensor $K_{ijlp}^{(3t)}$ of Equation (25) is obtained from Equation (26) as:

$$K_{ijlp}^{(3t)} = \hat{K}_{ijlp}^{(3t)} + K_{ijr}^{(2t)} \left[K^{(1t)} \right]_{rs}^{-1} K_{slp}^{(2t)} \quad (27)$$

Note that selecting the cubic stiffness tensor $K_{ijlp}^{(3t)}$ according to Equation (27) assures that the system will remain stable as the condensation of the decondensed model recovers the original condensed model which is stable.

3. VALIDATION CASE

The validation of this “decondensed” reduced order modeling approach was achieved first on the cantilevered beam subjected to an uniform static pressure. Shown in Figures 6 and 7 are the comparisons of the tip displacement obtained by Nastran, the condensed reduced order model, and the “decondensed” reduced order model. A similar comparison is shown when an additional, static compressive/tensile inplane force at the tip also exists of magnitude equal to 20% and 40% of the total transverse load applied. In all cases, it is found that the full reduced order model performs extremely well over a broad range of tip deflections, exceeding those expected in practice. Added to these validation cases are the comparison of the model with Nastran for dynamic transverse load. The “decondensed” model is then used to evaluate the buckling load and compared for the post buckling behavior.

Note, “decondensed” model represents the 4 transverse (as per condensed model) and 4 inplane (duals) from the full model. It is also referred as ROM(4t4d) in the figures below.

3.1 STATIC TRANSVERSE LOAD

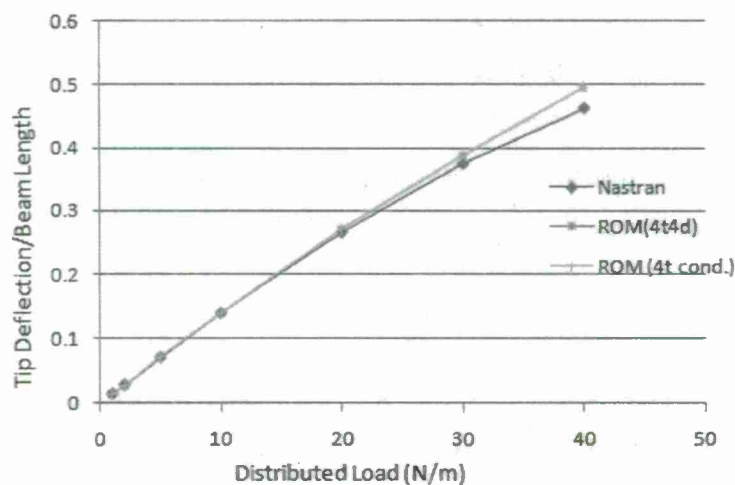


Figure 6 Tip Transverse Deflection vs. Static Load, Beam Model. Full Nastran, 4-Mode Condensed ("4t Cond."), and Transverse - 4 Dual Modes ("4t4d") Reduce Order Models ("ROM")

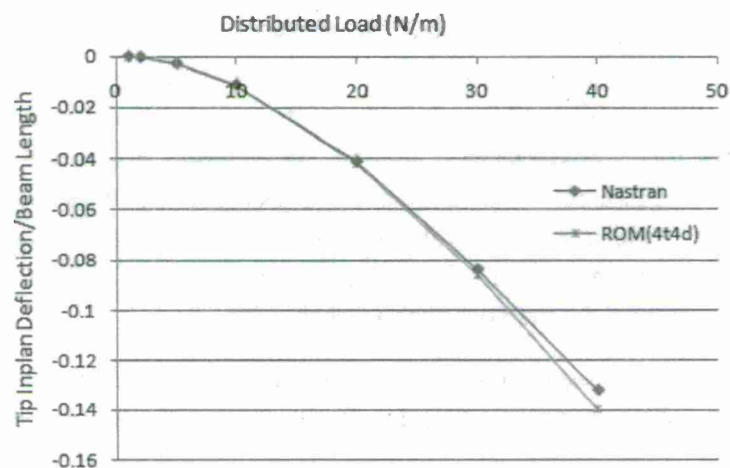


Figure 7 Tip Inplane Deflection vs. Static Load, Beam Model. Full Nastran and 4 Transverse - 4 Dual Modes Reduced Order Model ("ROM(4t4d)")

The "decondensed" (4t4d) model captures the inplane motion with high accuracy of 7% relative error at 12% beam length deflection. Also the tip transverse deflection matches that of the condensed model.

3.2 STATIC TRANSVERSE AND STATIC INPLANE LOAD

A similar comparison is shown with an additional, tensile/compressive inplane load at the tip of magnitude equal to 20% and 40% of the total transverse load (applied as tip force) respectively.

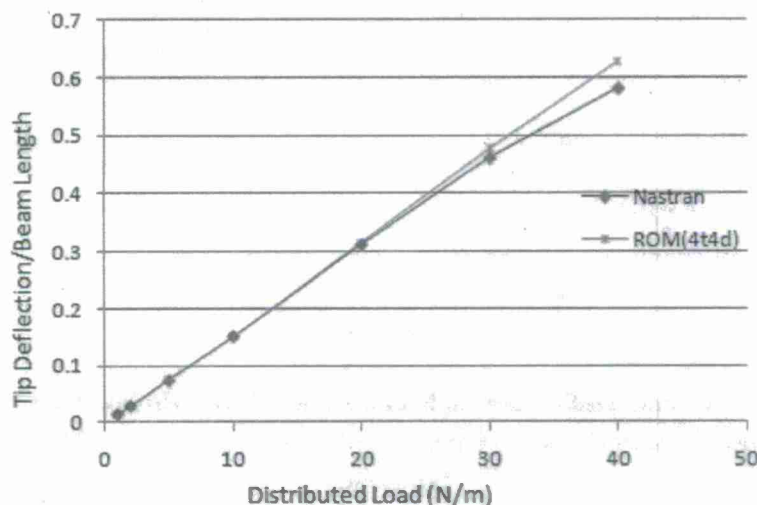


Figure 8 Tip Transverse Deflection vs. Static Load, Beam Model. Full Nastran and 4-Transverse - 4 Dual Modes Reduced Order Model ("ROM(4t4d)"), 20% Inplane Compressive Tip Load

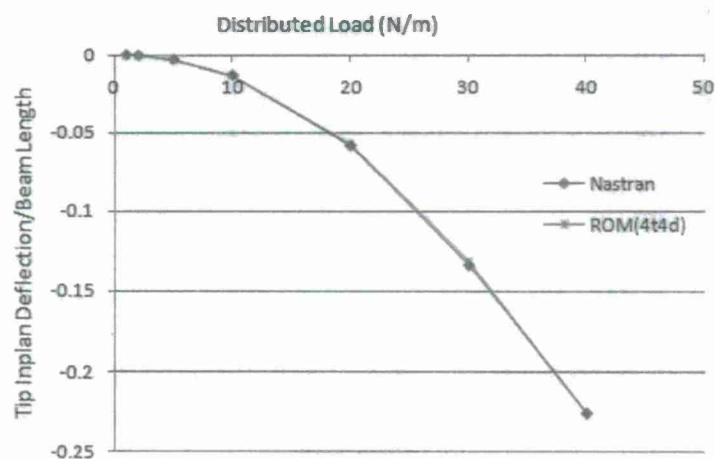


Figure 9 Tip Inplane Deflection vs. Static Load, Beam Model. Full Nastran and 4-Transverse - 4 Dual Modes Reduced Order Model ("ROM(4t4d)"), 20% Inplane Compressive Tip Load

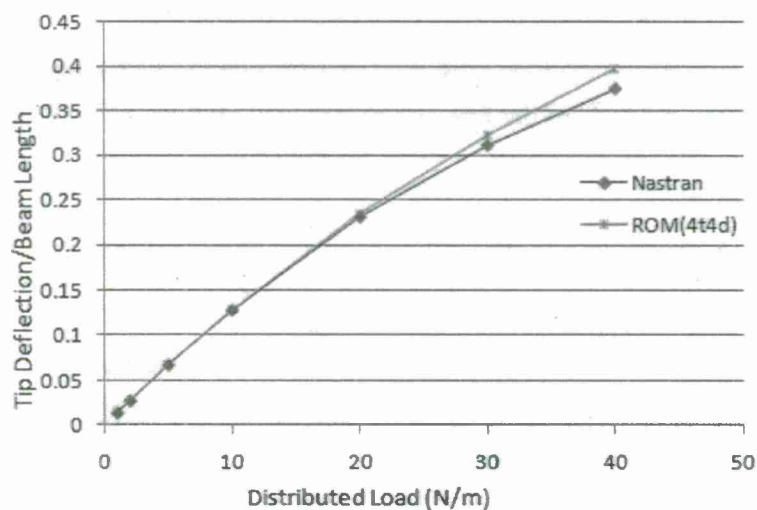


Figure 10 Tip Transverse Deflection vs. Static Load, Beam Model. Full Nastran and 4-Transverse – 4 Dual Modes Reduced Order Model (“ROM(4t4d)”), 20% Inplane Tensile Tip Load

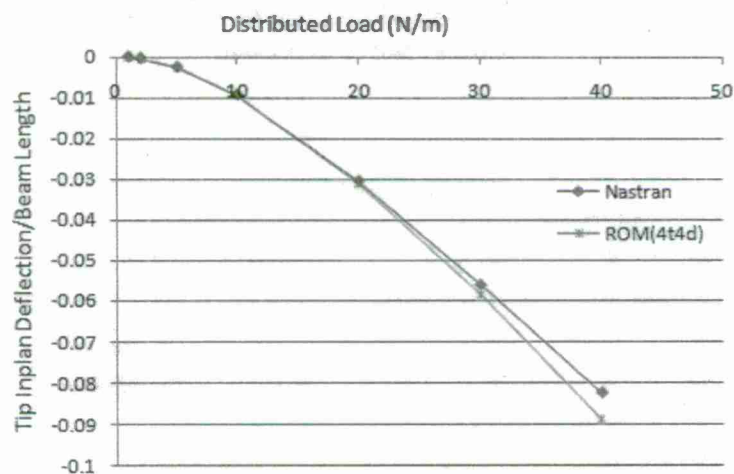


Figure 11 Tip Inplane Deflection vs. Static Load, Beam Model. Full Nastran and 4-Transverse – 4 Dual Modes Reduced Order Model (“ROM(4t4d)”), 20% Inplane Tensile Tip Load

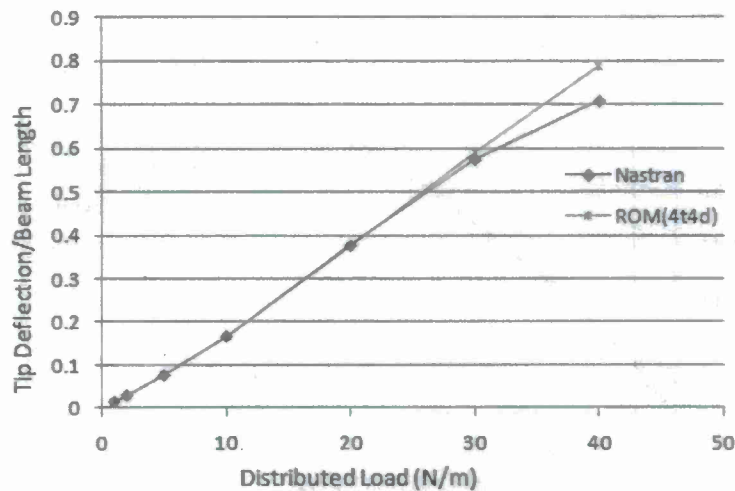


Figure 12 Tip Transverse Deflection vs. Static Load, Beam Model. Full Nastran and 4-Transverse - 4 Dual Modes Reduced Order Model ("ROM(4t4d)"), 40% Inplane Compressive Tip Load

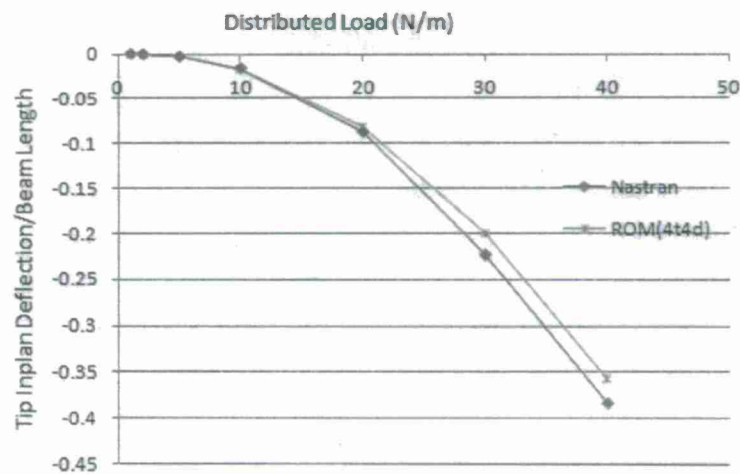


Figure 13 Tip Inplane Deflection vs. Static Load, Beam Model. Full Nastran and 4-Transverse - 4 Dual Modes Reduced Order Model ("ROM(4t4d)"), 40% Inplane Compressive Tip Load

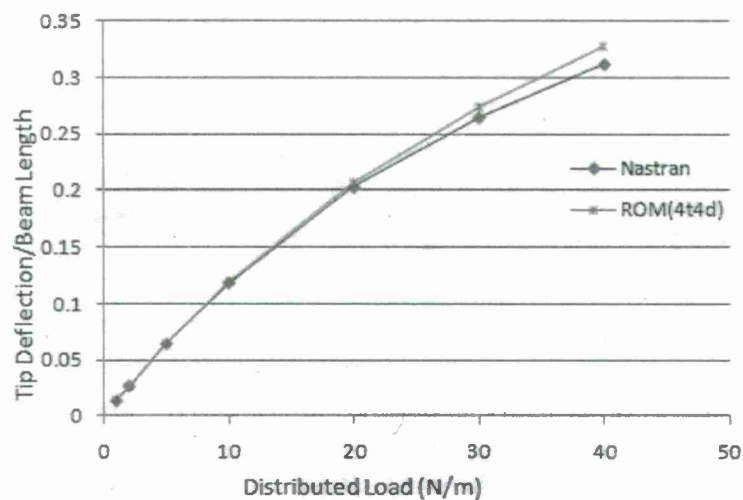


Figure 14 Tip Transverse Deflection vs. Static Load, Beam Model. Full Nastran and 4-Transverse – 4 Dual Modes Reduced Order Model (“ROM(4t4d)”), 40% Inplane Tensile Tip Load

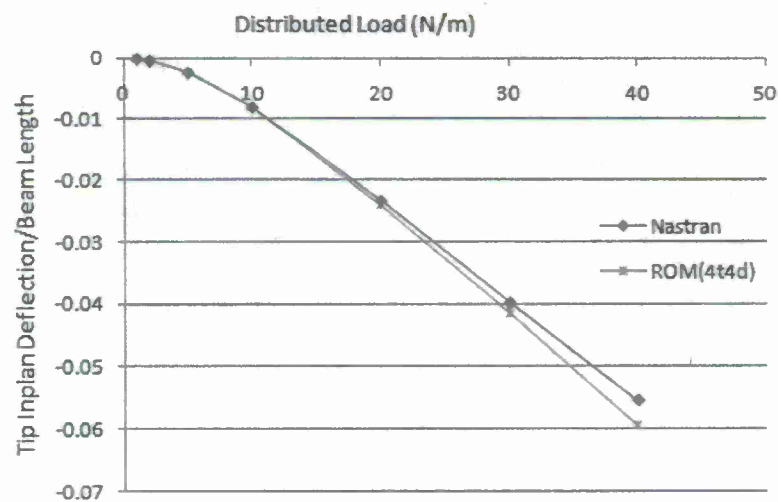


Figure 15 Tip Inplane Deflection vs. Static Load, Beam Model. Full Nastran and 4-Transverse – 4 Dual Modes Reduced Order Model (“ROM(4t4d)”), 40% Inplane Tensile Tip Load

These plots demonstrate the capability of the “decondensed” model to generate transverse and inplane displacements of the model, for static load, with high precision.

3.3 DYNAMIC TRANSVERSE LOAD

Acknowledging the validated of the “decondensed” reduced order model in static situations, it was desired next to assess its predictive capabilities in dynamic situations. To this end, a random excitation, white noise in the frequency domain [0,600] Hz, was applied in the transverse direction without axial load. Three different excitation levels were considered corresponding to standard deviations of 6, 24, and 48 N/m. The power spectrum of the tip displacement in the transverse and axial directions are shown in Figure 16 and 17 for the former and latter excitation case, respectively, for both Nastran SOL 400 and the 4 transverse - 4 dual decondensed reduced order model. Note the near perfect matching between the Nastran and reduced order model predictions over the entire frequency range of excitation and for all the cases.

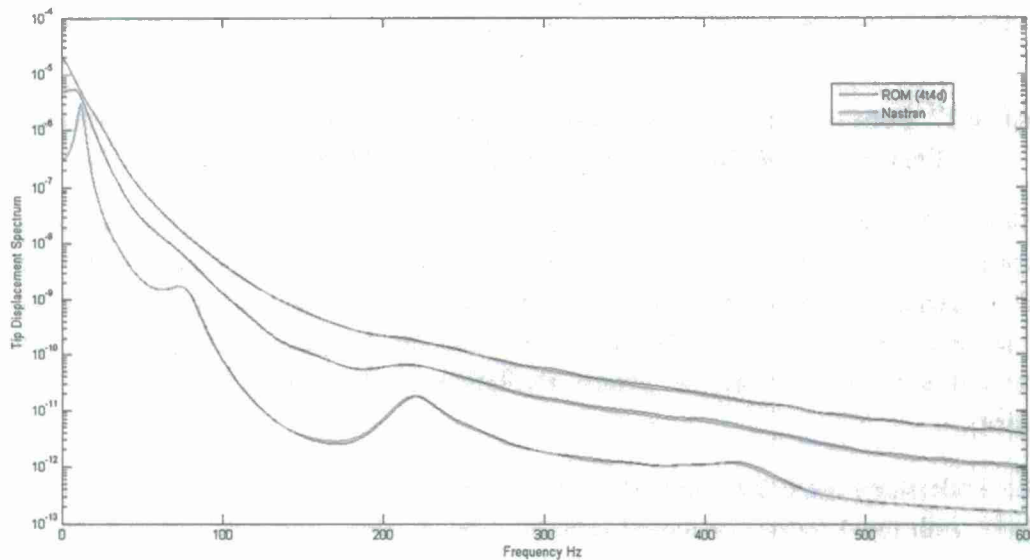


Figure 16 Power Spectra of the Random Tip Transverse Response Full Nastran and 4 Transverse – 4 Dual Modes Reduced Order Model ('ROM(4t4d)')

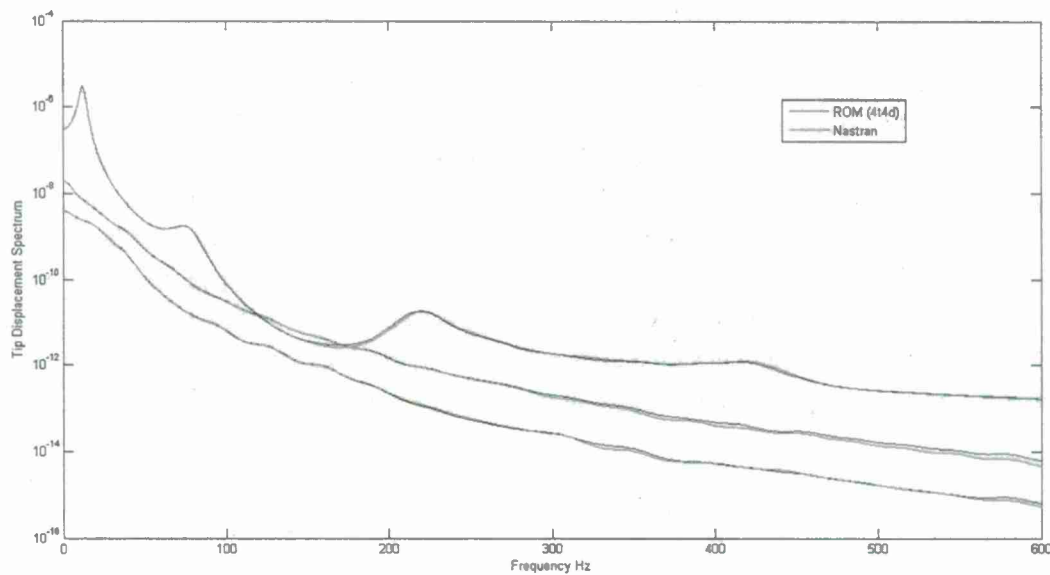


Figure 17 Power Spectra of the Random Tip Inplane Response Full Nastran and 4 Transverse – 4 Dual Modes Reduced Order Model ('ROM(4t4d)')

Interestingly, the two corresponding standard deviations of the transverse tip displacement are not in the ratio 1 to 8 as the excitation as might have been construed from the near linearity of the static displacement vs. load of Figure 2. These standard deviations are 0.0062, 0.0132, and 0.0192 m or 2.7%, 5.8%, and 8.5% of the beam length. In fact, the shape of the transverse displacement spectra, even at the lowest excitation level, clearly suggest the presence of nonlinearity.

To better understand these seemingly different results, similar response computations were also carried out with the 4-mode condensed reduced order model. These results, e.g. see Figure 8, demonstrate indeed that the condensed model behaves nearly linearly. This observation is further supported by the standard deviations of the tip transverse displacements which were found to be 0.0228, 0.0912, and 0.15514 m or 10%, 39.9%, and 67.9%. Thus, the condensed model is nearly linear until the largest load case.

As expected by construction, see Figure 18, the condensed model predictions match their decondensed counterparts (and the Nastran results) in the zero frequency limit but deviate otherwise demonstrating that the increased nonlinearity observed in the dynamic case as opposed to the static one originates from the inertia and damping terms of the inplane motions. These results indicate that the considered condensed model of cantilever structures may reflect well the static nonlinear behavior but may not be appropriate in dynamic conditions.

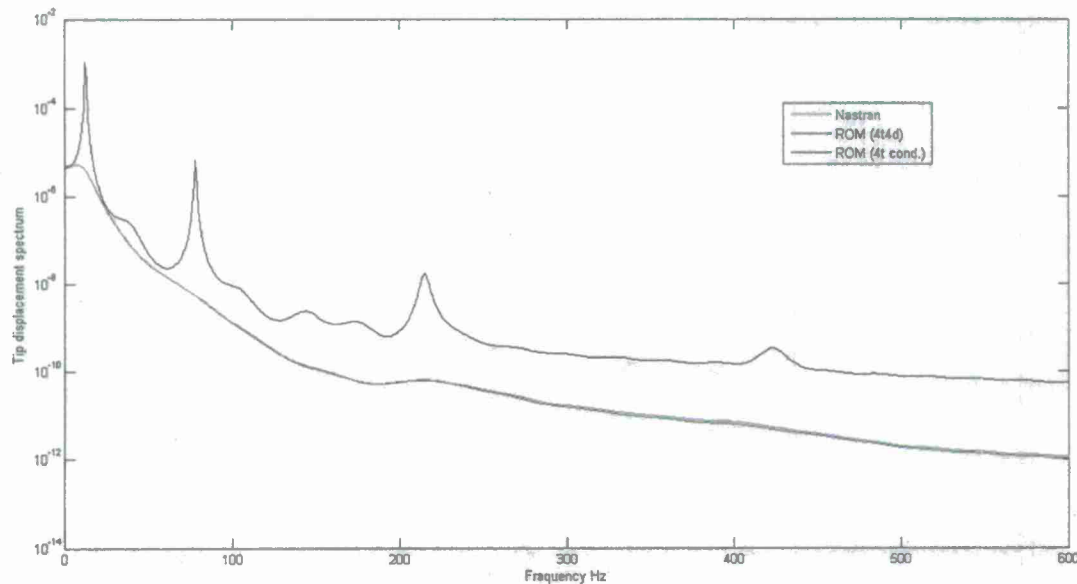


Figure 18 Power Spectra of the Random Tip Transverse Response, 24N/m RMS Excitation. Full Nastran, 4 Transverse – 4 Dual Modes Reduced Order Model ('ROM(4t4d)'), and 4 Transverse Condensed Reduced Order Model ('ROM(4t Cond.)')

3.4 DYNAMIC TRANSVERSE AND STATIC INPLANE LOAD

Having successfully demonstrated the validation for dynamic transverse loading, now the model is subjected to dynamic transverse combined with static inplane load. The same excitation is used for loading in transverse direction i.e. white noise in the frequency domain [0,600] Hz, with corresponding standard deviations of 6 and 24 N/m, with an static inplane load added to it. The inplane load is applied as 40% and 80% of the buckling load (estimated from Nastran Sol105) of the beam structure. These standard deviations for 6N/m and 24N/m dynamic transverse load, with 40% and 80% buckling static load inplane load, are 0.0113, 0.0168, 0.0268 and 0.0339 m or 5%, 7.3%, 11.7% and 14.8% of beam length respectively.

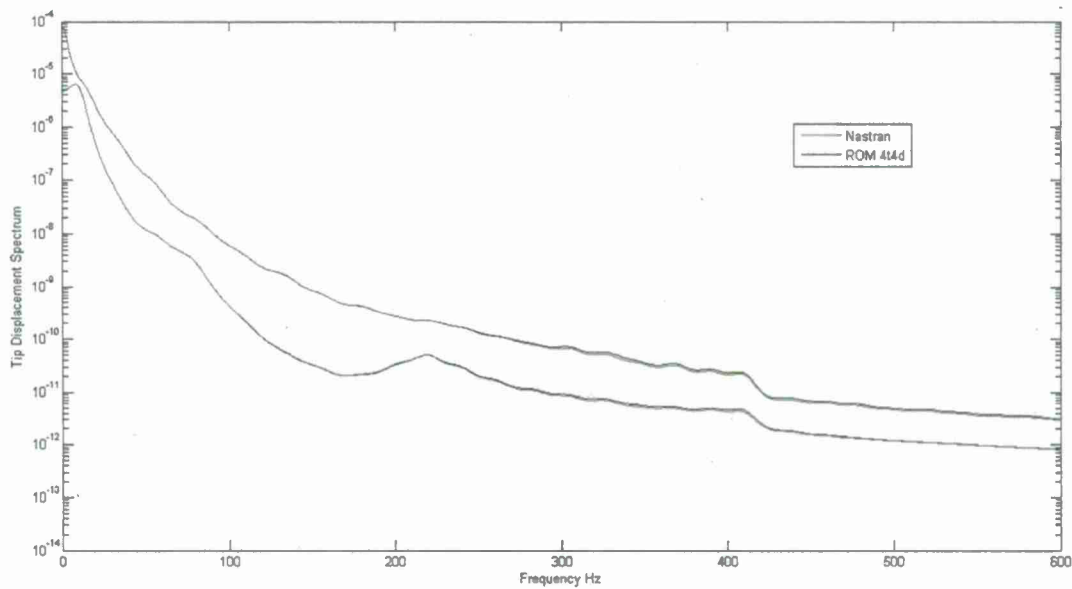


Figure 19 Power Spectra of the Random Tip Transverse Response Full Nastran and “Decondensed” Reduced Order Model (‘ROM(4t4d)’) for 40% Static Inplane Buckle Load

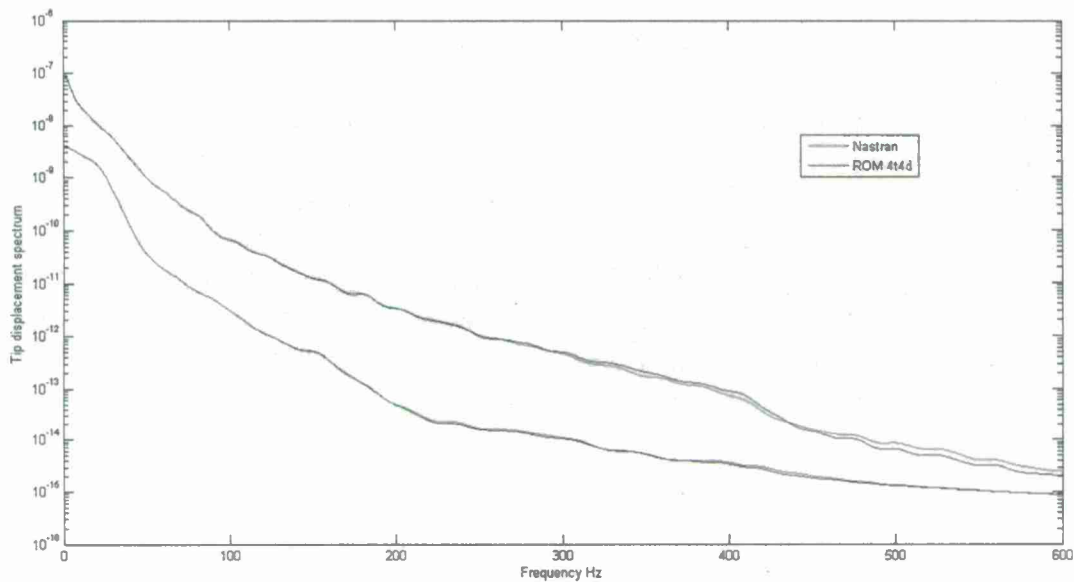


Figure 20 Power Spectra of the Random Tip Inplane Response Full Nastran and “Decondensed” Reduced Order Model (‘ROM(4t4d)’) for 40% Static Inplane Buckle Load

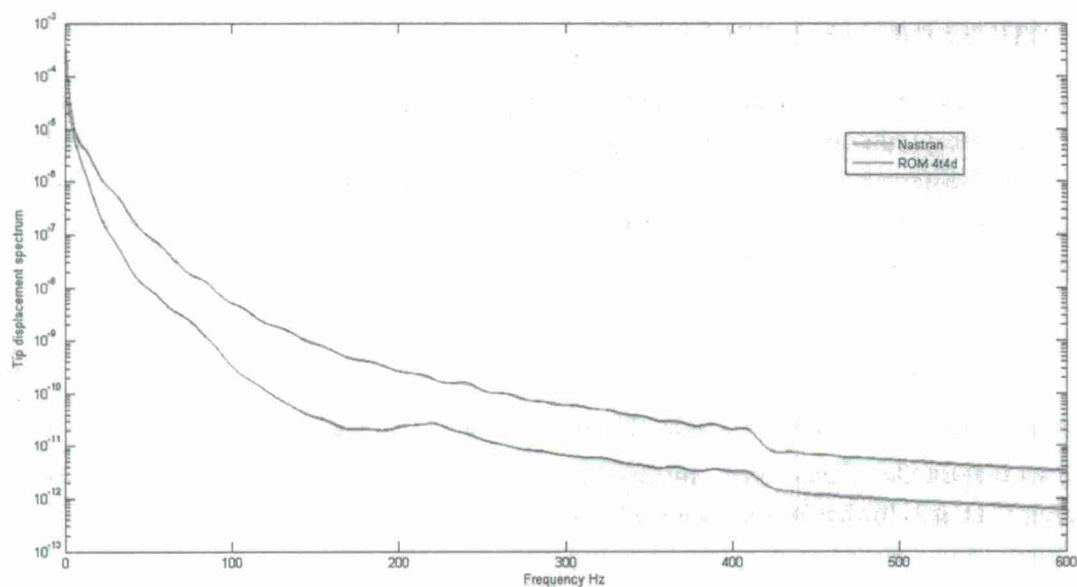


Figure 21 Power Spectra of the Random Tip Transverse Response Full Nastran and “Decondensed” Reduced Order Model (‘ROM(4t4d)’ for 80% Static Inplane Buckle Load

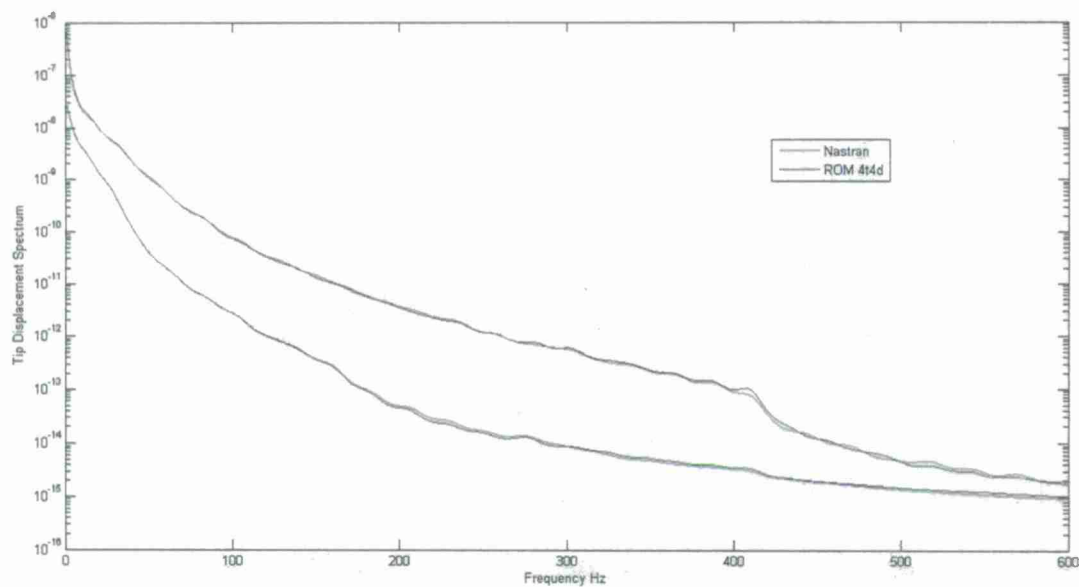


Figure 22 Power Spectra of the Random Tip Inplane Response Full Nastran and “Decondensed” Reduced Order Model (‘ROM(4t4d)’ for 80% Static Inplane Buckle Load

3.5 BUCKLING LOAD PREDICTION

The last validation of the reduced order modeling strategy and the decondensation procedure focused on the prediction of the buckling tip load and of the post-buckling deflection of the beam. The Nastran buckling load was obtained using SOL 105 and was found to be 5.00lbs. The estimate of this load from the reduced order model was obtained under similar linear static assumptions, i.e. the inplane Equation (18) were solved first to yield

$$q_j^{(i)} = [K^{(ii)}]_{ji}^{-1} F_i^{(i)} N \quad (28)$$

where $F_i^{(i)}$ denote the inplane modal forces associated with a unit tip force while N is the unknown magnitude of this force. Introducing the above expression in the transverse equations, Equation (21), and further linearizing lead in the static case to the condition

$$K_{ij}^{(ii)} q_j^{(i)} = (-N) \left\{ K_{ijl}^{(2i)} [K^{(ii)}]_{lp}^{-1} F_p^{(i)} \right\} q_j^{(i)} \quad (29)$$

which is recognized as a generalized eigenvalue problem in which $-N$ is the eigenvalue. This process led to the estimate of 5.01lbs for the tip load.

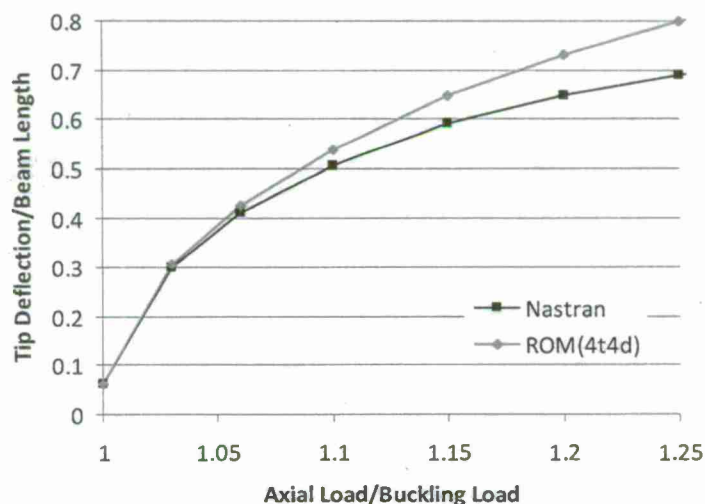


Figure 23 Post Buckling Tip Transverse Deflection vs. Axial Only Load. Full Nastran and Transverse – 4 Dual Modes Reduced Order Model (“ROM(4t4d)”)

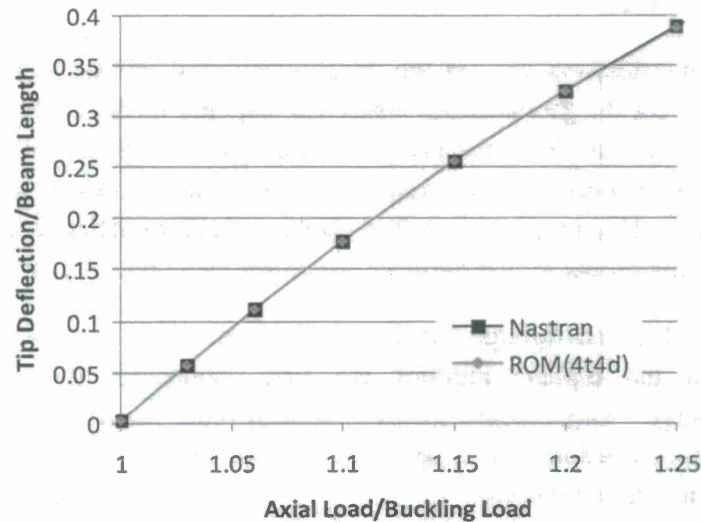


Figure 24 Post Buckling Tip Inplane Deflection vs. Axial Only Load. Full Nastran and Transverse – 4 Dual Modes Reduced Order Model (“ROM(4t4d)”)

Given this very good matching of the buckling load, an analysis of the post-buckling behavior was undertaken. That is, the tip load was increased past its buckling value and the static displacement of the beam tip in both transverse and inplane directions was computed by both NASTRAN SOL 106 and the 8-mode reduced order model. These results are shown in Figures 23 and 24.

It is clearly seen that the reduced order model accurately captures the post buckling behavior for transverse deflections as large as 40%-50% of the beam length. For larger deflections, a steadily growing difference with the Nastran results is observed, similarly to Figures 3 and 8-11. This difference with Nastran is rooted in the specification in the reduced order model of the linearly elastic behavior between the undeformed stress and strain tensors. This is in contrary to Nastran which specifies a similar property between the deformed stress and strain tensors. As discussed in Equations (2)-(5), this difference becomes increasing more visible as the level of deformation increases and the deformation gradient tensor $\underline{\underline{F}}$ becomes less and less identity-like, exactly as seen in Figures 3, 6-10, and 11.

4. CONCLUSION

The focus of this investigation was on the development and validation of structural dynamic reduced order models for the geometrically nonlinear response of flat cantilevered structures, e.g. beams and plates. It was first observed that the static displacement vs. load curves of cantilevered structures exhibit a rather weak nonlinearity as compared to those for structures supported on all sides. This property was then shown to lead to difficulties in obtaining a stable nonlinear reduced order model for cantilevered structures using recently proposed algorithms.

This difficulty was resolved through the introduction of a two-step reduced order modeling approach in which the inplane motions are first condensed, then reintroduced in the "decondensation" stage. This process led to a reduced order model exhibiting both transverse and inplane degrees of freedom that is applicable for all loading conditions: transverse forces, inplane forces or combination thereof.

This reduced order modeling approach was assessed primarily on a cantilever beam model subjected first to static transverse alone, transverse-inplane, and inplane alone (buckling and post buckling) loads. In all cases, an excellent agreement with the corresponding Nastran results was observed for transverse displacements up to 40%-50% of beam length. Above that range, it was demonstrated that the difference between the reduced order model and Nastran results originates from a difference in the definition of the linearly elastic behavior, which is stated between the undeformed stress and strain tensors in the reduced order model and the deformed ones in Nastran.

An assessment of the reduced order model under dynamic transverse loads was also carried out with the same success and demonstrated the need to include the inplane inertia and damping terms in the model for an accurate prediction of the response.

REFERENCES

- Bonet, J., and Wood, R.D., 1997: *Nonlinear continuum mechanics for finite element analysis*, Cambridge University Press, Cambridge.
- Fung, Y.C., and Tong, P., 2001: *Classical and computational solid mechanics*, World Scientific, River Edge, New Jersey.
- Gordon R.W., and Hollkamp, J.J., 2006: "Reduced-order modeling of the random response of curved beams using implicit condensation," AIAA-2006-1926.
- Hollkamp, J.J., Gordon, R.W., and Spottswood, S.M., 2005: "Nonlinear modal models for sonic fatigue response prediction: a comparison of methods," *Journal of Sound and Vibration*, 284, pp. 1145-1163.
- Kim, K., Kim, Y.C., Mignolet, M.P., Liu, D.D., Chen, P.C., Lee, D.H., 2007: "Random aeroelastic response due to strong hypersonic unsteady-wave/shock interaction with acoustic loads," *Proceedings of the 48th Structures, Structural Dynamics and Materials Conference*, Honolulu, Hawaii, Apr. 23-26. AIAA Paper AIAA-2007-2014.
- Kim, K., Wang, X.Q., and Mignolet, M.P., 2008: "Nonlinear reduced order modeling of functionally graded plates," *Proceedings of the 49th Structures, Structural Dynamics and Materials Conference*, Schaumburg, Illinois, Apr. 7-10. AIAA Paper AIAA-2008-1873.
- McEwan, M.I., Wright, J.R., Cooper, J.E., and Leung, A.Y.T., 2001: "A combined modal/finite element analysis technique for the dynamic response of a nonlinear beam to harmonic excitation," *Journal of Sound and Vibration*, 243, pp. 601-624.
- Mignolet, M.P., Radu, A.G., and Gao, X., , 2003 "Validation of reduced order modeling for the prediction of the response and fatigue life of panels subjected to thermo-acoustic effects," *Proceedings of the 8th International Conference on Recent Advances in Structural Dynamics*, Southampton, United Kingdom, Jul. 14-16.
- , and Soize, C., 2008: "Stochastic reduced order models for uncertain geometrically nonlinear dynamical systems," *Computer Methods in Applied Mechanics and Engineering*.
- Muravyov, A.A., and Rizzi, S.A., 2003: "Determination of nonlinear stiffness with application to random vibration of geometrically nonlinear structures," *Computers and Structures*, 81, pp. 1513-1523.
- Przekop A., and Rizzi S.A., 2006: "Nonlinear reduced order random response analysis of structures with shallow curvature," *AIAA Journal*, 44 (8), pp. 1767-1778.
- Radu, A., Yang, B., Kim, K., and Mignolet, M.P., 2004: "Prediction of the dynamic response and fatigue life of panels subjected to thermo-acoustic loading," *Proceedings of the 45th*

Structures, Structural Dynamics and Materials Conference, Palm Springs, California, Apr. 19-22,. Paper AIAA-2004-1557.

Spottswood, S.M., Holikamp, J.J., and Eason, T.G., 2008: "On the use of reduced-order models for a shallow curved beam under combined loading," *Proceedings of the 49th Structures, Structural Dynamics and Materials Conference*, Schaumburg, Illinois, Apr. 7-10. AIAA-2008-1873.

REPORT DOCUMENTATION PAGE					Form Approved OMB No. 0704-0188	
The public reporting burden for this collection of information is estimated to average 1 hour per response, including the time for reviewing instructions, searching existing data sources, gathering and maintaining the data needed, and completing and reviewing the collection of information. Send comments regarding this burden estimate or any other aspect of this collection of information, including suggestions for reducing the burden, to the Department of Defense, Executive Service Directorate (0704-0188). Respondents should be aware that notwithstanding any other provision of law, no person shall be subject to any penalty for failing to comply with a collection of information if it does not display a currently valid OMB control number.						
PLEASE DO NOT RETURN YOUR FORM TO THE ABOVE ORGANIZATION.						
1. REPORT DATE (DD-MM-YYYY) 31-03-2010		2. REPORT TYPE Final Technical		3. DATES COVERED (From - To) 01-10-2078 -- 31-03-2010		
4. TITLE AND SUBTITLE Continuous Dynamic Simulation of Nonlinear Aerodynamics/Nonlinear Structure Interaction (NANSI) for Morphing Vehicles				5a. CONTRACT NUMBER FA9550-08-C-0004		
				5b. GRANT NUMBER		
				5c. PROGRAM ELEMENT NUMBER		
				5d. PROJECT NUMBER		
6. AUTHOR(S) PI: Ping-Chih Chen, pc@zonatech.com				5e. TASK NUMBER		
				5f. WORK UNIT NUMBER		
7. PERFORMING ORGANIZATION NAME(S) AND ADDRESS(ES) ZONA Technology, Inc. 9489 E. Ironwood Square Drive Scottsdale, AZ 85258 Tel (480) 945-9988 / Fax (480) 945-6588				8. PERFORMING ORGANIZATION REPORT NUMBER		
9. SPONSORING/MONITORING AGENCY NAME(S) AND ADDRESS(ES) Air Force Office of Scientific Research 875 North Randolph Street, Suite 325, Room 3112 Arlington, VA 22203-1977				10. SPONSOR/MONITOR'S ACRONYM(S) AFOSR		
				11. SPONSOR/MONITOR'S REPORT NUMBER(S) AFRL-OSR-VA-TR-2012-0154		
12. DISTRIBUTION/AVAILABILITY STATEMENT Distribution A						
13. SUPPLEMENTARY NOTES						
14. ABSTRACT In this report, we present the ZONA team's effort for this Phase II project. The ZONA team is made up of ZONA Technology, Inc. (ZONA), Arizona State University (Research Institute), and Professor Feng Liu (Consultant). The objective for this project was to develop a nonlinear aerodynamic and nonlinear structural interaction (NANSI) methodology as an expedient aeroelastic tool to handle continuous dynamic motion of morphing vehicles/wings from incompressible/subsonic to transonic flight regimes. The proposed vehicle for method demonstration was the Lockheed Folding wing (the Folding wing). Results showing the Flutter LCO of the Folding wing in continuous pitching and the Finite Element Model (FEM) development/aeroelastic stability analysis of a morphing MAV, or the Gull wing/MAV, are presented.						
15. SUBJECT TERMS						
16. SECURITY CLASSIFICATION OF:			17. LIMITATION OF ABSTRACT SAR	18. NUMBER OF PAGES 289	19a. NAME OF RESPONSIBLE PERSON Ping-Chih Chen	
a. REPORT U	b. ABSTRACT U	c. THIS PAGE U			19b. TELEPHONE NUMBER (Include area code) (480) 945-9988	